Numerical investigation of particle-fluid interaction system based on discrete element method

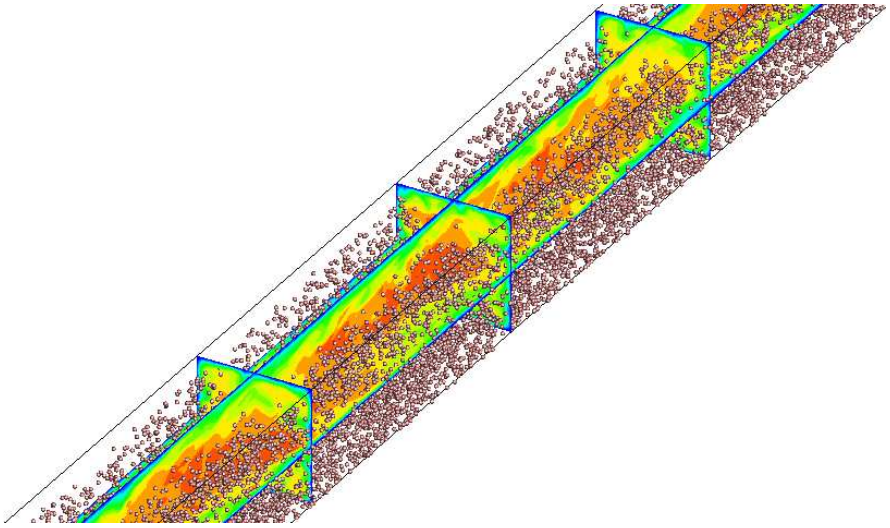

Centre Tecnològic de Transferència de Calor
Departament de Màquines i Motors Tèrmics
Universitat Politècnica de Catalunya

Hao Zhang

Doctoral Thesis

Numerical investigation of particle-fluid interaction system based on discrete element method

Hao Zhang

TESI DOCTORAL

presentada al

Departament de Màquines i Motors Tèrmics
E.T.S.E.I.A.T.
Universitat Politècnica de Catalunya

per a l'obtenció del grau de

Doctor per la Universitat Politècnica de Catalunya

Terrassa, Novembre, 2014

Numerical investigation of particle-fluid interaction system based on discrete element method

Hao Zhang

Directors de la Tesi

Dr. Assensi Oliva Llena
Dr. Francesc Xavier Trias Miquel

Tribunal Qualificador

Dr. Antonio Lecuona Neumann
Universidad Carlos III de Madrid

Dr. Antonio Pascau Benito
Universidad de Zaragoza

Dr. Carlos David Pérez Segarra
Universitat Politècnica de Catalunya

A mi precioso hijo, Yanbo,
mi encantadora esposa,
mis queridos padres.

Agradecimientos

Me gustaría aprovechar esta oportunidad para expresar mis sinceros agradecimientos mis supervisores : Prof. Assensi Oliva Llena y Dr. Francesc Xavier Trias Miquel. Quiero agradecer a Assensi por darme la oportunidad de estudiar en el CTTC. Para mí, es simplemente difícil de describir con palabras mi vida estos cuatro años en Barcelona. Quiero decir que la trayectoria de mi vida ha cambiado desde que yo viví y trabajé en el CTTC , a una mejor dirección, estoy seguro. Gracias, Assensi! Xavi jugó muchos papeles durante estos años como un tutor de la tesis en el trabajo, un amigo en la vida, un socio en la investigación y un compañero de equipo en los partidos de fútbol. La mayor parte del trabajo en esta tesis se ha terminado con la ayuda de Xavi, la mayor parte de las ideas en esta tesis se ha producido a través de las conversaciones con Xavi y la mayor parte de las publicaciones en esta tesis se han realizado con la cuidadosa supervisión de Xavi. Me gustaría decir en forma tanto privada y pública, que una de los mejores cosas que me han pasado en Terrassa o incluso en toda mi vida, es tener al frente a un profesor y amigo como Xavi.

Gracias al Prof. Carlos D. Pérez Segarra y Joaquim Rigola, por sus disposiciónes a preocuparse de mi trabajo en el CTTC. Una cosa que es imposible a borrar de mi mente es que cuando mis familias tuvieron algunos problemas en China, David y Assensi me dieron valiosas sugerencias y consejos, y nos han apoyaron para superar las dificultades. Apreciamos todas estas ayudas, sinceramente.

Gracias al Dr. Andrey V. Gorobets que es uno de los hombres más inteligente que he conocido, el siempre podía resolver los problemas fácilmente pero que me hacían sufrir mucho. Andrey me ayudó a comprender y utilizar el código de DNS y nunca se sintió molesto en dar respuesta a mis preguntas. Para ser honesto, las partículas no pueden ni siquiera hacer un movimiento en el Turbulent flows sin la ayuda de Moscú. Por favor, Andrey mantén fluyendo las partículas.

Gracias a Xiaofei Hou, mi hermano. Es muy difícil imaginar la vida de cuatro años en Terrassa sin él. Seguramente la historia sería distinta, supongo. Desde el momento en que yo estaba en China, antes de todo lo que pasó, él me ayudaba con los problemas del Visado y la preparación para comenzar la vida en España. Él ha estado conmigo y me ayuda desde el momento más difícil hasta ahora, la amistad nunca termina. Gracias, tío.

Gracias a Guillermo Oyarzun, Santiago Torras, Pedro Galione y Nicolás Ablanque, los jugadores permanentes en el partido de fútbol de rutina del CTTC. No podría pedir más cuando tengo estos amigos que hacen que mi vida de colores.

Gracias a Firas Dabbagh, Ahmed Hachicha, Oussama Souaihi y Hamdi Kessentini, la Primavera Árabe. Gracias a todos los miembros en el CTTC por hacerme sentir como una gran familia.

Gracias a mis profesores de castellano, Raura y Montse. Para mí sería imposible hablar o escribir español sin ellos. Admiro sus pasión por la enseñanza y aprecio su cuidadosa orientación en mi estudio.

Agradecimiento especial a Prof. Yuanqiang Tan, Prof. Shi Shu, Prof. Yunqing Huang, Prof. Mingjun Li y Prof. Xiaodong Niu de la Universidad de Xiangtan en China, Dr. Dongmin Yang y Dr. Yong Sheng de la Universidad de Leeds en UK. Son mis orientadores y modelos a seguir en lo que quiero ser. Gracias por el gran apoyo recibido de todos ustedes.

Durante estos años, mi esposa Hui ha sacrificado mucho, nada de otros momentos de felicidad es comparable con cualquier momento que me quedo con ella y mi precioso hijo, Yanbo. Os amo.

La tesis está dedicada a la memoria cariñosa de mi difunta suegra, señora Juhua Xu. Te extrañamos mucho.

Finalmente, me gustaría agradecer la beca de doctorado FI-AGAUR otorgado por la Secretaria d'Universitats i Recerca (SUR) del Departament d'Economia i Coneixement (ECO) de la Generalitat de Catalunya, y por el Fondo Social Europeo. Las simulaciones en esta tesis se han realizado en el IBM MareNostrum supercomputadora del Centro de Supercomputación de Barcelona. El autor agradece a estas instituciones.

Abstract

At present, a lot of phenomena in the particle-fluid system has not been well understood yet. The essential reason is the lack of understanding of the interaction mechanism between the fluid and solid phase as well as the inter-particle collisions. Due to the stochastic nature of the solid particle behaviors, the particle-fluid interaction problems are often too complex to be solved analytically or observed by physical experiments. Therefore, they have to be analyzed by means of numerical simulations. This thesis focuses on the numerical investigation of the particle-fluid systems based on the Discrete Element Method (DEM). The whole thesis consists of three parts, in each part we have coupled the DEM with different schemes/solvers on the fluid phase. In the first part, we have coupled DEM with Direct Numerical Simulation (DNS) to study the particle-laden turbulent flow. In the second part, we have coupled DEM with Lattice Boltzmann Method (LBM) to study the particle sedimentation in Newtonian laminar flow. In the last part, we have coupled DEM with averaged Navier-Stokes equations (NS) to study the particle transportation and wear process on the pipe wall. The contents of each chapter are presented as below:

In the first chapter, the background of the thesis was briefly introduced, a survey on the research status relevant to this thesis was conducted. The research contents and motivation of this thesis were presented.

In the second chapter, the theoretical and numerical issues of DEM were introduced. A parallelization of a DEM based code titled Trubal was implemented. Trubal was reconstructed in two steps and numerical simulations were carried out to present the benefits of this research. Firstly, two simulations of die filling with a moving shoe involving 6000 and 60000 two-dimensional particles were conducted under (i) NVIDIA Tesla C2050 card together with Intel Core-Duo 2.93 GHz CPU and (ii) NVIDIA Tesla K40c card along with Intel Xeon 3.00GHz CPU. Average speedups of (i) 4.69 and 12.78 and (ii) 6.52 and 18.60 in computational time were obtained, respectively. Then, a simulation of die filling with a stationary shoe containing 20000 three-dimensional particles was carried out under the same conditions where average speedups of (i) 12.90 and (ii) 19.66 in computational time were obtained, respectively.

In the third chapter, the effect of collisions on the particle behavior in fully developed turbulent flow in a straight square duct at $Re_\tau = 300$ was numerically investigated. The hydrodynamic modeling of the fluid phase was based on DNS. The kinematics and trajectory of the particles as well as the collisions were described by the DEM. Three sizes of particles were considered with diameters equal to 50 μm, 100 μm and 500 μm. Firstly, the particle transportation by turbulent flow was studied in the absence of the gravitational effect. Then, the particle deposition was studied under the effect of the wall-normal gravity force in which the influence of collisions on

the particle resuspension rate and the final stage of particle distribution on the duct floor were discussed, respectively.

In the forth chapter, a novel combined LBM-Immersed Boundary Method(IBM)-DEM scheme was presented with its application to model the sedimentation of two-dimensional circular particles in incompressible Newtonian flows. The hydrodynamic model of the incompressible Newtonian flow was based on the Bhatnagar-Gross- Krook LBM, and a momentum exchange-based IBM was adopted to calculate the fluid-solid interaction force. The kinematics and trajectory of the discrete particles were evaluated by DEM. Case studies of single sphere settling in a cavity, and two particles settling in a channel were carried out, the velocity characteristics of the particle during settling and near the bottom were examined. At last, a numerical example of sedimentation involving 504 particles was finally presented to demonstrate the capability of the combined scheme.

In the fifth chapter, a Particulate Immersed Boundary Method (PIBM) for simulating the fluid-particle multiphase flow was presented and assessed in both two- and three-dimensional applications. The idea behind the PIBM derived from the conventional momentum exchange-based IBM by treating each Lagrangian point as a solid particle. Compared with the conventional IBM, dozens of times speedup in two-dimensional simulation and hundreds of times in three-dimensional simulation can be expected under the same particle and mesh number. Numerical simulations of particle sedimentation in the Newtonian flows were conducted based on a combined LBM - PIBM - DEM, showing that the PIBM could capture the feature of the particulate flows in fluid and was indeed a promising scheme for the solution of the fluid-particle interaction problems.

In the sixth chapter, a coupling model of NS-DEM was developed to study the solid-fluid multiphase flow problem in concrete pumping progress. The motion of the continuous fluid phase was evaluated by a Navier-Stokes solver, and a pressure gradient force model was adopted to calculate the solid-fluid interaction force. A case of pneumatic conveying was utilized to demonstrate the capability of the coupling model. The concrete pumping process was then simulated, where the hydraulic pressure and velocity distribution of the fluid phase were obtained. The frequency of the particles impacting on the bended pipe was monitored, a new time average collision intensity model based on impact force was proposed to investigate the wear process of the elbow. The location of maximum erosive wear damage in elbow was predicted. Furthermore, the influences of slurry velocity, bend orientation and angle of elbow on the puncture point location were discussed.

Finally, in the last chapter, the contents and innovations of this thesis were briefly summarized with the future researches prospected.

Contents

Acknowledgements **9**

Abstract **11**

1 Introduction **25**
1.1 Short history of Discrete Element Method . . . 25
1.2 Particle-laden turbulent flow in a square duct . . . 26
1.2.1 Single phase turbulent flows in straight square ducts . . . 27
1.2.2 Particle-laden turbulent flow in a square duct . . . 27
1.2.3 Motivation and summary of the present work . . . 29
1.3 LBM-IBM-DEM . . . 30
1.3.1 Motivation and summary of the present work . . . 32
1.4 LBM-PIBM-DEM . . . 33
1.4.1 Motivation and summary of the present work . . . 34
1.5 Particle transportation and wear investigation . . . 35
1.5.1 Motivation and summary of the present work . . . 36
References . . . 37

2 Discrete element method and its application **49**
2.1 Short introduction of GPU-DEM . . . 50
2.2 Governing equations of DEM . . . 51
2.3 Contact detection between the elements . . . 53
2.4 Difference scheme and the timestep . . . 54
2.5 CPU vs GPU . . . 55
2.5.1 Numerical strategy: Two simulators under CPU . . . 55
2.5.2 GPU Computing and a simulator under CPU-GPU . . . 57
2.6 Numerical experiments . . . 59
2.6.1 Die filling with a moving shoe: two-dimensional Case . . . 60
2.6.2 Die filling with a stationary shoe: three-dimensional Case . . . 65
2.7 Conclusions . . . 68
References . . . 68

3 Effect of collisions on the particle behavior in a turbulent square duct flow **71**
3.1 Mathematical descriptions . . . 73
3.1.1 Governing equations and numerical methods for DNS . . . 73
3.1.2 Modeling of particle-fluid and particle-particle interactions . . . 74
3.1.3 Subcyling approaching on the timesteps . . . 74
3.2 Verification and validation . . . 75

3.2.1 Verification of the DNS code . . . 75
3.2.2 Verification of the simulation: Comparing with Gavrilakis [11] . 76
3.3 Results and discussion . . . 80
3.3.1 Particle transportation . . . 80
3.3.2 Particle resuspension . . . 86
3.3.3 Particle deposition . . . 96
3.4 Concluding remarks . . . 102
References . . . 104

4 Numerical investigation on the role of discrete element method in combined LBM-IBM-DEM modeling 107
4.1 Governing equations . . . 109
4.1.1 Lattice Boltzmann model with single-relaxation time collision . 109
4.1.2 Immersed boundary method and the hydrodynamics interaction force . . . 110
4.2 Coupling scheme . . . 112
4.3 Numerical results and discussions . . . 113
4.3.1 Sedimentation of a circular particle in a cavity I . . . 113
4.3.2 Sedimentation of a circular particle in a cavity II . . . 115
4.3.3 Bouncing motion of particles near bottom . . . 116
4.3.4 Sedimentation of two circular particles in a channel . . . 118
4.3.5 Sedimentation of 504 circular particles in a cavity . . . 122
4.4 Concluding remarks . . . 130
References . . . 130

5 PIBM: Particulate immersed boundary method for fluid-particle interaction problems 133
5.1 Governing equations . . . 134
5.1.1 Lattice Boltzmann model with single-relaxation time collision . 134
5.1.2 Particulate immersed boundary method (PIBM) . . . 135
5.2 Results and discussions . . . 137
5.2.1 Falling of a single particle . . . 138
5.2.2 Sedimentation of two-dimensional particles in Newtonian flows 140
5.2.3 Sedimentation of three-dimensional particles in Newtonian flows 140
5.3 Concluding remarks . . . 152
References . . . 153

6 Numerical investigation of the wear process on the pipe wall in particle transportation 155
6.1 Equations of slurry motion . . . 157
6.2 The fluid-particle interaction force . . . 157

6.2.1 Two models for the coupling force . . . 157
6.2.2 The drag force . . . 159
6.3 DEM: The linear model . . . 160
6.4 Simulation condition . . . 161
6.5 Results and discussion . . . 162
6.5.1 Pneumatic conveying simulation . . . 162
6.5.2 Concrete pumping simulation: The standard case . . . 163
6.5.3 Effect of the slurry velocity on the puncture point location . . . 169
6.5.4 Effect of the bend orientation on the puncture point location . . . 173
6.6 Concluding remarks . . . 176
References . . . 178

7 Conclusions and future work **181**
7.1 Main conclusions . . . 182
7.1.1 Chapter II . . . 182
7.1.2 Chapter III . . . 182
7.1.3 Chapter IV . . . 183
7.1.4 Chapter V . . . 184
7.1.5 Chapter VI . . . 185
7.2 Future work . . . 185
7.2.1 Chapter II . . . 185
7.2.2 Chapter III . . . 185
7.2.3 Chapter IV . . . 185
7.2.4 Chapter V . . . 186
7.2.5 Chapter VI . . . 186
References . . . 186

A Test case on the fluidized bed **187**
References . . . 190

B From the physical units to the LB units **193**
B.1 The dimensional NS equations . . . 193
B.2 From the physical units to the Non-dimensional units . . . 194
B.3 From the LB units to the Non-dimensional units . . . 194
B.4 From the physical units to the LB units . . . 195
B.5 From the relaxation parameter to the physical time step . . . 195

List of Figures

1.1 The sketch map of concrete pumping apparatus. 35
2.1 Schematic diagram of contact process 52
2.2 Schematic diagram of contact detection scheme 53
2.3 Flowchart of simulators under CPU 56
2.4 NVIDIA Fermi GPU architecture. 57
2.5 NVIDIA Kelper GPU architecture. 58
2.6 Flowchart of simulator under CPU-GPU. 60
2.7 The illustration of sum reduction using warp-synchronous. 61
2.8 Sketch map of the two-dimensional die filling process. 62
2.9 Comparison on the distributions of particles in two-dimensional simulation: Trubal-org-s, Trubal-new-s and Trubal-new-p. 63
2.10 Comparison on the distributions of particles in three-dimensional simulation: Trubal-org-s, Trubal-new-s and Trubal-new-p. 67
3.1 Numerical errors versus mesh size for convective (left) and divergence (right) perators for second-, fourth-, sixth- and eighth-order discretizations. 75
3.2 (a) Instantaneous velocity in $x-$direction in a square duct at $Re_\tau = 300$. (b) Mean secondary flows in $y-$ and $z-$directions. 76
3.3 Two-point correlations at nine monitoring locations. 77
3.4 Quadrant-averaged profiles at five locations in the duct for the mean streamwise velocity.$(-)$Present DNS, (o) Gavrilakis [11]. 78
3.5 Quadrant-averaged profiles at five locations in the duct for rms fluctuations in streamwise velocity.$(-)$Present DNS, (o) Gavrilakis [11]. . . 78
3.6 Quadrant-averaged profiles at five locations in the duct for the mean lateral velocity.$(-)$Present DNS, (o) Gavrilakis [11]. 79
3.7 Quadrant-averaged profiles at five locations in the duct for rms fluctuations in lateral velocity.$(-)$Present DNS, (o) Gavrilakis [11]. 79
3.8 Contour: Instantaneous distribution of streamwise fluid velocity on two (x, y) planes. Top: $z/h = 0.50$, Bottom: $z/h = 0.05$ at $t = 24s$. $(\cdot)$: Instantaneous distribution of the 50 μm particles at corresponding locations and time. Without collisions. 81
3.9 Contour: Instantaneous distribution of streamwise fluid velocity on two (x, y) planes. Top: $z/h = 0.50$, Bottom: $z/h = 0.05$ at $t = 24s$. $(\cdot)$: Instantaneous distribution of the 100 μm particles at corresponding locations and time. Without collisions. 82

3.10 Contour: Instantaneous distribution of streamwise fluid velocity on two (x, y) planes. Top: $z/h = 0.50$, Bottom: $z/h = 0.05$ at $t = 24s$. $(\cdot)$: Instantaneous distribution of the 500 μm particles at corresponding locations and time. Without collisions. 82
3.11 PDF along the $y-$direction for the (a) 50 μm, (b) 100 μm and (c) 500 μm particles, without collisions. (d) PDF of the 500 μm particles at the $z/h = 0.05$ plane, with and without collisions. 83
3.12 Instantaneous distribution of the 500 μm particles on the (x, y) plane of $z/h = 0.05$. Top: with collisions. Bottom: without collisions. 84
3.13 Instantaneous distribution of the 500 μm particles on the (x, y) plane of $z/h = 0.02$. Top: with collisions. Bottom: without collisions. 84
3.14 Contour: Instantaneous distribution of streamwise fluid velocity on two (x, y) planes. Top: $z/h = 0.50$, Middle: $z/h = 0.05$ Bottom: $z/h = 0.02$ at $t = 24s$. $(\cdot)$: Instantaneous distribution of the 100 μm particles at corresponding locations and time. Without collisions. 85
3.15 Instantaneous distribution of the 500 μm particles on the (x, y) plane of $z/h = 0.5$. Top: with collisions. Bottom: without collisions. 85
3.16 Instantaneous distribution of the 500 μm particles on the (x, y) plane of $z/h = 0.05$. Top: with collisions. Bottom: without collisions. 85
3.17 Instantaneous distribution of the 500 μm particles on the (x, y) plane of $z/h = 0.02$. Top: with collisions. Bottom: without collisions. 86
3.18 Trajectories of different particles from two starting points. (a) $(y/h = 0.4552, z/h = 0.0830)$ and (b) $(y/h = 0.0906, z/h = 0.4363)$. 87
3.19 2D snapshots of particle distribution with velocity vectors for (a) 50 μm particle at $t = 12s$, (b) 100 μm particle at $t = 12s$, (c) 500 μm particle at $t = 2.4s$ and 3D snapshot of particle distribution for (d) 100 μm at $t = 12s$, all with collisions. Red point for the particle, black arrow for the velocity. 89
3.20 Particle resuspension rate in the $z-$direction for $50\ \mu m$ particles. Solid line: with collisions. Dashed line: without collisions. 90
3.21 Particle resuspension rate in the $z-$direction for $100\ \mu m$ particles. Solid line: with collisions. Dashed line: without collisions. 91
3.22 Particle resuspension rate in the $z-$direction for $500\ \mu m$ particles. Solid line: with collisions. Dashed line: without collisions. 92
3.23 Contact number and average resuspension rate of the 50 μm and 100 μm particles at $t = 12s$, the 500 μm particles at $t = 2.4s$. 92
3.24 Distribution of contact for the 500 μm particles at $t = 2.4s$. Top: with collisions, Bottom: without collisions. 93
3.25 Schematic of the effect of secondary flow on particle behavior. 94

3.26 Particle deposition velocity in the $z-$direction according to Fig 3.19. Top: $50\ \mu m$ particles, Middle: $100\ \mu m$ particles. Bottom: $500\ \mu m$ particles. 95
3.27 Particle deposition velocity in the $z-$direction in terms of fitting lines. Top: 50 μm particles, Middle: 100 μm particles. Bottom: 500 μm particles. 96
3.28 Single 100 μm particle trajectory near the duct floor from Starting point (a) I, (b) II and (c) III. All with collisions. 97
3.29 Single 500 μm particle trajectory near the duct floor from Starting point (a) I, (b) II and (c) III. All with collisions. 97
3.30 Distribution of the 50 μm particles at the final stage of deposition. Top: with collisions, Bottom: without collisions. 99
3.31 Distribution of the 100 μm particles at the final stage of deposition. Top: with collisions, Bottom: without collisions. 99
3.32 Distribution of the 500 μm particles at the final stage of deposition. Top: with collisions, Bottom: without collisions. 100
3.33 Particle deposition rate along the $y-$direction for the (a) 50 μm, (b) 100 μm and (c) 500 μm particles. 101
4.1 Schematic diagram of the immersed boundary method. 110
4.2 Flow chart for the computational sequence. 114
4.3 Schematic diagram for a single particle settling in a cavity. 115
4.4 (a) longitudinal coordinate; (b) longitudinal velocity; 116
4.5 (a) Reynolds number; (b) translational kinetic energy; 116
4.6 Sedimentation of a sphere in a cavity at different time stages,Re = 1.5; . 117
4.7 (a) Comparisons of the measured and simulated height of the sphere; (b) Comparisons of the measured and simulated settling velocity; . . . 117
4.8 (a) Reynolds number; (b) translational kinetic energy; 118
4.9 Sedimentation of two circular particles in a channel at different time stages. (a) 0.0s; (b) 0.5s; (c) 1.5s; (d) 2.5s; (e) 3.5s; (f) 4.5s; 120
4.10 (a) Transverse coordinates of the centers of the two particles; (b) Longitudinal coordinates of the centers of the two particles. 121
4.11 (a) Transverse velocity components of the two particles; (b) Longitudinal velocity components of the two particles. 121
4.12 (a) The distance between surfaces of the two particles (red:DEM, green:LJ); (b) The interpolation scheme; 122
4.13 Positions of the 504 particles at time $t = 0s$. 123
4.14 Positions of the 504 particles at time $t = 1s$. 124
4.15 Positions of the 504 particles at time $t = 2s$. 124
4.16 Positions of the 504 particles at time $t = 3s$. 125
4.17 Positions of the 504 particles at time $t = 4s$. 126

4.18 (a) The flow field; (b) Distribution of the particle velocity at time $t = 4s$; 126
4.19 Positions of the 504 particles at time $t = 5s$. 127
4.20 Positions of the 504 particles at time $t = 8s$. 128
4.21 Positions of the 504 particles at time $t = 12s$. 128
4.22 Positions of the 504 particles at time $t = 24s$. 129
4.23 Positions of the 504 particles at time $t = 48s$. 129
5.1 Schematic diagram of the D3Q15 model[1]. 134
5.2 Schematic diagram of the PIBM. 135
5.3 (a) longitudinal coordinates and (b) longitudinal velocities of the particle under different h/d_p. 138
5.4 Instantaneous height of the $100\mu m$ particle with contour plots for v_f at time (a) $t = 0.0s$, (b) $t = 45.0s$, (c) $t = 67.5s$, (d) $t = 90.0s$. 139
5.5 Instantaneous particle distribution with the fluid velocities at time (a) $t = 0.0s$, (b) $t = 2.5s$, (c) $t = 5.0s$, (d) $t = 10.0s$. 141
5.6 Instantaneous particle distribution with the fluid velocities at time (a) $t = 20.0s$, (b) $t = 25.0s$, (c) $t = 50.0s$, (d) $t = 100.0s$. 142
5.7 Positions of the 8125 particles at time $t = 0.0s$. 143
5.8 Positions of the 8125 particles at time (a) $t = 2.5s$, (b) $t = 5.0s$, (c) $t = 7.5s$, (d) $t = 10.0s$. 144
5.9 Particle deposition velocity along the $x-$direction at time (a) $t = 2.5s$, (b) $t = 5.0s$, (c) $t = 7.5s$, (d) $t = 10.0s$. 145
5.10 Instantaneous fluid velocity distribution on the mid-length slice at time (a) $t = 2.5s$, (b) $t = 5.0s$, (c) $t = 7.5s$, (d) $t = 10.0s$. 146
5.11 Overall distribution of the particle deposition velocity at time (a) $t = 2.5s$, (b) $t = 5.0s$, (c) $t = 7.5s$, (d) $t = 10.0s$. 147
5.12 (a) Positions of the 8125 particles at time $t = 50.0s$ and (b) the final distribution. 148
5.13 Minimum particle height versus time at different initial porosity. . . . 149
5.14 Particle number versus the computational time in one time step. 150
5.15 Positions of the 8125 particles with obstacles at time (a) $t = 2.5.0s$, (b) $t = 5.0s$, (c) $t = 7.5s$, (d) $t = 10.0s$. 151
6.1 Drag forces acting on a 4 mm diameter particle as predicted using a combination of the Ergun [3] and Wen and Yu [4] correlations compared with the predictions from the Di Felice [5] correlation for a range of porosities at three superficial slip velocities 159
6.2 Diagram of the computational domain defined in current study 161
6.3 Spatial distribution of (a) particles near the elbow and (b) zoomed view of that. 163
6.4 The max impact force distribution of the elbow from (a) the top and (b) the bottom. 164

6.5 Hydraulic pressure distribution profile. 165
6.6 Velocity magnitude distribution profile of the particle-free slurry. . . . 165
6.7 Spatial distribution of the particles in the bend. 166
6.8 Spatial distribution of the rate of the fluid phase in the elbow at different time. 167
6.9 Spatial distribution of (a) porosity and (b) fluid-particle interaction force at 0.2 s. 168
6.10 (a) average impact intensity distribution and (b) the max impact force distribution of the elbow from the bottom view. 169
6.11 The destroyed pipe. 170
6.12 (a) average impact intensity distribution and (b) the max impact force distribution of the elbow from the bottom view. 170
6.13 The maximum impact force (N) distribution of the elbow from the bottom view at slurry velocity: $(a)6m/s; (b)9m/s; (c)18m/s; (d)36m/s$. 171
6.14 Peak magnitude of the maximum impact force at different slurry velocities. 172
6.15 The max impact force distribution on the outer wall of the elbow at different fluid velocities. 173
6.16 Spatial distribution of particles in: (a) no gravity considered pipe; (b) vertical to horizontally downward pipe; (c) horizontal to vertically inclined downward pipe; (d) horizontal to vertically downward pipe. . 174
6.17 The maximum impact force (N) distribution of the elbow from the bottom view of: (a) no gravity considered pipe; (b) vertical to horizontally downward pipe; (c) horizontal to vertically inclined downward pipe; (d) horizontal to vertically downward pipe. 175
6.18 The maximum impact force distribution on the outer wall in: (a) no gravity considered pipe; (b) vertical to horizontally downward pipe; (c) horizontal to vertically inclined downward pipe; (d) horizontal to vertically downward pipe. 177
A.1 The initial response of the bed to the introduction of gas injection at velocity 2.5 m/s. 188
A.2 Typical solid flow patterns at velocity 2.5 m/s. 189
A.3 Left: Variation of the bed pressure drop with time. Right: Interparticle contact fluctuations during simulation. 189

List of Tables

2.1 Specifications of two different testing platforms 59
2.2 Parameters of 2D simulation. 64
2.3 Wall time and Ratio/Speedup of partial simulations of two-dimensional 6000 particles. 64
2.4 Wall time and Ratio/Speedup of partial simulations of two-dimensional 60000 particles. 65
2.5 Parameters of three-dimensional simulation. 65
2.6 Wall time and Ratio/Speedup of partial simulations of three-dimensional 20000 particles. 66
3.1 Parameters relevant to the DNS. 76
3.2 Parameters relevant to the DNS. 77
3.3 Parameters of the particles relevant to the simulations. 80
3.4 Hydrodynamic force on the particle. 87
4.1 Properties of particles and fluid. 118
4.2 Properties of particles and fluid. 119
4.3 Properties of particles and fluid. 122
5.1 Properties of the particles and fluid. 137
5.2 The settling velocities at different particle size. 140
5.3 The settling velocities at different particle size. 148
6.1 parameters of material content of pneumatic conveying. 162
6.2 parameters of material content of concrete pumping. 162
A.1 Parameters and bed geometry used for fluidized bed simulation 187
B.1 Properties of particles and fluid. 193
B.2 Characteristic and Non-dimensional variables in the physical systems. 194
B.3 Characteristic and Non-dimensional variables in LBM systems. 195

Chapter 1

Introduction

'Granular matter, in 1998, is at the level of solid-state physics in 1930 [1]'. (– **Pierre-Gilles de Gennes**: The Nobel Prize laureate in physics in 1991.)

1.1 Short history of Discrete Element Method

The Discrete Element Method (DEM) * was firstly proposed by Cundall in the 1970s [2]. Comparing with other discrete particle modeling methods such as molecular dynamics [3], Monte Carlo method [4] and dissipative particle dynamics [5], the DEM can provide the instantaneous pattern of the particular matters as well as the force chain that are of high interest by the engineers but very difficult to obtain in the on-line experimental observation. Since the pioneering work of Cundall [2], DEM has been used to simulate particulate flows not only in rock system but also minerals engineering [6, 7, 8], particulate materials in mixer [9, 10, 11], filling process in pharmaceutical [12, 13, 14] and many other fields containing large number of solid particles.

Nearly in all the aforementioned processes, there are particle-fluid interactions accompanying with heat transfer sometimes. Understanding the fundamentals governing the system is not easy due to its multi-scale, multi-phase and multi-physics field combined feature which leads to the requirement of interdisciplinary research skills. Formulating suitable governing equations and constitutive relationships are of paramount importance to the formulation of strategies for the process development and control [15]. To do so, many models have been proposed at different length and time scales, it can be from atomic scale to characteristic scale which may cross several magnitudes. Among them, the macro-scale models play an important role

*WIKIPEDIA: A DEM-simulation is started by first generating a model, which results in spatially orienting all particles and assigning an initial velocity. The forces which act on each particle are computed from the initial data and the relevant physical laws and contact models. Generally, a DEM-simulation consists of three parts: the initialization, explicit timestepping, and postprocessing. This is often only performed periodically.

since they can borrow the formulation from traditional Computational Fluid Dynamics (CFD) and treat both the fluid- and solid-phase as continuum media (known as Two Flow Model) [16]. By solving the averaged Navier-Stokes (NS) equations with proper initial and boundary conditions, the macroscopic behavior of the multiphase flow can be described. The macro-scale model is preferred due to its computational convenience. However, the model does not contain particle properties but uses artificial parameters instead. This drawback makes the model unacceptable especially when the system contains intense inter-particle collisions. DEM may fill this gap by monitoring the motion of individual particles meanwhile the particles would be influenced by the fluid flow [17]. This framework prolongates two coupling schemes, namely the fully resolved and unresolved models. The advantages/disadvantages of the models mainly lie on a competition between the precision of the model and the computational effort. In other words, their different areas of expertise are determined by the characteristics of method. This thesis could be divided into three parts according to the different scheme/solvers on the fluid phase meanwhile the DEM was adopted to calculate the solid part throughout the whole thesis. In the first part, we have adopted the DEM coupled with Direct Numerical Simulation (DNS) to study particle-laden turbulent flow in a square duct. In the second part, the Lattice Boltzmann Method (LBM) was employed to solve the fluid behavior to study the particle deposition in Newtonian laminar flow. In the last part, averaged NS equations together with DEM were adopted to study the particle transportation and wear on the pipe wall in the third part.

1.2 Particle-laden turbulent flow in a square duct

Particle-laden turbulent square duct flows are commonly encountered in both engineering and environmental applications such as the management of dust in clean rooms, chemical reactions involving a particulate catalyst, the flow of liquid and gas mixtures through process equipment and in the combustion of liquid sprays [18]. This configuration is of high interest because the behavior of the solid particles can be affected by the secondary vortexes that are known as the secondary flow of Prandtl's second kind.

Under the action of the gravitational force, the particles may deposit on the duct floor and form solid beds. The depositions are highly related to the blockages and erosion on the duct wall which may cause a significant reduction of its life-span. Moreover, these processes are always accompanied by the particle resuspension and complex inter-particle collisions that make the problem even more difficult to be solved. A well understanding of how these flows behave is of clear benefit to assist the reliable scale-up and re-design of processes of different types.

1.2.1 Single phase turbulent flows in straight square ducts

Since the pioneering experiment by Nikuradse [19], the single phase turbulent square duct flow has been the subject of several experimental studies [20, 21, 22, 23]. The secondary flow of Prandtl's second kind consists of four pairs of counter-rotating vortexes normal to the streamwise direction, statistically these eight vortexes distribute symmetrically about the bisectors of the walls and the diagonals of the square cross-sections. The streamwise flow is flattened by the secondary motions with transferring the fluid momentum from the centerline to the duct corners. Besides the experimental studies, the adoption of numerical simulations can assist people in making decisions on trial conditions. Previous simulations of the turbulent square duct flow are broadly divided into three categories: DNS [24, 25, 26, 27, 28, 29, 30], Large-Eddy Simulations (LES) [31, 32, 33, 34, 35] and the solution of the Reynolds-averaged Navier-Stokes equations with turbulent models (RANS) [36, 37, 38]. In this thesis, we focus on the DNS part, a brief summary of this work is presented here. DNS aims at solving Navier-Stokes equations with the whole range of spatial and temporal scales of the turbulent relevant. Gavrilakis [24] performed a DNS of the turbulent square duct flow at $Re_\tau = 300$ providing a detailed description of the mean flow in the transverse plane and turbulent statistics along the wall bisectors. Huser and Biringen [25] expanded the database by simulating turbulent square duct flow at $Re_\tau = 600$ in which the corner influence on turbulent statistics and on the origin of the secondary flows were explained. Then, Huser et al. [26] assessed all the terms in the Reynolds stress transport equation. The DNS results of Uhlmann et al. [28] indicated that with the rise of the Reynolds number there is a marginal state before fully turbulent one. The marginal Reynolds number is around $Re_\tau = 160$ below which the flow exhibits totally different secondary flow structure alternating in time. Joung et al. [29] and Pinelli et al. [39] performed a series of DNS at $Re_\tau = 300$ to pursuit the basic physical mechanisms that are responsible for Prandtl's secondary motion of the second kind. Zhu et al. [40] examined the turbulent statistics along the wall bisectors at $Re_\tau = 600$. Xu [41] performed DNS to investigate the fully developed turbulent flow in a straight square annular duct at $Re_\tau = 200$. Piller and Nobile ($Re_\tau = 300$) [27], Ma et al. ($Re_\tau = 400$) [42] and Yang et al. ($Re_\tau = 600$) [43] performed DNS to investigate the effect of the mean secondary flow on the heat transfer rate in duct. From the survey of the literature, the DNS has been proven to be a robust method to investigate the turbulent duct flow at a relatively low Reynolds number.

1.2.2 Particle-laden turbulent flow in a square duct

It is a challenging work to track a large number of particle trajectories in a turbulent flow and obtain dynamic information of them by physical experimentation at this

stage of development. Experimental investigations of the particle-laden turbulent flow in a square duct are very limited and mainly focused on the airborne particles such as that on the particle resuspension rate in ventilation ducts [44], the deposition in horizontal ducts [45] and dispersion in a vertical ventilation duct [46].

Zhang and Ahamad [47] carried out a DNS coupled with a Lagrangian Particle Tracking (DNS-LPT) method to study the aerosol particle transportation and deposition in vertical and horizontal turbulent duct flows, they found that the wall coherent structure plays an important role in the particle deposition process. Winkler and Rani [48] conducted a LES-LPT simulation ($Re_\tau = 360$) to investigate the preferential concentration of particles in a downward fully developed turbulent square duct flow. They concluded that the particles tend to accumulate in the regions of low vorticity magnitude. However, near the wall, the particles show a tendency to accumulate in regions of high vorticity with this phenomenon increasing with the response time. Winkler et al. [49] also indicated that the lift forces due to secondary flow velocity gradients are not as important as those due to streamwise velocity gradients in a square duct flow.

The particle deposition in turbulent duct flow is of particular interest under the effect of the gravitational force. Yao and Fairweather [50] performed a LES-LPT simulation to investigate the particle resuspension mechanism in relative high $Re_\tau = 10550$ turbulent flows where the role of drag force and lift force on the particle resuspension were studied, the carried fluid was assumed to be water. Then this work was followed by Adams et al. [51] using RANS-LPT. Sharma and Phares [52, 53] carried out DNS-LPT simulations ($Re_\tau = 300$) to study the effect of the secondary flow on the transport and deposition of different inertia particles with the gravity effect ignored. They found that the higher-inertia particles accumulate close to the sidewalls during transportation and deposit close to the corners in deposition. Zhang and Li [54] studied the particle deposition in a horizontal turbulent duct flow using RANS coupled with a Lagrangian stochastic model who reported that the deposition rate increases with the dimensionless relaxing time. Fairweather and Yao [18] investigated the mechanisms of particle dispersion in a turbulent square duct flow via LES-LPT and showed that the secondary flows within the duct dominate small particle dispersion, whereas gravity promotes the deposition of large particles on the duct floor. Yao and Fairweather [55] used the same code to further investigate the particle deposition mechanism in turbulent duct flows. They mainly concluded that high inertia particles tend to deposit near the side wall in high $Re_\tau = 10500$ turbulent duct flows whereas the low inertia ones tend to deposit close to the centers of the duct floor. All the sizes of particles deposit in the center region in relative low $Re_\tau = 600$ turbulent duct flows. The particle deposition process in [55] can be described by the free-flight model.

1.2.3 Motivation and summary of the present work

The afore-mentioned simulations have mainly focused on the hydrodynamic interaction between the turbulent flow and the solid particles whereas the inter-particle collisions were neglected. The research of Tanaka and Tsuji [56] has shown that the effect of inter-particle collisions cannot be ignored even in dilute flow. They performed a numerical simulation to investigate gas-particle flow in a vertical pipe and found that the effect on the diffusion in the direction normal to the mean flow is especially important. Winkler et al. [57] studied the effect of the inter-particle collisions on the particle deposition in vertical duct turbulent flow, they noted that the collision effects can decrease the deposition velocity due to the fact the direction of the gravity is along the streamwise direction. Sommerfeld and Kussin [58, 59] made a detailed analysis of collision effects for turbulent gas-particle flow in a horizontal channel where the particle interaction was based on the stochastic collision model and thus the location and motion of neighboring particles were not required. They found that the wall roughness has an important effect on the horizontal particle mean velocity, the fluctuating components and the wall collision frequency. The inter-particle collisions play an important role in the redistribution of the particle phase fluctuating motion, namely a decrease of the streamwise component and an enhancement of the lateral component. To the best knowledge of the authors, no research has been reported on the effect of the inter-particle collisions on the particle behavior in horizontal duct turbulent flows or on the particle resuspension rate. However, similar studies by means of other geometries have been conducted such as the research of Yan et al. [60] on particle dispersion in a turbulent jet, Afkhami et al. [61] and Yamamoto et al. [62] in a channel.

In this study, we performed DNS coupled with DEM [2] to study the effect of inter-particle collisions on the behavior of particle-laden turbulent flow in a square duct. The friction Reynolds number adopted is $Re_\tau = 300$ which is defined as $Re_\tau = hu_\tau/\nu$ based on the duct hydraulic diameter h, the mean friction velocity u_τ and the kinematic viscosity ν. The DEM, as a typical Lagrangian method, has been continually adopted to investigate various particulate flows [63, 64, 65] in engineering field due to the fact that it can not only track the trajectories of the particles but also provide the transient forces acting on individual particles [15], this information is very difficult to observe on line by the physical experiments. Besides the collision force, the non-contact forces, such as gravitational, electrostatic and hydrodynamic force can be directly exerted on the particles numerically which enables multiphysics [66, 67] and multiphase [68, 69] coupling simulations based on DEM. In this thesis, the interaction in the DEM is based on the theoretical contact mechanics thereby it is possible to directly use the material properties of the particle in the calculation. A small overlap between the rigid particles is allowed to represent the physical deformation that takes place between the contacting elements.

1.3 LBM-IBM-DEM

Particle-fluid systems are ubiquitous in both engineering and environmental applications. However, the understanding of the fundamental physical mechanism involved in these systems are generally insufficient but of high demand. The stochastic nature of the dispersed-phase distribution in a particle-fluid flow makes it much more complex than the single phase flow. Over the last two decades, LBM has been widely adopted to simulate the particle-fluid interaction problems mainly due to the fact that the formulation of LBM is quite simpler than the conventional CFD methods. In LBM, the so called fluid density distribution, $f_\alpha(r,t)$, is used to represent the fluid elements. The general concept is to compute $f_\alpha(r,t)$ with a discrete velocity along the direction at spatial r and temporal space t as they move along the lattice and collide on the lattice node. In the early 1990s, Ladd [70, 71] firstly applied the LBM to simulate the particle-fluid suspension problem, in which the boundary points of the particle would be approximately located at the middle of the link between LBM nodes when the boundary of a solid particle intersects with the lattice link. This treatment educes a distinct simplification in programming however forms a stepwise representation of the solid particles simultaneously. A severe numerical oscillation of the calculated fluid-solid interface force has been observed when the solid particle crosses one lattice grid to another with large velocity. For the sake of overcoming the oscillation, IBM [72] was introduced into LBM. Since the pioneering work by Feng and Michaelides [73, 74], the immersed boundary-lattice Boltzmann method (IB-LBM) has been adopted by several researchers [75, 76, 77, 78, 79, 80, 81, 82].

In the context of a particulate flow simulation where the effect of the surrounding fluid cannot be ignored (the effect is sometime not considered when a large density ratio between the solid and fluid is encountered), it is very important to correctly estimate the fluid-solid interaction force in order to capture the essential physical behavior of the system, because the succeeding motion of solid particles mainly depends on the drag force exerted on them as well as the inter-particle collisions. So far a number of particle fluid interaction schemes have been proposed for IB-LBM. Feng and Michaelides firstly used a penalty method to calculate the fluid-solid interaction force [73] and then improved the calculation by using a direct forcing scheme which eliminates the need of determination of the penalty parameter [74]. Niu et al. proposed a simpler and more efficient approach to compute the force at the boundary point of solid particles, where the forcing term is simply calculated by the momentum exchange method [75]. The scheme of Niu et al. also contains no artificial parameters while keeps the same order of accuracy as the conventional LBM. Peng et al. [76] employed a multi-block approach to make their code more efficient by enhancing the grid refinement near the solid body while using relative coarse meshes at further locations. In order to guarantee the no-slip boundary condition,

Shu et al. [77, 78, 79, 80] proposed a series of new concepts of IB-LBM to overcome the drawback that some streamlines may pass through the solid body. The new schemes have been validated by 2D applications such as flow past a circular cylinder [77], flow past an airfoil [78], flow around moving objects [79] and particulate flow simulations [80]. The scheme of Shu et al. was further improved by Wu and Shu and expanded to 3D applications [81, 82], where a more efficient LBM solver on the non-uniform mesh was developed. Another family of 'Immersed-like' boundary methods coupling with LBM was proposed by Noble and Torczynski [83] which is known as Immersed Moving Boundary method (IMB). The basic idea of IMB is to seek a smoother and accurate presentation of solid particles which is similar with IBM to some extent. The IMB-LBM has been employed by a number of researchers to investigate particle-fluid problems [84, 85, 86, 87, 88, 89, 90, 91] that will be discussed below.

From the survey of the literature, it can be concluded that the LBM plus a Lagrangian particle tracking method is a promising scheme to simulate particle-fluid interaction problems. However, all the afore-mentioned IB-LBM research works are limited to the small-scale demonstration and may not be applicable for practical engineering problems due to the fact that the description of the collisions of the particles is relatively crude and lack of physical validation. For instance, Feng and Michaelides [73, 74] treated interparticle and wall collisions using a repulsive force, and Niu et al. [75] and Wu and Shu [80] calculated the particle-particle/wall interaction forces using Leonard-Jones potential. The drawback of those collision treatments is that they require many user-defined parameters, and thus a trial and error or empirical approach is needed in any new configuration even using the same method. Moreover, a 'safe zone' or threshold has to be introduced to eliminate the roils produced by the interaction law, and the function of the threshold is to keep the particles away from each other and use a remote force instead of the contact force. As pointed out by Yu and Xu [92], at this stage of development, the difficulty in particle-fluid flow modeling is mainly related to the solid phase rather than the fluid phase. Particle collisions play a very important role in particle-fluid systems especially when the particles are densely packed. Therefore, it is essential to use a felicitous method to treat the particle collisions accurately and efficiently.

Recently, DEM has been continually adopted to simulate the particulate flows due to its natural advantage to characterize the granular matters. Dynamic information such as the trajectories of and transient forces exerting on individual particles, which are extremely difficult to obtain by physical experimentation, can be provided in DEM [15]. Due to its excellent capability for handling large number of particles, DEM has been coupled with traditional CFD methods for various engineering applications such as the fluidized bed [93, 94, 95, 96], particle transportation [97, 68, 69] and complex particle-fluid systems in dense medium cyclone [97]. A detailed re-

view of these coupling models is given by Zhu et al. [15]. One important feature of the coupled CFD-DEM simulations is that one single fluid cell can contain several solid particles, and the solid-fluid interaction force is calculated based on the local porosity in the cell together with the superficial slip velocity between particle and fluid [98]. Alternatively, the LBM-DEM simulations show a different coupling way that the diameter of each particle can be equal to dozens of lattice units. Cook et al. [84] coupled the IMB-LBM with DEM to investigate the fluid-induced erosive failure of a cemented particulate constriction. Han et al. [85, 86, 87, 88, 89] have successfully used coupled LBM-IMB-DEM to simulate particle transport in turbulent fluid flows and heat transfer in granular materials. Zhang et al. [90] carried out a coupled LBM-IMB-DEM simulation to monitor the motion of abrasive particles in Chemical Mechanical Polishing (CMP) process. Wang et al. [90] combined a time-driven hard-sphere model and IMB-LBM to simulate a fluidized process. Recently Wang et al. [99] made a new combination of a time-driven hard-sphere model and LBM to simulate a bubbling bed with jet flow, where a so-called Energy-minimization Multi-scale (EMMS) [100] drag model was adopted for the coupling between solid and gas phase. However, the EMMS drag model is more like a traditional CFD-DEM combined modeling since the evaluation of the local porosity is still necessary.

1.3.1 Motivation and summary of the present work

In this thesis, we present a combined LBM-IBM-DEM scheme. Different to other LBM-IMB-DEM research works [84, 85, 86, 87, 88, 89, 90, 91], we calculate the fluid-solid interaction force by the IBM as proposed by Niu et al. [75]. As mentioned above, this scheme evaluates the momentum-exchange of the particles using two unrelated computational meshes. One is the moving Lagrangian mesh for the solid particle, the other is the stationary Eulerian mesh for the fluid field. Compared with IMB, it is not necessary in IBM to take care of the details of the boundary positions and the intersections of two meshes with the movement of the solid particles. The fluid density distribution functions on particle boundary are interpolated by the Lagrangian polynomicals from the underlying Eulerian mesh. The momentum-exchange based scheme is simpler and more convenient than the other two ways of calculation of the fluid-solid interaction force for IB-LBM [73, 74] in different numerical examples. This IB-LBM scheme has been tested by Niu et al. [75]. And as the natural next step of the work initiated by Niu et al. [75], the primary objective of this paper is to further enhance the coupling scheme by incorporating DEM. The interaction law between the particles was based on the theoretical contact mechanics thereby it is possible to directly use material properties of the particle in the calculation. A small overlap is allowed between the rigid particles in contact to treat the particle collisions, this kind of collision treatment is also called the soft-particle DEM. Stevens and Hrenya [101] conducted a comparison of soft-particle models to

measurements of collision properties during normal impacts and found that utilization of the artificial penalty parameter can cause erroneous system behaviors.

1.4 LBM-PIBM-DEM

Due to the stochastic nature of the solid particle behaviors, the fluid-particle interaction problems are often too complex to be solved analytically or observed by physical experiments. Therefore, they have to be analyzed by means of numerical simulations. In last section, we have reported a numerical study of particle sedimentation process by using a combined LBM [102], IBM [72] and DEM [2] scheme. The LBM-IBM-DEM scheme is attractive because no artificial parameters are required in the calculation of both fluid-particle and particle-particle interaction force. However, the computational cost of this coupling scheme not only lies on the grid resolutions in LBM and the solid particle number N_P, but also highly depends on the number of the Lagrangian points N_{LP} distributed on the solid particle boundaries. Since N_{LP} on each particle should be large enough to ensure the accurate calculation of the fluid-particle interaction force and torque, the actual point number considered in the numerical interpolation is $N_P \times N_{LP}$ which makes the main calculation effort in the LBM-IBM-DEM modeling highly related to the IBM part. For the system of two-dimensional 504 particles with each particle containing 57 Lagrangian points [103], a calculating period of one month may be needed to simulate the entire sedimentation process in a $2\ cm \times 2\ cm$ cavity without additional parallel accelerations such as the graphics processing unit (GPU) [65] or Message Passing Interface (MPI) [104]. This computational efficiency is significantly lower than other coupling schemes based on the Navier-Stokes equations and DEM (NS-DEM) [30, 68, 69] when treating the same amount of solid particles. The bottleneck problem of the LBM-IBM-DEM scheme becomes dramatically serious in the three-dimensional applications. The important feature of the coupled NS-DEM simulations is that one single fluid cell can contain several solid particles, and the fluid-particle interaction force is calculated based on the local porosity in the cell together with the superficial slip velocity between particle and fluid [98]. In the NS-DEM simulations, the details of particle geometry are not considered when the size of the particles are significantly smaller than the system characteristic scale. Alternatively, the LBM-DEM simulations tell a different story in which each solid particle is constructed by dozens of lattice units (or more in three-dimensional cases) and the hydrodynamics force acting on each particle is the resultant of forces on the Lagrangian points and obtained by integrating around the circumference of the solid particle [84, 85, 63, 105]. Although the latter coupling scheme seems to be more rational, it is highly limited by the current computational capability as also argued by Zhu et al. [15] in their review paper, simulations of industrial scale problems are not computationally affordable. Yu and Xu [92] stated

that: "At this stage of development the difficulty in particle-fluid flow modeling is mainly related to the solid phase rather than the fluid phase." A numerical method that can be widely accepted in engineering application is the one with superior computational convenience. This paper aims at improving the computational efficiency of our previous LBM-IBM-DEM scheme [103] and extending the coupling scheme to three-dimensional. The idea of the traditional NS-DEM is borrowed here to treat each Lagrangian point directly as one solid particle, therefore, one single LBM grid is allowed to contain several solid particles spatially.

The available works on LBM-DEM have been reviewed in last section where the calculation of fluid-particle interaction force is regarded as the key point and it requires an accurate description of the boundaries of the solid particles. In general, there are two ways to do this, namely the IMB proposed by Noble and Torczynski [83] and the IBM proposed by Peskin [72]. Here, we focus on the IB-LBM simulation. Feng and Michaelides firstly proposed a penalty IB-LBM scheme [73] and then improved it via a direct forcing scheme [74]. Instead, Niu et al. [75] proposed a simpler, parameter-free and more efficient momentum exchange-based IB-LBM. The scheme of Niu et al. [75] has been inherited by numerous researchers to study the Fluid-Structure Interaction (FSI) problems [79, 106], thermal flows [107, 108] and particulate flows [80, 103] due to its natural advantage.

1.4.1 Motivation and summary of the present work

In this thesis, the fluid-particle interaction force is also evaluated by the scheme of Niu et al. [75] without introducing any artificial parameters. Unlike the aforementioned treatments in which the Lagrangian points were linked by stable solid bonds [80, 103] or flexible filaments [106], the constraints between the Lagrangian points are thoroughly removed. By doing so, the free floating of the Lagrangian points is allowed and the driving force on them is simply based on the momentum exchange of the fluid particles. Hereby, the new coupling scheme is called Particulate Immersed Boundary Method (PIBM) to show the difference to Niu et al. [75]. It is worthwhile mentioning that Wang et al. [109] carried out a coupled LBM-DEM simulation to study the gas-solid fluidization in which the size of the particles is smaller than the lattice spacing, and the Energy-Minimization Multi-Scale (EMMS) [100] drag model is adopted to calculate the coupling force between solid and gas phase. However, Wang et al. [109] only conducted two-dimensional simulations and the establishment of an empirical formula containing the local porosity is still needed. In addition, the EMMS has a lower computational performance than the direct momentum exchange-based scheme as adopted in current study.

1.5 Particle transportation and wear investigation

Damage of fluid handling equipment due to erosive wear can cause significant operation and reliability problems in oil and gas, coal, slurry, aerospace, pneumatic conveying, bulk material handling and other industries [110]. Severe erosion takes place on the pipe due to the impact of solid particles on the pipe wall, particularly at its elbow (As shown in Fig 1.1).

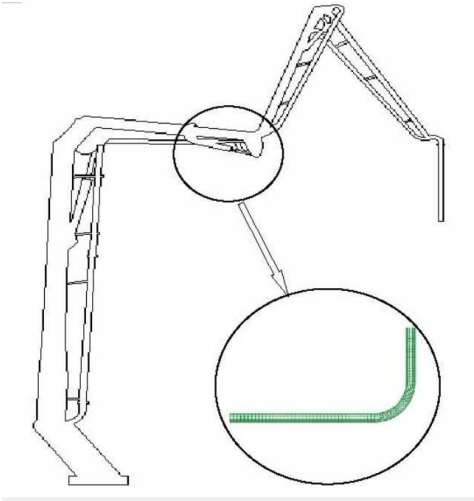

Figure 1.1: The sketch map of concrete pumping apparatus.

The erosion phenomenon is highly complicated due to a number of parameters affecting the erosion severity, such as production flow rate, entrained solid rate in production fluid, fluid properties, flow regime, solid particle properties, particle geometry, wall material of equipment, and geometry of the equipment as stated by Chen et al. [111]. For ductile materials, erosion is caused by localized plastic strain and fatigue of the metal surface. Finnie [112] proposed that in brittle materials, impacting particles can cause surface cracks and chipping of micro-size metal pieces. Solid particle velocity which affected by fluid velocity and fluid property has been recognized as the most significant factor for erosion by some investigators [113, 114] and several models were proposed based on that for single-phase liquid or gas flow contained solid particles [115]. To prevent process equipment failure and downtime, it's necessary to identify the puncture point location. Experimental investigations were carried out by Mazumder et al. [110, 116] and Selmer-Olsen [117] to characterize the location and magnitude of erosion in elbow specimens. Selmer-Olsen's

experiments were conducted in gas-liquid (mixture) multi-phase vertical annular flow with quartz particles, and during Mazumder's investigation, experiments were conducted in both single and multiphase flows in elbows to identify the location of maximum erosion. A mechanistic model for multiphase flow was proposed in [116]. Research into the bend failure on a pneumatic conveyor undertaken by Burnett [118] mentioned that the puncture locations of the bends might vary with different bend geometry. However, the effect of variations in bend orientation was not included in his study. Deng et al. [119] conducted experiments with four bend orientations to investigate the effect of bend orientation on puncture point location, finding that the puncture point location is indeed significantly influenced by the bend orientations. Some erosion prediction models [120, 121] have been developed based on empirical data, but the accuracy of those models was limited to the flow conditions of the experiments. While there are models based on CFD for calculating erosion in single-phase [122] flow conditions, but these models still require many simplifying assumptions for calculating erosion in multiphase flow. In these multi-phase flow simulations, the trajectory of solid particles was described using a Lagrangian Particle Track (LPT) method, the particle velocities and the impact angle were employed to evaluate the erosion, however LPT method is difficult to deal with problems when solid volume loading is high. Although there are some experimental and numerical studies on erosion prediction of elbow or tee, there is not the study of erosion prediction on concrete pumping process in multi-phase flow condition to the author's knowledge.

1.5.1 Motivation and summary of the present work

In this thesis, we used a fluid-solid multi-phase flow model to investigate the erosion in the elbow during transportation, where the continuum modeling proposed by Anderson and Jackson [123] was employed to evaluate the flow field of the slurry. A fluid density-based buoyancy model (FDB) [124] was adopted to approach the interaction force between slurry fluid and the solid particles, while DEM [2] was used to describe the trajectory of particles and interactions between the particles or between particles and wall. As pointed out by Yu and Xu [92], the current CFD-DEM coupling scheme is attractive because of its superior computational convenience as compared to DNS [125, 126] or LBM-DEM [84] and capability to capture the particle physics as compared to TFM [127]. The focus of this study is to model and simulate the motion of suspended particles in slurry, to investigate the wear process of the pipe and eventually to predict the location of maximum erosive wear damage in the elbow. Particle-wall interaction force is the key factors responsible for the wear process, and they can be readily obtained by the DEM simulation, impacting forces on the piping wall have been analysed to understand the wear mechanism. The focus of this study is to model and simulate the motion of suspended particles in

concrete slurry, to investigate the wear process of the pipe and predict the location of maximum erosive wear damage in the elbow. In particular, the effect of slurry velocity, bend orientation and angle of elbow on the puncture point location were investigated. Numerical results at different slurry velocities are compared with the experimental results in [110] and [117], while numerical results with different bend orientations are compared with the experimental results in [119]. Note that particle-wall interaction force was adopted to stand for the erosion severity in this studywhile the experimental investigationswere primarily focused on the determination of mass loss or thickness loss on the wall, so the validation of numerical modeling against experimental data is qualitative.

It is noted that several assumptions are made in this thesis: 1. The abrasive particles are all spherical and the particle-free slurry is treated as incompressible Newtonian fluid (although a number of studies have shown that the concrete mixture is Non-Newtonian [128, 129], the difference is neglected in this study). 2. The fluid is laminar flow; 3. For the fluid-solid interaction, only the pressure gradient force and the drag force are considered in this study; 4. The gravitation action is neglected, though it could be an important factor of the abrasion of the pipe in some situations.

References

[1] Pierre-Gilles de Gennes. Granular matter: a tentative view. *Reviews of Modern Physics*, 71(2):S374, 1999.

[2] P. Cundall. A computer model for simulating progressive large scale movements in blocky system. *In: Muller led, ed. Proc Symp Int Soc Rock Mechanics, Rotterdam: Balkama A A*, 1:8–12, 1971.

[3] Michael P Allen and Dominic J Tildesley. *Computer simulation of liquids*. Oxford university press, 1989.

[4] S Yuu, K Nohara, D Futai, and T Umekage. Numerical simulation of air and particle motions in turbulent fluidized bed using DSMC method. *Kagaku Kogaku Ronbunshu*, 23(6):811–819, 1997.

[5] Patrick B Warren. Dissipative particle dynamics. *Current opinion in colloid & interface science*, 3(6):620–624, 1998.

[6] CT Jayasundara, RY Yang, and AB Yu. Effect of the size of media on grinding performance in stirred mills. *Minerals Engineering*, 33:66–71, 2012.

[7] KJ Dong and AB Yu. Numerical simulation of the particle flow and sieving behaviour on sieve bend/low head screen combination. *Minerals Engineering*, 31:2–9, 2012.

[8] Matthew J Metzger and Benjamin J Glasser. Numerical investigation of the breakage of bonded agglomerates during impact. *Powder Technology*, 217:304–314, 2012.

[9] Dariusz Gudin, Roman Turczyn, Hiroshi Mio, Junya Kano, and Fumio Saito. Simulation of the movement of beads by the dem with respect to the wet grinding process. *AIChE journal*, 52(10):3421–3426, 2006.

[10] M Lemieux, G Léonard, J Doucet, L-A Leclaire, F Viens, J Chaouki, and F Bertrand. Large-scale numerical investigation of solids mixing in a v-blender using the discrete element method. *Powder Technology*, 181(2):205–216, 2008.

[11] PE Arratia, Nhat-hang Duong, FJ Muzzio, P Godbole, and S Reynolds. A study of the mixing and segregation mechanisms in the bohle tote blender via dem simulations. *Powder Technology*, 164(1):50–57, 2006.

[12] Guo, Y and Kafui, KD and Wu, C-Y and Thornton, C and Seville, Jonathan PK. A coupled DEM/CFD analysis of the effect of air on powder flow during die filling. *AIChE Journal*, 55(1):49–62, 2009.

[13] Y Guo, C-Y Wu, KD Kafui, and C Thornton. Numerical analysis of density-induced segregation during die filling. *Powder Technology*, 197(1):111–119, 2010.

[14] Y Guo, C-Y Wu, and C Thornton. The effects of air and particle density difference on segregation of powder mixtures during die filling. *Chemical Engineering Science*, 66(4):661–673, 2011.

[15] HP Zhu, ZY Zhou, RY Yang, and AB Yu. Discrete particle simulation of particulate systems: theoretical developments. *Chemical Engineering Science*, 62(13):3378–3396, 2007.

[16] D. Gidaspow. Multiphase flow and fluidization. *San Diego, USA: Academic Press*, 1994.

[17] AB Yu. Discrete element method: An effective way for particle scale research of particulate matter. *Engineering Computations*, 21(2/3/4):205–214, 2004.

[18] Michael Fairweather and Jun Yao. Mechanisms of particle dispersion in a turbulent, square duct flow. *AIChE Journal*, 55(7):1667–1679, 2009.

[19] J. Nikuradse. Untersuchungen uber die geschwindigkeitsverteilung in turbulenten stromungen. *Ph.D. Thesis, Gottingen. VDI Forsch*, 281, 1926.

[20] H.J. Perkins. The formation of streamwise vorticity in turbulent flow. *Journal of Fluid Mechanics*, 44:721–740, 1970.

[21] F.B. Gessner. The origin of secondary flow in turbulent flow along a corner. *Journal of Fluid Mechanics*, 58:1–25, 1973.

[22] R.J. Goldstein, M.Y. Jabbari, and J.P. Brekke. The near-corner mass transfer associated with turbulent flow in a square duct. *Warme-und Stoffubertragung*, 27(4):265–272, 1992.

[23] J. Zhang, B. Tao, and J. Katz. Turbulent flow measurement in a square duct with hybrid holographic piv. *Experiments in Fluids*, 23:373–381, 1997.

[24] S. Gavrilakis. Numerical simulation of low-Reynolds-number turbulent flow through a straight square duct. *Journal of Fluid Mechanics*, 244:101–129, 1992.

[25] A. Huser and S. Biringen. Direct numerical simulation of turbulent flow in a square duct. *Journal of Fluid Mechanics*, 257:65–95, 1993.

[26] Asmund Huser, Sedat Biringen, and Ferhat F. Hatay. Direct simulation of turbulent flow in a square duct: Reynolds-stress budgets. *Physics of Fluids*, 6(9):3144–3152, 1994.

[27] M. Piller and E. Nobile. Direct numerical simulation of turbulent heat transfer in a square duct. *International Journal of Numerical Methods for Heat and Fluid Flow*, 6:658–686, 2002.

[28] M. Uhlmann, A. Pinelli, G. Kawahara, and A. Sekimoto. Marginally turbulent flow in a square duct. *Journal of Fluid Mechanics*, 588:153–162, 2007.

[29] Y. Joung, S.U. Choi, and J. Choi. Direct numerical simulation of turbulent flow in a square duct: analysis of secondary flows. *Journal of engineering mechanics*, 133:213–221, 2007.

[30] H. Zhang, F. X. Trias, Y.Q. Tan, Y.Sheng, and A. Oliva. Parallelization of a DEM/CFD code for the numerical simulation of particle-laden turbulent flow. *23rd International Conference on Parallel Computational Fluid Dynamics, Barcelona*, pages 1–5, 2011.

[31] R.K. Madabhushi and S.P.Vanka. Large eddy simulation of turbulence-driven secondary flow in a square duct. *Physics of Fluids A*, 3:2734–2745, 1991.

[32] H.Y. Xu and A. Pollard. Large eddy simulation of turbulent flow in a square annular duct. *Physics of Fluids*, 13:3321–3337, 2001.

[33] M.S. Vazquez and O. Metaisa. Large-eddy simulation of the turbulent flow through a heated square duct. *Journal of Fluid Mechanics*, 453:201–238, 2002.

[34] J Pallares and Lars Davidson. Large-eddy simulations of turbulent flow in a rotating square duct. *Physics of Fluids*, 12:2878, 2000.

[35] F. Xavier Trias, Andrey Gorobets, Hao Zhang, and Assensi Oliva. New differential operators and discretization methods for eddy-viscosity models for LES. *Procedia Engineering*, 61:179 – 184, 2013.

[36] G Mompean, S Gavrilakis, L Machiels, and MO Deville. On predicting the turbulence-induced secondary flows using nonlinear k-e models. *Physics of Fluids*, 8:1856, 1996.

[37] Ming Yin, Feng Shi, and Zhong Xu. Renormalization group based k-e turbulence model for flows in a duct with strong curvature . *International Journal of Engineering Science*, 34(2):243 – 248, 1996.

[38] Hassan Raiesi, Ugo Piomelli, and Andrew Pollard. Evaluation of turbulence models using direct numerical and large-eddy simulation data. *Journal of Fluids Engineering*, 133(2), 2011.

[39] A. Pinelli, M. Uhlmann, A. Sekimoto, and G. Kawahara. Reynolds number dependence of mean flow structure in square duct turbulence. *Journal of Fluid Mechanics*, 644:107–122, 2010.

[40] Z.J. Zhu, H.X. Yang, and T.Y. Chen. Direct numerical simulation of turbulent flow in a straight square duct at reynolds number 600. *Journal of Hydrodynamics, Ser. B*, 21(5):600–607, 2009.

[41] H.Y. Xu. Direct numerical simulation of turbulence in a square annular duct. *Journal of Fluid Mechanics*, 621:23–57, 2009.

[42] L.D. Ma, Z.Y. Li, and W.Q. Tao. Direct numerical simulation of turbulent flow and heat transfer in a square duct with natural convection. *Heat and Mass transfer*, 44:229–250, 2007.

[43] H.X. Yang, T.Y. Chen, and Z.J. Zhu. Numerical study of forced turbulent heat convection in a straight square duct. *International Journal of Heat and Mass Transfer*, 52:3128–3136, 2009.

[44] Shuo Wang, Bin Zhao, Bin Zhou, and Zhongchao Tan. An experimental study on short-time particle resuspension from inner surfaces of straight ventilation ducts. *Building and Environment*, 53(0):119 – 127, 2012.

[45] T. Barth, G. Lecrivain, and U. Hampel. Particle deposition study in a horizontal turbulent duct flow using optical microscopy and particle size spectrometry. . *Journal of Aerosol Science*, 60:47–54, 2013.

[46] Nguyen Lu Phuong and Kazuhide Ito. Experimental and numerical study of airflow pattern and particle dispersion in a vertical ventilation duct. *Building and Environment*, 59:466–481, 2013.

[47] H. Zhang and G. Ahmad. Aerosol particle transport and deposition in vertical and horizontal turbulent duct flows. *Journal of Fluid Mechanics*, 406:55–80, 2000.

[48] C.M. Winkler, Sarma L. Rani, and S.P. Vanka. Preferential concentration of particles in a fully developed turbulent square duct flow. *International Journal of Multiphase Flow*, 30(1):27 – 50, 2004.

[49] C.M. Winkler and Sarma L. Rani. Relative importance of the lift force on heavy particles due to turbulence driven secondary flows. *Powder Technology*, 190(3):310 – 318, 2009.

[50] J. Yao and M. Fairweather. Inertial particle resuspension in a turbulent, square duct flow. *Physics of Fluids*, 22(3):03330301–15, 2010.

[51] J.F.W. Adams, M. Fairweather, and J. Yao. Modelling and simulation of particle re-suspension in a turbulent square duct flow. *Computers and Chemical Engineering*, 35(5):893 – 900, 2011.

[52] Gaurav Sharma and Denis J. Phares. Turbulent transport of particles in a straight square duct. *International Journal of Multiphase Flow*, 32(7):823 – 837, 2006.

[53] Denis J. Phares and Gaurav Sharma. A DNS Study of Aerosol Deposition in a Turbulent Square Duct Flow. *Aerosol Science and Technology*, 40(11):1016–1024, 2006.

[54] Jinping Zhang and Angui Li. CFD simulation of particle deposition in a horizontal turbulent duct flow . *Chemical Engineering Research and Design*, 86(1):95 – 106, 2008.

[55] J. Yao and M. Fairweather. Particle deposition in turbulent duct flows. *Chemical Engineering Science*, 84(0):781 – 800, 2012.

[56] T. Tanaka and Y. Tsuji. Numerical simulation of gas-solid two-phase flow in a vertical pipe: on the effect of inter-particle collision. *ASME/FED Gas-Solid flow*, 121:123–128, 1991.

[57] C.M. Winkler, Sarma L. Rani, and S.P. Vanka. A numerical study of particle wall-deposition in a turbulent square duct flow. *Powder Technology*, 170(1):12 – 25, 2006.

[58] M Sommerfeld. Analysis of collision effects for turbulent gas-particle flow in a horizontal channel: Part i. particle transport. *International Journal of Multiphase Flow*, 29(4):675 – 699, 2003.

[59] M Sommerfeld and J Kussin. Analysis of collision effects for turbulent gas-particle flow in a horizontal channel. part ii. integral properties and validation. *International Journal of Multiphase Flow*, 29(4):701 – 718, 2003.

[60] Jie Yan, Kun Luo, Jianren Fan, Yutaka Tsuji, and Kefa Cen. Direct numerical simulation of particle dispersion in a turbulent jet considering inter-particle collisions. *International Journal of Multiphase Flow*, 34(8):723 – 733, 2008.

[61] M. Afkhami, A. Hassanpour, M. Fairweather, and D. Njobuenwu. Particle-interaction effects in turbulent channel flow. *Computer Aided Chemical Engineering*, 32:847–852, 2013.

[62] Y. Yamamoto, M. Potthoff, T. Tanaka, T. Kajishima, and T. Tsuji. Large-eddy simulation of turbulent gas-particle flow in a vertical channel: effect of considering inter-particle collisions. *Journal of Fluid Mechanics*, 442:303–334, 2001.

[63] H. Zhang, Y. Tan, and M. Li. A Numerical Simulation of Motion of Particles under the Wafer in CMP. *International Conference on Computer Science and Software Engineering*, 3:31–34, 2008.

[64] Yuanqiang Tan, Dongmin Yang, and Y. Sheng. Study of polycrystalline Al2O3 machining cracks using discrete element method. *International Journal of Machine Tools and Manufacture*, 48(9):975 – 982, 2008.

[65] Xiaoqiang Yue, Hao Zhang, Congshu Luo, Shi Shu, and Chunsheng Feng. Parallelization of a DEM Code Based on CPU-GPU Heterogeneous Architecture. *Parallel Computational Fluid Dynamics*, pages 149–159, 2014.

[66] ZY Zhou, AB Yu, and P Zulli. A new computational method for studying heat transfer in fluid bed reactors. *Powder Technology*, 197(1):102–110, 2010.

[67] Zhi-Gang Feng and Samuel Gem Musong. Direct numerical simulation of heat and mass transfer of spheres in a fluidized bed . *Powder Technology*, 262:62 – 70, 2014.

[68] Yuanqiang Tan, Hao Zhang, Dongmin Yang, Shengqiang Jiang, Junhua Song, and Yong Sheng. Numerical simulation of concrete pumping process and investigation of wear mechanism of the piping wall. *Tribology International*, 46(1):137 – 144, 2012.

[69] Hao Zhang, Yuanqiang Tan, Dongmin Yang, Francesc Xavier Trias, Shengqiang Jiang, Yong Sheng, and Assensi Oliva. Numerical investigation of the location of maximum erosive wear damage in elbow: Effect of slurry velocity, bend orientation and angle of elbow. *Powder Technology*, 217:467 – 476, 2012.

[70] A.J.C. Ladd. Numerical simulations of particulate suspensions via a discretized boltzmann equation part i. theoretical foundation. *Journal of Fluid Mechanics*, 271:285–310, 1994.

[71] A.J.C. Ladd. Numerical simulations of particulate suspensions via a discretized boltzmann equation part ii. numerical results. *Journal of Fluid Mechanics*, 271:311–339, 1994.

[72] Charles S Peskin. Numerical analysis of blood flow in the heart. *Journal of Computational Physics*, 25(3):220 – 252, 1977.

[73] Zhi-Gang Feng and Efstathios E Michaelides. The immersed boundary-lattice Boltzmann method for solving fluid-particles interaction problems. *Journal of Computational Physics*, 195(2):602 – 628, 2004.

[74] Zhi-Gang Feng and Efstathios E. Michaelides. Proteus: a direct forcing method in the simulations of particulate flows. *Journal of Computational Physics*, 202(1):20 – 51, 2005.

[75] X.D. Niu, C. Shu, Y.T. Chew, and Y. Peng. A momentum exchange-based immersed boundary-lattice Boltzmann method for simulating incompressible viscous flows. *Physics Letters A*, 354(3):173 – 182, 2006.

[76] Y. Peng, C. Shu, Y.T. Chew, X.D. Niu, and X.Y. Lu. Application of multi-block approach in the immersed boundary lattice Boltzmann method for viscous fluid flows. *Journal of Computational Physics*, 218(2):460 – 478, 2006.

[77] C. Shu, N. Liu, and Y.T. Chew. A novel immersed boundary velocity correction-lattice Boltzmann method and its application to simulate flow past a circular cylinder. *Journal of Computational Physics*, 226(2):1607 – 1622, 2007.

[78] J. Wu and C. Shu. Implicit velocity correction-based immersed boundary-lattice Boltzmann method and its applications. *Journal of Computational Physics*, 228(6):1963 – 1979, 2009.

[79] J. Wu, C. Shu, and Y. H. Zhang. Simulation of incompressible viscous flows around moving objects by a variant of immersed boundary-lattice Boltzmann method. *International Journal for Numerical Methods in Fluids*, 62(3):327–354, 2010.

[80] J. Wu and C. Shu. Particulate Flow Simulation via a Boundary Condition-Enforced Immersed Boundary-Lattice Boltzmann Scheme. *Communications in Computational Physics*, 7:793–812, 2010.

[81] J. Wu and C. Shu. An improved immersed boundary-lattice Boltzmann method for simulating three-dimensional incompressible flows. *Journal of Computational Physics*, 229(13):5022 – 5042, 2010.

[82] J. Wu and C. Shu. Simulation of three-dimensional flows over moving objects by an improved immersed boundary-lattice Boltzmann method. *International Journal for Numerical Methods in Fluids*, 68(8):977–1004, 2012.

[83] D. R. Noble and J. R. Torczynski. A Lattice-Boltzmann Method for Partially Saturated Computational Cells. *International Journal of Modern Physics C*, 09(08):1189–1201, 1998.

[84] B.K. Cook, D.R. Noble, and J.R. Williams. A direct simulation method for particle-fluid systems. *Engineering Computation*, 21:151–168, 2004.

[85] K. Han, Y.T. Feng, and D.R.J. Owen. Coupled lattice Boltzmann and discrete element modelling of fluidâparticle interaction problems. *Computers and Structures*, 85(11-14):1080 – 1088, 2007.

[86] Y. T. Feng, K. Han, and D. R. J. Owen. Coupled lattice Boltzmann method and discrete element modelling of particle transport in turbulent fluid flows: Computational issues. *International Journal for Numerical Methods in Engineering*, 72(9):1111–1134, 2007.

[87] YT Feng, K Han, and DRJ Owen. Combined three-dimensional lattice Boltzmann method and discrete element method for modelling fluid–particle interactions with experimental assessment. *International journal for numerical methods in engineering*, 81(2):229–245, 2010.

[88] K Han, YT Feng, and DRJ Owen. Three-dimensional modelling and simulation of magnetorheological fluids. *International Journal for Numerical Methods in Engineering*, 84(11):1273–1302, 2010.

[89] DRJ Owen, CR Leonardi, and YT Feng. An efficient framework for fluid–structure interaction using the lattice Boltzmann method and immersed moving boundaries. *International Journal for Numerical Methods in Engineering*, 87(1-5):66–95, 2011.

[90] Hao Zhang, Yuanqiang Tan, and Mingjun Li. A numerical simulation of motion of particles under the wafer in cmp. In *Computer Science and Software Engineering, 2008 International Conference on*, volume 3, pages 31–34. IEEE, 2008.

[91] Limin Wang, Guofeng Zhou, Xiaowei Wang, Qingang Xiong, and Wei Ge. Direct numerical simulation of particle–fluid systems by combining time-driven hard-sphere model and lattice boltzmann method. *Particuology*, 8(4):379–382, 2010.

[92] A B Yu and B H Xu. Particle-scale modelling of gas–solid flow in fluidisation. *Journal of Chemical Technology and Biotechnology*, 78(2-3):111–121, 2003.

[93] Y. Tsuji, T. Kawaguchi, and T. Tanaka. Discrete particle simulation of two-dimensional fluidized bed. *Powder Technology*, 77(1):79 – 87, 1993.

[94] BPB Hoomans, JAM Kuipers, WJ Briels, and WPM Van Swaaij. Discrete particle simulation of bubble and slug formation in a two-dimensional gas-fluidised bed: a hard-sphere approach. *Chemical Engineering Science*, 51(1):99–118, 1996.

[95] BH Xu and AB Yu. Numerical simulation of the gas-solid flow in a fluidized bed by combining discrete particle method with computational fluid dynamics. *Chemical Engineering Science*, 52(16):2785–2809, 1997.

[96] KD Kafui, C Thornton, and MJ Adams. Discrete particle-continuum fluid modelling of gas–solid fluidised beds. *Chemical Engineering Science*, 57(13):2395–2410, 2002.

[97] KW Chu and AB Yu. Numerical simulation of complex particle–fluid flows. *Powder Technology*, 179(3):104–114, 2008.

[98] Di. R. Felice. The Voidage Function for Fluid-particle Interaction Systems. *International Journal on Multiphase Flow*, 20:153–159, 1994.

[99] Limin Wang, Bo Zhang, Xiaowei Wang, Wei Ge, and Jinghai Li. Lattice Boltzmann based discrete simulation for gas-solid fluidization . *Chemical Engineering Science*, 101(0):228 – 239, 2013.

[100] Jinghai Li. *Particle-fluid two-phase flow: the energy-minimization multi-scale method*. Metallurgical Industry Press, 1994.

[101] AB Stevens and CM Hrenya. Comparison of soft-sphere models to measurements of collision properties during normal impacts. *Powder Technology*, 154(2):99–109, 2005.

[102] Qian, YH and d'Humières, Dominique and Lallemand, Pierre. Lattice BGK models for Navier-Stokes equation. *EPL (Europhysics Letters)*, 17(6):479, 1992.

[103] Hao Zhang, Yuanqiang Tan, Shi Shu, Xiaodong Niu, Francesc Xavier Trias, Dongmin Yang, Hao Li, and Yong Sheng. Numerical investigation on the role of discrete element method in combined LBM-IBM-DEM modeling. *Computers & Fluids*, 94:37 – 48, 2014.

[104] K.D. Kafui, S. Johnson, C. Thornton, and J.P.K. Seville. Parallelization of a Lagrangian-Eulerian DEM/CFD code for application to fluidized beds. *Powder Technology*, 207:270–278, 2011.

[105] Xilin Cui, Jun Li, Andrew Chan, and David Chapman. Coupled DEM-LBM simulation of internal fluidisation induced by a leaking pipe. *Powder Technology*, 254:299 – 306, 2014.

[106] Hai-Zhuan Yuan, Xiao-Dong Niu, Shi Shu, Mingjun Li, and Hiroshi Yamaguchi. A momentum exchange-based immersed boundary-lattice Boltzmann method for simulating a flexible filament in an incompressible flow. *Computers & Mathematics with Applications*, 67(5):1039 – 1056, 2014.

[107] Y. Wang, C. Shu, and C.J. Teo. Thermal lattice Boltzmann flux solver and its application for simulation of incompressible thermal flows. *Computers & Fluids*, 94:98 – 111, 2014.

[108] Yang Hu, Xiao-Dong Niu, Shi Shu, Haizhuan Yuan, and Mingjun Li. Natural Convection in a Concentric Annulus: A Lattice Boltzmann Method Study with Boundary Condition-Enforced Immersed Boundary Method. *Advances in Applied Mathematics and Mechanics*, 5:321–336, 2013.

[109] Limin Wang, Bo Zhang, Xiaowei Wang, Wei Ge, and Jinghai Li. Lattice Boltzmann based discrete simulation for gas-solid fluidization. *Chemical Engineering Science*, 101:228–239, 2013.

[110] Quamrul H Mazumder, Siamack A Shirazi, and Brenton McLaury. Experimental investigation of the location of maximum erosive wear damage in elbows. *Journal of Pressure Vessel Technology*, 130(1), 2008.

[111] Xianghui Chen, Brenton S McLaury, and Siamack A Shirazi. Effects of applying a stochastic rebound model in erosion prediction of elbow and plugged tee.

In *ASME 2002 Joint US-European Fluids Engineering Division Conference*, pages 247–254. American Society of Mechanical Engineers, 2002.

[112] Iain Finnie. Erosion of surfaces by solid particles. *Wear*, 3(2):87–103, 1960.

[113] W Blatt, T Kohley, U Lotz, and E Heitz. The influence of hydrodynamics on erosion-corrosion in two-phase liquid-particle flow. *Corrosion*, 45(10):793–804, 1989.

[114] GP Tilly. Erosion caused by airborne particles. *Wear*, 14(1):63–79, 1969.

[115] RL Stoker. Erosion due to dust particles in a gas stream. *Industrial & Engineering Chemistry*, 41(6):1196–1199, 1949.

[116] Quamrul H Mazumder, Siamack A Shirazi, and Brenton S McLaury. Prediction of solid particle erosive wear of elbows in multiphase annular flow-model development and experimental validations. *Journal of Energy Resources Technology*, 130:023001, 2008.

[117] S Selmer-Olsen. Medium pressure flow studies of particulated and concurrent annular gas/liquid flow with relevance to material loss in unprocessed hydrocarbon systems. In *Third International Conference on Multiphase Flow, Paper*, number K4, 1987.

[118] Anthony John Burnett. *The use of laboratory erosion tests for the prediction of wear in pneumatic conveyor bends*. PhD thesis, University of Greenwich, 1996.

[119] T Deng, M Patel, I Hutchings, and MSA Bradley. Effect of bend orientation on life and puncture point location due to solid particle erosion of a high concentration flow in pneumatic conveyors. *Wear*, 258(1):426–433, 2005.

[120] SA Shirazi, JR Shadley, BS McLaury, and EF Rybicki. A procedure to predict solid particle erosion in elbows and tees. *Journal of Pressure Vessel Technology*, 117(1):45–52, 1995.

[121] Brenton S McLaury and Siamack A Shirazi. An alternate method to API RP 14E for predicting solids erosion in multiphase flow. *Journal of Energy Resources Technology*, 122(3):115–122, 2000.

[122] Jianrong Wang and Siamack A Shirazi. A CFD based correlation for erosion factor for long-radius elbows and bends. *Journal of Energy Resources Technology*, 125(1):26–34, 2003.

[123] T Bo Anderson and Roy Jackson. Fluid mechanical description of fluidized beds. equations of motion. *Industrial & Engineering Chemistry Fundamentals*, 6(4):527–539, 1967.

[124] R Di Felice. The voidage function for fluid-particle interaction systems. *International Journal of Multiphase Flow*, 20(1):153–159, 1994.

[125] Howard H Hu. Direct simulation of flows of solid-liquid mixtures. *International Journal of Multiphase Flow*, 22(2):335–352, 1996.

[126] TW Pan, DD Joseph, R Bai, R Glowinski, and V Sarin. Fluidization of 1204 spheres: simulation and experiment. *Journal of Fluid Mechanics*, 451:169–192, 2002.

[127] JAM Kuipers and WPM Van Swaaij. Application of computational fluid dynamics to chemical reaction engineering. *Reviews in Chemical Engineering*, 13(3):1–118, 1997.

[128] Chiara F Ferraris, Karthik H Obla, and Russell Hill. The influence of mineral admixtures on the rheology of cement paste and concrete. *Cement and Concrete Research*, 31(2):245–255, 2001.

[129] Nicolas Roussel. Steady and transient flow behaviour of fresh cement pastes. *Cement and Concrete Research*, 35(9):1656–1664, 2005.

Chapter 2

Discrete element method and its application

Part of the contents of this chapter have been published as:

X Yue, ***H Zhang***, C Luo, S Shu, C Feng. Parallelization of a DEM code based on CPU-GPU heterogeneous architecture. *Parallel Computational Fluid Dynamics, 405(2013), 146-159.*

X Yue, ***H Zhang***, C Ke, C Luo, S Shu, Y Tan, C Feng. A GPU-based discrete element modelling code and its application in die filling. *Computers & Fluids. n(2015),x-y.*

Abstract.

In this chapter, the theoretical and numerical issues of the DEM were introduced. A parallelization of a DEM code titled Trubal was implemented based on the CPU-GPU heterogeneous architecture. Both two- and three-dimensional cases were assessed. In Trubal, the particle-particle/particle-wall interaction rules are governed by theoretical contact mechanics which enables the direct use of real particle properties in the calculation. We reconstructed Trubal in two steps: (1) Reconstruction of the static storage structure; (2) Essential parallelism on the relative newer code. Numerical simulations were carried out to present the benefits of this research. Firstly, two simulations of die filling with a moving shoe involving 6000 and 60000 two-dimensional particles were conducted under (i) NVIDIA Tesla C2050 card together with Intel Core-Duo 2.93 GHz CPU and (ii) NVIDIA Tesla K40c card along with Intel Xeon 3.00GHz CPU. Average speedups of (i) 4.69 and 12.78 and (ii) 6.52 and 18.60 in computational time were obtained, respectively. Then, a simulation of die filling with a stationary shoe containing 20000 three-dimensional particles was carried out under the same conditions where average speedups of (i) 12.90 and (ii) 19.66 in computational time were obtained, respectively. It is shown that the final version parallel code gave a substantial acceleration on the original Trubal.

2.1 Short introduction of GPU-DEM

Trubal is a software package based on DEM which was originally developed by Cundall [1]. Thornton et al. [2, 3] from Aston University proposed some interaction laws and introduced them into Trubal where more multi-physical factors were considered. Sheng [4] used Trubal to investigate the powder compaction processes. Wu et al. [5, 6, 7] have coupled Trubal with a Computational Fluid Dynamics (CFD) solver to simulate complex particle-fluid interaction problems. It should be stressed that the computational capability of DEM relies strongly on the numerical scheme as well as the hardware environment and thus a bottle neck is reached when a large amount of particles are handled which highly restricts its application. For instance, the aforementioned researches are limited by the system scale since the serial characteristics of the original Trubal. High requirement on the time step for small particles makes the calculation load even heavier, the costs sometimes exceed the presently available computing resource and thus the parallelization of Trubal is highly needed. Trubal was parallelized by Kafui et al. [8] using a single program multiple data strategy together with a CFD solver, and successfully applied the new code to three dimensional (3D) applications [9]. Another parallelization work of Trubal was carried out by Washington and Meegoda [10] who ported the parallel Trubal on the CM-5 architecture at the Pittsburgh supercomputing center and used it to solve geotechnical problems. Ghaboussi [11] also made a parallel version Trubal using neural networks on the connection machine (CM-2) with 32,768 processors. Due to the high demand of scaling up the particle number to enable industrial scale simulation, parallelization of other DEM-based code also gains popularity. Maknickas et al. [12] parallelized the DEMMAT code to simulate visco-elastic frictional granular media utilizing the spatial domain decomposition strategy, where a speedup around 11 has been obtained on 16 processors. Darmana et al. [13] parallelized an Euler-Lagrange model using mixed domain decomposition and a mirror domain technique. They applied their code to simulate dispersed gas-liquid two-phase flow and obtained a maximum speed-up up to 20 using 32 processors. At the same time, the widely used commercial software like EDEM and PFC3D also exploited partial parallel functions to meet the requirements from the users and tried to push the mimicking results closer to the actual engineering problems.

From the survey of references, it is found that the existing acceleration work of DEM is mainly on the MPI/OpenMP programming environment. Graphics Processing Units (GPUs) are computer chips that can be accessed and controlled by CPUs via a peripheral component interconnect (PCI) express bus. They are originally served as hardware acceleration in rendering three-dimensional images, and nowadays manifest substantial performance and energy-efficiency improvements by almost one order of magnitude in scientific and engineering applications since the success of general purpose graphics processing units (GPGPUs). CPU-GPU hetero-

geneous architecture has become an important trend in the development of high performance computers [14]. Shigeto et al. [15] proposed a new algorithm for multi-thread parallel computation of DEM, and pointed out that their calculation speed ratio of the GPU to CPU was up to 3.4 using single-precision floating-point numbers. However the superiority in speed of the GPU decreased as the number of calculated particles increased. Recently, Li et al. developed a DEM based software named GDEM, exploited certain GPU technologies to accelerate the continuous-based DEM and achieved an average 650 times speedup using a NVIDIA GTX VGA card to Intel Core-Dual 2.66 GHz CPU [16]. Ye et al. [17] proposed a spatial subdivision algorithm to partition space into a uniform grid and sorted the particles base on their hash values, their results showed that the rendering speed of large-scale granular flow scene can still reach as high as 37.9 frames per second when the number of particles reaches 200,000. Radeke et al. proposed an approach of using massively parallel compute unified device architecture (CUDA) technique on GPUs for the implementation of the DEM algorithms which enables for simulations of more than two million particles per Giga Byte of memory [18]. More recently Ren et al. investigated the mixing and flow of granular materials in a conical tote blender using a GPU-based DEM software [19]. Generally speaking, applications of GPU based-DEM are limited but more and more popular nowadays, and numerical simulations with actual-engineeringlevel numbers of particles are of especially high demand.

In this chapter, we reconstruct the Trubal based on a CPU-GPU heterogeneous architecture. For a clearer comparison of the acceleration, numerical samples of die filling processes are selected from Wu et al. [5, 6, 7], who have successfully used serial Trubal to simulate the die filling process. The numerical cases are assessed in two platforms (i) NVIDIA Tesla C2050 card together with Intel Core-Duo 2.93 GHz CPU and (ii) NVIDIA Tesla K40c card along with Intel Xeon 3.00GHz CPU, respetively.

2.2 Governing equations of DEM

The basic idea behind DEM is to calculate the trajectory of every single element based on the Newtonian second law. Meanwhile the collisions between the moving particles were considered and treated using interaction laws. The dynamic equations of the discrete element can be symbolically expressed as

$$m\frac{d^2r}{dt^2} + \beta v = mg + F_c = F_{res} \tag{2.1}$$

$$I\frac{\partial^2\theta}{\partial t^2} + \beta\omega = \tau_c \tag{2.2}$$

where m and I are respectively the mass and the moment of inertia of the particle, r is the particle position, β is the damping coefficient, v is the velocity, θ is the angular displacement, β is the angular velocity, g is the acceleration of gravity if considered, F_c and τ_c are the contact force and moment of force respectively generated by the direct collisions. F_{res} denotes the resultant force.

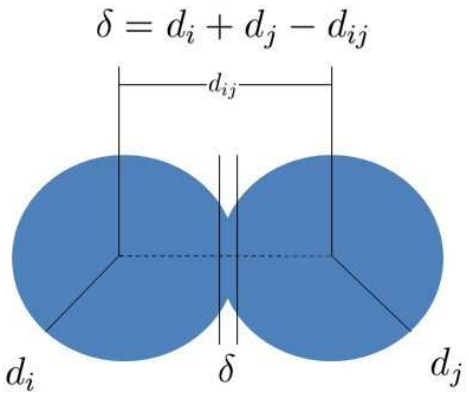

Figure 2.1: Schematic diagram of contact process

Among the most commonly used interaction laws are the hard contact based on conservation of momentum, linear law and the nonlinear law as adopted in this thesis. The calculation of the interaction force is not necessary in the hard contact model. The latter two are called soft contact models where a small overlap δ_n is allowed between the contacting particles to represent the physical deformation which takes place at the interface (as shown in Fig. 2.1). The linear model will be introduced in sixth chapter of this thesis. The nonlinear interaction law is based on classical contact mechanics and improves the reliability of the numerical results than the former two. In Trubal the normal force-displacement relationship of the particles are calculated based on the theory of Hertz [20]. For two particles of radius R_i, Young's modulus E_i , shear modulus G_i and Poisson's ratios ν_i $(i = 1, 2)$, the normal force-displacement relationship reads

$$F_n = \frac{4}{3} E^* R^{*1/2} \delta_n^{3/2} \tag{2.3}$$

where

$$\frac{1}{R^*} = \frac{1}{R_1} + \frac{1}{R_2} \tag{2.4}$$

and

$$\frac{1}{E^*} = \frac{1-\nu_1^2}{E_1} + \frac{1-\nu_2^2}{E_2} \tag{2.5}$$

The incremental tangential force arising from an incremental tangential displacement depends on the loading history as well as the normal force and is given by Mindlin and Deresiewicz [21]

$$\Delta T = 8G^* r_a \theta_k \Delta\delta_t + (-1)^k \mu \Delta F_n (1-\theta_k) \tag{2.6}$$

where

$$\frac{1}{G^*} = \frac{1-\nu_1^2}{G_1} + \frac{1-\nu_2^2}{G_2} \tag{2.7}$$

$r_a = \sqrt{\delta_n R^*}$ is radius of the contact area. $\Delta\delta_t$ is the relative tangential incremental surface displacement, μ is the coefficient of friction, the value of k and θ_k changes with the loading history.

2.3 Contact detection between the elements

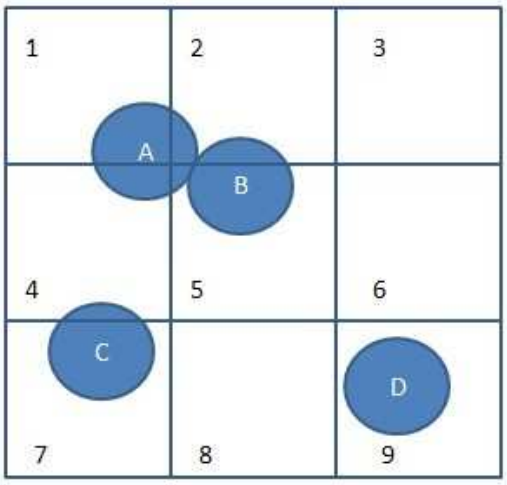

Figure 2.2: Schematic diagram of contact detection scheme

Contact detection is achieved using linked-list scheme. The work space, rectangle in 2 dimension or cube in 3 dimension, is divided into a number of boxes. The

number of box should be set prior to the main calculation. It follows a rule that he box size is normally less than twice the largest particle diameter for an efficient contact search scheme

$$d_{max} < l_{box} < 2d_{max}$$

Each particle is mapped into any box in which and part of the particle lies (as shown in Fig. 2.2). The addresses of all particles that map into any box are thus are available through a linked-list for that box. A second mapping, which used a circumscribing cube dimension of $2(R + TOL)$, ensures that particles which are near box boundaries are also mapped into these boxes. In the contact search for any particle, only particles that held in the linked-list of each box in which the particle is mapped are examined for contact. All the particle linked by a same box are assumed to have a 'potential' contact with each other, therefore another searching is needed to eliminate the fake contacts. For example, in Fig. 2.2, Particle-A should be mapped into Box-1, 2, 4 and 5 at the same time. Particle-B should be mapped into Box-2 and 5. Particle-C should be mapped into Box-4 and 7. Particle-D is only mapped into Box-9. Once the link lists are established, the next particle remapping and contact search is only triggered when the accumulated component of translational displacement increment exceeds a set value XRES.

2.4 Difference scheme and the timestep

The central difference form of Eq. 2.1 is given by

$$m\frac{\dot{x}^{n+1/2} - \dot{x}^{n-1/2}}{\Delta t} + \beta\frac{\dot{x}^{n+1/2} + \dot{x}^{n-1/2}}{2} = F_{res} \tag{2.8}$$

x^n denotes the particle position at time n.

$$\dot{x}^{n+1/2} = \frac{x^{n+1} - x^n}{\Delta t} \tag{2.9}$$

$$\dot{x}^{n-1/2} = \frac{x^n - x^{n-1}}{\Delta t} \tag{2.10}$$

according to Eq.2.8, we get

$$\dot{x}^{n+1/2} = (m + \frac{\Delta t}{2}\beta)^{-1}[\Delta t F_f^n + (m - \frac{\Delta t}{2}\beta)\dot{x}^{n-1/2}] \tag{2.11}$$

together with Eq. 2.9 and 2.10, we get the particle position at next time step

$$x^{n+1} = x^n + \dot{x}^{n+1/2}\Delta t \tag{2.12}$$

Eq. 2.2 has the same difference scheme as Eq. 2.1.

For each timestep the translational and rotational accelerations are assumed to be constant over the small timestep and a numerical integration yields undated velocities and positions of each particle. Here the timestep is based on the based on the Rayleigh wave speed of force transmission on the surface of elastic bodies.

$$\Delta t_{cr}^{i} = \frac{\pi R}{v_R^i} = \frac{\pi R}{0.163\nu + 0.877}\sqrt{\frac{G}{\rho}} \tag{2.13}$$

For an assembly of spherical particles, the highest frequency of Reyleigh wave propgation is determined by the smallest particles leading to critical timestep given by $\Delta t_{cr} = min\Delta t_{cr}^{i}$.

2.5 CPU vs GPU

The idea of the reconstruction on Tubal is following two steps: (1) Reconstruction of the static storage structure on CPU; (2) An essential parallelism on the relative newer code using shared memory without bank conflict and texture memory to maximize the frequency of GPU memory bandwidth based on a CPU-GPU heterogeneous architecture. During this process, three simulators will be denoted, namely Trubal-org-s and Trubal-new-s only based on CPU and Trubal-new-p based on a CPU-GPU heterogeneous architecture. The comparison of performance of these simulators will appear in the next section.

2.5.1 Numerical strategy: Two simulators under CPU

Functionally, Trubal can be broadly divided into three parts which includes setup phrase, solving phrase and post-processing phrase. The setup phrase aims at reading parameters, such as the number and physical properties of particles and walls, geometry of calculation domains, and preparing available data that solving phrase requires to further calculation, such as time-step and initial contact situations of the elements. Solving phrase computes explicitly the linear and angular velocity and displacement, composite force and resultant moment of each particle at each time step. Post-processing phrase saves the computing results into files and displays their images to analyze the validity of the simulation. The entire calculation flow of Trubal is shown in Fig. 2.3. One thing should be emphasized is that the contact detection in Trubal is based on a linked-list scheme where it firstly executes a rough search to gain a list of particles and walls with potential contacts, and then examines those lists accurately to eliminate the pair without overlap. Moreover, the particle sizes

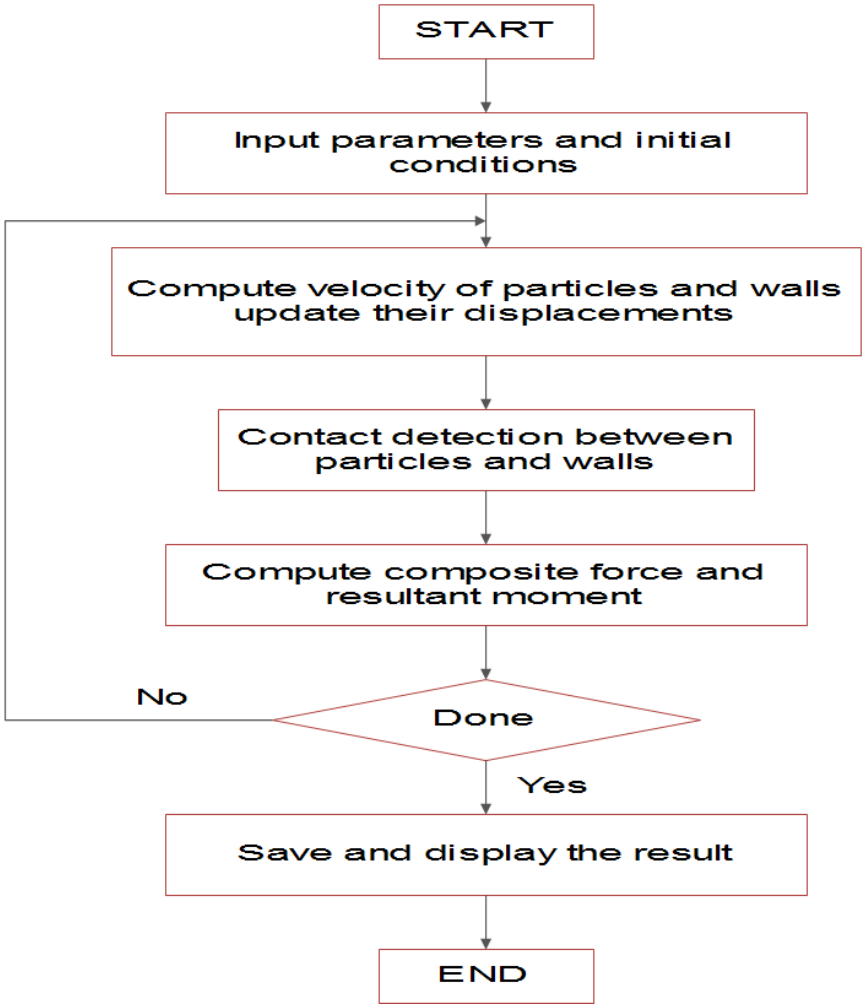

Figure 2.3: Flowchart of simulators under CPU

were artificially expanded in neighbor search stage with the purpose of extremely decreasing the invoking times of the contact detection module.

The main storage structure in Trubal is a globally static array with single precision. This structure educes a distinct simplification in programming, data-accessing and memory-saving, but it's prone to interrupt the simulation because the assessing of the necessary memory during the simulation becomes impossible. Therefore, the

regular solution is to set up the maximum storage of the used machine. This original simulator is denoted as Trubal-org-s in what follows in this study.

For the sake of avoiding the above shortcomings of the static storage structure, we dynamically spared the required local arrays according to the number of particles, walls or contacts. This can prevent a waste of memory then enhance the computational capability to handle more particles than Trubal-org-s does. In the following, we named this new simulator as Trubal-new-s.

2.5.2 GPU Computing and a simulator under CPU-GPU

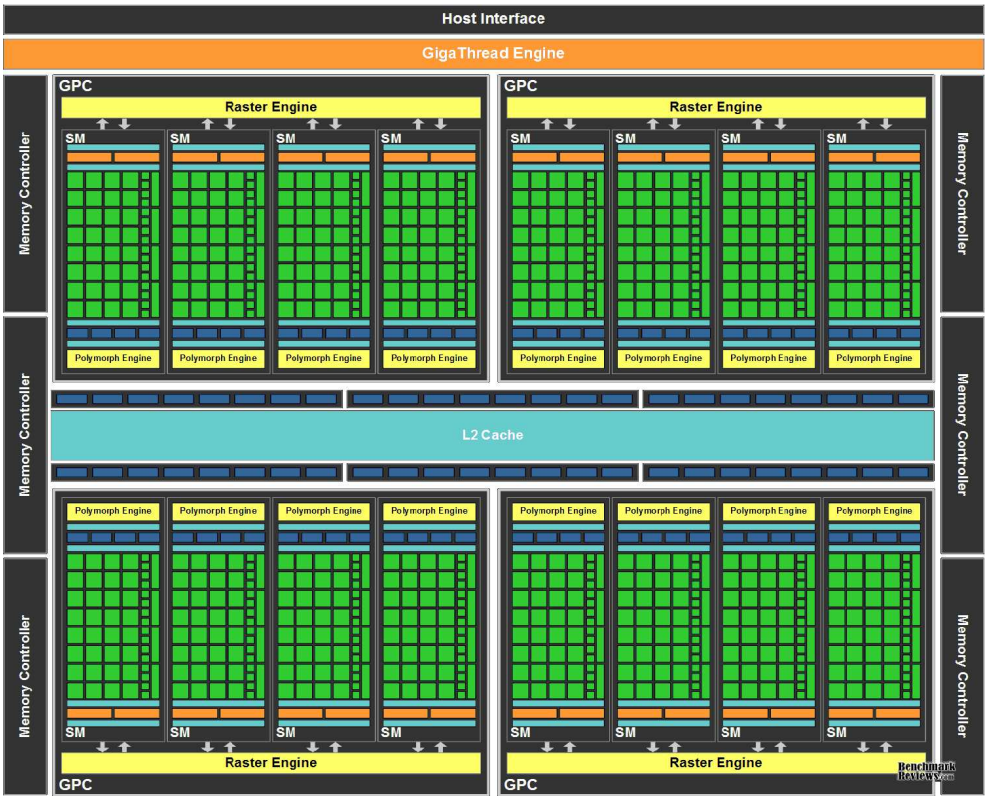

Figure 2.4: NVIDIA Fermi GPU architecture.

In this subsection, we propose a GPU-based simulator and undertake an investigation on its performance under two GPU architectures: Fermi and Kepler. Based

on NVIDIA Fermi GPU architecture, as shown in Fig. 2.4, Tesla C2050 GPUs deliver equivalent supercomputing performance at 1/10th the cost and 1/20th the power consumption comparing to the latest quad-core CPUs. Tesla C2050 has 14 streaming multiprocessors (SMs) with warp size as 32, and each SM has 32 streaming processors (SPs) or CUDA cores. Each SM has its own L1 cache (16 KB), shared memory (48 KB) and 32-bit registers (32,768 available per block). They share L2 cache (768 KB), constant memory (64 KB), texture memory and global memory (3.0 GB, 2.625 GB with ECC on). While the recently launched Kepler-based Tesla K40c [42], whose architecture diagram is illustrated in Fig. 2.5, sustains more than 3 times performance per watt and 2 times larger data applications. It has 15 SMXs (Kepler's new streaming multiprocessors) and 2880 CUDA cores in total, besides the amount of registers per block and L2 cache size are doubled, and the global memory is quadrupled in comparison with Tesla C2050.

Figure 2.5: NVIDIA Kelper GPU architecture.

Fig. 2.6 shows the entire calculation flow under CPU-GPU heterogeneous architecture. We indicated this simulator as Trubal-new-p hereinafter. The CPU-GPU heterogeneous architecture consists of two parts, wherein CPU (host) is responsi-

Platform	CPU	GPU	Operating System
C2050	Interl(R) CPU E7500	Tesla C2050	Linux
	2.0 GB	3.0 GB	Linux
	2 Cores	14×32 CUDA Cores	Fedora 13-2.6.34
	2.93 GHz	1.15 GHz	Fedora 13-2.6.34
K40c	Interl(R) CPU E5-2690 v2	Tesla K40c	Linux
	64.0 GB	12.0 GB	Linux
	40 Cores	15×192 CUDA Cores	CentOS 6.5 x86_64
	3.0 GHz	0.88 GHz	CentOS 6.5 x86_64

Table 2.1: Specifications of two different testing platforms

ble for computations unsuitable to be parallelized, like complex logical transactions and organizations of data flow, yet GPU (device) handles large-scale intensive calculations. As we all know, CUDA released by NVIDIA in 2006 doesn't encapsulate the heterogeneous nature of the whole storage system, we thus boost up the overall performance by optimizing the usage of various types of memory, such as shared memory to reduce access latency by hanging threads temporarily, and texture memory to randomly access for maximizing the frequency of memory bandwidth.

For example, the calculations on various forms of energy can be boiled down to a sum reduction operation in double precision. The illustration of the sum reduction using warp-synchronous is given in Fig. 2.7 where reduction is operated in shared memory and is completely unrolled without any bank conflicts.

2.6 Numerical experiments

The die filling process has wide applications ranging from pharmacy and metallurgy to food processing. Wu et al. have successfully used Trubal to simulate the die filling processes [7]. For a clearer comparison of acceleration, numerical samples of die filling processes were selected to compare the efficiencies of the three simulators. Due to the fact that two- and three-dimensional calculation blocks are relatively isolated in Trubal though they share the same interaction laws, therefore, the two cases are discussed separately in the following subsections.

Table. 2.1 lists the specifications of two different testing platforms. For the sake of fairness, we compile the Trubal-org-s and Trubal-new-s with optimization options as '-O2 -IPA', '-arch=sm_20 -O2' for platform C2050 and '-arch=sm_35 -O2' for platform K40c to compile Trubal-new-p, respectively.

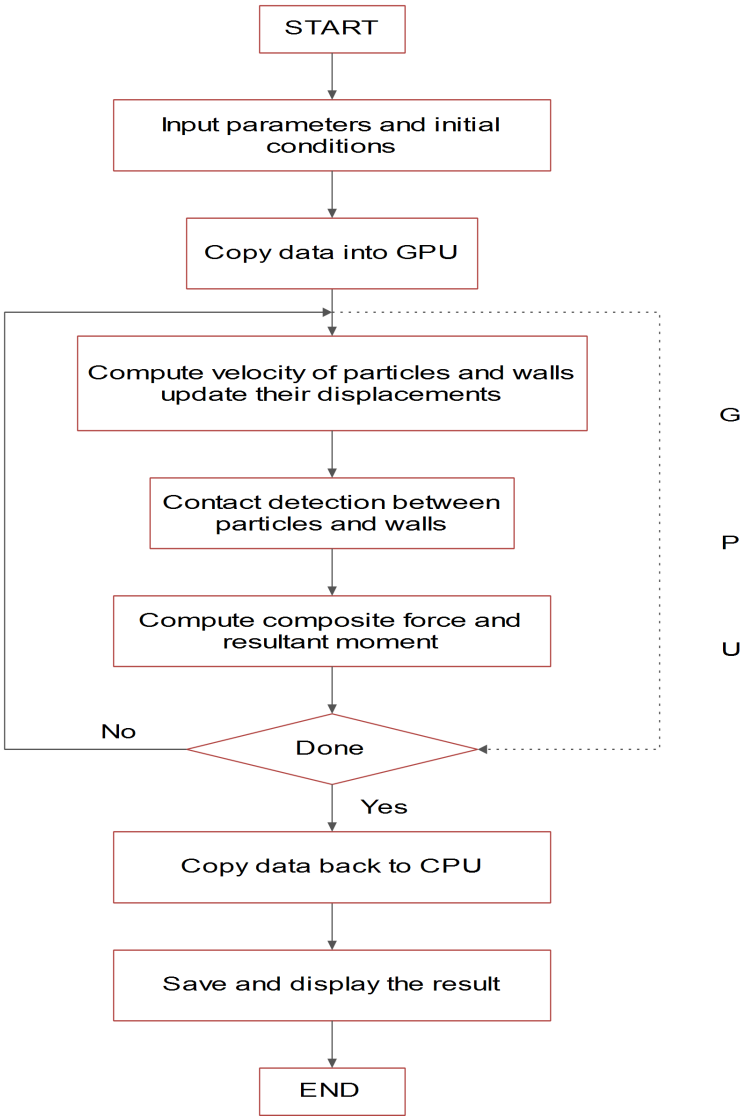

Figure 2.6: Flowchart of simulator under CPU-GPU.

2.6.1 Die filling with a moving shoe: two-dimensional Case

In this subsection, two-dimensional simulation of die filling with a moving shoe is performed, the schematics of the calculating domain is shown in Fig. 2.8. The

```
__global__ void SumReductionBKernel( double *e, int size )
{
    int td_idx = threadIdx.x;            |  __syncthreads();
    int bk_idx = blockIdx.x;             |  if (td_idx < 64)
    int bk_dim = blockDim.x;             |    s[td_idx] += s[td_idx+64];
    int gd_dim = gridDim.x;              |  __syncthreads();
    int stride = bk_dim * gd_dim;        |  if (td_idx < 32)
    double w = 0.0;                      |    s[td_idx] += s[td_idx+32];
    int index;                           |  if (td_idx < 16)
                                         |    s[td_idx] += s[td_idx+16];
    for (index = bk_dim*bk_idx+td_idx;   |  if (td_idx < 8)
          index < size; index += stride) |    s[td_idx] += s[td_idx+8];
        w += e[index];                   |  if (td_idx < 4)
    __shared__ double s[512];            |    s[td_idx] += s[td_idx+4];
    s[td_idx] = w;                       |  if (td_idx < 2)
    __syncthreads();                     |    s[td_idx] += s[td_idx+2];
    if (td_idx < 256)                    |  if (td_idx < 1)
      s[td_idx] += s[td_idx+256];        |    s[td_idx] += s[td_idx+1];
    __syncthreads();                     |  __syncthreads();
    if (td_idx < 128)                    |  if (td_idx == 0)
      s[td_idx] += s[td_idx+128];        |    e[bk_idx] = s[0];
}
```

Figure 2.7: The illustration of sum reduction using warp-synchronous.

particles are initially generated and deposit in the shoe until a steady state is reached, then the particle agglomerate is carried by the shoe from right to left. The shoe has no a bottom, therefore the particles are delivered into the die since it begins to cover the top of the die forming a nose shaped profile. In this study, a vacuum environment is assumed so that the profile of the particle flow will not be influenced by air. The parameters of particles and walls relevant to the simulation are shown in Table. 2.2.

Fig. 2.9 lists several typical events of the moving shoe die filling sequence from Trubal-org-s, Trubal-new-s and Trubal-new-p at t = 0.0382 s, 0.0763 s, 0.0915 s, 0.114 s, 0.130 s, 0.168 s, 0.244 s and 0.305 s. It is shown that the results from these three

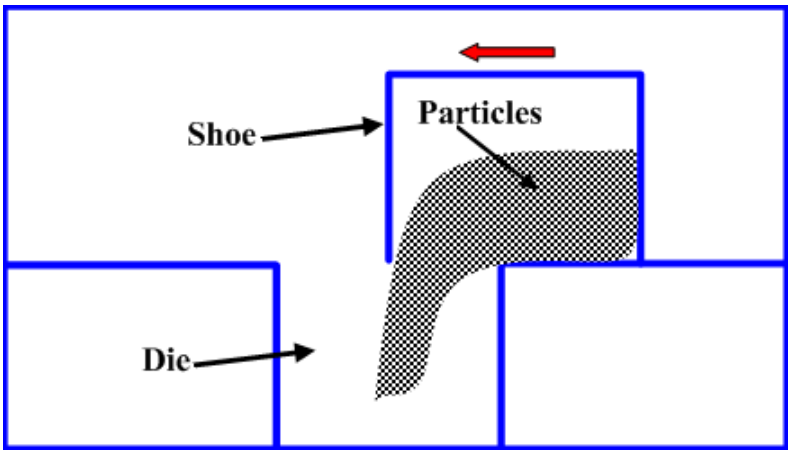

Figure 2.8: Sketch map of the two-dimensional die filling process.

simulators all have good agreement with each other, which verifies the validities of the new simulators. It is worthwhile mentioning that a clerical error on the wall treatment is found in Trubal-org-s source, namely the original Trubal by several numerical experiments. The typo can cause a blast of particle assemble when they are swept by a moving wall with high speed. Therefore, a modification has been done in Trubal-new-s which makes the distinction in the distributions of particles between Trubal-org-s and Trubal-new-s. Trubal-org-s begins to produce the same distributions as Trubal-new-s when the typo is revised. However, there are slightly differences between Trubal-new-s and Trubal-new-p, which can be due to the different precisions in floating point calculations between CPU and GPU, and the accumulation of cyclic steps.

The comparison on the wall time and ratio/speedup of two-dimensional case among Trubal-org-s, Trubal-new-s and Trubal-new-p during 200000 time-steps from four classical moments are shown in Table. 2.3 where the specified thread hierarchies of 'grid-block-thread' in CUDA is '1-12-512'. These moments match along with when the shoe arrives at the die (0.0382 s), covers the die (0.0763 s), starts to leave the die (0.130 s) and prepares to get entirely away from the die (0.305 s), respectively. As shown, Trubal-new-s is a little bit faster than Trubal-org-s. Trubal-new-p reaps speedups of 4.77, 4.70, 4.75 and 4.56 in contrast with Trubal-org-s with the average speedup of 4.69 under platform C2050, while it yields 6.74, 6.26, 6.65 and 6.41 over Trubal-org-s with the average speedup of 6.52 under platform K40c, where Ratio=-1+Trubal-org-sTrubal-new-s and Speedup=Trubal-org-sTrubal-new-p and Motion Speedup is the speedup of motion subroutine only which is derived

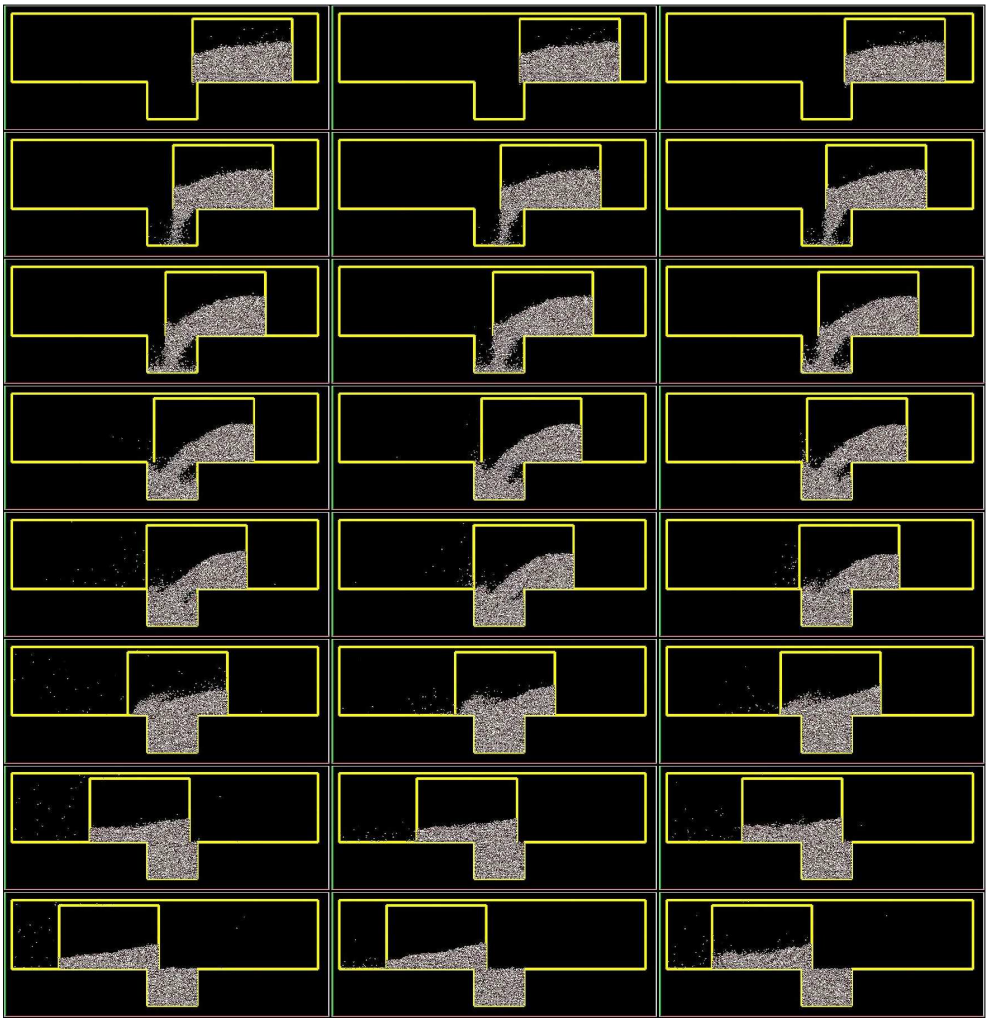

Figure 2.9: Comparison on the distributions of particles in two-dimensional simulation: Trubal-org-s, Trubal-new-s and Trubal-new-p.

Parameter	Value
Number of light, heavy particles and walls	$3000, 3000, 11$
Density of light, heavy particles (kg/m^3)	$400, 7800$
Diameter of particles (m)	1.3×10^{-4}
(Young's modulus (Pa), Poisson's ratio) of particles, walls	$(8.7 \times 10^9, 0.30), (2.1 \times 10^{11}, 0.30)$
Friction of particle-particle, particle-wall	$0.3, 0.3$
Acceleration of gravity (m/s^2)	9.8
Domain of die (m^2)	$(0.002, 0.009) \times (0.020, 0.027)$
Domain of shoe (m^2)	$(0.009, 0.021) \times (0.029, 0.043)$
The whole domain (m^2)	$(0.0, 0.0455) \times (0.0, 0.0234)$
Velocity of the shoe (m/s)	0.07
Time step of the simulation (s)	7.6283×10^{-9}
Size of each box (m^2)	0.00065×0.00065

Table 2.2: Parameters of 2D simulation.

Platform	Physical time	Trubal-org-s Wall time	Trubal-new-s Wall time	Ratio	Trubal-new-p Wall time	Speedup
C2050	0.0382 s	3464.99 s	3459.67 s	0.154%	726.27 s	4.77
	0.0763 s	2878.35 s	2871.09 s	0.253%	612.83 s	4.70
	0.1300 s	2473.77 s	2467.99 s	0.234%	520.65 s	4.75
	0.3050 s	3333.51 s	3316.78 s	0.504%	731.40 s	4.56
K40c	0.0382 s	2886.91 s	2862.33 s	0.086%	428.34 s	6.74
	0.0763 s	2516.69 s	2459.85 s	0.231%	401.81 s	6.26
	0.1300 s	2152.25 s	2106.98 s	0.214%	323.67 s	6.65
	0.3050 s	2782.70 s	2689.04 s	0.348%	434.16 s	6.41

Table 2.3: Wall time and Ratio/Speedup of partial simulations of two-dimensional 6000 particles.

from Eq. 2.8.

Table. 2.4 gives the corresponding comparison among Trubal-org-s, Trubal-new-s and Trubal-new-p on simulating two-dimensional 60000 particles during 200000 time-steps calculation at two classical moments. The same parameters are adopted as listed in Table. 2.2 except the domain of die, the dimension of shoe is modified larger to $(0.09171, 0.13598) \times (0.02846, 0.06641), (0.06325, 0.08538) \times (0.006325, 0.02846)(m^2)$ to contain more particles, and the corresponding thread hierarchies of 'grid-block-thread' is selected as '1-118-512'. It is shown that Trubal-new-p reaps speedups of

Platform	Physical time	Trubal-org-s Wall time	Trubal-new-s Wall time	Ratio	Trubal-new-p Wall time	Speedup
C2050	0.0575 s	26458.14 s	26410.61 s	0.180%	2080.24 s	12.72
	0.1780 s	32483.85 s	32418.33 s	0.202%	2531.57 s	12.83
K40c	0.0575 s	22832.09 s	22615.87 s	0.96%	1229.36 s	18.57
	0.1780 s	29307.68 s	28562.43 s	0.261%	1573.13 s	18.63

Table 2.4: Wall time and Ratio/Speedup of partial simulations of two-dimensional 60000 particles.

12.72 and 12.83 with the average speedup of 12.78 over platform C2050, while it yields 18.57 and 18.63 over Trubal-org-s with the average speedup of 18.60 under platform K40c.

By comparing the two-dimensional results in Table. 2.3 and Table. 2.4, it may come to a conclusion that Trubal-new-p can gave a substantial acceleration on Trubal-org-s, and the speedup increases with the particle and contact number.

2.6.2 Die filling with a stationary shoe: three-dimensional Case

Parameter	Value
Number of large, small particles & walls	$2500, 17500, 14$
Density of particles (kg/m^3)	1500
Diameter of large, small particles (m)	$3.6 \times 10^{-4}, 0.9 \times 10^{-4}$
(Young's modulus (Pa), Poisson's ratio)	
of particles, walls	$(8.7 \times 10^9, 0.30), (2.1 \times 10^{11}, 0.30)$
Friction of par-par, particle-wall	$0.3, 0.3$
Yield stress of particles, walls (MPa)	1.9306×10^3
Acceleration of gravity (m/s^2)	9.8
Domain of die (m^3)	$(0.0042, 0.0112) \times (0.0007, 0.0077) \times (0.0007, 0.0021)$
The whole domain (m^3)	$(0.0, 0.0154) \times (0.0, 0.0189) \times (0.0, 0.0028)$
Time step of the simulation (s)	5.1134×10^{-9}
Size of each box (m^3)	$0.00043 \times 0.00043 \times 0.00043$

Table 2.5: Parameters of three-dimensional simulation.

A three-dimensional model is further considered to demonstrate the capability of the new simulator by simulating a die filling with a stationary shoe. For the current case, the shoe is initially installed above the die to be filled. Same to the moving shoe die filling, the particles are firstly generated in the shoe, the motion of particles is controlled by a shutter which is set at the bottom of the shoe. Once the shutter is open, the particles directly deposit into the die under the action of gravitational force. The parameters of particles and walls relevant to the three-dimensional simulation are shown in Table. 2.5.

Fig. 2.10 displays the distributions of particles in three-dimensional simulation from Trubal-org-s, Trubal-new-s and Trubal-new-p on 0.02454 s, 0.06855 s, 0.10133 s, 0.12220 s. The first moment matches when the particles are settled down to the bottom of the shoe under gravity before the shutter being suddenly removed, and the other three moments characterize the particle distributions in the stationary shoe flowing down to the die. Exact agreements among the three groups of results can be found. The comparison on the wall time and ratio/speedup among Trubal-org-s, Trubal-new-s and Trubal-new-p on simulations of 200000 time-steps from four classical moments are shown in Table. 2.5 where the choice of 'grid-block-thread' in CUDA is '1-40-512'.

Platform	Physical time	Trubal-org-s Wall time	Trubal-new-s Wall time	Ratio	Trubal-new-p Wall time	Speedup
C2050	0.02454 s	6443.17 s	6326.24 s	1.85%	508.82 s	12.66
	0.06855 s	7407.86 s	7189.56 s	3.04%	575.48 s	12.87
	0.10133 s	7514.02 s	7308.73 s	2.81%	580.32 s	12.95
	0.12220 s	8847.17 s	8342.61 s	6.05%	674.79 s	13.11
K40c	0.02454 s	5805.68 s	5364.52 s	8.22%	302.73 s	19.18
	0.06855 s	6792.10 s	6166.34 s	10.15%	344.95 s	19.69
	0.10133 s	6839.89 s	6138.67 s	11.42%	346.27 s	19.75
	0.12220 s	7909.57 s	6828.48 s	15.83%	395.25 s	20.01

Table 2.6: Wall time and Ratio/Speedup of partial simulations of three-dimensional 20000 particles.

As shown in Table. 2.6 , Trubal-new-s is also faster than Trubal-org-s in three-dimensional simulation, and Trubal-new-s strengthens its sequential efficiency. Trubal-new-p reaps speedups of 12.66, 12.87, 12.95 and 13.11 with the average speedup of 12.90 under platform C2050, while it yields 19.18, 19.69, 19.75 and 20.01 over Trubal-org-s with the average speedup of 19.66 under platform K40c. Moreover, we can conclude that the acceleration in the three-dimensional case would be better than the two-dimensional case though less particles are considered, this may due to the

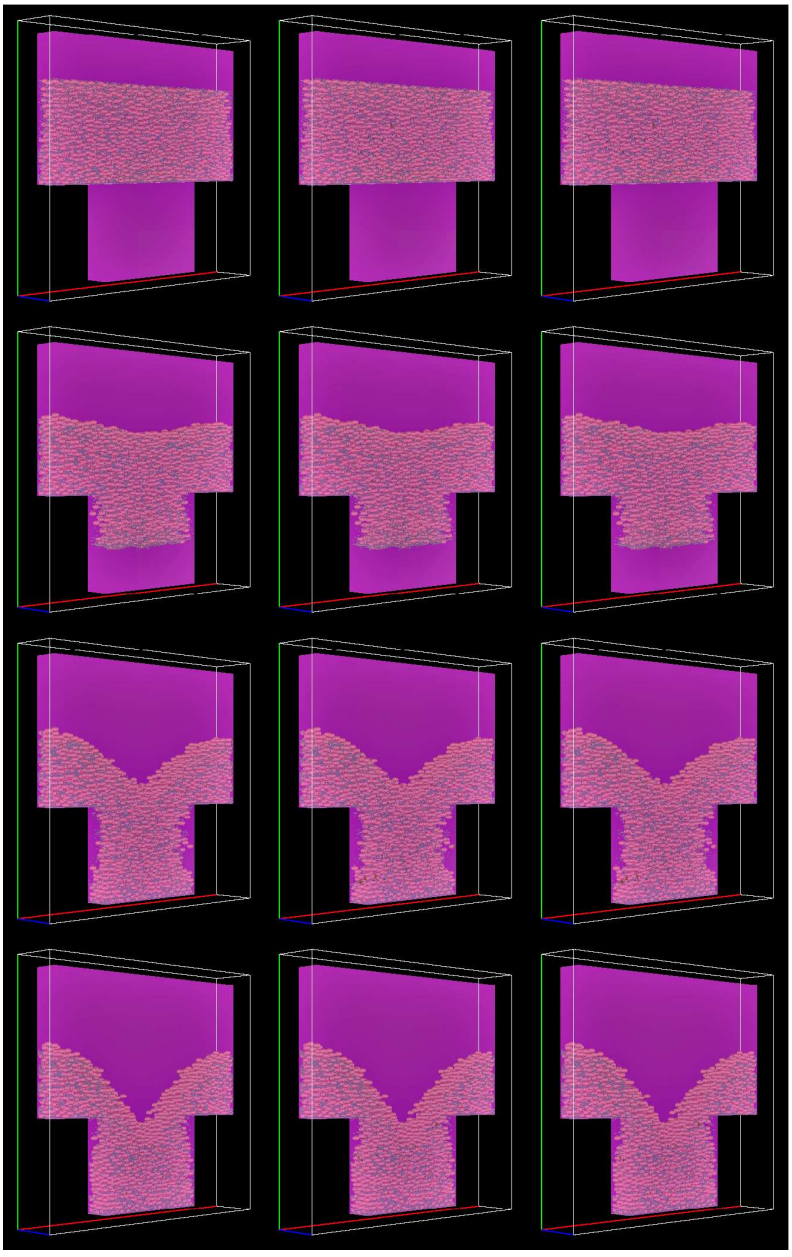

Figure 2.10: Comparison on the distributions of particles in three-dimensional simulation: Trubal-org-s, Trubal-new-s and Trubal-new-p.

complex contact formed in three-dimensional simulation.

The algorithm for contact detections between particles and walls, implemented in Trubal, is rather difficult to be parallelized under CPU-GPU heterogeneous architecture. The former numerical results of Trubal-new-p are based on the contact-detection module executed sequentially on a single CUDA core. Trubal-new-p is designed in this way because of the small proportion of the module, such as 0.21% in the entire simulation of two-dimensional 6000 particles. Even so, a more accurate detection algorithm may decrease the computation complexity of DEM in a way.

2.7 Conclusions

In this chapter, a parallelization of a serial discrete particle algorithm titled Trubal was carried out by following two steps: (1) Reconstruction of the static storage structure; (2) An essential parallelism on the relative newer code using shared memory without bank conflict and texture memory to maximize the frequency of GPU memory bandwidth based on a CPU-GPU heterogeneous architecture. The numerical cases were assessed in two platforms (i) NVIDIA Tesla C2050 card together with Intel Core-Duo 2.93 GHz CPU and (ii) NVIDIA Tesla K40c card along with Intel Xeon 3.00GHz CPU, respectively. Numerical results showed that the final version parallel code gave a substantial acceleration on the Trubal. By simulating 6000 and 60000 two-dimensional particles using a NVIDIA Tesla C2050 card together with Intel Core-Duo 2.93 GHz CPU, average speedups of 4.69 and 12.78 under platform C2050 and 6.52 and 18.60 under platform K40c in computational time were obtained, respectively. And higher speedup was achieved in three-dimensional simulation containing 20000 particles where an average speedup of 12.90 under platform C2050 and 19.66 under platform K40c in computational time were obtained. Our results reveal that the efficiency of the final version parallel code increases with the particle number as well as the contact number. Three-dimensional simulation exhibits higher acceleration than two-dimensional one. However, the list-linked contact-detection algorithm in Trubal seems to limit the effect of current study to some extent, an essential reconstruction on this part will be our work in next step.

References

[1] P. Cundall. A computer model for simulating progressive large scale movements in blocky system. *In: Muller led, ed. Proc Symp Int Soc Rock Mechanics, Rotterdam: Balkama A A*, 1:8–12, 1971.

[2] Colin Thornton and KK Yin. Impact of elastic spheres with and without adhesion. *Powder technology*, 65(1):153–166, 1991.

[3] Colin Thornton and Zemin Ning. A theoretical model for the stick/bounce behaviour of adhesive, elastic-plastic spheres. *Powder technology*, 99(2):154–162, 1998.

[4] Y Sheng, CJ Lawrence, BJ Briscoe, and C Thornton. 3D DEM simulations of powder compaction. In *Discrete Element Methods: Numerical Modeling of Discontinua*, pages 305–310. ASCE, 2002.

[5] Y Guo, KD Kafui, C-Y Wu, C Thornton, and Jonathan PK Seville. A coupled DEM/CFD analysis of the effect of air on powder flow during die filling. *AIChE Journal*, 55(1):49–62, 2009.

[6] Y Guo, C-Y Wu, KD Kafui, and C Thornton. Numerical analysis of density-induced segregation during die filling. *Powder Technology*, 197(1):111–119, 2010.

[7] Y Guo, C-Y Wu, and C Thornton. The effects of air and particle density difference on segregation of powder mixtures during die filling. *Chemical Engineering Science*, 66(4):661–673, 2011.

[8] DK Kafui, S Johnson, C Thornton, and Jonathan PK Seville. Parallelization of a Lagrangian–Eulerian DEM/CFD code for application to fluidized beds. *Powder Technology*, 207(1):270–278, 2011.

[9] Chuan-Yu Wu and Yu Guo. Numerical modelling of suction filling using DEM/CFD. *Chemical Engineering Science*, 73:231–238, 2012.

[10] David W Washington and Jay N Meegoda. Micro-mechanical simulation of geotechnical problems using massively parallel computers. *International journal for numerical and analytical methods in geomechanics*, 27(14):1227–1234, 2003.

[11] J. Ghaboussi, M. Basole, and S. Ranjithan. Three dimensional discrete element analysis on massively parallel computers. *2nd International Conference on Discrete Element Methods*, pages 95–104, 1993.

[12] Algirdas Maknickas, Arnas Kačeniauskas, Rimantas Kačianauskas, Robertas Balevičius, and Algis Džiugys. Parallel DEM software for simulation of granular media. *Informatica*, 17(2):207–224, 2006.

[13] D Darmana, NG Deen, and JAM Kuipers. Parallelization of an euler–lagrange model using mixed domain decomposition and a mirror domain technique: Application to dispersed gas–liquid two-phase flow. *Journal of Computational Physics*, 220(1):216–248, 2006.

[14] Chunsheng Feng, Shi Shu, Jinchao Xu, and Chen-Song Zhang. Numerical study of geometric multigrid methods on cpu–gpu heterogeneous computers. *arXiv preprint arXiv:1208.4247*, 2012.

[15] Yusuke Shigeto and Mikio Sakai. Parallel computing of discrete element method on multi-core processors. *Particuology*, 9(4):398–405, 2011.

[16] Zhao Song Ma, Chun Feng, Tian Ping Liu, and Shi Hai Li. A gpu accelerated continuous-based discrete element method for elastodynamics analysis. *Advanced Materials Research*, 320:329–334, 2011.

[17] Jian Ye, Jing-Xiong Chen, Xiao-Qing Chen, and He-Ping Tao. Modeling and rendering of real-time large-scale granular flow scene on gpu. *Procedia Environmental Sciences*, 10:1035–1045, 2011.

[18] Charles A Radeke, Benjamin J Glasser, and Johannes G Khinast. Large-scale powder mixer simulations using massively parallel gpuarchitectures. *Chemical Engineering Science*, 65(24):6435–6442, 2010.

[19] Xinxin Ren, Huabiao Qi, Lijie Cui, Jinghai Li, et al. Gpu-based discrete element simulation on a tote blender for performance improvement. *Powder Technology*, 2013.

[20] K.L. Johnson. Contact mechanics. *Cambridge: Cambridge University Press*, 1985.

[21] R.D. Mindlin, R.D. Mindlin, and H. Deresiewicz. Elastic spheres in contact under varying oblique forces. *Journal of Applied Mechanics*, 20:327–344, 1953.

Chapter 3

Effect of collisions on the particle behavior in a turbulent square duct flow

Part of the contents of this chapter have been published as:

H Zhang, FX Trias, A Gorobets, A Oliva, D Yang, Y Tan, Y Sheng. Effect of collisions on the particle behavior in a turbulent square duct flow. *Powder Technology. 269(2015), 320-336.*

H Zhang, FX Trias, A Gorobets, A Oliva, D Yang, Y Tan, Y Sheng. Numerical investigation on particle resuspension in turbulent duct flow via DNS-DEM: Effect of collisions. *11th. World Congress on Computational Mechanics (WCCM XI). Barcelona, Spain, 2014*

Abstract.

In this chapter, the effect of collisions on the particle behavior in fully developed turbulent flow in a straight square duct at $Re_\tau = 300$ was numerically investigated. The hydrodynamic modeling of the fluid phase was based on direct numerical simulation. The kinematics and trajectory of the particles as well as the collisions were described by the DEM. Three sizes of particles were considered with diameters equal to 50 μm, 100 μm and 500 μm. Firstly, the particle transportation by turbulent flow was studied in the absence of the gravitational effect. It is found that the collisions play an important role in the particle distribution especially in the near-wall regions. The inter-particle collisions enhance the particle diffusion in the direction perpendicular to streamwise flow and make the particles distribute more uniformly near the wall. Then, the particle deposition was studied under the effect of the wall-normal gravity force in which the influence of collisions on the particle resuspension rate and the final stage of particle distribution on the duct floor are discussed, respectively. The collisions were found

to have influence on the particle resuspension rate near the duct floor whereas hardly affect the particle behavior near the duct center. Under the gravitational effect the 50 μm particles deposit more efficiently near the side walls but the 100 μm and 500 μm particles preferentially deposit near the center of the duct floor. Moreover, all the sizes of particles tend to concentrate near the center of the duct floor at the final stage of the particle deposition when the inter-particle collisions are considered.

3.1 Mathematical descriptions

3.1.1 Governing equations and numerical methods for DNS

In this chapter, we consider the simulation of incompressible turbulent flows of Newtonian fluids. Under these assumptions, the governing equations of the fluid phase read

$$\begin{array}{rcl} \nabla \cdot u_f & = & 0 \\ \frac{\partial u_f}{\partial t} + \nabla \cdot (u_f \otimes u_f) & = & -\nabla p + \nu \nabla^2 u_f \end{array} \tag{3.1}$$

where $u_f = (u, v, w)$ and p represent the fluid velocity and kinematic pressure fields, respectively. ν is the kinematic viscosity. In this study, the solid particle phase is considered to be dilute enough to neglect the effect on the turbulent flow and thus one-way coupled.

The incompressible Navier-Stokes (NS) equations (3.1) are discretized on a staggered Cartesian grid using a symmetry-preserving discretization [1]. Shortly, the temporal evolution of the spatially discrete staggered velocity vector, u_h, is governed by the following operator-based finite-volume discretization of Eqs.(3.1),

$$\Omega \frac{du_h}{dt} + C(u_h)u_h + Du_h - M^T p_h = 0_h \tag{3.2}$$

where the discrete incompressibility constraint is given by $Mu_h = 0_h$. The diffusive matrix D is symmetric and positive semi-definite, it represents the integral of the diffusive flux, $-\nu \nabla u \cdot n$, through the faces. The diagonal matrix, Ω, describes the sizes of the control volumes and the approximate, convective flux is discretized as in [1]. The resulting convective matrix C is skew-symmetric, *i.e* $C = -C^T$. Then, for the temporal discretization, a second-order explicit one-leg scheme is used for both the convective and diffusive terms [2]. Finally, the pressure-velocity coupling is then solved by means of a classical fractional step projection method [3]: a predictor velocity u_h^p is explicitly evaluated without considering the contribution of the pressure gradient. By imposing the incompressibility constraint, $Mu_h^{n+1} = 0_h$, it leads to a Poisson equation for p_h^{n+1} to be solved once each time-step,

$$Lp^{n+1} = Mu_h^p \qquad \text{with} \qquad L = -M\Omega^{-1}M^T \tag{3.3}$$

where the discrete Laplacian operator L is represented by a symmetric negative semi-definite matrix. For details about the numerical algorithms and the verification of the DNS code the reader is referred to [4].

3.1.2 Modeling of particle-fluid and particle-particle interactions

When the particles collide directly with other particles or the walls, the DEM [5] is employed to calculate the collision force. Including the collision force and hydrodynamic force, the dynamic equations of the particle can be expressed as:

$$m\frac{\partial^2 S}{\partial t^2} = (1-\frac{\rho_f}{\rho_p})g + F_c + F_{fpi} \tag{3.4}$$

$$I\frac{\partial^2 \theta}{\partial t^2} = \tau \tag{3.5}$$

where m and I are the mass and the moment of inertia of the particle, respectively. S is the particle position and θ is the angular position. ρ_f and ρ_p are the densities of the fluid and particle, respectively. g is the gravitational acceleration if considered, τ is the torque. Considered forces at the right hand side of Eq. 3.4 are the gravitational force, the buoyant force, the collision force F_c and the fluid-particle interaction force F_{fpi}. In this study, the particles and walls are directly specified by material properties in the simulation such as density, Young's modulus and friction coefficient. When the collisions take place, the theory of Hertz [6] is used for modeling the force-displacement relationship while the theory of Mindlin and Deresiewicz [7] is employed for the tangential force-displacement calculations.

The fluid-particle interaction force F_{fpi} is constituted by the Stokes drag force and the lift force that are related to the relative velocity between the fluid and particle, $U_r = u_f - u_p$.

$$F_{fpi} = 0.5\rho_f A_p C_D |U_r| U_r + 1.615 m_p d_p \rho_f \nu Re_s^{0.5} c_{ls} \frac{[U_r \times \omega]}{|\omega|} \tag{3.6}$$

where A_p is the cross-sectional area of the particle which is given as $A_p = 0.25\pi d_p^2$, d_p is the diameter of the particle. $C_D = 24(1 + 0.15Re_p^{0.687})/Re_p$ is the drag coefficient. The particle Reynolds number $Re_p = |U_r|d_p/\nu$. $Re_s = \rho_p d_p^2 |\omega|/(\rho_f \nu)$ is the particle Reynolds number of the shear flow in which ω stands for the fluid rotation. When $Re_p > 40$, $c_{ls} = 0.0524(\beta Re_p)^{0.5}$. When $Re_p \leq 40$, $c_{ls} = (1 - 0.3314\beta^{0.5})e^{-Re_p/10} + 0.3314\beta^{0.5}$. Here, β is a parameter given by $\beta = 0.5Re_s/Re_p$ (for $0.005 < \beta < 0.4$).

3.1.3 Subcyling approaching on the timesteps

In the context of DNS, the timestep Δt_{DNS} is determined by a two-step linear explicit scheme on a fractional-step method proposed by Trias and Lehmkuhl [2]. Its main advantage relies on its capacity to dynamically adapt the time step to the maximum possible value while at the same time it is kept within the stability limits.

An explicit finite-difference scheme is also used to solve the particle motion by incrementally calculating the various forces in DEM. Δt_{DEM} is determined based on the Rayleigh wave speed of force transmission on the surface of elastic bodies [8]. At each Δt_{DEM}, the translational and rotational accelerations of each particle are assumed to be constant and a numerical integration yields updated velocities and positions of each particle. The new positions are used to calculate the relative approach and interaction force between contacting particles. Contact detection and the force calculation are the most time-consuming parts in the DEM simulation. In this study, the calculation domain is divided into cubes, each particle is mapped into the cubes that it lies in. Contact detection is carried out in each cube with the mapping refreshed during several timesteps. Due to the fact that there are two timesteps, Δt_{DNS} and Δt_{DEM}, in the coupling simulation, a subcycling approach is needed. It has been found that Δt_{DEM} is significantly less than Δt_{DNS} in this study, therefore it is allowed the execution of a number, $N_{ratio} = \Delta t_{DNS}/\Delta t_{DEM}$, of consecutive DEM time steps within a single DNS time step, during the DEM subcycling the hydrodynamic force is not updated. Since Δt_{DEM} is constant and determined prior to the simulation, N_{ratio} may fluctuate corresponding to the self-adaptive strategy in [2]. Our numerical experiments show that this scheme works well in general.

3.2 Verification and validation

3.2.1 Verification of the DNS code

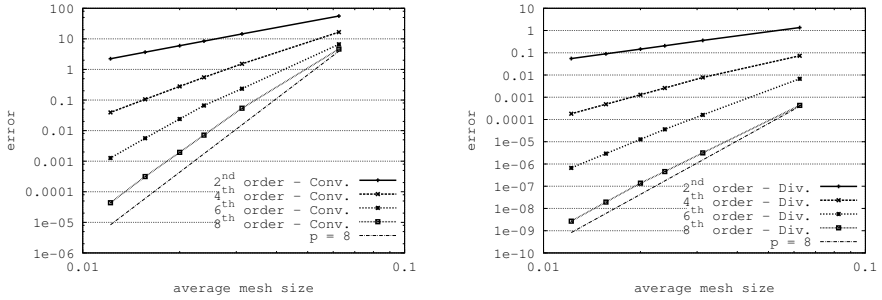

Figure 3.1: Numerical errors versus mesh size for convective (left) and divergence (right) perators for second-, fourth-, sixth- and eighth-order discretizations.

The DNS code was verified using the Method of Manufactured Solutions [9] where an arbitrary analytic function u_a is chosen, and tested for several benchmark reference results. Fig. 3.1 displays convergence tests for convective and divergence

operators for orders of accuracy from second up to eighth. The norm of the errors is given by $\parallel R_h((u_a \cdot \nabla)u_a) - C(R_h u_a)R_h u_a \parallel_\infty$ and $\parallel MR_h u_a \parallel_\infty$, respectively. The analytical velocity field u_a is given by a C^∞ divergence-free function and R_h is the operator that defines pointwise restrictions on mesh nodes. Results show a very good agreement with the expected order of accuracy, p. For more details about the code verification the reader is referred to our previous DNS works [4, 10].

3.2.2 Verification of the simulation: Comparing with Gavrilakis [11]

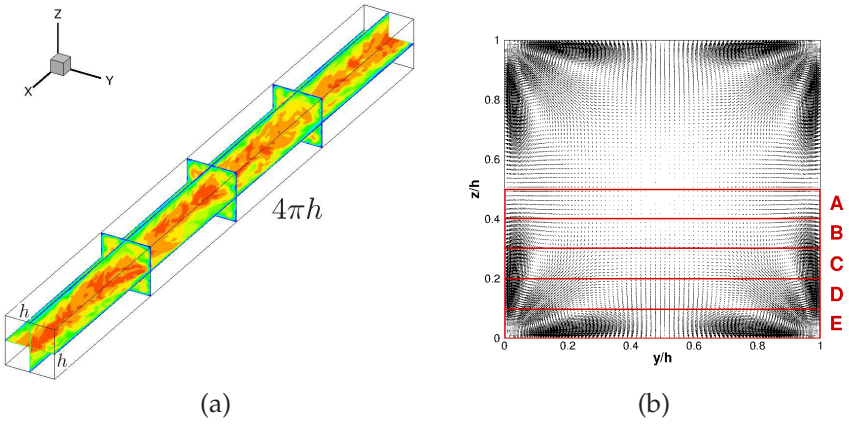

(a) (b)

Figure 3.2: (a) Instantaneous velocity in $x-$direction in a square duct at $Re_\tau = 300$. (b) Mean secondary flows in $y-$ and $z-$directions.

The configuration of interest in this study is displayed in Fig. 3.2 (a). The computational domain is $4\pi h \times h \times h$ in the streamwise and wall-normal directions, $h = 0.02m$. The Reynolds number based on the friction velocity, u_τ and the hydraulic diameter, h, is $Re_\tau = 300$. Periodic boundary conditions are applied in the streamwise direction. The flow is driven by means of a constant pressure gradient in the streamwise direction. No-slip boundary conditions are imposed at the walls. The direction of the gravitational action is set along $z-$direction downwards if considered.

Re_τ	L_x	L_z	$N_x \times N_y \times N_z$	L_x^+	L_z^+	Δx^+	Δz^+_{min}
300	$4\pi h$	h	$322 \times 202 \times 202$	3770	300	11.78	0.75

Table 3.1: Parameters relevant to the DNS.

Since no subgrid-scale model is used in the computation, the grid resolution and

the time step have to be fine enough to resolve all the relevant turbulent scales. We have used a $322 \times 202 \times 202$ uniform staggered grids to cover the computational domain. The parameters relevant to the DNS are given in Table. 3.1, the variable with superscript $'+'$ denotes the wall length unit. The grid resolution in the $x-$direction is $\Delta x^+ = 11.78$ wall units and the grid point closest to the sidewalls is at $\Delta z^+_{min} = 0.75$ which is significantly less than the Kolmogorov length scale. The parameters in the $y-$direction are same as that in the $z-$direction therefore not shown.

Researchers	Gavrilakis [11]	Sharma and Phares [12]	This study
$T_{statistics}(\frac{h}{2u^a_\tau})$	5	16	20
Streamwise length	$10\pi h$	$4\pi h$	$4\pi h$

Table 3.2: Parameters relevant to the DNS.

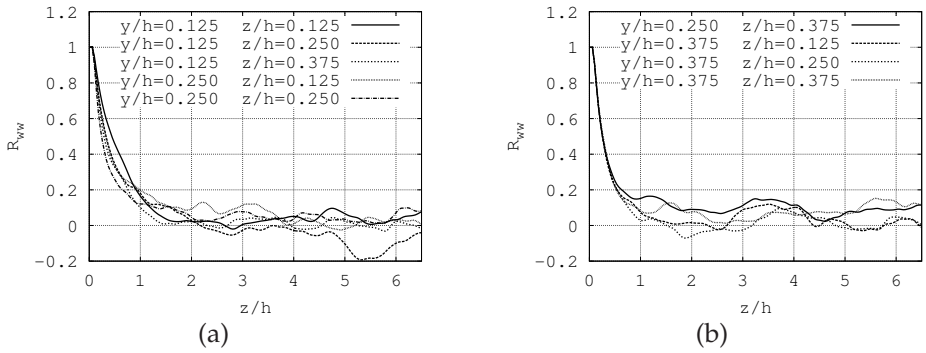

Figure 3.3: Two-point correlations at nine monitoring locations.

The starting time for averaging and the time integration period must be long enough to evaluate the flow statistics properly. Table. 3.2 displays those parameters adopted in previous references and this study. The period necessary for flow statistics increases with the decrease of the streamwise length adopted in the simulation. In this study, the flow statistics are obtained over a period of 20 $turnovers$ where 1 $turnover = h/(2u^a_\tau)$.

A sufficient length in the periodic $x-$direction is required to ensure that the two-point streamwise correlations of the velocity have to decay sufficiently for separations equal to half the streamwise length. This issue has been fully discussed in [11], however a long length ($10\pi h$) was employed by the author for safety. Based on the research of Uhlmann et al. [13], the minimum value for the streamwise period of the computational domain measures is around 190 wall units and roughly indepen-

dently of the Reynolds number. In order to ensure the length in the streamwise direction, a two-point correlation was conducted before the main simulations. To do so, streamwise two-point correlations, $R_{\phi\phi}(\Delta x, y, z) = \frac{<\phi'(x,y,z)\phi'(x+\Delta x,y,z)>}{<\phi'^2(x,y,z)>}$, at different $(y, z)-$locations have been used to check the suitability of the numerical simulation parameters in the x-direction, where $< \cdot >$ represent the average over time. In Fig. 3.3, two-point correlations of the velocity component, R_{ww}, at nine different $(y, z)-$locations are shown. In all the cases, the correlation values fall to zero for separations lower than one half-period. The computational domain in the streamwise direction is sufficiently large by means of the current choice. From Fig. 3.3 it also shows the possibility to use a shorter streamwise length like $2\pi h$ in [14]. However, any cut on the streamwise length leads to a marked increase on the statistics period.

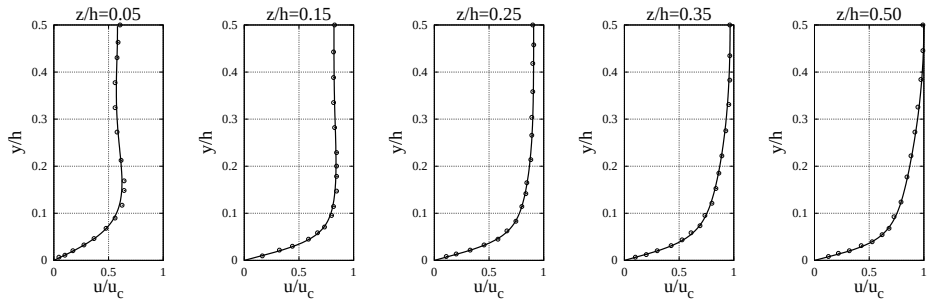

Figure 3.4: Quadrant-averaged profiles at five locations in the duct for the mean streamwise velocity.(−)Present DNS, (o) Gavrilakis [11].

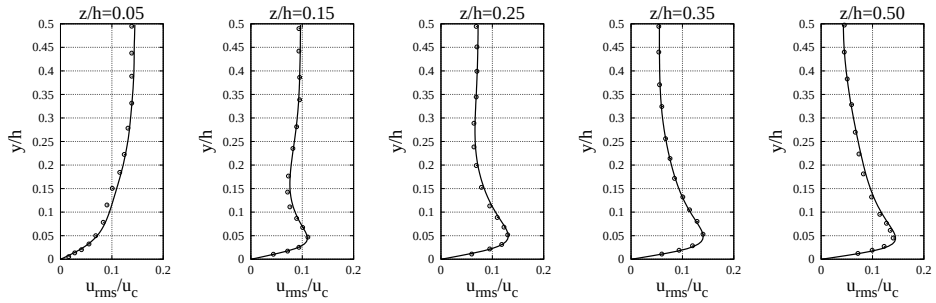

Figure 3.5: Quadrant-averaged profiles at five locations in the duct for rms fluctuations in streamwise velocity.(−)Present DNS, (o) Gavrilakis [11].

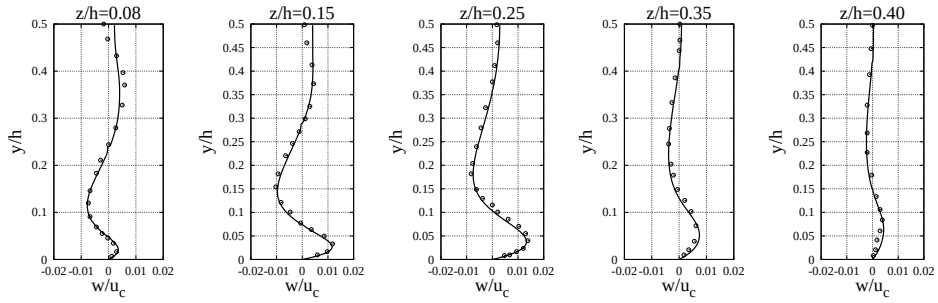

Figure 3.6: Quadrant-averaged profiles at five locations in the duct for the mean lateral velocity.(−)Present DNS, (o) Gavrilakis [11].

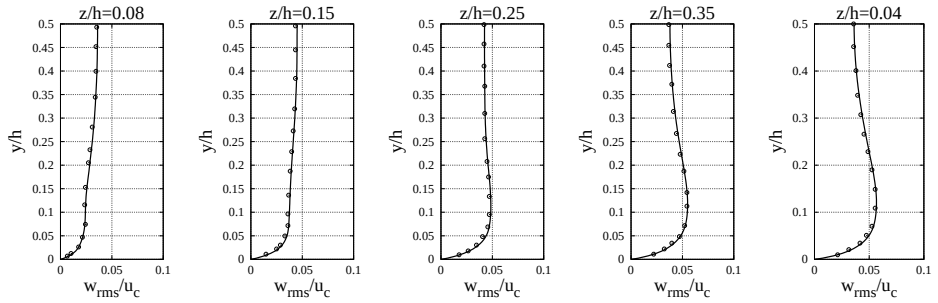

Figure 3.7: Quadrant-averaged profiles at five locations in the duct for rms fluctuations in lateral velocity.(−)Present DNS, (o) Gavrilakis [11].

Figure 3.2 (b) displays the quadrant-averaged $v - w$ velocity vectors in the cross-section of the duct. As expected there are four pairs of counter-rotating vortexes with a symmetrical distribution. The velocity vectors are from the core to the corners which deliver fluid momentum. When approaching the corners, the fluid turns half a right-angle then flows along the wall until encounters another flow from the other corner, they flow back into the duct center together. Figure 3.2 (a) gives a perspective view of instantaneous distributions of the streamwise velocity at different planes and locations. It is shown that the three slices normal to the streamwise direction present significant discrepancies. The local distributions of u_f are in chaos whereas globally the largest velocity exists near the centerline and the velocities that near the sidewalls are much lower due to the no-slip boundaries. Quantitative results are presented in Figure 3.4, 3.5, 3.6 and 3.7 where quadrant-averaged profiles for the magnitude and rms fluctuations in streamwise and lateral velocities are compared with those

d_p (μm)	d_p^+ (-)	E_i (GPa)	ρ_p ($kg \cdot m^{-3}$)	ν_i (-)	τ_p (s)	St (-)
50	0.75	68.95	2500	0.33	3.46×10^{-4}	0.078
100	1.5	68.95	2500	0.33	1.38×10^{-3}	0.321
500	7.5	68.95	2500	0.33	3.46×10^{-2}	7.816

Table 3.3: Parameters of the particles relevant to the simulations.

reported by Gavrilakis [11], u_c is the centerline velocity. It is shown that very good agreements have been found in these comparisons.

3.3 Results and discussion

In Section 3.3, the results concerning the particle transportation and deposition in the turbulent square duct flow are presented. The above fully developed turbulent flow is used as an initial condition for the multiphase flow simulation, the time is set to zero. The carrier fluid is water with density $\rho_f = 1000kg/m^3$ and kinematic viscosity $\nu = 1.004 \times 10^{-6} m^2 s^{-1}$, $h = 0.02m$. Three kinds of particles are considered namely the small particles with diameter 50 μm, the medium-sized particles with diameter 100 μm and the large particles with diameter 500 μm. The properties of the particles are given in Table 3.3 where the dimensional and non-dimensional particle relaxation time are defined as $\tau_p = \rho_p d_p^2/(18\rho_f \nu)$ and $St = \tau_p u_\tau^2/\nu$, respectively. Particle transportation is treated firstly in the absence of the gravitational effect in Section 3.3.1. Then, particle deposition from turbulent flow in a horizontal square duct is studied where the effect of the inter-particle collisions on the particle resuspension rate and final stage of particle deposition are discussed in Section 3.3.2 and Section 3.3.3, respectively.

3.3.1 Particle transportation

Multi particle:20000

Initially, 20000 particles are randomly generated in the fully developed turbulent flow, three sizes of particles are considered with diameters 50 μm, 100 μm and 500 μm. The particles would have the same velocity as the fluid flow, this time is defined as the starting time. The periodic boundary conditions are used for the particles in the streamwise direction. The collisions between the particles and between the particles and the four bounded walls are treated via DEM, the walls have the same physical properties as the particles as shown in Table 3.3. These boundary conditions are assumed below unless otherwise stated. The particle number employed here is about

twice the number in Yao and Fairweather [15] whereas the whole calculation domain is one quarter. Therefore, it is believed that the particle number is sufficient to ensure the statistical independence of the particle results. Two sets of simulations are carried out with and without collisions. Figure 3.8, 3.9 and 3.10 display the instantaneous distribution of the particles without collisions superimposed onto contours of the streamwise fluid velocity at $t = 24s$ (10 $turnovers$) from the starting time, the isocontours are uniformly distributed from 0 to u_c, two heights are selected $z/h = 0.50$, $z/h = 0.05$ or $z^+ = 150$, $z^+ = 15$ in wall units. In Figure 3.8, 3.9 and 3.10 (top), the particles that located within 6 wall units to the $z^+ = 150$ plane are picked and shown. In Figure 3.8, 3.9 and 3.10 (bottom) where the fluid velocity presents more streaky distributions, the particles located from 0 to 15 wall units in the $z-$direction are picked. Due to the low mass load of the small and medium-sized particles at the current particle number, the inter-particle collisions hardly have effect on the particle distributions. Almost no difference is observed between the two cases with and without collisions, therefore, the 50 μm and 100 μm particle distributions with collisions are not given, the difference between the 500 μm particle distributions with and without collisions will be discussed below.

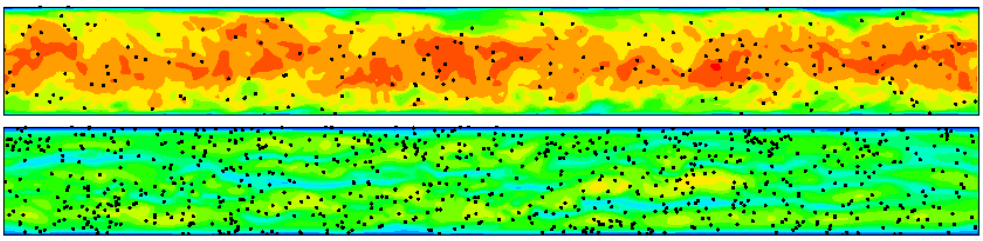

Figure 3.8: Contour: Instantaneous distribution of streamwise fluid velocity on two (x, y) planes. Top: $z/h = 0.50$, Bottom: $z/h = 0.05$ at $t = 24s$. $(\cdot)$: Instantaneous distribution of the 50 μm particles at corresponding locations and time. Without collisions.

From Figure 3.8, 3.9 and 3.10 (top), it can be seen that all the sizes of particles distribute irregularly near the duct center, the patterns of the particle distribution are similar with the high velocities and the medium-sized particles tend to follow the trend of the instantaneous turbulent flow better than the small and large ones, this is due to the fact that the St of the medium-sized particles is closer to unit. These observations consist well with that reported in [12] and [16]. Figure 3.8, 3.9 and 3.10 (bottom) display the particle distributions of different size in the near wall region, it is shown that streaky particle distributions are formed corresponding to the wall coherent structure of the turbulent flows, and the large particles. For the high inertia particles, turbulent vortexes are not sufficiently energetic to entrain them, therefore,

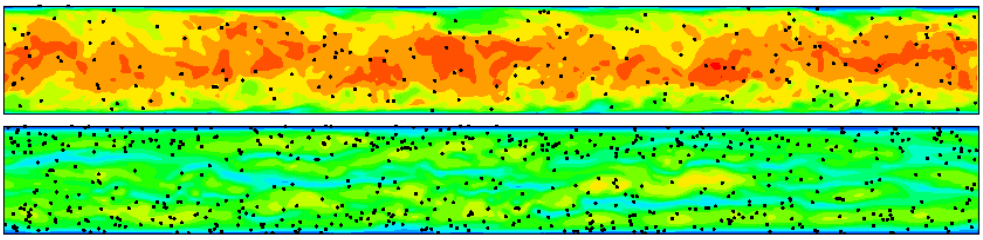

Figure 3.9: Contour: Instantaneous distribution of streamwise fluid velocity on two (x, y) planes. Top: $z/h = 0.50$, Bottom: $z/h = 0.05$ at $t = 24s$. $(\cdot)$: Instantaneous distribution of the 100 μm particles at corresponding locations and time. Without collisions.

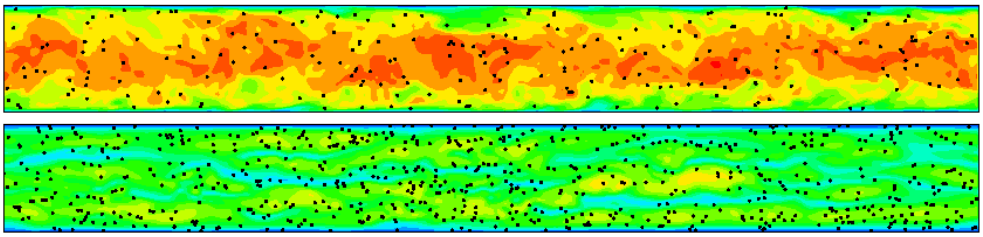

Figure 3.10: Contour: Instantaneous distribution of streamwise fluid velocity on two (x, y) planes. Top: $z/h = 0.50$, Bottom: $z/h = 0.05$ at $t = 24s$. $(\cdot)$: Instantaneous distribution of the 500 μm particles at corresponding locations and time. Without collisions.

they are segregated in the low-velocity areas. The preferential concentration behavior of the particles in the near-wall regions of turbulent flows have been observed both in numerical simulations [17, 16] and experimental measurements [18]. Moreover, the medium-sized and large particles in the wall region tend to accumulate close to the corners due to the effect of the secondary flow. These findings show the same trend as reported by Sharma and Phares [12, 19] who also ignored the gravity force.

Quantitative results are presented in Figure 3.11 (a), (b) and (c) which show the probability density function (PDF = Local number of particles/Total number of particles in the plane) lines of different particles along the $y-$direction at three planes of $z/h = 0.50$, $z/h = 0.05$ and $z/h = 0.02$. The particles located from 0 to 6 wall units in the $z-$direction are picked for the $z/h = 0.02$ plane. It is shown in Figure 3.11 (a) that the 50 μm particles are well-mixed through the cross-section of the duct due

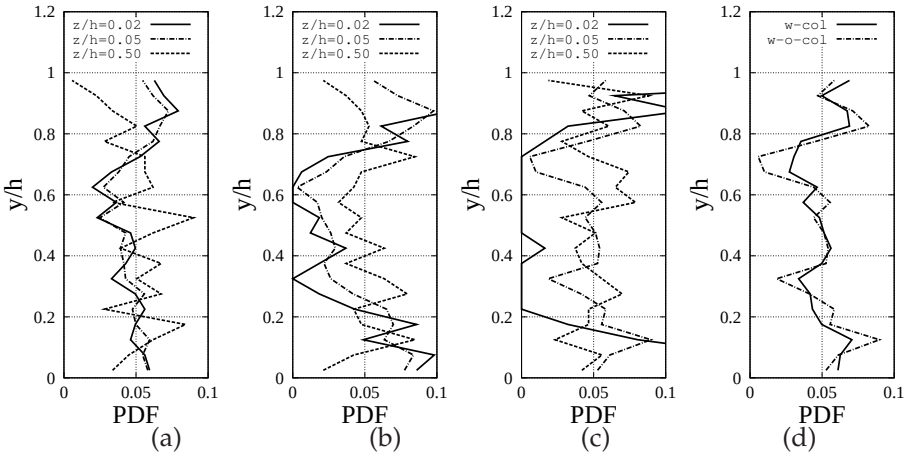

Figure 3.11: PDF along the $y-$direction for the (a) 50 μm, (b) 100 μm and (c) 500 μm particles, without collisions. (d) PDF of the 500 μm particles at the $z/h = 0.05$ plane, with and without collisions.

to the low inertia. In Figure 3.11 (b) and (c), the 100 μm and 500 μm particles near the duct center distribute uniformly with the PDF fluctuating around 5%. However, the 100 μm and 500 μm particles in the near-wall regions are found to significantly concentrate to the corners. This is because the secondary vortexes flow from the duct center to the corners which take both the 100 μm and 500 μm particles towards the corners. The particles in the corners are then carried by the secondary flow towards the wall center. Unlike the 100 μm particles, some 500 μm particles are also found to concentrate near the wall center. This can be due to the high inertia of the 500 μm particles. The effect of the secondary flows on the 500 μm particles is relatively weak in the duct interior but increases significantly when the large particles approach the wall, especially on the particle movement perpendicular to the streamwise direction. Therefore, in the near-wall regions, the secondary flows carry the large particles towards the bisector of the wall but are not strong enough to take them back into the duct interior. Details on this part are given in Section 3.3.3 on the particle deposition.

The effect of the inter-particle collisions on the particle distributions increases with the particle size. In the near-wall regions as shown in Figure 3.12, the collisions obviously change the instantaneous distribution of the 500 μm particles, a more streaky distribution is shown when the inter-particle collisions are not considered. The collisions are found to enhance the diffusion in the direction perpendicular to the streamwise flow especially near the corners, this finding is confirmed in Figure 3.11 (d) where the PDF of the 500 μm particles at $z/h = 0.05$ with and without

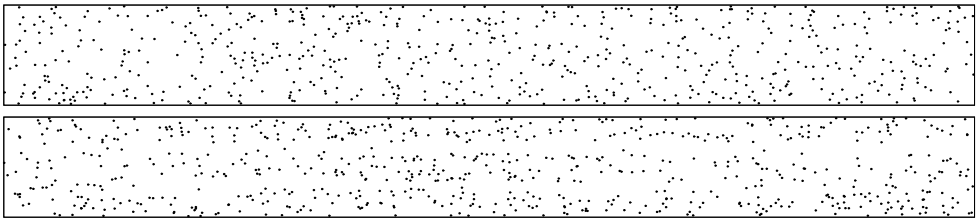

Figure 3.12: Instantaneous distribution of the 500 μm particles on the (x, y) plane of $z/h = 0.05$. Top: with collisions. Bottom: without collisions.

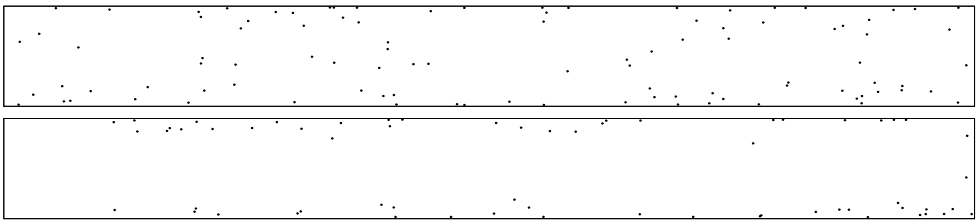

Figure 3.13: Instantaneous distribution of the 500 μm particles on the (x, y) plane of $z/h = 0.02$. Top: with collisions. Bottom: without collisions.

collisions are given. It is shown that the peaks near the corners have been flattened by the collisions. In the regions very close to the walls as shown in Figure 3.13, the particle distribution without collisions is very dilute.

Multi particle:50000

For a better understanding, a second numerical simulation is conducted containing more particles. Totally 50000 particles are randomly planted in the fully developed flow field. Here two kinds of particles are considered: 100 μm and 500 μm with the physical parameters unchanged. It is found that the inter-particle collisions have no significant effect of the 100 μm particles even increasing the mass load. Figure 3.14 displays the instantaneous distribution of the 100 μm particles without collisions and the contours of the streamwise fluid velocity at $t = 24s$. Basically the same trend can be found as shown in Figure 3.9 with the particle number increasing in each planes.

However, the effect of the inter-particle collisions increases with the particle number for the 500 μm particles as shown in Figure 3.15, 3.16 and 3.17. More collisions are suspected to take place to uniform the particle distribution especially in the near-wall regions. Overall, the main findings on the particle transportation may be summarized as follows: the inter-particle collisions hardly affect the behavior of

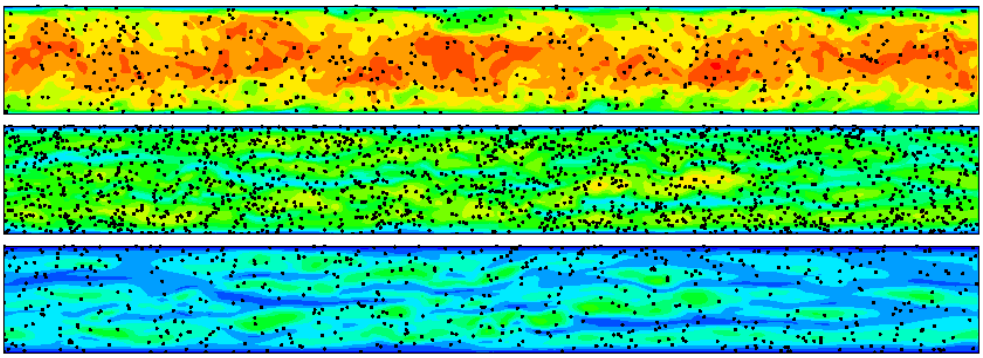

Figure 3.14: Contour: Instantaneous distribution of streamwise fluid velocity on two (x, y) planes. Top: $z/h = 0.50$, Middle: $z/h = 0.05$ Bottom: $z/h = 0.02$ at $t = 24s$. $(\cdot)$: Instantaneous distribution of the 100 μm particles at corresponding locations and time. Without collisions.

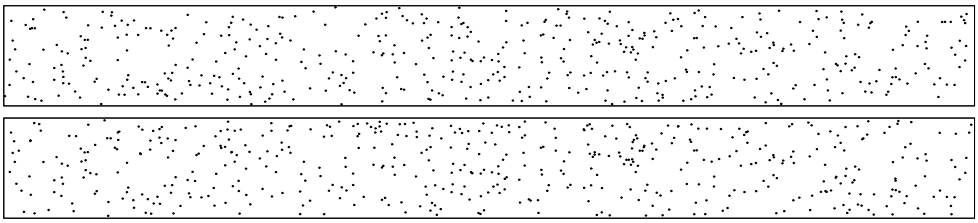

Figure 3.15: Instantaneous distribution of the 500 μm particles on the (x, y) plane of $z/h = 0.5$. Top: with collisions. Bottom: without collisions.

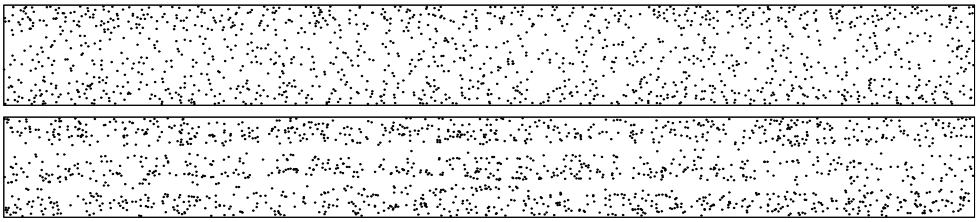

Figure 3.16: Instantaneous distribution of the 500 μm particles on the (x, y) plane of $z/h = 0.05$. Top: with collisions. Bottom: without collisions.

the 50 μm and 100 μm particles through the whole duct as well as the 500 μm parti-

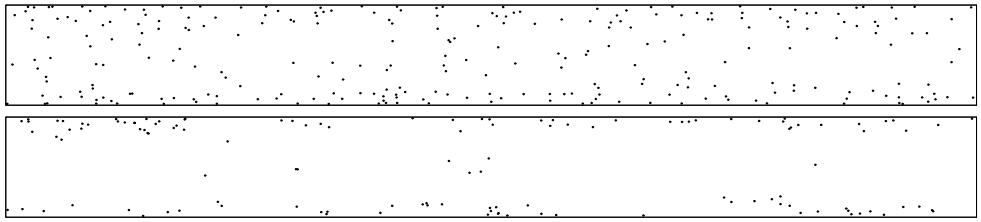

Figure 3.17: Instantaneous distribution of the 500 μm particles on the (x, y) plane of $z/h = 0.02$. Top: with collisions. Bottom: without collisions.

cles near duct center. The 100 μm and 500 μm particles show streaky distributions in the near-wall region and tend to concentrate to the corners. The particle interaction plays an important role in the distribution of the 500 μm particles especially in the near-wall regions. The inter-particle collisions enhance the particle diffusion in the direction perpendicular to streamwise flow and make the particles distribute more uniformly near the wall. This trend increases with the particle number. In the region very close to the wall, there are more particles in the case with collisions than without collisions.

3.3.2 Particle resuspension

In this and following sections, the gravitational action is considered and the direction is set along the $z-$direction downwards as shown in Figure 3.2 (a). Due to the fact that the $Re_\tau = 300$ adopted in the current study is significantly lower than that in the previous works [15, 20], it is necessary to examine the strength of the particle resuspension. To do so, single particle test is conducted in Section 3.3.2 before the multi-particle simulation in the next subsection.

Single particle

The examination is carried out by releasing different particles at two starting positions at the saddle region between two pairs of counter-rotating vortexes in the first quadrant as shown in Figure 3.2 (b). Starting point I is at ($y/h = 0.4552, z/h = 0.0830$) or ($y^+ = 137, z^+ = 25$) in wall units, Starting point II is at ($y/h = 0.0906, z/h = 0.4363$) or ($y^+ = 27, z^+ = 131$) in wall units, from where we check the resuspension effect in the vertical ($z-$) and horizontal ($y-$) direction, respectively. Three particles are considered namely particles with a diameter 50 μm, 100 μm and 500 μm. Each particle at rest floats in the same fluid. The trajectories of the particles are depicted in Figure 3.18. We can see that there is particle resuspension for the small and medium-

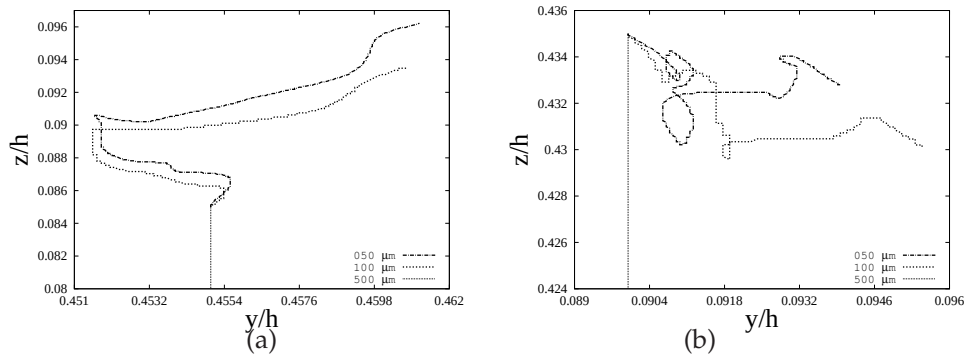

Figure 3.18: Trajectories of different particles from two starting points. (a) ($y/h = 0.4552, z/h = 0.0830$) and (b) ($y/h = 0.0906, z/h = 0.4363$).

Diameter (μm)	Starting point Start	I End	Starting point Start	II End
	$\mid w_f - w_p \mid$ (m/s)		$\mid v_f - v_p \mid$ (m/s)	
50	0.012	0.007	0.014	0.007
100	0.012	0.005	0.014	0.009
500	0.012	0.06	0.014	0.002
	Drag force (N) $z-$direction		Drag force (N) $y-$direction	
50	9.214×10^{-9}	-3.491×10^{-9}	1.189×10^{-8}	-3.841×10^{-9}
100	2.249×10^{-8}	-6.127×10^{-9}	3.041×10^{-8}	-1.001×10^{-8}
500	2.207×10^{-7}	7.906×10^{-7}	3.291×10^{-7}	2.317×10^{-8}
	Lift force (N) $z-$direction		Lift force (N) $y-$direction	
50	1.369×10^{-9}	6.087×10^{-9}	2.690×10^{-9}	4.301×10^{-9}
100	3.110×10^{-9}	2.172×10^{-8}	4.226×10^{-9}	1.779×10^{-8}
500	4.667×10^{-8}	1.450×10^{-7}	1.401×10^{-7}	9.418×10^{-8}

Table 3.4: Hydrodynamic force on the particle.

sized particles even in relative low $Re_\tau = 300$ turbulent flow. The 50 and 100 μm particles can respond to the local structure of surrounding fluid due to the low relaxation time. The trends of the two trajectories are quite similar and the 50 μm particle is rose higher than the 100 μm particle. This indicated that the low-inertia particle is

more affected by the rising force against gravity action. On the contrary, the 500 μm particle has hardly respond on the fluid structure and deposits directly to the duct floor. The same trend can be observed from Figure 3.18 (b), it is shown that due to the secondary flows in the horizontal direction, the 50 and 100 μm particles are pushed further away from the sidewall. At the same time, the velocity of the large particle drops vertically downwards under the action of gravity without any resuspension. All these observations are in good agreements with those reported in [15] at higher Re_τ.

Quantitative results are presented in Table 3.4. At the starting time, the hydrodynamic forces in the $z-$direction on the 50 and 100 μm particles are larger than their gravitational forces, therefore, the particle resuspension takes place as soon as the particles are released in the flow field. The magnitude of the drag forces in the $z-$direction on the 50 and 100 μm particles decrease because they follow the fluid flow and the relative velocities between the fluid and the particle decrease during the particle resuspension process. This is also true for the magnitude of the drag forces in the $y-$direction for all the three particles. Moreover, the drag forces on the 50 and 100 μm particles have negative signs caused by the negative relative velocities, this prevents further resuspension of the particles. The drag force in the $z-$direction on the 500 μm particle increases with the deposition velocity due to the large inertia. However, the increasing drag force is not sufficiently large to raise the large particle. The gravitational force of the largest particle is larger than the opposite force from the starting to the ending time therefore no resuspension occurs. The lift force plays an important role and increases in the particle resuspension process. For all the sizes of particles, the lift force is significantly less than the drag force at the starting time. However, around the ending time, the lift force can be comparable to the drag force especially for the large particles. The lift force in the $z-$direction is larger than in the $y-$direction due to the gravity effect, which is consists with that reported by Yao and Fairweather [15]. It is shown that the lift force enhances the particle resuspension and thus cannot be neglected in the simulation.

Multi particle

Initially, 20000 particles are randomly placed in the same flow field, again the same three kinds of particles are considered. The properties of the particles are given in Table 3.3. Figure 3.19 displays the snapshots of the particle and velocity distributions in the duct with collisions. For the sake of presenting better visual, only 20% of the particles are shown in the 2D snapshots in Figure 3.19 (a), (b) and (c) without changing the main trend of the distribution characteristic. Figure 3.19 (a) shows the 2D snapshot of the 50 μm particles at $t = 12s$ from the starting time. It is shown that the instantaneous distribution of the small particles are obviously influenced by the secondary flows, the velocities of the particles emerge almost random distributions

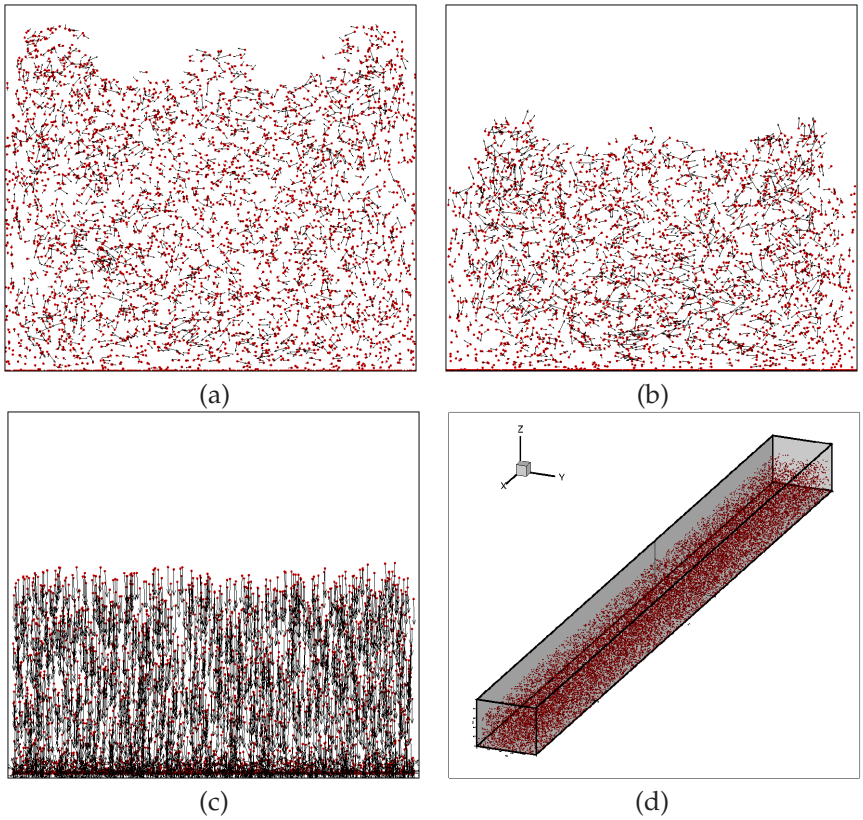

Figure 3.19: 2D snapshots of particle distribution with velocity vectors for (a) 50 μm particle at $t = 12s$, (b) 100 μm particle at $t = 12s$, (c) 500 μm particle at $t = 2.4s$ and 3D snapshot of particle distribution for (d) 100 μm at $t = 12s$, all with collisions. Red point for the particle, black arrow for the velocity.

that are related with the local fluid structure. However, the intimate motions are decoupled by the gravitational force that leads to a progressive segregation of the particles within the upper half of the duct and accumulation within the lower half. Due to the fact that the secondary velocities are towards the corners, two arms are lifted within the upper half of the duct that also prevent the particle deposition. Figure 3.19 (b) and (d) show the 2D and 3D snapshots of the $100\ \mu m$ particles at $t = 12s$, respectively. Obviously the $100\ \mu m$ particles are more affected by the gravity and deposit more rapidly than the $50\ \mu m$ particles. This trend becomes more serious with the increase of the particle size. As shown in Figure 3.19 (c), the majority of

the $50\ \mu m$ particles are seen to deposit on the duct floor within $t = 2.4s$. The typical times in Figure 3.19 are chosen before the upper surface of the particle aggregation is beyond the half height of the duct. These patterns of the particle distributions have perfect agreements with those reported at higher Re_τ particle-laden turbulent flows [17, 15, 21].

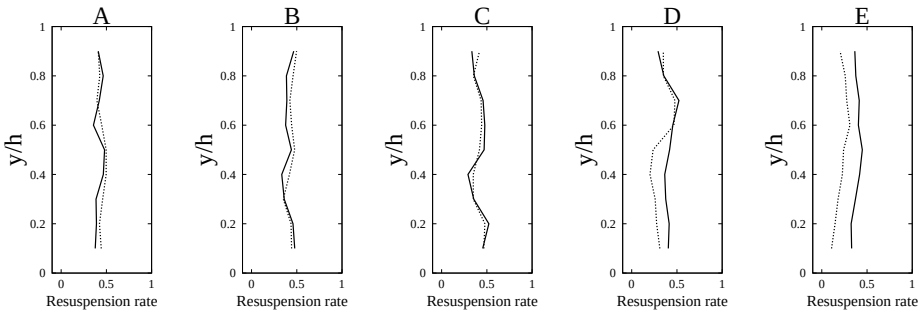

Figure 3.20: Particle resuspension rate in the $z-$direction for $50\ \mu m$ particles. Solid line: with collisions. Dashed line: without collisions.

In this section, special attention is paid on the particle resuspension rate at the lower half of the duct, and thus the lower half of the duct is separated into 50 squares, namely five partitions in the $z-$direction and ten partitions in the $y-$direction, each region in the $z-$direction containing ten squares is marked by A, B, C, D, E as shown in Figure 3.2 (b). The resuspension rate is defined as the ratio of the number of resuspended particles to the total number of particles within each square. The effect of the inter-particle collisions on the particle resuspension rate is shown in Figure 3.20, 3.21 and 3.22. In these figures, the solid lines stand for the resuspension rate with collisions while the dashed lines stand for those without collisions. Figure 3.20 shows the resuspension rate of the $50\ \mu m$ particles. The average resuspension rate, which is defined as the total resuspension rate in the lower half of the duct, is higher when the inter-particle collisions are considered. The average resuspension rates with and without collisions are 41.30% and 29.41%, respectively. From left to right, it is shown that the resuspension rate without collisions decreases with height which agrees with the strength of the secondary flows at different heights. The resuspension rates with collisions at different heights do not change significantly because the inter-particle collisions try to return the perturbed system into equilibrium. It is shown in the center regions far from the duct floor, such as A and B, that the effect of the inter-particle collisions is not very significant. However, compared with the same size particles in the transportation process in the absence of the gravitational action, the effect of the inter-particle collisions is obviously stronger here. This is because of the progressive accumulation of the particles in the lower half of the duct.

In Regions A and B, the resuspension rate with collisions is a little bit lower than that without collisions. This is due to the fact that the secondary flows play a main role in the horizontal transportation normal to the streamwise direction in these regions, the resuspension is restrained by the lateral transfer of momentum between the particles caused by the collisions. The resuspension rate with collisions is higher than without collisions in Regions C, D and E where the strength of the secondary flows is relative low. As the particle deposition goes on, the particle number density is higher and higher near the bottom of the duct, therefore, more collisions take place when these particles encounter the falling particles. Especially in Region E, the resuspension rates with and without collisions show large discrepancies. The resuspension rates with collisions are high because the particles with collisions impact on the duct floor then bounce back into the flow, the bounce raises the resuspension rate. In the case without collisions, the resuspension rate without collisions is quite low, the particles are prevented to bounce back from the duct floor numerically, this treatment is to some extent like the adhesive coating in [22]. To further understand the effect of the collisions, the instantaneous contact number corresponding to Figure 3.19 is shown in Figure 3.23. Here the contact is taken to mean the overlap formed between the particles or between the particles and the wall. As mentioned above, in the case with collisions, the DEM is adopted to calculate the contact force when the overlap is formed and thus the contacting particles will be separated by the force. However, in the case without collisions the contact force is not calculated therefore the penetration between the particles is allowed. As expected, it is shown in Figure 3.23 that there are more contacts when the inter-particle collisions are not considered.

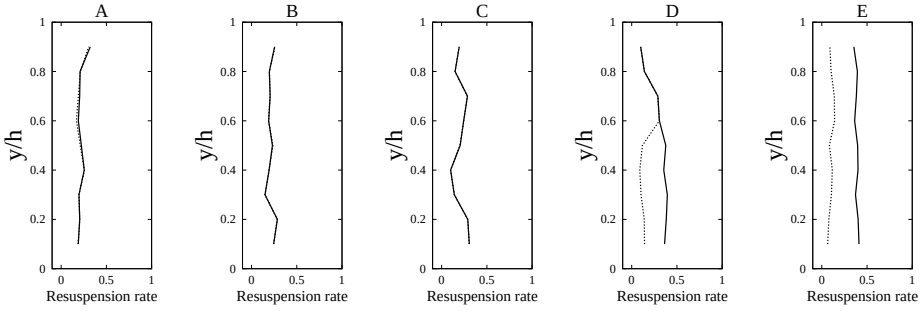

Figure 3.21: Particle resuspension rate in the $z-$direction for $100\ \mu m$ particles. Solid line: with collisions. Dashed line: without collisions.

Figure 3.21 shows the resuspension rates of the $100\ \mu m$ particles with and without collisions, the average resuspension rates with and without collisions are 33.27% and 13.79%, respectively. The $100\ \mu m$ particles are more affected by the gravitational force than the $50\ \mu m$ particles, therefore, it is presented a significantly lower average

particle resuspension rate. Unlike the small particles, the two lines of the 100 μm particles in the center regions, A, B and C, show no difference. As mentioned above, the 100 μm particles can follow the trend of the turbulent flow better than other two sizes in the duct center. It is indicated that the behavior of the particles is the consequence of the competition among secondary flows, gravitational force and inter-particle collisions. In the near-floor regions such as D and E, the particles without collisions can hardly be resuspended due to the low turbulent strength. The resuspension rate with collisions in Region E is high because of the collisions between the particles and the duct floor. The contact numbers with and without collisions are high and comparable for the 100 μm particles as shown in Figure 3.23.

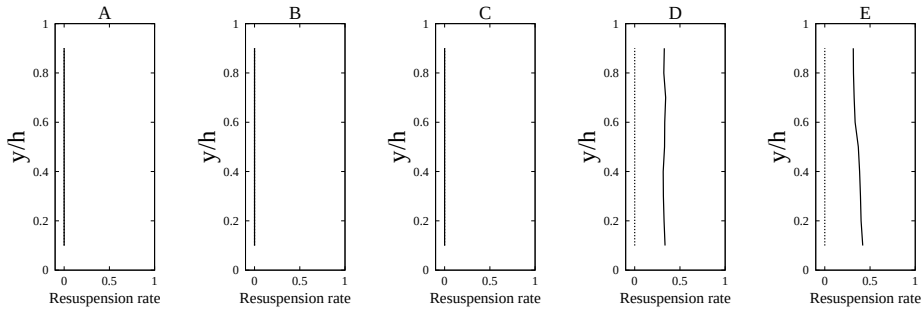

Figure 3.22: Particle resuspension rate in the $z-$direction for 500 μm particles. Solid line: with collisions. Dashed line: without collisions.

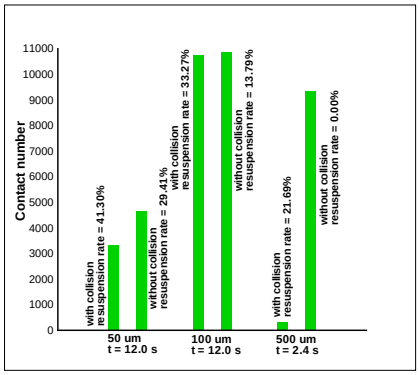

Figure 3.23: Contact number and average resuspension rate of the 50 μm and 100 μm particles at $t = 12s$, the 500 μm particles at $t = 2.4s$.

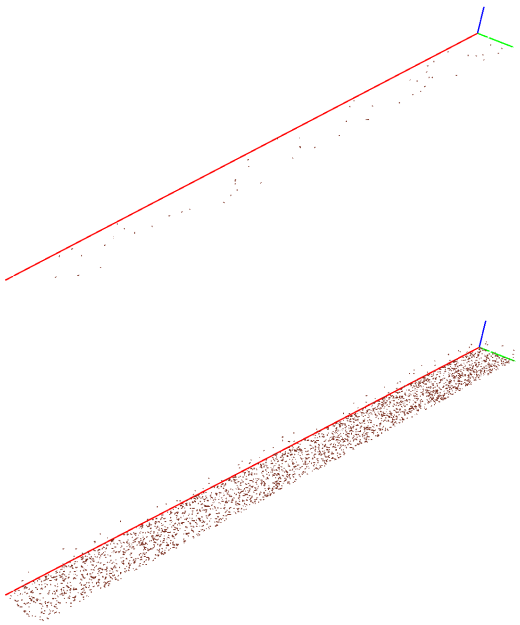

Figure 3.24: Distribution of contact for the 500 μm particles at $t = 2.4s$. Top: with collisions, Bottom: without collisions.

Figure 3.22 shows the resuspension rates of the $500\ \mu m$ particles with and without collisions, the average resuspension rates with and without collisions are 21.69% and 0.00%, respectively. The resuspension rates of the $500\ \mu m$ particles with and without collisions are zero in the inner regions A, B and C. This is because the secondary flow is not strong enough to rise the $500\ \mu m$ particles up. This observation coincides with the single particle investigation in Section 3.3.2. The resuspension rates of the $500\ \mu m$ particles in the regions D and E are similar as the smaller ones. As shown in Figure 3.23, the contact number in the case without collisions is significantly higher than that with collisions. The positions of the contacts for the $500\ \mu m$ particles are printed in Figure 3.24, it is shown that most of the contacts are formed close to the duct floor. It should be stressed that the selected time of the large particles is much shorter than that for the small and medium-sized particles because they deposit very rapidly. As argued by Yao and Fairweather [15, 21], the deposition velocity of the 500 μm particles while high at early times decreases significantly as the majority of the particles become deposited. In the case with collisions, the particles bounce back as soon as the particle impacts the duct floor. This phenomenon

can be vividly observed in Figure 3.19(c), a long cloudy region is formed above the duct floor where a large number of bounce-back particles concentrate. An important finding is that the particles in this region have horizontal velocities under the effect of the secondary flow, this is not observed in the inner regions. The horizontal movement plays an important role in the final stage of particle deposition, detailed description on this part is given in the next section.

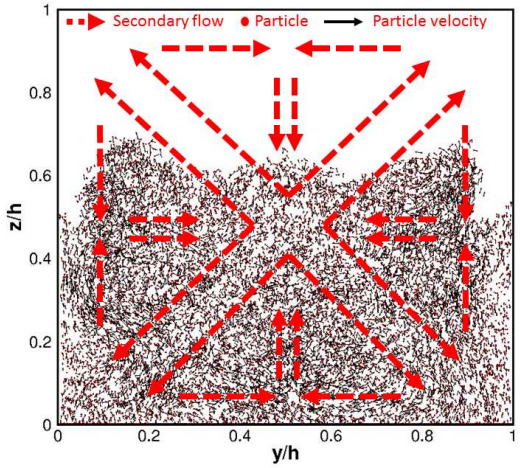

Figure 3.25: Schematic of the effect of secondary flow on particle behavior.

The effect of secondary flow on particle behavior may be summarized by the schematic given as Figure 3.25 in which two-dimensional snapshot of the $100\ \mu m$ particles is shown at $t = 12s$. Here, only 20% of the particles are displayed without changing the main trend of the distribution characteristic. Overall, the secondary flow in a square duct has the effect of enhancing the lateral mixing and advective transport of solid particles. When the wall-normal gravitational force is considered, the secondary flow plays an important role in the resuspension process as a balance force to gravity. The resuspension is dominant especially close to the central plane and the sidewalls in the lower half of the duct where the flow velocities are upwards. Finally, the lateral secondary flows close to the duct bottom also play an important role to transport particles from the corners to the center. The effect is a critical factor in the final stage of particle deposition which will be emphasized in the next section.

Finally, since the particle deposition velocities in the inner duct are very important for the efficiency of the final deposition and may lead to a non-uniform distribu-

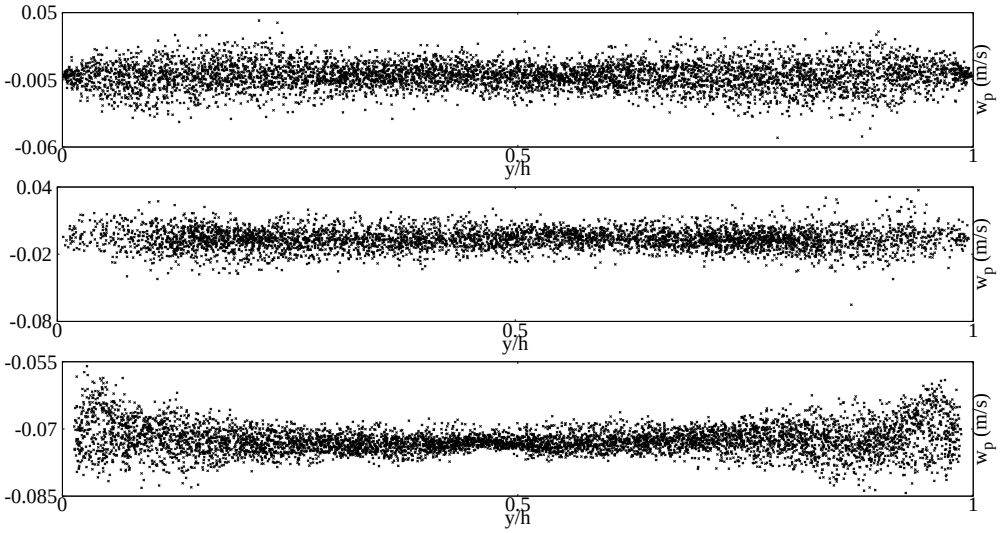

Figure 3.26: Particle deposition velocity in the $z-$direction according to Fig 3.19. Top: 50 μm particles, Middle: 100 μm particles. Bottom: 500 μm particles.

tion on the duct floor. Figure 3.26 shows the distributions of particle velocity in the $z-$direction (w_p) located in A, B and C regions where the particle-floor collisions can be negligible. It is shown that the deposition velocity increases with the particle size. For the 50 μm and 100 μm particles, the deposition velocity remains at an approximately constant level due to the high strength of the secondary flows in the middle height of the duct, therefore, the resuspension rate of the 50 μm and 100 μm particles in these regions is about 40%. For the 500 μm particles, all the velocities in A, B and C region have negative velocities fluctuating around $-0.07m/s$. For all the sizes of particles, the velocity fluctuations are found to be dominant near the side walls.

The main trends of the particle deposition velocities in A, B and C regions are shown in Figure 3.27 in terms of fitting lines. It is shown that the 50 μm particles deposit more efficiently near the side walls whereas the 100 μm and 500 μm particles preferentially deposit near the center. These findings have a good agreement with the results of Yao and Fairweather at low $Re_\tau = 600$ [21] but are contrary with those at high $Re_\tau = 10500$ in the same paper.

From the above analysis, it can be concluded that the gravity, collisions and secondary flow effects are all influential in determining the particle behaviors in a turbulent square duct flow. For the 50 μm particles, the secondary flow plays the major role in determining their distribution. For the 500 μm particles, it is the gravity that dominates particle behavior and deposition. The 50 μm particles deposit more ef-

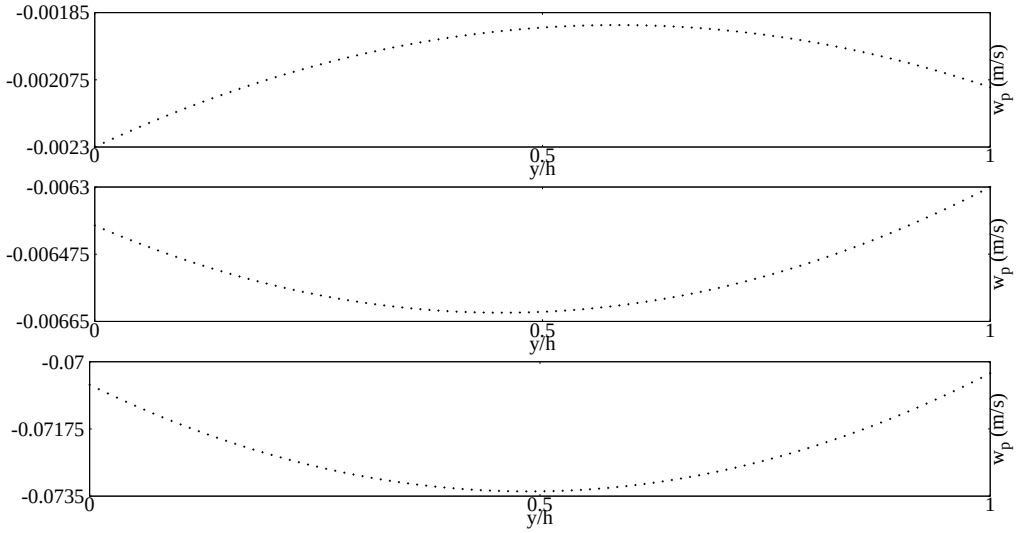

Figure 3.27: Particle deposition velocity in the $z-$direction in terms of fitting lines. Top: 50 μm particles, Middle: 100 μm particles. Bottom: 500 μm particles.

ficiently near the side walls of the duct whereas the 100 μm and 500 μm particles preferentially deposit near the center of the duct floor. The inter-particle collisions play a role like relaxation that try to return the perturbed system into equilibrium. In the inner regions, the inter-particle collisions increase the deposition rates of the 50 μm particles but do not alter the behaviors of the 100 and 500 μm particles. In the region near the duct floor, the particle resuspension rates are significantly enhanced by the collisions.

3.3.3 Particle deposition

In the previous studies like [21], the particle deposition was defined when a particle was within 1.5 particle diameters of the wall. In this way, the computational cost is significantly reduced because it is not needed to reach the final stage of deposition. In this section, all the investigations are carried out at the final stage of deposition where the particle velocity in the $z-$direction is approaching zero. Unlike the elastic treatment on the collisions between the particles and the duct floor in [21], DEM is adopted in this study. Zhang et al. [8] have shown that the soft-sphere DEM can provide more reliable results than other artificial methods in describing the particle bouncing movement near the floor. Firstly, the way of the particles of different size landing on the duct floor is examined by releasing two sizes of particles in the fully

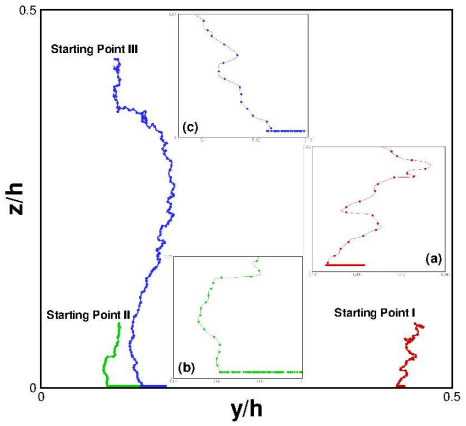

Figure 3.28: Single 100 μm particle trajectory near the duct floor from Starting point (a) I, (b) II and (c) III. All with collisions.

developed turbulent flow in the next subsection. Then, the multi-particle simulations are conducted in Section 3.3.3.

Single particle

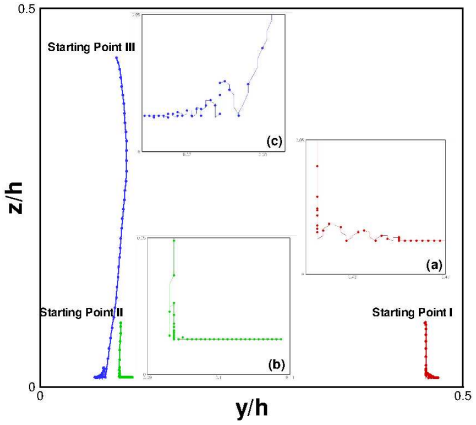

Figure 3.29: Single 500 μm particle trajectory near the duct floor from Starting point (a) I, (b) II and (c) III. All with collisions.

In this case, the diameters selected are 100 μm and 500 μm. The physical properties of the particles are given in Table 3.3. Three starting points at the saddle region between two pairs of counter-rotating vortexes are selected: Starting point I is at $(y/h = 0.4552, z/h = 0.0831)$ or $(y^+ = 137, z^+ = 25)$ in wall units, Starting point II is at $(y/h = 0.094, z/h = 0.0831)$ or $(y^+ = 28, z^+ = 25)$ in wall units and Starting point III is at $(y/h = 0.0906, z/h = 0.4363)$ or $(y^+ = 27, z^+ = 131)$ in wall units. The trajectories of the particles near the duct floor are depicted in Figure 3.28 and 3.29. The trajectories of the medium-sized particles are flexuous under the effect of the secondary flows. A 'soft landing' is observed for all the three 100 μm particles from different heights and the bounce-back heights are quite small. The landing point in Figure 3.28 (a) is close to the bisector of the floor, and the landing points in Figure 3.28 (b) and (c) are near the side wall. Under the horizontal effect of the secondary flows, all the three 100 μm particles are blew to move towards the bisector of the duct floor after landing. On the other hand, a 'hard landing' takes place for the 500 μm particles as shown in Figure 3.29. The trajectories of the 500 μm particles are almost vertical. This is because the deposition of the large particle is promoted by gravity and hardly affected by local turbulent flow structure. The particles are found to bounce back as soon as they impact on the duct floor, the bounce-back heights at first time are very comparable at different landing locations. This bouncing process then repeats until the particles fully settle down on the duct floor. An interesting phenomenon is that the large particles begin to respond the fluid structure when they approach the duct floor especially after the collisions, this can be due to the lift force that caused by the large velocity gradient adjacent the duct floor. Yao and Fairweather [21] also concluded that the influence of the largest lift force taks place on the 500 μm particles and its effect becomes significant as the particles approach to the duct floor. Similar to the 100 μm particles, the landing point of the 500 μm particle from Starting point I as shown in Figure 3.29 (a) is closer to the bisector of the floor than the other two, and the particle then jumps towards the bisector with the bounce-back height decreasing with the bouncing times until a steady stage is reached. Different to the 100 μm particles, the landing point in Figure 3.29 (c) is closest to the side wall because no resuspension in the horizontal direction takes place during the deposition, the 500 μm particle drops on the duct floor vertically then jumps towards the corner of the duct. Yao and Fairweather [21] and Phares and Sharma [19] also reported this tendency of the large particle to deposit in the duct corner. This is because the 500 μm particle from Starting point III deposits vertically, the trajectory begins to change when the large particle approaches the duct floor. In the region near the duct corner, the particle suffers strong vortex that pushes the particle to the corner, this observation is in line with that reported in [21] without the disturbing of other particles.

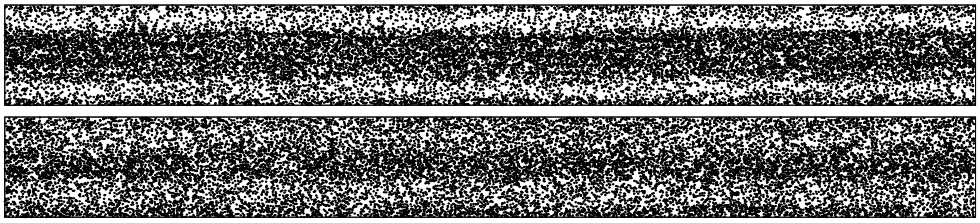

Figure 3.30: Distribution of the 50 μm particles at the final stage of deposition. Top: with collisions, Bottom: without collisions.

Multi particle

For the multi-particle investigation on the deposition, the same initial condition is adopted as in Section 3.3.2. With the passage in the fluid flow, the particles deposit under the action of the gravitational force. It is found that the large particles need significantly shorter time to reach the final deposition state than the small ones. The reasons have been discussed before. For the 50 μm particles it takes about $90.0s$ to reach the steady stage, for the 100 μm particles about $50.0s$ and for the 500 μm particles about $7.0s$, respectively.

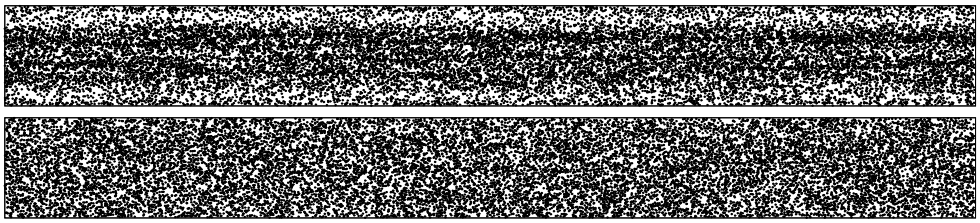

Figure 3.31: Distribution of the 100 μm particles at the final stage of deposition. Top: with collisions, Bottom: without collisions.

Figure 3.30 shows the final stage of deposition of the 50 μm particles with and without collisions. From both pictures it can be seen that most of the 50 μm particles concentrate in the center of the duct floor due to the effect of the secondary flows, this observation is in line with that reported in [15, 12, 19, 21]. Moreover, the particles that are near the center tend to congregate in streaks in the streamwise direction. This phenomenon has been explained as a correlation between the particle streaks and the low-speed streaks in a turbulent boundary layer [23, 24]. It is demonstrated that the turbulent flow structure plays an important role in the deposition process of the small particles. The degree of concentration in the case with collisions is higher

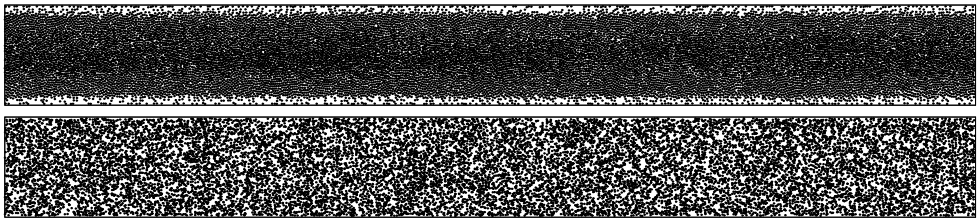

Figure 3.32: Distribution of the 500 μm particles at the final stage of deposition. Top: with collisions, Bottom: without collisions.

than that without collisions. This is because intense collisions happen in the near-floor region especially in the locations close to the side walls where the strength of the secondary flows are high. One strong evidence is that two columns that lack of particles are formed in the streamwise direction close to the side walls. In these columns, the particles with collisions are further swept towards the bisector by the secondary flows after they land on the duct floor. Above findings are confirmed in Figure 3.33 (a) which shows the PDF lines of the 50 μm particles along the $y-$direction on the duct floor. It is shown that the two cases share the same trend but inter-particle collisions enhance the preferential concentration. In the region close to the bisector of the duct floor, the particles fly from the two sides with the secondary flow and impact with each other, these collisions form another valley on the PDF of the case with collisions. For the particles that deposit close to the corners, the observation here is contrary with that in [19] also at $Re_\tau = 300$. Phares argued that the secondary flows could cause a decrease in deposition closer to the corners for the lower-inertia particles. On the contrary, the finding in this study reveals that the secondary flows make more effect on the large particles close to the corners as shown below. However, none of the gravity force, lift force and particle collisions were considered in [19], the former two factors have been proved to play very important roles in the particle deposition process in turbulent duct flows [25, 15, 21].

Figure 3.31 displays the final stage of deposition of the 100 μm particles with and without collisions. Large discrepancy is shown between the two cases. For the case with collisions, Figure 3.31 (top) presents a similar trend as the 50 μm particles as shown in Figure 3.30 (top). Yao and Fairweather [21] also reported that the 50 μm and 100 μm particles have similar magnitude of the PDF at low $Re_\tau = 600$. However, Figure 3.31 (bottom) presents an almost flat distribution in which no significant preferential concentration can be observed. This is due to the fact that the effect of the gravity increases with the particle size. The 100 μm particles deposit much faster than the 50 μm ones. The secondary flows cannot change the particle distribution significantly before they land on the duct floor. On the contrary, the 100 μm particles

with collisions can bounce back from the duct floor and continue to move under the effect of the horizontal secondary flows. Moreover, the particles close to the floor center suffer serious run-off due to the inter-particle collisions, this again indicates the fact that the final particle distribution is a combinational consequence of the secondary flows, particle collisions and the gravitational force. Figure 3.33 (b) presents the PDF corresponding to Figure 3.31, it is shown that an even deeper valley is found at the middle point of the duct floor for the case with collisions and the two peaks are further with each other than that in Figure 3.33 (a). For the case without considering inter-particle collisions, the particles are distributed nearly uniformly except those close to the corners.

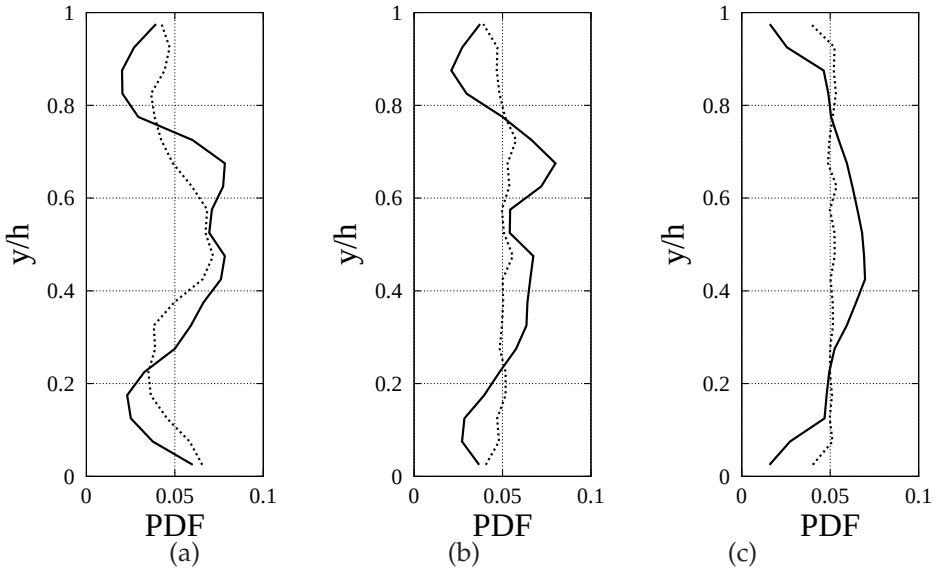

Figure 3.33: Particle deposition rate along the $y-$direction for the (a) 50 μm, (b) 100 μm and (c) 500 μm particles.

Figure 3.32 displays the final stage of deposition of the 500 μm particles with and without collisions. Overall, the distributions of the large particles are more uniform than the smaller ones. In the case with collisions, most of the 500 μm particles concentrate in the center of the duct floor. There are very few 500 μm particles depositing in the corners. Again this finding has a good agreement with [21, 26]. As discussed in the single particle investigation, the large particles begin to respond the local fluid structure in the near-floor regions. Since the mean secondary flow moving along the duct floor is from the duct corners to the bisector, the particle jumps towards the

bisector of duct floor. Therefore, a concentration is observed with the concentration rate increasing to maximum in the center region of the floor. However, in the case without collisions, the particles distribute nearly uniformly on the duct floor except in the region near the corners. Since the particle without collisions cannot bounce back from the duct floor, the gaps are believed to be formed by the secondary flow close to the corners which is also true for the 100 μm particles without collisions. From the PDF of the 500 μm particles with collisions as shown in Figure 3.33 (c), it can be seen that only one peak is formed near the middle line of the duct floor, the concentration rate increases gradually from the sidewall to the center. The minimum PDF is at the near-corner region, this is also due to the collisions. As shown in Figure 3.29 (c), the 500 μm particles may jump towards the corners after the landing. However, a lower PDF value is observed in this region instead of accumulation. Inter-particle collisions play an important role in this process. The PDF of the 100 μm and 500 μm particles without collisions shows a very similar almost flat profile in the center region.

From the above analysis, it can be concluded that the final distribution of the particles on the duct floor is a combination consequence of the gravitational, secondary flow and inter-particle collision effects. For the small particles, the secondary flow plays the major role in determining their distributions and make the small particles concentrate near the duct center, the inter-particle collisions enhance this preferential concentration. For the medium-sized and large particles, the gravitational and inter-particle collision effects play the major role in determining the final distributions. It is showing a nearly uniform distribution when the inter-particle collisions are not considered. The particles move towards the bisector of the duct floor when they approach the bottom. However, the medium-sized and large particles show different behaviors during the movement. The large particles tend to jump with the bounce-back height decreasing with the collisions times while the medium-sized particles are likely to roll.

3.4 Concluding remarks

In this chapter, the effect of collisions on the particle behavior in a fully developed turbulent flow in a square duct is investigated via DNS-DEM. The particle transportation by turbulent flow is studied firstly in the absence of the gravitational effect. Then, particle deposition from turbulent flow in a horizontal square duct is studied. The effect of the inter-particle collisions on the particle suspension rate and final stage of particle distribution on the duct floor are discussed. According to the results, the following conclusions can be made.

In the particle transportation process, the inter-particle collisions hardly affect the behavior of the 50 μm and 100 μm particles through the whole duct as well as

the 500 μm particles near duct center. However, the particle interaction plays an important role in the distribution of the 500 μm particles especially in the near-wall regions. The inter-particle collisions enhance the particle diffusion in the direction perpendicular to streamwise flow and make the particles distribute more uniformly near the wall. This trend increases with the particle number. The 100 μm and 500 μm particles show streaky distributions in the near-wall region and tend to concentrate to the corners. In the region very close to the wall, there are more particles in the case with collisions than without collisions.

In the particle deposition process, the gravity, collisions and secondary flow effects are all influential in determining the particle behaviors in a turbulent square duct flow. For the 50 μm particles, the secondary flow plays the major role in determining their distribution. For the 500 μm particles, it is the gravity that dominates particle behavior and deposition. The 50 μm particles deposit more efficiently near the side walls of the duct whereas the 100 μm and 500 μm particles preferentially deposit near the center of the duct floor. The inter-particle collisions play a role like relaxation that try to return the perturbed system into equilibrium. In the inner regions, the inter-particle collisions increase the deposition rates of the 50 μm particles but do not alter the behaviors of the 100 and 500 μm particles. In the region close to the duct floor, the particle resuspension rates are significantly enhanced by the collisions.

The final distribution of the particles on the duct floor is a combination consequence of the gravitational, secondary flow and inter-particle collision effects. For the 50 μm particles, the secondary flow plays the major role in determining their distributions and make the small particles concentrate near the duct center, the inter-particle collisions enhance this preferential concentration. For the 100 μm and 500 μm particles, the gravitational and inter-particle collision effects play the major role in determining the final distributions. It is showing a nearly uniform distribution when the inter-particle collisions are not considered. The particles move towards the bisector of the duct floor when they approach the bottom. However, the medium-sized and large particles show different behaviors during the movement. The large particles tend to jump with the bounce-back height decreasing with the collisions times while the medium-sized particles are likely to roll.

Through the work, it is clearly shown that the particle behavior can be affected by the collisions. As stated by Yu and Xu [27]: "At this stage of development the difficulty in particle-fluid flow modeling is mainly related to the solid phase rather than the fluid phase." Inter-particle collisions may play a key role in particle-fluid systems especially when the particles are densely packed. Therefore, it is essential to use a felicitous method to treat the particle collisions accurately and efficiently [8]. From this point of view, the DNS-DEM scheme is a promising solution on the particle-laden turbulent flow.

References

[1] R. W. C. P. Verstappen and A. E. P. Veldman. Symmetry-Preserving Discretization of Turbulent Flow. *Journal of Computational Physics*, 187:343–368, 2003.

[2] F X Trias and O Lehmkuhl. A self-adaptive strategy for the time integration of navier-stokes equations. *Numerical Heat Transfer, Part B: Fundamentals*, 60(2):116–134, 2011.

[3] A. J. Chorin. Numerical Solution of the Navier-Stokes Equations. *Journal of Computational Physics*, 22:745–762, 1968.

[4] F. X. Trias, M. Soria, A. Oliva, and C. D. Pérez-Segarra. Direct numerical simulations of two- and three-dimensional turbulent natural convection flows in a differentially heated cavity of aspect ratio 4. *Journal of Fluid Mechanics*, 586:259–293, 2007.

[5] P. Cundall. A computer model for simulating progressive large scale movements in blocky system. *In: Muller led, ed. Proc Symp Int Soc Rock Mechanics, Rotterdam: Balkama A A*, 1:8–12, 1971.

[6] K.L. Johnson. Contact mechanics. *Cambridge University Press, Cambridge*, 1985.

[7] R.D. Mindlin and H. Deresiewicz. Elastic spheres in contact under varying oblique forces. *Journal of Applied Mechanics*, 20:327–344, 1953.

[8] Hao Zhang, Yuanqiang Tan, Shi Shu, Xiaodong Niu, Francesc Xavier Trias, Dongmin Yang, Hao Li, and Yong Sheng. Numerical investigation on the role of discrete element method in combined LBM-IBM-DEM modeling. *Computers & Fluids*, 94:37 – 48, 2014.

[9] Patrick J. Roache. Code Verification by the Method of Manufactured Solutions. *Journal of Fluids Engineering, Transactions of ASME*, 124:4–10, 2002.

[10] M. Soria, F. X. Trias, C. D. Pérez-Segarra, and A. Oliva. Direct numerical simulation of a three-dimensional natural-convection flow in a differentially heated cavity of aspect ratio 4. *Numerical Heat Transfer, part A*, 45:649–673, April 2004.

[11] S. Gavrilakis. Numerical simulation of low-Reynolds-number turbulent flow through a straight square duct. *Journal of Fluid Mechanics*, 244:101–129, 1992.

[12] Gaurav Sharma and Denis J. Phares. Turbulent transport of particles in a straight square duct. *International Journal of Multiphase Flow*, 32(7):823 – 837, 2006.

[13] M. Uhlmann, A. Pinelli, G. Kawahara, and A. Sekimoto. Marginally turbulent flow in a square duct. *Journal of Fluid Mechanics*, 588:153–162, 2007.

[14] Hassan Raiesi, Ugo Piomelli, and Andrew Pollard. Evaluation of turbulence models using direct numerical and large-eddy simulation data. *Journal of Fluids Engineering*, 133(2), 2011.

[15] J. Yao and M. Fairweather. Inertial particle resuspension in a turbulent, square duct flow. *Physics of Fluids*, 22(3):03330301–15, 2010.

[16] Y. Pan and S. Banerjee. Numerical simulation of particle interactions with wall turbulence. *Physics of Fluids (1994)*, 8(10), 1996.

[17] Michael Fairweather and Jun Yao. Mechanisms of particle dispersion in a turbulent, square duct flow. *AIChE Journal*, 55(7):1667–1679, 2009.

[18] D. Kaftori, G. Hetsroni, and S. Banerjee. Particle behavior in the turbulent boundary layer. i. motion, deposition, and entrainment. *Physics of Fluids (1994)*, 7(5), 1995.

[19] Denis J. Phares and Gaurav Sharma. A DNS Study of Aerosol Deposition in a Turbulent Square Duct Flow. *Aerosol Science and Technology*, 40(11):1016–1024, 2006.

[20] J.F.W. Adams, M. Fairweather, and J. Yao. Modelling and simulation of particle re-suspension in a turbulent square duct flow. *Computers and Chemical Engineering*, 35(5):893 – 900, 2011.

[21] J. Yao and M. Fairweather. Particle deposition in turbulent duct flows. *Chemical Engineering Science*, 84(0):781 – 800, 2012.

[22] S. K. Friedlander and H. F. Johnstone. Deposition of suspended particles from turbulent gas streams. *Industrial and Engineering Chemistry*, 49(7):1151–1156, 1957.

[23] Mehrzad Shams, Goodarz Ahmadi, and Hasan Rahimzadeh. A sublayer model for deposition of nano- and micro-particles in turbulent flows. *Chemical Engineering Science*, 55(24):6097 – 6107, 2000.

[24] C. Marchioli and A. Soldati. Mechanisms for particle transfer and segregation in a turbulent boundary layer. *Journal of Fluid Mechanics*, 468:283–315, 2002.

[25] H. Zhang and G. Ahmad. Aerosol particle transport and deposition in vertical and horizontal turbulent duct flows. *Journal of Fluid Mechanics*, 406:55–80, 2000.

[26] C.M. Winkler, Sarma L. Rani, and S.P. Vanka. A numerical study of particle wall-deposition in a turbulent square duct flow. *Powder Technology*, 170(1):12 – 25, 2006.

[27] A B Yu and B H Xu. Particle-scale modelling of gas–solid flow in fluidisation. *Journal of Chemical Technology and Biotechnology*, 78(2-3):111–121, 2003.

Chapter 4

Numerical investigation on the role of discrete element method in combined LBM-IBM-DEM modeling

Part of the contents of this chapter have been published as:

H Zhang Y Tan, S Shu, X Niu, FX Trias, D Yang, H Li, Y Sheng. Numerical investigation on the role of discrete element method in combined LBM-IBM-DEM modeling. *Computers & Fluids. 94(2014), 37-48.*

Abstract.

Particle collisions play a very important role in determining the fluid-particle multiphase flow, and thus it is crucial to treat the particle-particle interaction using a felicitous method in numerical simulations. A novel combined LBM - IBM - DEM scheme was presented in this chapter with its application to model the sedimentation of two-dimensional circular particles in incompressible Newtonian flows. The hydrodynamic model of the incompressible Newtonian flow was based on the Bhatnagar-Gross-Krook LBM, and a momentum exchange-based IBM was adopted to calculate the fluid-solid interaction force. The kinematics and trajectory of the discrete particles were evaluated by DEM, in which the particle-particle interaction rules were governed by theoretical contact mechanics to enable the direct use of real particle properties. This eliminated the need of artificial parameters and also improves the reliability of the numerical results. By using a more accurate and physical description of particle interaction, a 'safe zone' or threshold was also no longer required. Case studies of single particle settling in a cavity, and two particles settling in a channel were carried out, the velocity characteristics of the particle during settling and near the bottom were examined. A numerical example of

sedimentation involving 504 particles was finally presented to demonstrate the capability of the combined scheme.

4.1 Governing equations

4.1.1 Lattice Boltzmann model with single-relaxation time collision

The motion of the incompressible Newtonian flow is numerically evaluated using LBM-D2Q9 model [1]. The discretization of the flow domain is undertaken using square lattices with uniform lattice spacing h, those nine lattice velocities defined between the lattice nodes are given by

$$\delta_h(a) = \begin{cases} (0,0)c, & \alpha = 0 \\ (cos[(\alpha-1)\pi/2], sin[(\alpha-1)\pi/2])c & \alpha = 1,2,3,4 \\ \sqrt{2}(cos[(\alpha-5)\pi/2+\pi/4], sin[(\alpha-5)\pi/2+\pi/4])c & \alpha = 5,6,7,8 \end{cases} \quad (4.1)$$

where c is termed by the lattice speed. The formulation of the lattice BGK model is

$$f_\alpha(r + e_\alpha\delta_t, t + \delta_t) = f_\alpha(r,t) - \frac{f_\alpha(r,t) - f_\alpha^{eq}(r,t)}{\tau} + F_b\delta_t \quad (4.2)$$

where $f_\alpha(r,t)$ represents the fluid density distribution function, $r = (x,y)$ stands for the space position vector, t denotes time and τ denotes the non-dimensional relaxation time, $F_b\delta_t$ denotes the fluid-solid interaction force term which is given in the next section, the equilibrium density distribution function, $f_\alpha^{eq}(r,t)$, can be written as

$$f_\alpha^{eq}(r,t) = \rho\omega_\alpha[1 + 3(e_\alpha \cdot u) + \frac{9}{2}(e_\alpha \cdot u)^2 - \frac{3}{2}(u \cdot u)] \quad (4.3)$$

where the value of weights are: $\omega_0 = 4/9$, $\omega_1 = \omega_2 = \omega_3 = \omega_4 = 1/9$ and $\omega_5 = \omega_6 = \omega_7 = \omega_8 = 1/36$. u denotes the macro velocity at each lattice node which can be calculated by

$$u = \frac{\sum_{\alpha=0}^{8} f_\alpha e_\alpha}{\rho} \quad (4.4)$$

the macro fluid density is obtained by

$$\rho = \sum_{\alpha=0}^{8} f_\alpha \quad (4.5)$$

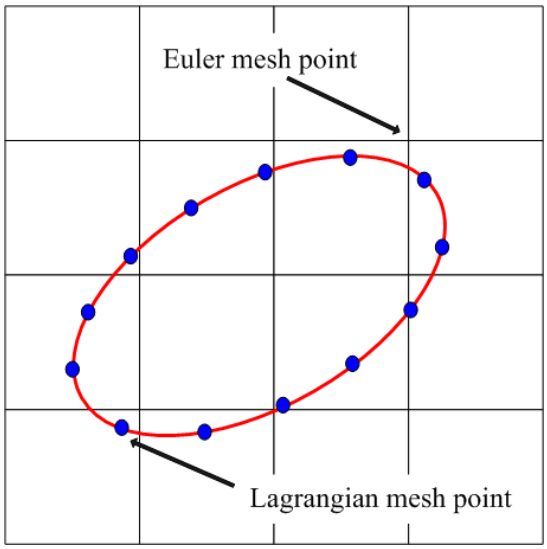

Figure 4.1: Schematic diagram of the immersed boundary method.

4.1.2 Immersed boundary method and the hydrodynamics interaction force

The flow field is covered by the Eulerian square lattices, and the density distribution functions of fluid are defined on the lattice nodes. The existence of the solid particles is represented by another set of meshes, which are intitled as Lagrangian points because the locations of the points change along the movement of the particles as depicted in Fig. 4.1. The fluid density distribution functions on the Lagrangian points are also considered but not directly solved by Eq. 5.2. Using numerical extrapolation from the circumambient fluid points, f_α on the Lagrangian points at each timestep is approximated

$$f_\alpha(X_l,t)=\sum_{ij}\Big(\prod_{k=1,k!=i}^{i_{max}}\frac{X_l-x_{kj}}{x_{ij}-x_{kj}}\Big)\Big(\prod_{m=1,m!=j}^{j_{max}}\frac{Y_l-y_{im}}{y_{ij}-y_{im}}\Big)f_\alpha(r_{ij},t) \tag{4.6}$$

where , $X_l(X,Y)$ is the coordinates of the Lagrangian boundary points. Here the third order polynomials are used for the extrapolation, i_{max} and j_{max} are the numbers of the Eulerian points used at each direction. Totally nine Eulerian points are used to obtain the value on single Lagrangian point.

To include the effect of the moving solid boundary on the flow field, the fluid density distribution functions on the Lagrangian points should be further modified

by the velocity of the solid particle

$$f_\beta(X_l, t+\delta_t) = f_\alpha(X_l, t) - 2\omega_\alpha \rho \frac{e_\alpha U_{BC}}{c_s^2} \tag{4.7}$$

where β represents the opposite direction of α, $U_{BC} = U_p + \Omega_p \times (X_l - X_p)$ is the velocity of the Lagrangian node, U_p and Ω_p denote the translational and angular velocities of the particle, X_p stands for the coordinate of the particle. Based on the momentum exchange of fluid particles, the force density at the Lagrangian point can be calculated using f_α and f_β

$$g(X_l, t) = \sum_\beta e_\beta [f_\beta(X_l, t) - f_\alpha(X_l, t)] \tag{4.8}$$

In each calculation cycle, $g(X_l, t)$ must firstly be evaluated because it is 'bidirectional' and it bridges the two phase calculations. The motion of the particles will be influenced by the environmental fluid among being pushed, pulled or rotated. On the contrary the flow field will be of course disturbed by the particles movement. Both of the bidirectional contributions are related to $g(X_l, t)$

The effect on the flow fields from the solid boundary is the body force term $F_b \delta_t$ in Eq. 5.2, where F_b can be expressed by

$$F_b = (1 - \frac{1}{2\tau})\omega_\alpha (3\frac{e_\alpha - u}{c^2} + 9\frac{e_\alpha \cdot u}{c^4} e_\alpha) F(r, t) \tag{4.9}$$

and

$$F(r, t) = \sum_l g(X_l, t) D_{ij}(r_{ij} - X_l) \Delta s_l \tag{4.10}$$

Δs_l is the arc length of the boundary element. D_{ij} is used to restrict the feedback force to only take effect on the neighbor of interface that is given by

$$D_{ij}(r_{ij} - X_l) = \frac{1}{h^2} \delta_h(\frac{x_{ij} - X_l}{h}) \delta_h(\frac{y_{ij} - Y_l}{h}) \tag{4.11}$$

with

$$\delta_h(a) = \begin{cases} \frac{1}{4}(1 + cos(\frac{\pi a}{2})), & when \mid a \mid \leq 2 \\ 0, & otherwise \end{cases} \tag{4.12}$$

where h is the mesh spacing. It should be stressed that by adding a body force on the flow field, the macro moment flux has to be also modified by the force $\rho u = \sum_{\alpha=1}^{8} f_\alpha e_\alpha + \frac{1}{2} F(r, t) \delta t$

On the other hand, the fluid-solid interaction force density exerted on the solid boundary point can be regarded as the reaction force of $g(X_l, t)$

$$F(X_l, t) = -g(X_l, t) \tag{4.13}$$

By integrating around the circumference of the solid particle, the total force exerting on the mass center F_T and the torque T_T acting on the particle can be obtained as

$$F_T = \sum_l F(X_l, t)\Delta s_l \tag{4.14}$$

$$T_T = \sum_l (X_l - X_p) \times F(X_l, t)\Delta s_l \tag{4.15}$$

4.2 Coupling scheme

In the coupled LBM-IBM-DEM scheme, Feng and Michaelides [2, 3] argued that when the particle collisions are treated via a penetration- allowed method, numerical instability may occur when a strong repulsive force is generated according to large overlap. Therefore a threshold or 'safe zone' should be set between the particles' surfaces to avoid the particle penetration. In our opinion this would depend on the interaction law and the numerical time step adopted in the discrete particle modeling as described below.

1. Different to the work of Feng and Michaelides [2, 3], in which an artificial 'stiffness' should be given, the 'stiffness' of the particle and wall is fixed as soon as the physical property of the particles are specified in this study. It is described in a more detailed and physical way than the linear one.

2. The time step of LBM, Δt_{LBM}, is based on the mesh resolution of the flow field and the property of the fluid flow. Whereas the time step, Δt_{DEM}, in the discrete particle model is based on the Rayleigh wave speed of force transmission on the surface of elastic bodies

$$\Delta t_{DEM} = \frac{\pi d_{pmin}}{2(0.1631\nu + 0.8766)} (\frac{\rho_p}{G})^{1/2} \tag{4.16}$$

where G is the shear modulus and ν is the Poisson's ratio of the particle. Owen et al. [4] made an extensive discussion on the determination of the subcycling between Δt_{LBM} and Δt_{DEM}. Owen et al. suggested that "when $\Delta t_{LBM} < \Delta t_{DEM}$, both the solution time steps can be simply forced to the less value, Δt_{LBM}. When Δt_{DEM}, a subcyling approach can be taken to allow the execution of a number of consecutive DEM time steps within a single LBM time step, during the DEM subcycling the DEM

mapping and hydrodynamic force and torque are not updated." In this chapter, it has been found that $\Delta t_{LBM} > \Delta t_{DEM}$ is significantly less than Δt_{LBM}. For the sake of getting a larger time step of DEM without losing the order of accuracy, the density of the particle is numerically enlarged when we determined Δt_{DEM}. 100 times enlargement on the density leads a 10 times enlargement on Δt_{DEM}. Similar treatments were also found by Sheng et al. [5]. By doing this, we can always choose a time step that ensures $\Delta t_{LBM} = \Delta t_{DEM}$. Our numerical experiments show that this artificial scheme works well in general.

A flow chart for the coupling code is shown in Fig. 4.2. In this work, we couple a BGK-LBM fluid solver to a DEM code to provide the fluid-solid interaction force. The program begins with defining the size of working space, the number, initial positions and properties of the particles, the gravity field and physical properties of the fluid flow. All these procedures can be accomplished prior to the main cycle with the data saved in files. A 'relay simulation mode' enables the code to read the files as an initial condition. The 'relay simulation mode' works both on the DEM and LBM parts.

4.3 Numerical results and discussions

4.3.1 Sedimentation of a circular particle in a cavity I

Sedimentation of single particle settling in cavity has been the subject of several studies, here this case is presented to check the validation of LBM-IBM-DEM scheme as well as the timestep treatment discussed above. The configuration of interest is a rectangular cavity with four solid boundaries as shown in Fig. 4.3. The width is $0.02m$ and the height is $0.06m$. The cavity is filled with stagnant Newtonian fluid with viscosity $0.01Pa \cdot s$ and density 1000 kg/m^3. A computational domain of 201×601 is used in the simulations. The relaxation time is $\tau = 0.8$, this leads to a physical timestep of $0.0001s$. One particle with a diameter $0.0025m$ and a density $1250kg/m^3$ is set at $(0.01m, 0.04m)$. The particle is initially at rest and starts to fall down under the action of the gravity field.

In Fig. 4.4 and Fig. 4.5, the longitudinal coordinate, longitudinal velocity, Reynolds number and translational kinetic energy of the particle are monitored to compare with those results obtained by Wan and Turek [6] and Wu and Shu [7] who used other numerical methods. It is shown that all the four quantities are comparable until the particle collides the bottom. Due to the fact that different discrete particle method was used, exact agreement may not be expected after the collision.

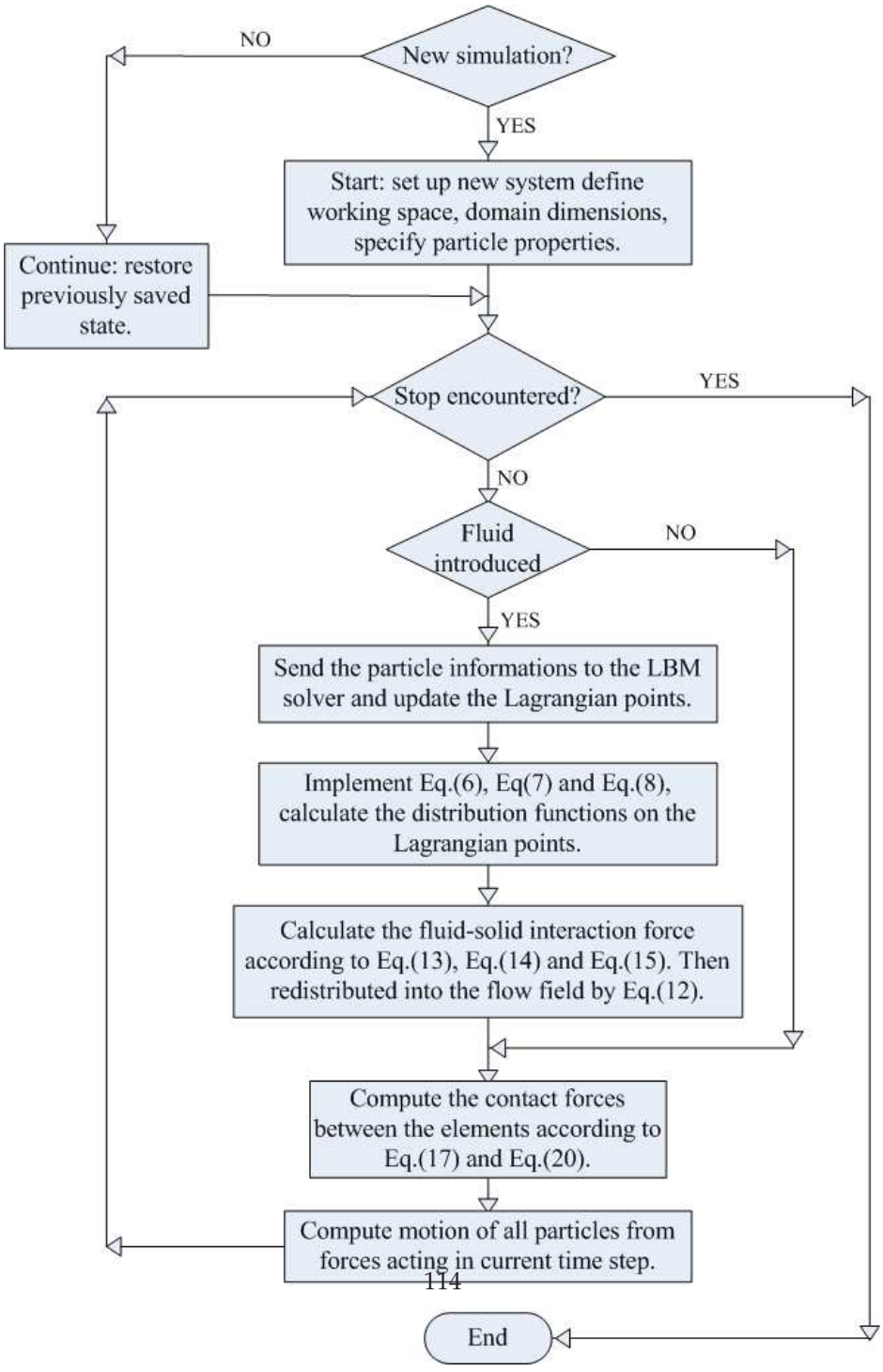

Figure 4.2: Flow chart for the computational sequence.

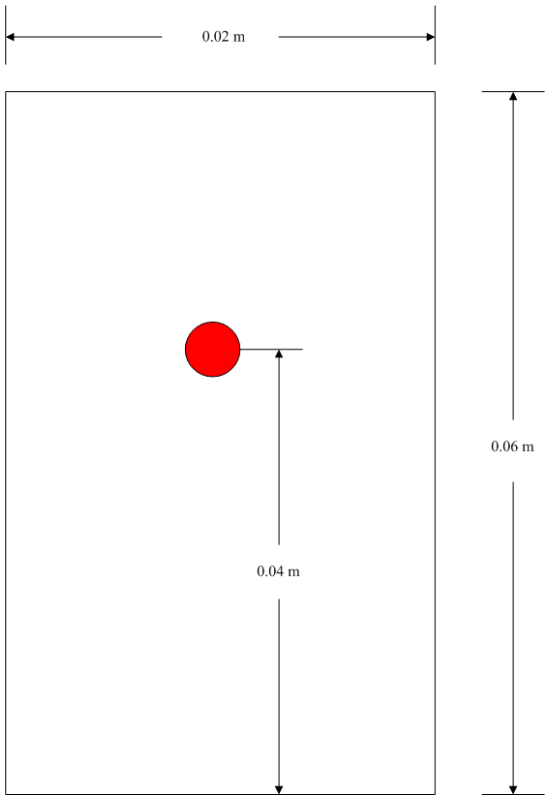

Figure 4.3: Schematic diagram for a single particle settling in a cavity.

4.3.2 Sedimentation of a circular particle in a cavity II

Several numerical tests were carried out according to the LBM parameters provided in [2, 3], the results were compared with the experimental data provided [8]. The configuration of interest is a rectangular cavity with four solid boundaries. The width is $0.10m$ and the height is $0.16m$. The cavity is filled with stagnant Newtonian fluid, the properties of the fluid can be found in Table.1, a uniform mesh of 101×161 is used in the simulations. One sphere with a diameter $0.015m$ is set at $(0.05m, 0.1275m)$. The sphere is initially at rest and its density is 1120 kg/m . The particle falls down under the action of the gravity field.

Fig. 4.6 shows three typical locations of the sphere with contour plots for u velocity at several selected instances when Re=1.5 . It should be stressed that we also tested the effect of the number of Lagrangian points on the results. In all the simula-

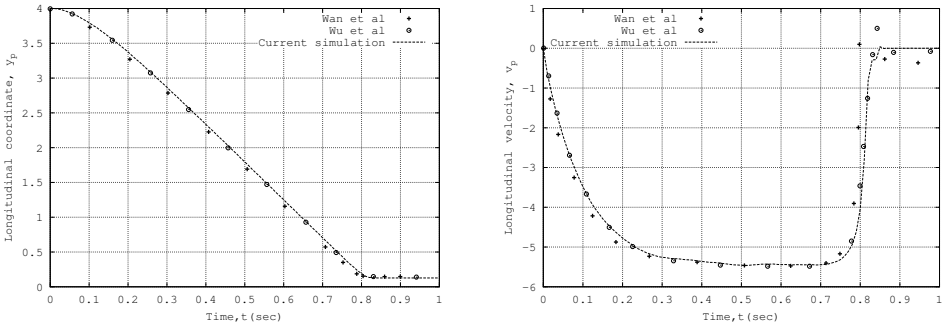

Figure 4.4: (a) longitudinal coordinate; (b) longitudinal velocity;

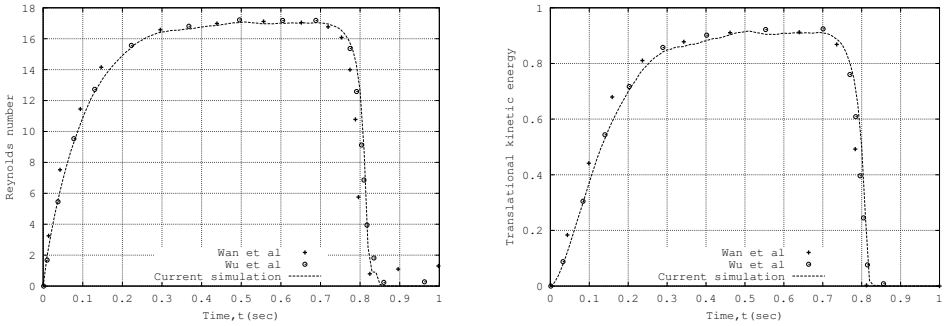

Figure 4.5: (a) Reynolds number; (b) translational kinetic energy;

tions conducted in this chapter we used $\Delta s_l = 0.29h$, namely about 100 Lagrangian nodes were used to represent the surface of solid boundary, almost identical results were found when we used $\Delta s_l = 0.49h$ and $\Delta s_l = 0.89h$.

Detailed comparisons of the numerical solutions and the experimental data were given in Fig. 4.6. As shown the current LBM-IBM-DEM scheme did a good job to predict both the trajectories and velocities at different Reynolds numbers. The gaps between the simulation and measured velocities may due to the 2D simplification effect and the presence of the bottom wall, the same slowing phenomenon was also found in [2, 3].

4.3.3 Bouncing motion of particles near bottom

The validation of the presented discrete particle method is accomplished by comparing the results of bouncing motion of spherical particles with the experimental

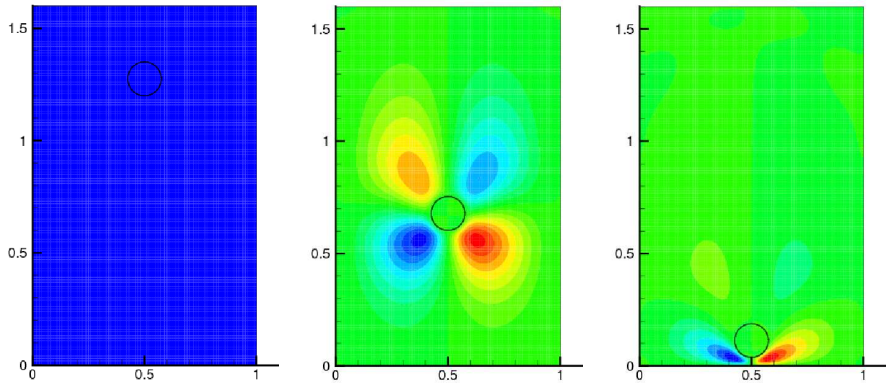

Figure 4.6: Sedimentation of a sphere in a cavity at different time stages,Re $= 1.5$;

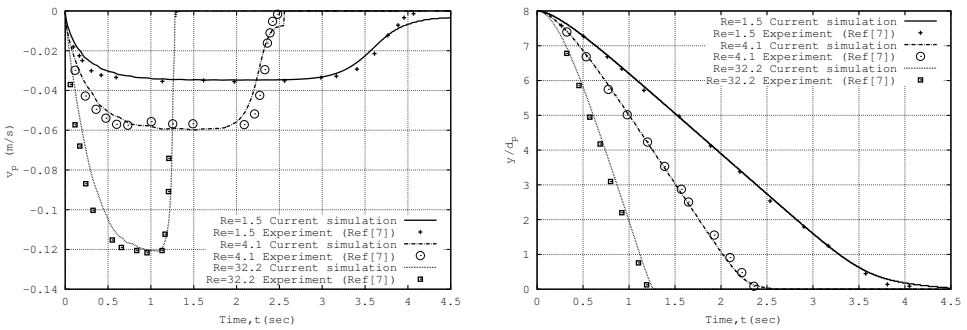

Figure 4.7: (a) Comparisons of the measured and simulated height of the sphere; (b) Comparisons of the measured and simulated settling velocity;

measurements by Gondret [9]. To match the experimental conditions the same physical parameters are adopted as in [9]. A stainless steel particle settles from rest at a height $0.00744m$ in silicon oil RV10 under gravity, the parameters of the fluid and the particle are listed in Table.4.1. A computational domain of 501×501 is used in the simulations. The relaxation time is $\tau = 0.65$ which leads to a physical timestep of $0.00004675s$.

Fig. 4.8 shows the evolution of the longitudinal coordinate and velocity of the particle with respect to time. It is observed that the simulation results have good consistency with the experimental measurements. The longitudinal velocity of the

Table 4.1: Properties of particles and fluid.

Solid phase		Fluid phase	
Number of particles	1	Viscosity ($kg \cdot m^{-1} \cdot s^{-1}$)	1.0e-2
Density ($kg \cdot m^{-3}$)	7800	Density ($kg \cdot m^{-3}$)	935
Young's Module (GPa)	240	Cavity height (m)	0.05
Poisson ratio ($N \cdot m^{-1}$)	0.33	Cavity width (m)	0.05
Friction coefficient	0.33	Lattice height (m)	0.0001
Diamater (m)	0.0003	Lattice width (m)	0.0001

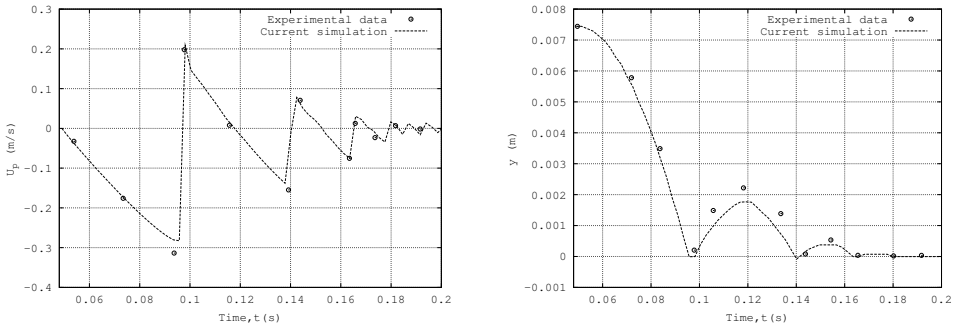

Figure 4.8: (a) Reynolds number; (b) translational kinetic energy;

particle agrees well with the experimental data during settling but is slowed when it approaches the cavity bottom. The slowing leads to a reduction of the rebound height as shown in Fig. 4.8 (b). This discrepancy between numerical result and experimental data near bottom is also reported by Feng and Michaelides in [3]. The reason is considered to be the presence of the bottom wall. Additional simulations in the same configuration but with different particle parameters are conducted, and it is shown that the choice of the physical parameters plays an important role in the accurate simulation of the collision process. The collision time and frequency are very different when the physical parameters are changed. From this point of view, DEM provides more reliable results than other artificial penalty methods.

4.3.4 Sedimentation of two circular particles in a channel

For the movement of particles in Newtonian liquids, the so-called drafting-kiss-tumbling (DKT) problem has been widely investigated by several researchers [3, 10, 11, 12] for a benchmarking purpose. This case study is performed in this study to

Table 4.2: Properties of particles and fluid.

Solid phase		Fluid phase	
Number of particles	2	Viscosity ($kg \cdot m^{-1} \cdot s^{-1}$)	1.0e-3
Density ($kg \cdot m^{-3}$)	1010	Density ($kg \cdot m^{-3}$)	1000
Young's Module (GPa)	68.95	Channel height (m)	0.08
Poisson ratio ($N \cdot m^{-1}$)	0.33	Channel width (m)	0.02
Friction coefficient	0.33	Lattice height (m)	0.0001
Diamater (m)	0.002	Lattice width (m)	0.0001

check the effect of DEM on the inter-particle collisions. The configuration of the simulation used here is based on the simulation by Niu et al. [10]. A $0.02m$ (width) $\times$ $0.08m$ (height) channel is defined with the top and base open, and the no-slip boundary is adopted on the left- and right-hand side boundaries of the channel. 2 circular particles each of diameter 0.002 m are located at $(0.000999m, 0.072m)$ and $(0.001m, 0.068m)$ respectively. The particles fall down under the action of the gravity field. The properties of the particles and the surrounding fluid are given in Table B.1. A 201×801 computational fluid lattices are used for the simulation. The relaxation time is $\tau = 0.65$, it leads to a physical timestep of $0.0005s$.

The drafting-kissing-tumbling sequence is illustrated in Fig. 4.9 with contour plots for v velocity of fluid at several selected instances. The leading particle creates a wake of low pressure. Since the trailing particle is caught in this wake, it falls faster. After a period of chasing strategy, the trailing particle eventually catches up with the leading one and kisses it. The two kissing particles form a single long body and fall together until separated by hydrodynamic force. As a result, the pair of kissing particles tumbles to a side-by-side configuration before falling without further lateral migrations.

Quantitative comparisons between current results and those obtained by other numerical studies are given in Fig. 4.10 and Fig. 4.11. an additional simulation using the Lennard-Jones (L-J) potential model (same as Niu [10]) is conducted to calculate the repulsive force between the particles, the results are also included. As seen in Fig. 4.10 all the positions and velocities agree very well with each other before the tumbling part of the process. For the discrepancy after tumbling, different modes of tumbling have been reported in the literature [12]. Fortes et al. [13] has pointed out that the tumbling process is essentially a breakup of an unstable configuration of the particles positions which is highly influenced by the particle-collision law and the numerical method to handle the fluid flow. It is shown that the LBM-IBM-DEM scheme provides the longest tumbling process. This is due to the adoption of soft-sphere DEM. Fig. 4.12(a) shows the distance between the surfaces

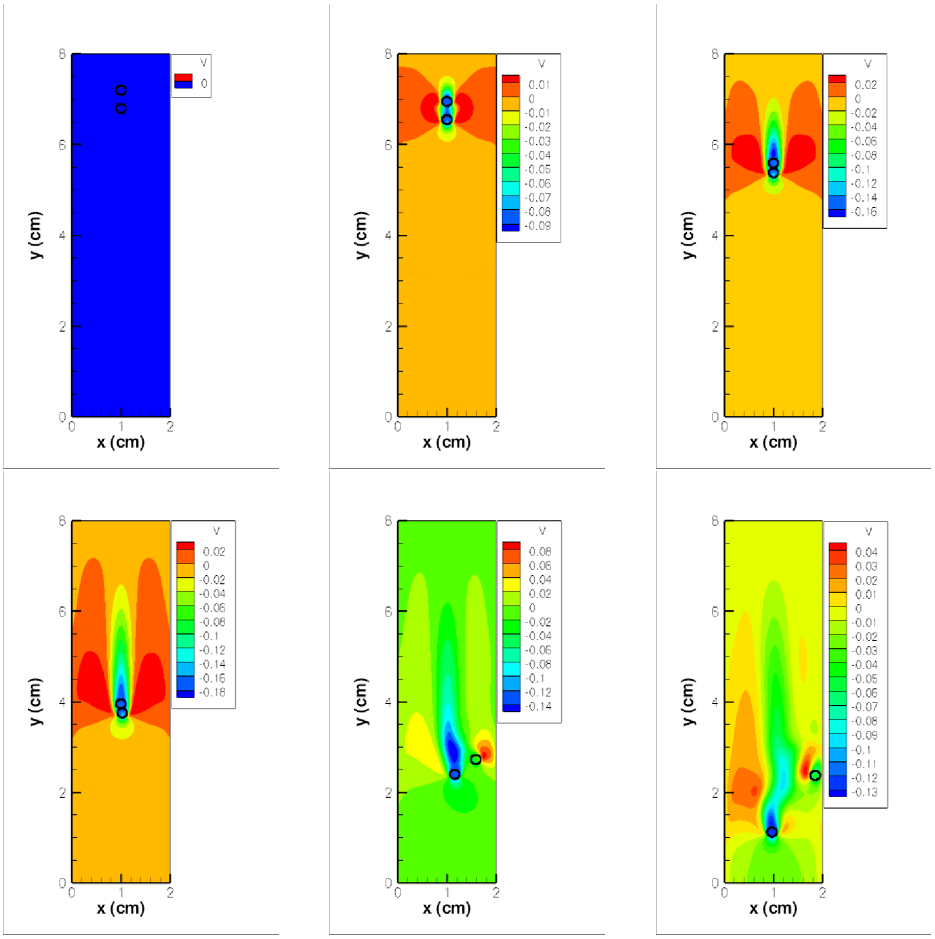

Figure 4.9: Sedimentation of two circular particles in a channel at different time stages. (a) 0.0s; (b) 0.5s; (c) 1.5s; (d) 2.5s; (e) 3.5s; (f) 4.5s;

of the two particles during the DKT process. The solid line represents the results obtained by LBM-IBMâDEM while the dashdot line represents the results obtained by LBM-IBM-(L-J). A good agreement can be seen before 'Kissing' and the two lines stay at one certain value with small fluctuation during the tumbling process. The value of the dashdot line is a little bit larger than 0.01 cm, namely about one lattice unit. The distance between the two surfaces is due to the adoption of the threshold which keeps the surfaces staying away from each other. The value of the solid line

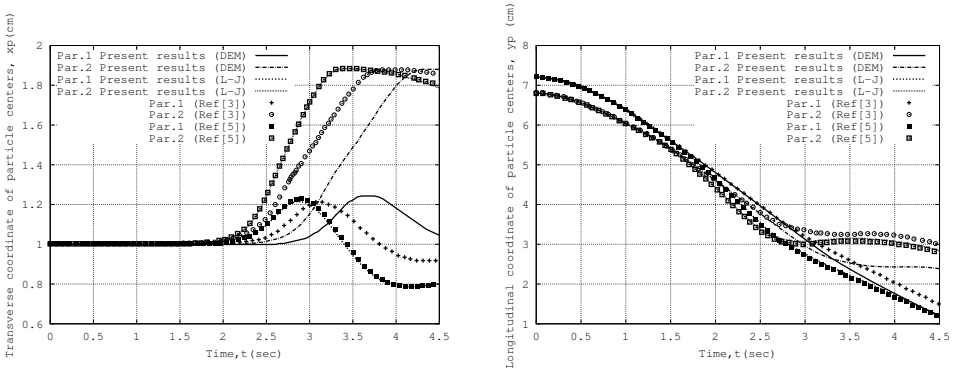

Figure 4.10: (a) Transverse coordinates of the centers of the two particles; (b) Longitudinal coordinates of the centers of the two particles.

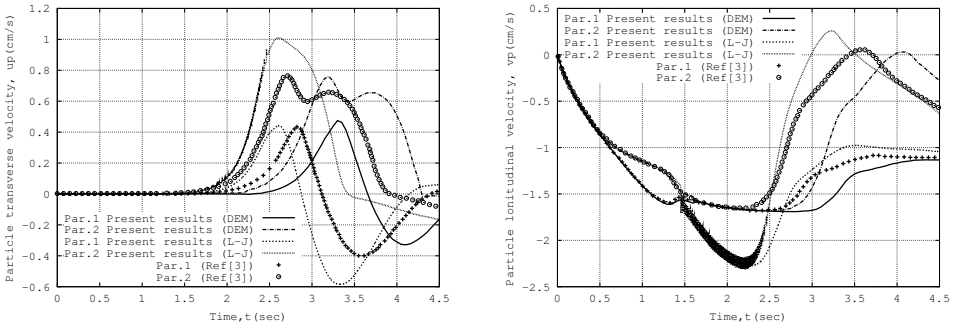

Figure 4.11: (a) Transverse velocity components of the two particles; (b) Longitudinal velocity components of the two particles.

fluctuates around 0 cm because the overlap is allowed in soft-sphere DEM. The distance between the particle surfaces can influence that tumbling process, Feng and Michaelides [2] compared the IB-LBM results with those using simple LBM, where a much shorter tumbling process was found in the LBM case. We have found that the physical parameters of the particles do not play a significant role in this process. An 'invalidation' of the interpolation scheme may be encountered under a high overlap as shown in Fig. 4.12(b) because a nine point interpolation scheme was adopted to obtain the fluid density distribution on the Lagrangian polynomicals from the Eulerian meshes.

Transverse and longitudinal velocity components of the two particles are also compared. It is shown in Fig. 4.11 that an artificial model like Lennard-Jones (L-J) potential model may predict a deviant force and velocity (from 1.4 s to 2.5 s),

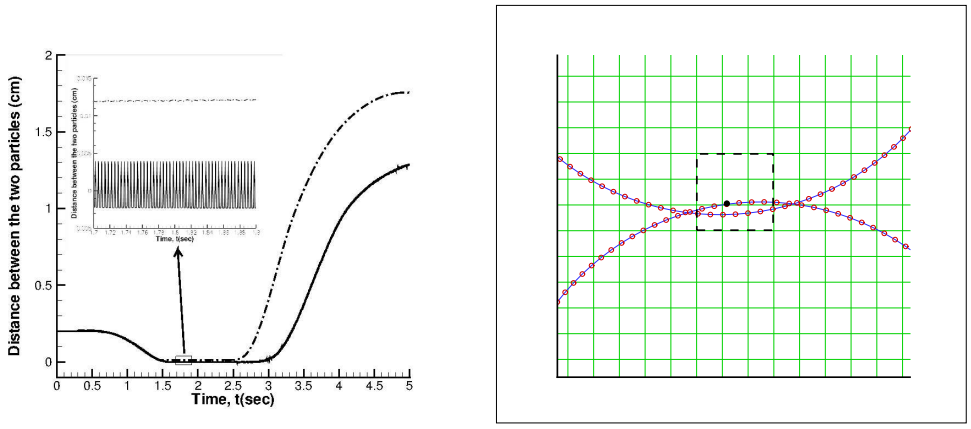

Figure 4.12: (a) The distance between surfaces of the two particles (red:DEM, green:L-J); (b) The interpolation scheme;

which may be fatal when it is used to handle large number of particles with frequent collisions. From this point of view, DEM does a better job in providing the dynamic information of the particles.

4.3.5 Sedimentation of 504 circular particles in a cavity

Table 4.3: Properties of particles and fluid.

Solid phase		Fluid phase	
Number of particles	504	Viscosity ($kg \cdot m^{-1} \cdot s^{-1}$)	1.0e-3
Density ($kg \cdot m^{-3}$)	1010	Density ($kg \cdot m^{-3}$)	1000
Young's Module (GPa)	68.95	Cavity height (m)	0.02
Poisson ratio ($N \cdot m^{-1}$)	0.33	Cavity width (m)	0.02
Friction coefficient	0.33	Lattice height (m)	0.00004
Diamater (m)	0.000625	Lattice width (m)	0.00004

In order to examine the LBM-IBM-DEM scheme for handling system containing large number of inter-particle collisions as well as particle-wall collisions, a simulation of sedimentation of 504 circular particles in a cavity is conducted. The initial setup of the problem is illustrated in 4.13, which is similar with that used by Feng et al. [2] . The properties of the particles and the surrounding fluid are given in Ta-

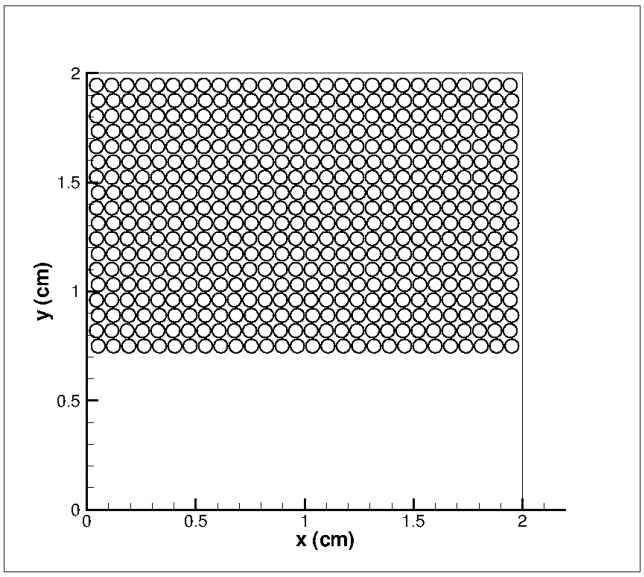

Figure 4.13: Positions of the 504 particles at time $t = 0s$.

ble 4.3. 504 circular particles of diameter $d = 0.000625m$ are positioned in a closed two-dimensional square cavity of side length $0.002m$. There are 18 lines of particles, in each line there are 28 particles. The gap between horizontal neighboring particles in each lines and between each two neighboring lines is $d/8$. The gap between the upmost line and the upper wall is $3d/8$. The gap between the left wall and the leftmost particle in all the odd-numbered horizontal lines is $2d/8$. The gap between the left wall and the leftmost particle in all the even-numbered horizontal lines is $3d/8$. The fluid domain is divided into a 512×512 square lattice, so the diameter of each particle is equal to 16 lattice units. The criterion for generating the computational grid is based on the result of Feng and Michaelides [2] . It has been shown that the current resolution is fine enough to capture the flow behavior. The relaxation time is $\tau = 0.9915$. The no-slip boundary is adopted on the four boundaries of the cavity. Initially the particles and the fluid are stationary and the particles fall down under the action of the gravity field.

The configuration presented is regarded to behave similarly as two layers of fluids with different densities, it is known that the Rayleigh-Taylor instability of the interface may take place between the two fluids when the lighter fluid is pushing the heavier fluid. This phenomenon has been vividly captured in the simulation results, as shown in Fig. 4.14, 4.15 and 4.16. Initially all the particles start to settle

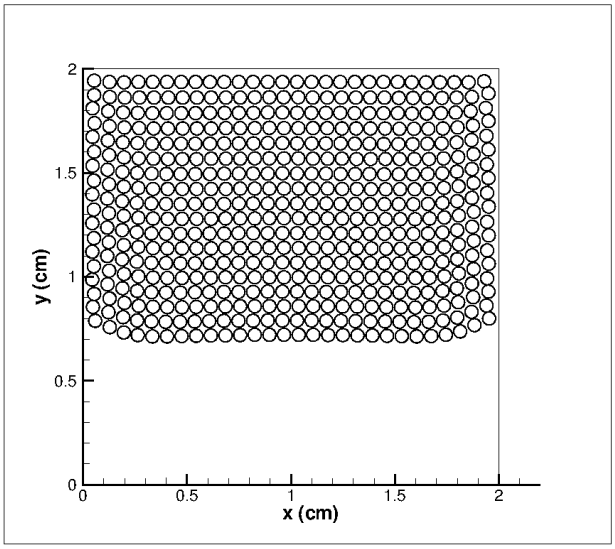

Figure 4.14: Positions of the 504 particles at time $t = 1s$.

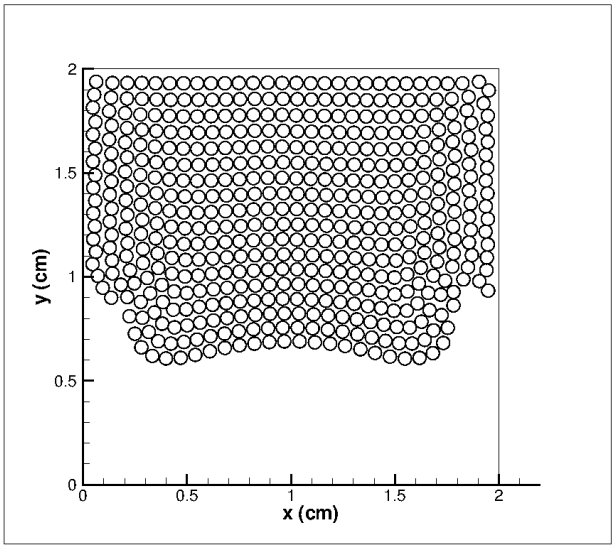

Figure 4.15: Positions of the 504 particles at time $t = 2s$.

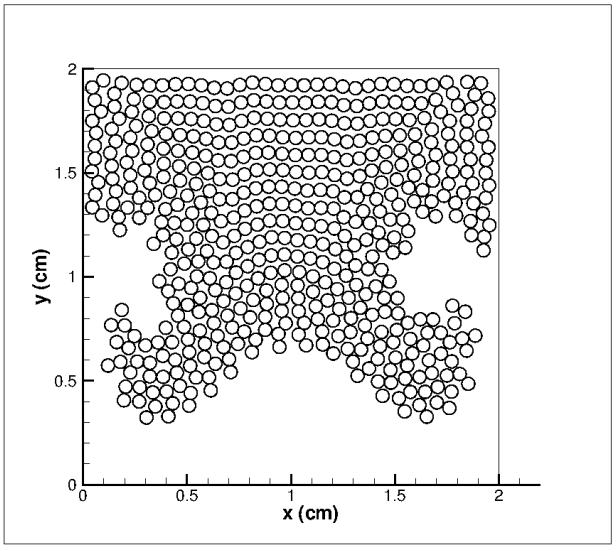

Figure 4.16: Positions of the 504 particles at time $t = 3s$.

uniformly, the stagnation of the fluid beside the walls hindered the particles nearby. Hence the particles in the center move faster than the particles beside the walls, thus the interface appears to be a parabola curve as depicted in Fig. 4.14. Then two small vortexes are generated beside the two vertical walls respectively, the vortex beside the left boundary rotates clockwise as well as the other rotates anticlockwise. They pull the particles downwards, which further changes the shape of the interface curve (see Fig. 4.15). When the lighter fluid pushes into the particle cluster, two branches are formed each heading for the corners of the cavity (shown in Fig. 4.16). The flow patterns before$3s$ have a good agreement with those reported by Feng and Michaelides [2] .

The evolution of the flow pattern shows differences after multicollisions taking place between the particles and between the the particles and walls. At $t = 4s$, the two branches sweep across the cavity corners and head for the perpendicular bisector of the base. The tips of the particle branches move slower than those given by Feng and Michaelides [2] . Due to the fact that both the flow fields are evaluated by LBM with same parameters used, the discrepancy is most probably due to the forcing term and the method that accounts for the collisions. In the study of Feng and Michaelides [2], the friction between the particle-particle and particle-wall were neglected, whereas in this study we calculate this effect according to Mindlin-Deresiewicz theory[14]. It is believed that the particle flows are hindered when they

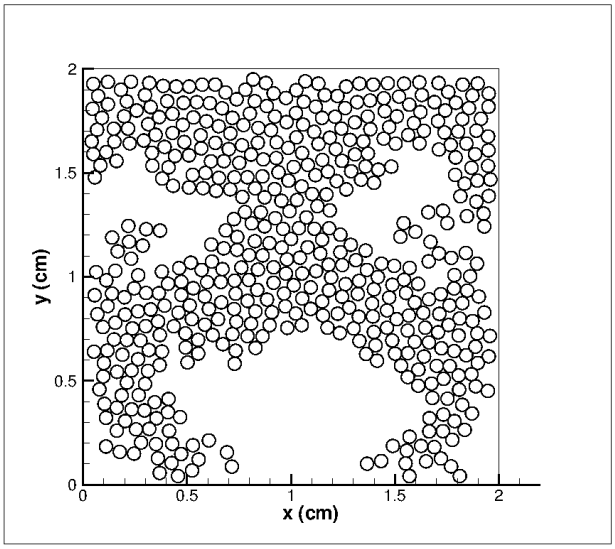

Figure 4.17: Positions of the 504 particles at time $t = 4s$.

travel around the corner of the box (shown in Fig 4.17) by the collisions and friction.

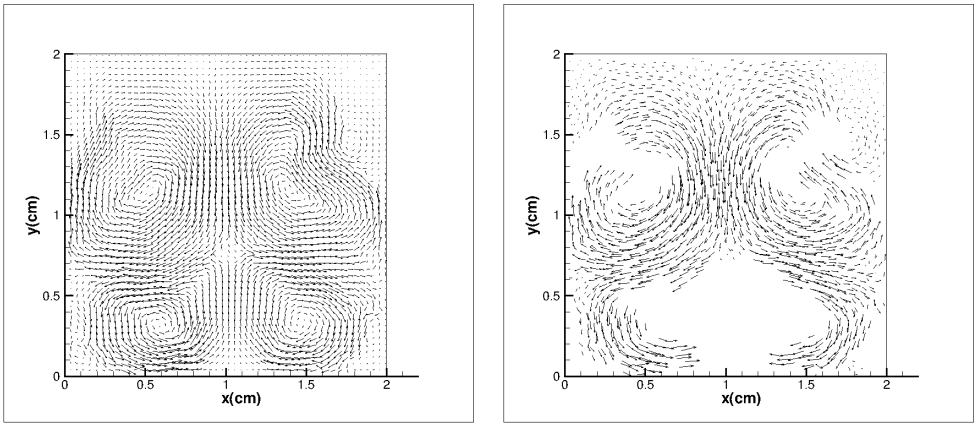

Figure 4.18: (a) The flow field; (b) Distribution of the particle velocity at time $t = 4s$;

When the two particle branches insert into the lower half of the cavity, another

two small vortexes are formed in the circular region surrounded by the two particle arms, as depicted in Fig. 4.18 (a). Subsequently, the two lower vortexes, one at each side of the cavity, grow and start to pull particles downwards, as depicted in Fig. 4.18 (b) At the same time the two upper vortexes tear the particle clusters to blocks and pull the particles beside the walls upwards and the particles in the center downwards into the two vortexes below. As more particles are transferred downwards, the two lower vortexes become the dominant force in the enclosure

At $t = 5s$, the two particle branches carried by the vortex impact at the perpendicular bisector of the base. The impact shoots the particles up into the circular region and two fluid pockets are formed, as seen in Fig. 4.19. At the same time, some particles in the center are rose but against the falling particles. Frequent collisions between the particles tear those two vortexes at the upper half to small eddies. Some of the small eddies further merge into big ones while others are dissipated. Complex interactions between the particles and fluid take place until all the particles settle at the bottom of the cavity and an equilibrium state is reached.

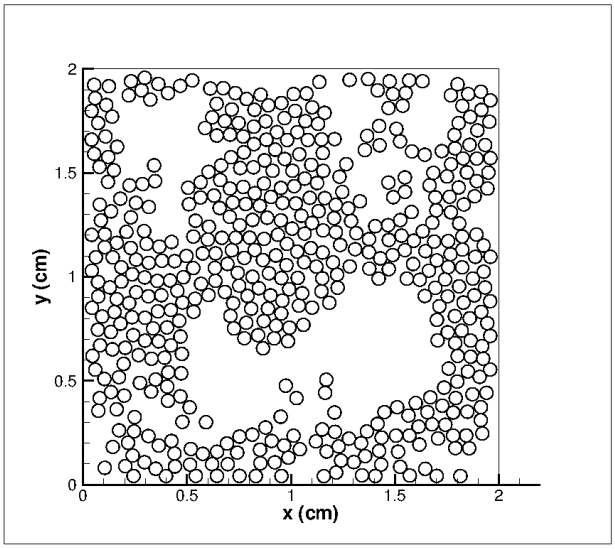

Figure 4.19: Positions of the 504 particles at time $t = 5s$.

Fig. 4.20, 4.21, 4.22 and 4.23 show the further stages of the settling process, the evolution of the particle bed height has a good agreement with that obtained by Feng and Michaelides [2] . However, main differences are found near the base of the cavity when the particles fall down. The packing is not as orderly as that shown in the results of Feng and Michaelides. Our simulation shows that the evolution of the par-

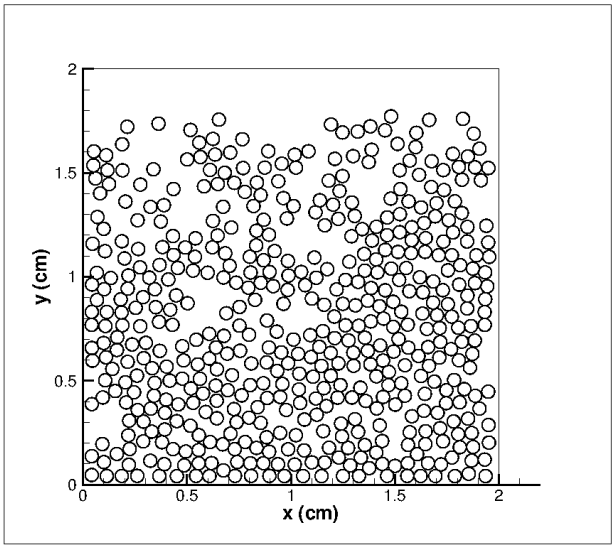

Figure 4.20: Positions of the 504 particles at time $t = 8s$.

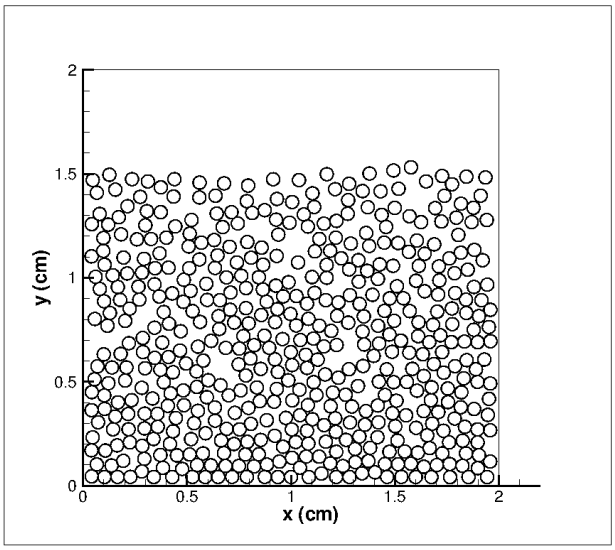

Figure 4.21: Positions of the 504 particles at time $t = 12s$.

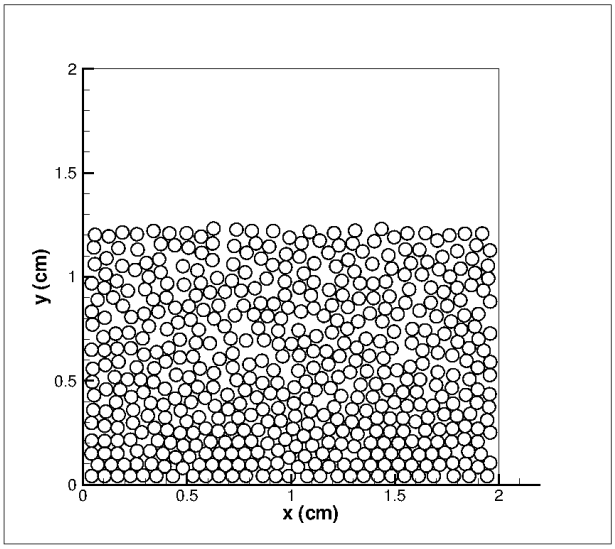

Figure 4.22: Positions of the 504 particles at time $t = 24s$.

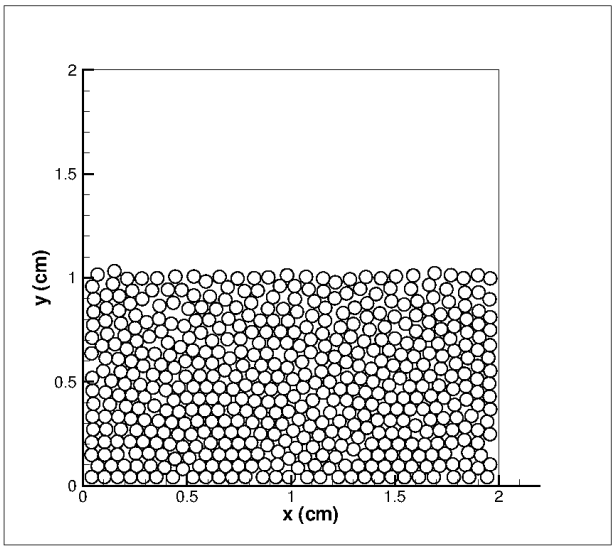

Figure 4.23: Positions of the 504 particles at time $t = 48s$.

ticle patterns can be markedly influenced by the initial set of the particles. The initial condition adopted here is slightly different with that adopted in [2] . This difference has not made any discrepancy on the particle distribution until $t = 5s$ (Fig. 4.19). In ref [2] , the two particle arms seem to be synchronously shot up and then fall down vertically. This gives rise to the generation of two small gaps when $t = 24s$. Whereas as shown in Fig. 4.19 in this study, at $t = 5s$ the the left branch has more power and beats the right one, the strike shifts the prospective vertical motion into transverse ones. The succeeding results show that the transverse movement does not change the sedimentation speed evidently but does flat the gaps. An exactly same initial set as in [2] has been tried, however a more serious deviation was found. Another reason of all this discrepancy can be due to the interaction law as discussed above. The evidence is that some arched holes are formed at the lowest line of particles, which cannot happen when the surface friction is not taken into account.

4.4 Concluding remarks

This chapter presents a novel coupled LBM-IBM-DEM methodology for the numerical simulation of particle-fluid problems. The fluid field is solved by LBM, the hydrodynamic interactions between fluid and particles are realized through the momentum exchange of the particles. The coupling scheme preserves the merits of LBM and IBM by using two unrelated computational meshes, an Eulerian mesh for the flow domain and a Lagrangian mesh for the moving particles. In particular the particle interactions are modeled by the DEM based on contact mechanics. The combined model has been validated by comparing the results with those from previous simulations on the settling of single sphere and the DKT problem, where good agreement was observed. It is observed that the collision scheme and parameters play a very important role in the accurate simulation of particulate flow and the LBM-IBM-DEM scheme can work well when the real physical parameters of the particles were adopted in the simulation. Finally, by conducting a numerical simulation of sedimentation we have shown that the proposed approach is a promising numerical solution for the simulation of particle-fluid interaction problems.

References

[1] Qian, YH and d'Humières, Dominique and Lallemand, Pierre. Lattice BGK models for Navier-Stokes equation. *EPL (Europhysics Letters)*, 17(6):479, 1992.

[2] Zhi-Gang Feng and Efstathios E Michaelides. The immersed boundary-lattice Boltzmann method for solving fluid-particles interaction problems. *Journal of Computational Physics*, 195(2):602 – 628, 2004.

[3] Zhi-Gang Feng and Efstathios E. Michaelides. Proteus: a direct forcing method in the simulations of particulate flows. *Journal of Computational Physics*, 202(1):20 – 51, 2005.

[4] DRJ Owen, CR Leonardi, and YT Feng. An efficient framework for fluid–structure interaction using the lattice Boltzmann method and immersed moving boundaries. *International Journal for Numerical Methods in Engineering*, 87(1-5):66–95, 2011.

[5] Y Sheng, CJ Lawrence, BJ Briscoe, and C Thornton. Numerical studies of uniaxial powder compaction process by 3D DEM. *Engineering Computations*, 21(2/3/4):304–317, 2004.

[6] Decheng Wan and Stefan Turek. Direct numerical simulation of particulate flow via multigrid FEM techniques and the fictitious boundary method. *International Journal for Numerical Methods in Fluids*, 51(5):531–566, 2006.

[7] J. Wu and C. Shu. Particulate Flow Simulation via a Boundary Condition-Enforced Immersed Boundary-Lattice Boltzmann Scheme. *Communications in Computational Physics*, 7:793–812, 2010.

[8] A Ten Cate, CH Nieuwstad, JJ Derksen, and HEA Van den Akker. Particle imaging velocimetry experiments and lattice-Boltzmann simulations on a single sphere settling under gravity. *Physics of Fluids*, 14:4012, 2002.

[9] P Gondret, M Lance, and L Petit. Bouncing motion of spherical particles in fluids. *Physics of fluids*, 14:643, 2002.

[10] X.D. Niu, C. Shu, Y.T. Chew, and Y. Peng. A momentum exchange-based immersed boundary-lattice Boltzmann method for simulating incompressible viscous flows. *Physics Letters A*, 354(3):173 – 182, 2006.

[11] Howard H Hu, Neelesh A Patankar, and MY Zhu. Direct numerical simulations of fluid–solid systems using the arbitrary Lagrangian–Eulerian technique. *Journal of Computational Physics*, 169(2):427–462, 2001.

[12] Neelesh A Patankar, Pushpendra Singh, Daniel D Joseph, Roland Glowinski, and T-W Pan. A new formulation of the distributed lagrange multiplier/fictitious domain method for particulate flows. *International Journal of Multiphase Flow*, 26(9):1509–1524, 2000.

[13] Antonio F Fortes, Daniel D Joseph, and Thomas S Lundgren. Nonlinear mechanics of fluidization of beds of spherical particles. *Journal of Fluid Mechanics*, 177:467–83, 1987.

[14] R.D. Mindlin, R.D. Mindlin, and H. Deresiewicz. Elastic spheres in contact under varying oblique forces. *Journal of Applied Mechanics*, 20:327–344, 1953.

Chapter 5

PIBM: Particulate immersed boundary method for fluid-particle interaction problems

Part of the contents of this chapter have been published as:

H Zhang, FX Trias, A Oliva, D Yang, Y Tan, Y Sheng. PIBM: Particulate immersed boundary method for fluid-particle interaction problems. *Powder Technology. n(2015), x-y.*

Abstract.

It is well known that the number of particles should be scaled up to enable industrial scale simulation. The calculations are more computationally intensive when the motion of the surrounding fluid is considered. Besides the advances in computer hardware and numerical algorithms, the coupling scheme also plays an important role on the computational efficiency. In this chapter, a Particulate Immersed Boundary Method (PIBM) for simulating the fluid-particle multiphase flow was presented and assessed in both two- and three-dimensional applications. The idea behind PIBM derives from the conventional momentum exchange-based immersed boundary method (IBM) by treating each Lagrangian point as a solid particle. This treatment enables Lattice Boltzmann Method (LBM) to be coupled with fine particles residing within a particular grid cell. Compared with the conventional IBM, dozens of times speedup in two-dimensional simulation and hundreds of times in three-dimensional simulation can be expected under the same particle and mesh number. Numerical simulations of particle sedimentation in Newtonian flows were conducted based on a combined LBM - PIBM - DEM scheme, showing that the PIBM can capture the feature of particulate flows in fluid and is indeed a promising scheme for the solution of the fluid-particle interaction problems.

5.1 Governing equations

5.1.1 Lattice Boltzmann model with single-relaxation time collision

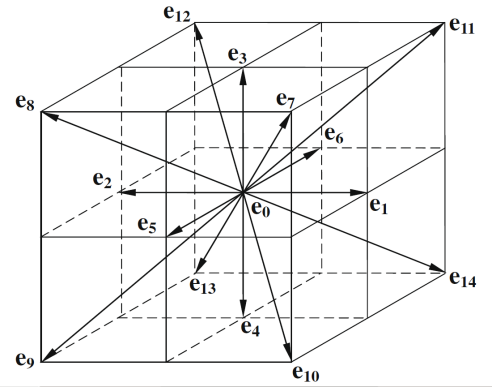

Figure 5.1: Schematic diagram of the D3Q15 model[1].

We consider the simulation of the incompressible Newtonian fluids where the LBM-D3Q15 model [2] is adopted, and the spatial distribution of the velocities is shown in Figure 5.1. Following the same notation used by Wu and Shu[1], those 15 lattice velocities are given by

$$e_\alpha = \begin{cases} (0,0,0)c & \alpha = 0 \\ (\pm 1,0,0)c, (0,\pm 1,0)c, (0,0,\pm 1)c & \alpha = 1-6 \\ (\pm 1,\pm 1,\pm 1)c & \alpha = 7-14 \end{cases} \tag{5.1}$$

where c is termed by the lattice speed. The formulation of the lattice Bhatnagar-Gross-Krook model is

$$f_\alpha(r + e_\alpha \delta_t, t + \delta_t) = f_\alpha(r,t) - \frac{f_\alpha(r,t) - f_\alpha^{eq}(r,t)}{\tau} + F_b \delta_t \tag{5.2}$$

where $f_\alpha(r,t)$ represents the fluid density distribution function, $r = (x,y,z)$ stands for the space position vector, t denotes time and τ denotes the non-dimensional relaxation time, $F_b\delta_t$ denotes the fluid-solid interaction force term which is given in the following section. The equilibrium density distribution function, $f_\alpha^{eq}(r,t)$, can be written as

$$f_\alpha^{eq}(r,t) = \rho_f \omega_\alpha [1 + 3(e_\alpha \cdot u) + \frac{9}{2}(e_\alpha \cdot u)^2 - \frac{3}{2} \mid u \mid^2] \tag{5.3}$$

where the value of weights are: $\omega_0 = 2/9$, $\omega_\alpha = 1/9$ for $\alpha = 1 - 6$ and $\omega_\alpha = 1/72$ for $\alpha = 7 - 14$. u denotes the macro velocity at each lattice node which can be calculated by $u = (\sum_{\alpha=0}^{14} f_\alpha e_\alpha)/\rho_f$, and the macro fluid density is obtained by $\rho_f = \sum_{\alpha=0}^{14} f_\alpha$.

5.1.2 Particulate immersed boundary method (PIBM)

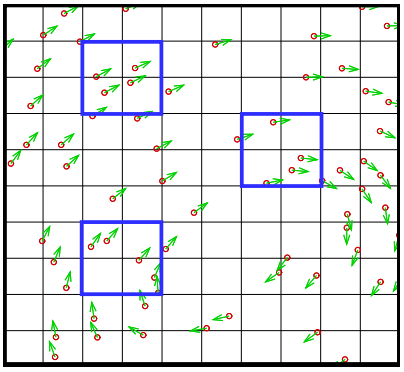

Figure 5.2: Schematic diagram of the PIBM.

For the sake of clarity, the two-dimensional schematic diagram of the PIBM is given in Figure 5.2 followed by three-dimensional equation systems. As shown, the fluid is described using the Eulerian square lattices and the solid particles are denoted by the Lagrangian points moving in the flow field. Instead of using several Lagrangian points to construct one large solid particle [3], each Lagrangian point is treated as one single solid particle in this study. The fluid density distribution functions on the solid particles are evaluated using the numerical extrapolation from the circumambient fluid points,

$$f_\alpha(X_l, t) = L \cdot f_\alpha(r, t) \tag{5.4}$$

where $X_l(X, Y, Z)$ is the coordinates of the solid particles, L is the three-dimensional Lagrangian interpolated polynomials,

$$L = \sum_{ijk} \left(\prod_{l=1,l!=i}^{i_{max}} \frac{X - x_{ljk}}{x_{ijk} - x_{ljk}} \right) \left(\prod_{m=1,m!=j}^{j_{max}} \frac{Y - y_{imk}}{y_{ijk} - y_{imk}} \right) \left(\prod_{n=1,n!=k}^{k_{max}} \frac{Z - z_{ijn}}{z_{ijk} - z_{ijn}} \right) \tag{5.5}$$

where i_{max}, j_{max} and k_{max} are the maximum numbers of the Eulerian points used in the extrapolation as shown by blocks in Figure 5.2. With the movement of the solid particle, $f_\alpha(X_l, t)$ will be further affected by the particle velocity, U_p,

$$f_\beta(X_l, t + \delta_t) = f_\alpha(X_l, t) - 2\omega_\alpha \rho_f \frac{e_\alpha U_p}{c_s^2} \tag{5.6}$$

where the subscript β represents the opposite direction of α. Based on the momentum exchange between fluid and particles, the force density, $g(X_l, t)$, at each solid particle can be calculated using f_α and f_β,

$$g(X_l, t) = \sum_\beta e_\beta [f_\beta(X_l, t) - f_\alpha(X_l, t)] \tag{5.7}$$

The effect on the flow fields from the solid boundary is the body force term $F_b \delta_t$ in Equation 5.2, where F_b can be expressed by

$$F_b = \left(1 - \frac{1}{2\tau}\right) \omega_\alpha \left(3\frac{e_\alpha - u}{c^2} + 9\frac{e_\alpha \cdot u}{c^4} e_\alpha\right) F(r, t) \tag{5.8}$$

and

$$F(r, t) = \sum_l g(X_l, t) D_{ijk}(r_{ijk} - X_l) A_p \tag{5.9}$$

A_p is the cross-sectional area of the particle which is given as $A_p = 0.25\pi d_p^2$, d_p is the diameter of the particle. D_{ijk} is used to restrict the feedback force to only take effect on the neighbor of interface and is given by

$$D_{ijk}(r_{ijk} - X_l) = \frac{1}{h^3} \delta_h \left(\frac{x_{ijk} - X_l}{h}\right) \delta_h \left(\frac{y_{ijk} - Y_l}{h}\right) \delta_h \left(\frac{z_{ijk} - Z_l}{h}\right) \tag{5.10}$$

with

$$\delta_h(a) = \begin{cases} \frac{1}{4}(1 + cos(\frac{\pi a}{2})), & when \mid a \mid \leq 2 \\ 0, & otherwise \end{cases} \tag{5.11}$$

Solid phase		Fluid phase	
Density ($kg \cdot m^{-3}$)	1010	Density ($kg \cdot m^{-3}$)	1000
Young's Module (GPa)	68.95	Viscosity ($kg \cdot m^{-1} \cdot s^{-1}$)	1.0e-3
Poisson ratio ($N \cdot m^{-1}$)	0.33	Lattice length (m)	0.0001
Friction coefficient ($-$)	0.33	Gravity acceleration ($m \cdot s^{-2}$)	9.8

Table 5.1: Properties of the particles and fluid.

where h is the mesh spacing. It should be stressed that by adding a body force on the flow field, the macro moment flux also has to be modified by the force $\rho_f u = \sum_{\alpha=0}^{14} f_\alpha e_\alpha + \frac{1}{2}F(r,t)\delta t$.

On the other hand, the fluid-solid interaction force exerted on the solid particle can be obtained as the reaction force of $g(X_l, t)$,

$$F_{fpi} = -g(X_l, t)A_p \tag{5.12}$$

5.2 Results and discussions

As stated in previous section, comparing with the conventional IBM, several essential simplifications have been made in the PIBM including removing the constraints between the Lagrangian particles and omitting the calculation of hydrodynamics torque. A natural question is that can the PIBM still success in the complex fluid-particle interaction problems with frequent momentum transfer? For the sake of demonstrating the capability of the PIBM, two- and three-dimensional simulations of particle sedimentation in Newtonian liquid in a cavity were carried out. This configuration is interesting because the Rayleigh-Taylor instability phenomenon may take place on the interface of the agglomerating particles and the fluid. In two-dimensional case [3], the fluid in the lower half of the cavity is found to insert into the upper half and this forms a fluid pocket of mushroom shape in the particle phase interior. Then, the relative smooth interface between the two phase is disturbed and the fluid pocket is teared to small ones. These fluid pockets have the appearance of irregular shape and travel at both vertical and horizontal speed until all the particles fall down on the cavity bottom. In this study, the two-dimensional results by PIBM were directly given due to the fact that the collision rule of the D2Q9 model is very similar to D3Q15 [2] and the two-dimensional code has been tested in [3]. In the rest of this section, the accuracy of the PIBM was firstly examined by simulating the falling process of a single particle in Newtonian flow and the results were compared

with the analytical solutions based on the Stokes' law. By means of the comparison, the parameters were also calibrated and adopted in the following multi-particle simulations. Then, the two- and three-dimensional results were presented in Section 5.2.2 and 5.2.3, respectively. The physical properties of the particles and the surrounding fluid are given in Table 5.1. It should be mentioned that the lattice spacing length, h, is $0.0001m$ in all the simulations.

5.2.1 Falling of a single particle

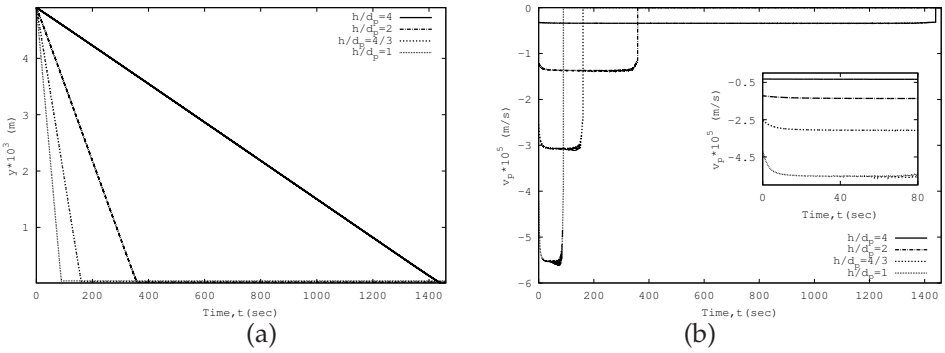

Figure 5.3: (a) longitudinal coordinates and (b) longitudinal velocities of the particle under different h/d_p.

Falling of the single particle in a cuboid cavity was firstly investigated. The length and width of the cuboid cavity are $0.1cm$ and the height is $0.5cm$. The initial position of the particle is at $(0.05cm, 0.05cm, 0.49cm)$. Four kinds of particles with different diameters are considered, namely $25\mu m$, $50\mu m$, $75\mu m$ and $100\mu m$ or $h/d_p = 4$, 2, $4/3$ and 1, respectively. The largest diameter is equal to one LBM grid spacing length. The longitudinal coordinates and velocities of different particles during the falling process are shown in Figure 5.3. The particles at rest begin to deposit under the effect of the gravitational force. After a period of acceleration, the particles fall with a constant settling velocity until they approaches to the bottom. The magnitude of the settling velocity increases with the particle size. Finally, the particles stay at the bottom of the cavity with zero longitudinal velocity. Figure 5.4 shows several typical snapshots of the falling process of the $100\mu m$ particle with contour plots for v_f, clear influence of the particle motion on the flow structure can be observed. For dilute suspensions, the settling velocity of a single particle in a viscous fluid flow can be evaluated by the Stokes' law which is given by

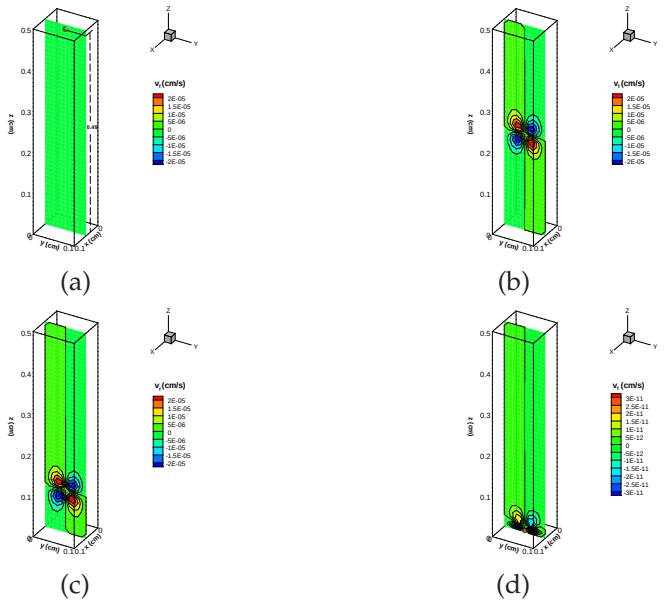

Figure 5.4: Instantaneous height of the $100\mu m$ particle with contour plots for v_f at time (a) $t = 0.0s$, (b) $t = 45.0s$, (c) $t = 67.5s$, (d) $t = 90.0s$.

$$V_s = \frac{(\rho_p - \rho_f)d_p^2 g}{18\mu} \tag{5.13}$$

where μ is the dynamic viscosity of the fluid. Quantitative comparison between the results based on the Stokes' law and the numerical ones are presented in Table 5.2. As shown, the settling velocities predicted by numerical simulation agree well with the Stokes' law. However, it is found that the particle may oscillate around the center line during the falling process and the fluctuation on the velocity increases with the particle size especially closing to the cavity bottom. Feng et al. [4] also reported this unsteadiness phenomenon using coupled Direct Numerical Simulation and DEM (DNS-DEM). In the following subsections of this study, $h/d_p = 4$ and 2 were chosen based on the similar criterion as adopted in the NS-DEM simulations [5]. Our numerical simulations show that this ratio works well in the multi-particle cases in general, however, further numerical and experimental validations may be needed to fully assess its effect on the particle behaviors.

h/d_p	Based on Stokes' law (cm/s)	Numerical results (cm/s)	τ	Physical timestep (s)
4	-3.40×10^{-4}	-3.41×10^{-4}	0.65	0.0005
2	-1.36×10^{-3}	-1.37×10^{-3}	0.72	0.0007
4/3	-3.06×10^{-3}	-3.07×10^{-3}	0.79	0.0010
1	-5.44×10^{-3}	-5.52×10^{-3}	0.85	0.0012

Table 5.2: The settling velocities at different particle size.

5.2.2 Sedimentation of two-dimensional particles in Newtonian flows

Two-dimensional simulations of the particle sedimentation in a square cavity have been conducted using various numerical methods [6, 7, 8, 3]. Here we consider a $1cm \times 1cm$ cavity with 5000 two-dimensional particles. The properties of the particles and the surrounding fluid are given in Table 5.1. The diameter of the particles are $25\mu m$ or $h/d_p = 4$. The relaxation time is $\tau = 0.65$, it leads to a physical timestep of $0.0005s$. Initially, the 5000 particles are randomly generated in the upper three-fifths domain and then deposit under the effect of the gravitational force. Figure 5.5 displays the changing process of the interface line from straight to curve. As expected, the fluid at the lower half of the cavity is swallowed into the the agglomerating particles forming a open hole of mushroom shape. The open hole is shattered to pieces when the particles fall down as shown in Figure 5.6. Generally speaking, the patterns observed in this simulation are very close to the results provided in the former references [6, 7, 8, 3]. However, compared with the results of large particles that calculated using conventional momentum exchange-based immersed boundary method [3], the whole sedimentation process takes much longer time due to the low settling velocity.

5.2.3 Sedimentation of three-dimensional particles in Newtonian flows

The sedimentation process

In this subsection, a three-dimensional $0.15cm \times 0.15cm \times 0.15cm$ cubic cavity is considered. The diameter of the particles is $50\mu m$ or $h/d_p = 2$. The relaxation time is $\tau = 0.72$ which leads to a physical timestep of $0.0007s$. Initially, 8125 particles are positioned in the upper three-fifths domain as shown in Figure 5.7, the solid fraction is 0.15, total volume occupied by the particle assembly is $1.9 \times 10^{-3} cm^3$, total volume of the particles is $5.3 \times 10^{-4} cm^3$ and thus the local porosity is 0.719. There are vertically 13 layers of particles, in each layer there are 625 particles forming a

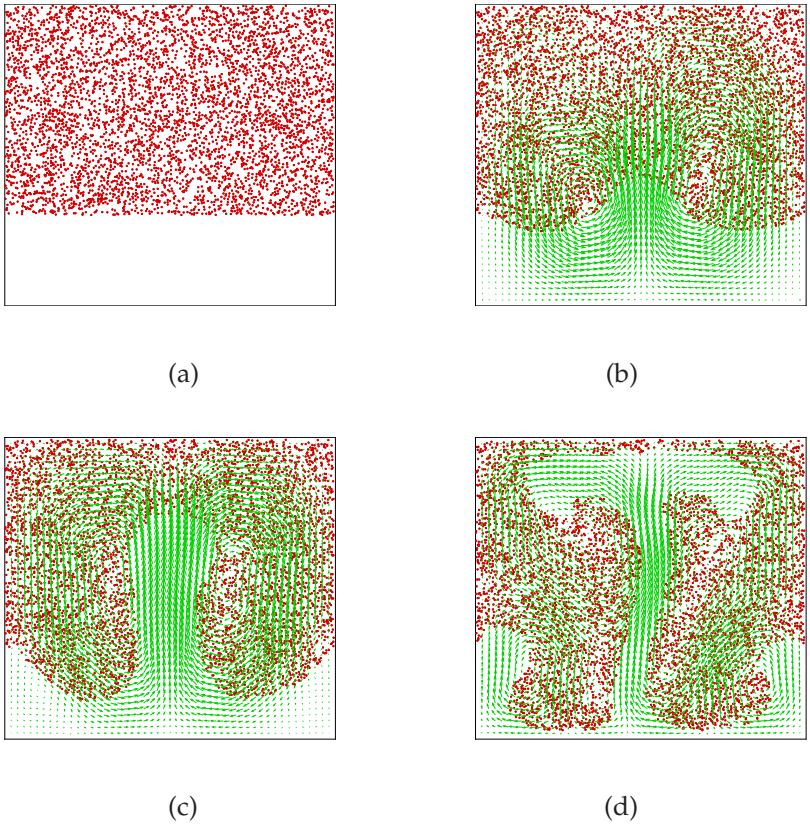

Figure 5.5: Instantaneous particle distribution with the fluid velocities at time (a) $t = 0.0s$, (b) $t = 2.5s$, (c) $t = 5.0s$, (d) $t = 10.0s$.

25×25 matrix. In each direction, the particles are uniformly distributed. The gap between the horizontal neighboring particles and between the closest particles and the side wall is about $0.001cm$. The gap between the vertical neighboring particles and between the highest particles and the top wall is about $0.0018cm$. The no-slip boundary is adopted on the six boundaries of the cavity, namely the fluid nearby the wall will have zero velocity.

In the initial stages of sedimentation, an overall falling of the particle agglomeration can be observed as shown in Figure 5.8 (a) and (b). Due to the fact that the initial porosity is low, the whole body at this stage can be regarded as a plug flow

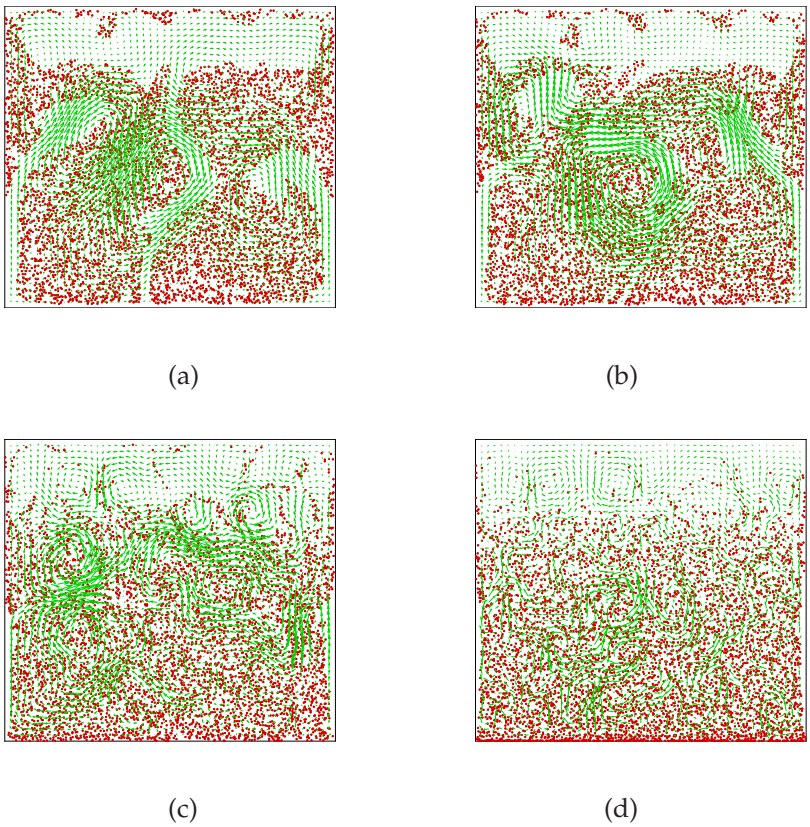

Figure 5.6: Instantaneous particle distribution with the fluid velocities at time (a) $t = 20.0s$, (b) $t = 25.0s$, (c) $t = 50.0s$, (d) $t = 100.0s$.

creeping in a channel. The distance between the highest particles and the top wall increases gradually and the particle distribution close to the walls does not change significantly. However, instead of settling uniformly, the difference of particle velocity inside and at the bottom of the body shows up shortly. This is because the particles close to the side walls are hindered by the stagnated fluid. Consequently, the particles in the center region move faster and pour down to suck the fluid to fill up the forming gap. The hump grows fast until it reaches the cavity bottom. It can be seen that the changing histories of the fluid-particle interface are different in two- and three-dimensional simulations. In the two-dimensional case, the updraft of

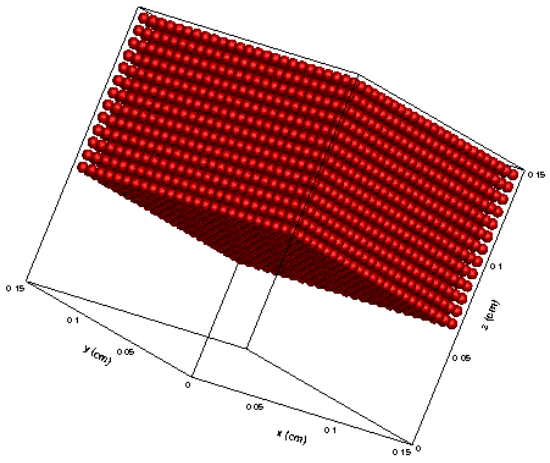

Figure 5.7: Positions of the 8125 particles at time $t = 0.0s$.

the fluid takes place mainly in the center. However, the three-dimensional particle-constructed pestle is too strong to break as shown in Figure 5.8 (b) and the fluid is pushed away to take a devious route (explained later in Figure 5.10). This observation is in line with the three-dimensional results reported by Robinson et al. [9] using Smoothed Particle Hydrodynamics (SPH)-DEM simulation. The discrepancy between two- and three-dimensional results is obviously due to the drawback of the two-dimensional assumption.

The following three-dimensional deposition processes show nearly opposite trend comparing with the two-dimensional case as shown in Figure 5.8 (c) and (d). In the two-dimensional case, a fluid hole is formed in the lower half of the cavity which is hugged by two particle arms, this typical phenomenon has been reported in several studies [6, 7, 8, 3]. However, in the three-dimensional case, it is more like a fluid hoop surrounding the particle pestle. The head of the pestle spreads out when it impacts on the bottom. The behavior is not difficult to understand because the successive falling particles keep moving downward and thus pushing on the head. At this time, the underriding of the particles becomes the dominating force in the system and most of the particles distribute in this center region.

Since the particle deposition velocities are very important for the efficiency of the final deposition and may lead to a non-uniform distribution on the bottom. Figure 5.9 displays the distributions of particle velocity along the $x-$direction before $10.0s$ where large discrepancy can be observed. It is shown that most of the veloci-

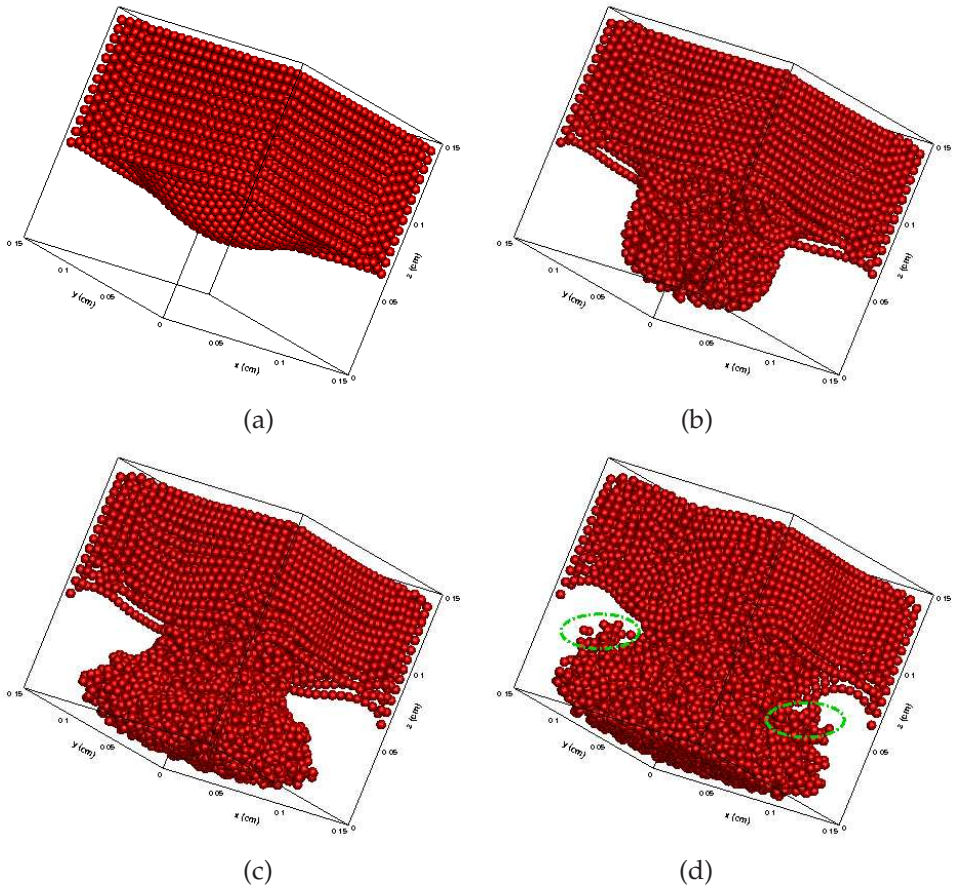

Figure 5.8: Positions of the 8125 particles at time (a) $t = 2.5s$, (b) $t = 5.0s$, (c) $t = 7.5s$, (d) $t = 10.0s$.

ties have negative signs and the larger deposition velocities concentrate in the center region. This finding is in line with the particle distribution patterns. Moreover, the magnitude of the deposition velocity increases with time until the particles impact on the bottom. It is also clearly seen that the majority of the velocities in the regions close to the side walls are positive due to the fact that the sucked fluid pushes the high particles up when the center particles sink down. This interesting FSI phenomenon can be clearly observed in Figure 5.10 where the instantaneous fluid velocity corresponding to Figure 5.9 is given. It is shown that the initial stagnant fluid is disturbed by

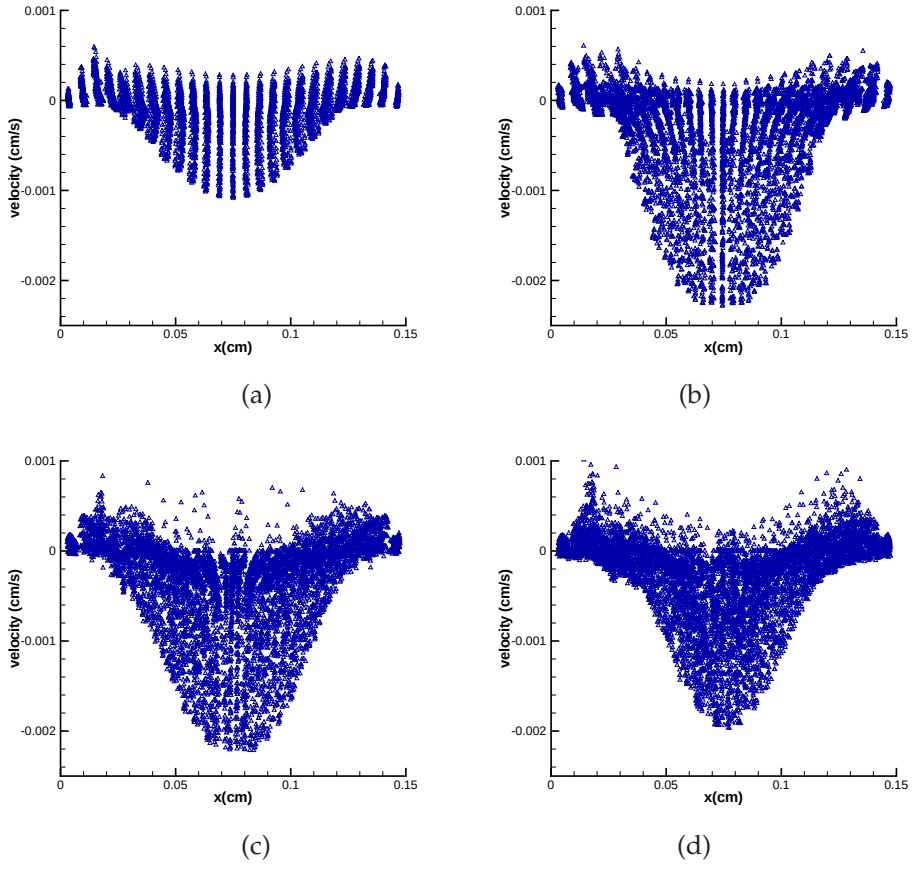

Figure 5.9: Particle deposition velocity along the $x-$direction at time (a) $t = 2.5s$, (b) $t = 5.0s$, (c) $t = 7.5s$, (d) $t = 10.0s$.

the particle motion and follows the trend of the solid particles. Two vortexes (hoop in three-dimensional geometry) are formed in the lower corners of the cavity and the fluid velocity near the side wall is upward. The vortexes are strong when the particle deposition velocities are large. As shown in Figure 5.9 (c) and (d), the particle deposition velocities begin to decrease after the particles reach the bottom, meanwhile the number of particles with positive velocities increases. These particles are risen by the vortexes and against the falling particles as shown in Figure 5.8 (d) highlighted by green ellipse. An overall distribution of the particle deposition velocities is given

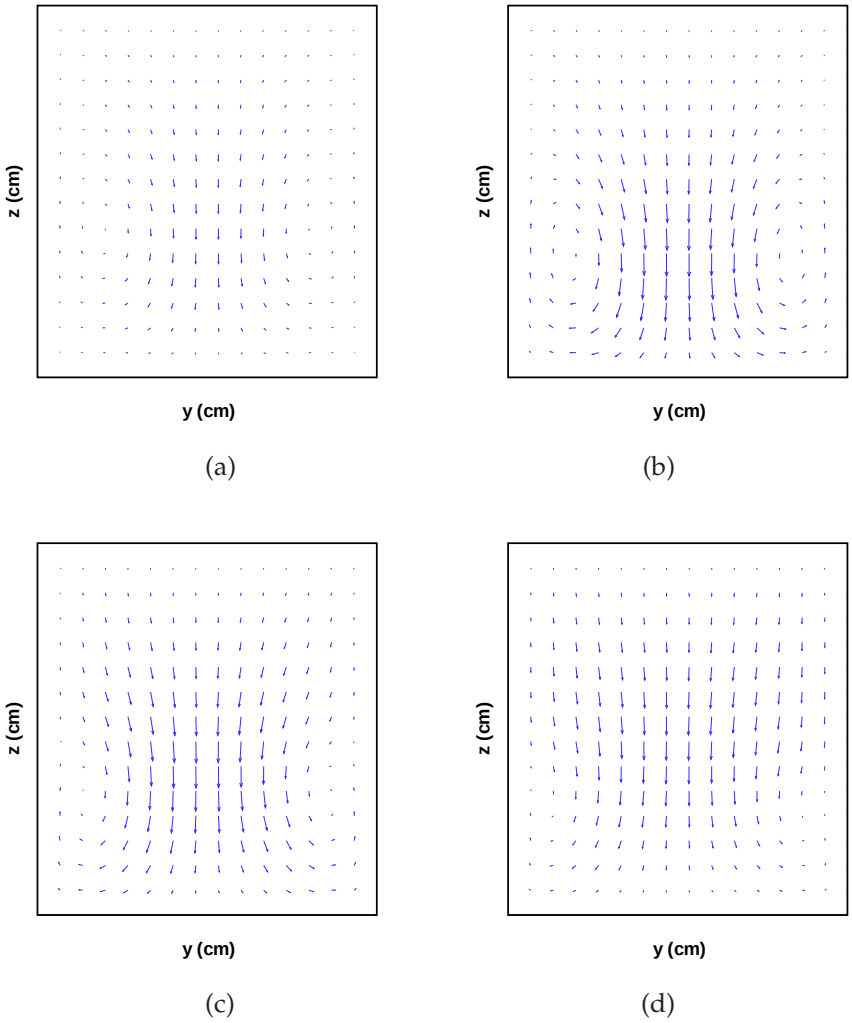

Figure 5.10: Instantaneous fluid velocity distribution on the mid-length slice at time (a) $t = 2.5s$, (b) $t = 5.0s$, (c) $t = 7.5s$, (d) $t = 10.0s$.

in Figure 5.11 in terms of mean values. Here, the whole bottom domain is divided by 30×30 squares and then the particles are mapped into the square that the particle

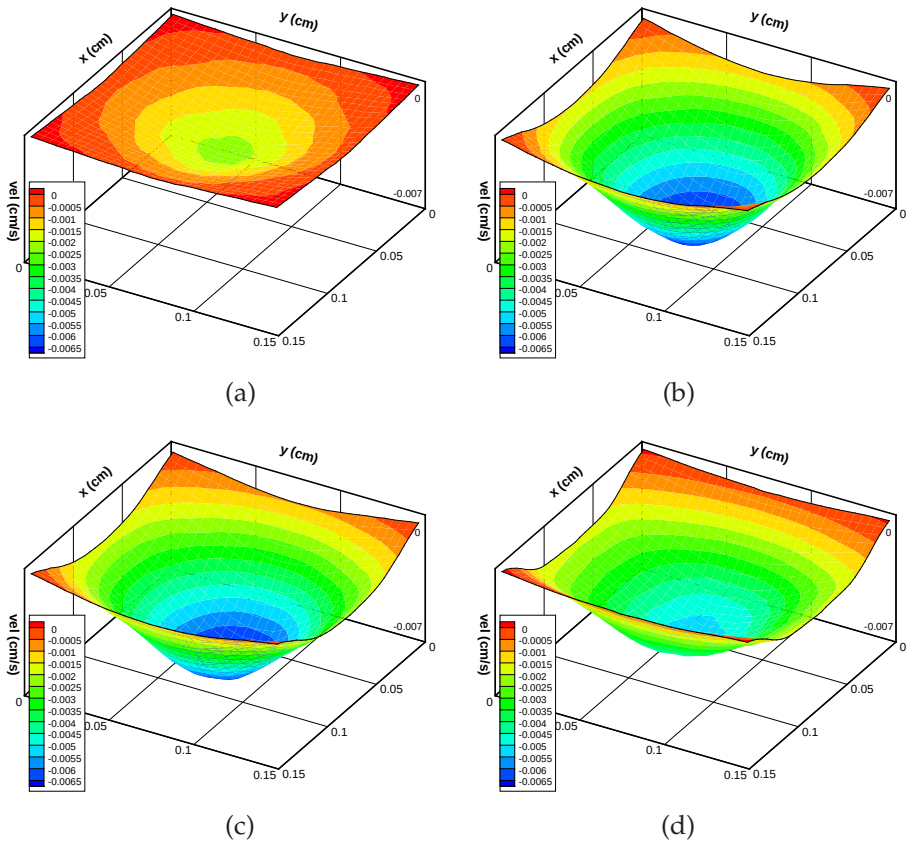

Figure 5.11: Overall distribution of the particle deposition velocity at time (a) $t = 2.5s$, (b) $t = 5.0s$, (c) $t = 7.5s$, (d) $t = 10.0s$.

center lies. The square holds the deposition velocity that mapped in it. If more than one particle is mapped into the same square, the arithmetic mean value will be employed. As shown, the mean velocities present a generally symmetrical distribution. The particles near the corners deposit significantly slower than the center as results of the fluid viscosity. The highly symmetrical distribution is broken when the particle contact with the bottom. However, a constant symmetrical distribution may not be expected due to the stochastic nature of the solid particles. From $t = 10.0s$, the collisions between the particles and particles/walls become the dominating force in the lower half of the cavity. The pestle slumps like an inverted cone and fills the

cavity bottom.

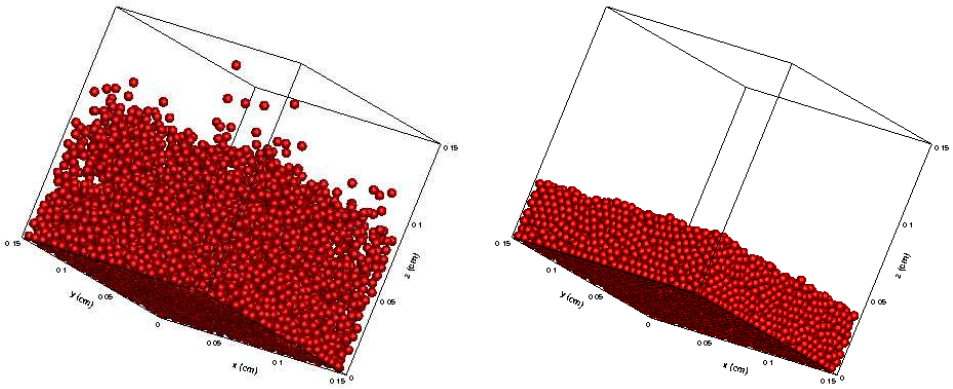

(a) (b)

Figure 5.12: (a) Positions of the 8125 particles at time $t = 50.0s$ and (b) the final distribution.

Figure 5.12 (a) and (b) display the later stages of the depositing process. In Figure 5.12 (a), the initially orderly arranged particles are totally disorganized and settle on the cavity bottom length by length.

Effect of the initial porosity

Particle number	Initial porosity	Solid fraction	Initial distribution
8125	0.719	0.15	$25 \times 25 \times 13$
5200	0.813	0.10	$20 \times 20 \times 13$
2925	0.888	0.056	$15 \times 15 \times 13$

Table 5.3: The settling velocities at different particle size.

It has been well known that the porosity can play an important role in the sedimentation of multi particles. Here, different numbers of particles were positioned in the same region as previous subsection. In other words, the particles would deposit with different initial porosity. The physical properties of the fluid and particles can be found in Table 5.2. The minimum particle height was monitored to characterize the sedimentation efficiency. The parameters relevant to these simulations are listed in Table. 5.3.

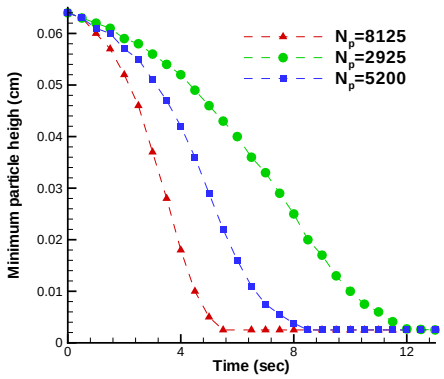

Figure 5.13: Minimum particle height versus time at different initial porosity.

Figure 5.13 shows the minimum particle height versus time with different initial porosity. It can be seen that the sedimentation efficiency increases with the decrease of the initial porosity even identical particles were used, this finding is consistent with the analytical results from Robinson et al. [9]. Moreover, a significant deceleration of settling velocity can be observed when the lowest particles approach to the cavity bottom, this phenomenon has also been reported in [8] and [3] .

Effect of the particle number on the total computational cost

At last, for the sake of examining the effect of the particle number (the number of the Lagrangian point in conventional IBM) on the total computational cost, several simulations were carried out with different particle number. As shown in Figure 5.14, the total computational cost increases almost linearly with the particle number and the slope is even larger when the particle number increases from 6000 to 8000. It is worthwhile mentioning that Figure 5.14 was obtained when there are no particle collisions in the system. We also tested the computing time of each part of the solver in above 8125 particle simulation at time $t = 30.0s$, we found that the calculation of the fluid-particle interaction force spends about 84.4% of total simulation time in one time step and the total particle collision number is 6610. Therefore, we come to a conclusion that the total computational cost can be significantly reduced by decreasing the number of the Lagrangian point. Comparing with the conventional LBM-IBM-DEM [3], dozens of times (divided by N_{LP}) speedup can be expected in two-dimensional simulation and hundreds of times in three-dimensional simulation under the same particle and mesh number. However, it is worthwhile mentioning

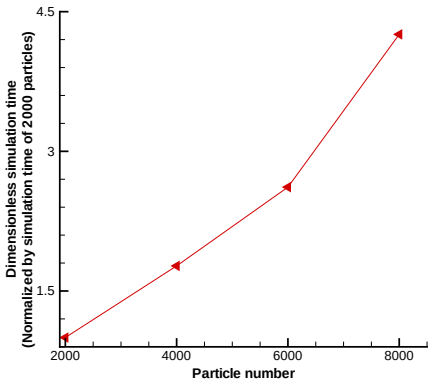

Figure 5.14: Particle number versus the computational time in one time step.

that this conclusion is reached only from a computational efficiency point of view. For a certain problem with large range of sizes of particles, a hybrid IBM-PIBM may be needed to achieve high performance calculation which will be discussed in next subsection.

Overall, the main findings of the two- and three-dimensional simulations are summarized as follows: The patterns observed in the two-dimensional simulation are close to the results provided in former references [6, 7, 8, 3]. However, the three-dimensional results show large discrepancy with the two-dimensional results which is most probably due to the two-dimensional assumption. Imaging a case in a enclosed container like a fluidization bed, the fluid is unpenetrable into a two-dimensional well-packed particle bed without breaking the compact structure, whereas penetration into a three-dimensional bed is somehow possible because the geometry is much more polyporous and complex.

Hybrid IBM-PIBM modeling

It is common to encounter a system containing various sizes of particles. A multi-scale analysis is preferred when the size range is large. If all the particles are treated using the conventional IBM, the number of grids required to construct the finest particle would make the whole simulation too expensive. On the contrary, if all the coupling work is carried out based on the PIBM, the grid required to embody the largest particle would be too coarse to accurately reflect the fluid flow. A more frequently encountered requirement is to build the complex boundaries or irregular elements using IBM. In other words, a hybrid IBM-PIBM method is needed. Using a simply

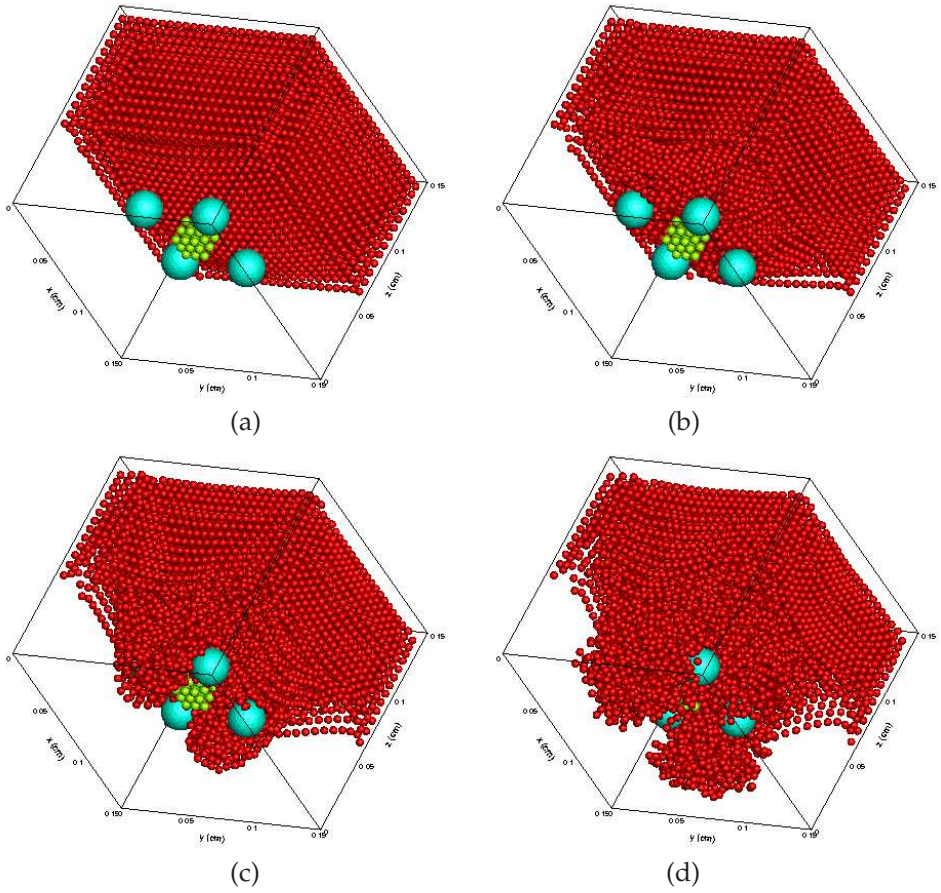

Figure 5.15: Positions of the 8125 particles with obstacles at time (a) $t = 2.5.0s$, (b) $t = 5.0s$, (c) $t = 7.5s$, (d) $t = 10.0s$.

sample as shown in Figure 5.12, the advantage of this mixed approach can be seen where five stationary obstacles are fixed below the particles (four large particles and one cube consisting of 27 small particles). The four large particles are established using the conventional IBM while the rest, including the 27 particle for the cube, are treated using PIBM. The criterion to choose different methods is the ratio between the particle size and the lattice spacing. In general, the grid size can be specified at 10 times the particle sizes in the Eulerian-Eulerian model [10] and about 5 times in the Eulerian-Lagrangian model based on NS-DEM [5]. However, the results from

current study indicate that the ratio can be 2 in LBM-PIBM-DEM though the optimal ratio is still in question.

5.3 Concluding remarks

A PIBM for simulating the particulate flow in fluid was presented. Compared with the conventional momentum exchange-based IBM, no artificial parameters are introduced and the implementation is simpler. The PIBM is more suitable for simulating the motion of a large number of particles in fluid, particularly in the three-dimensional cases where particle collisions dominate. Dozens of times speedup can be expected in two-dimensional simulation and hundreds of times in three-dimensional simulation under the same particle and mesh number.

Numerical simulations were carried out based on the LBM-PIBM-DEM scheme, our result of falling of single particle reveals that the settling velocity predicted by numerical simulation agrees well with the Stokes' law. Further multi-particle simulation results confirm that the LBM-PIBM-DEM scheme can capture the feature of the particulate flows in fluid and is a promising strategy for the solution of the particle-fluid interaction problems. By comparing two- and three-dimensional results, essential discrepancy was found due to the drawback of the two-dimensional assumption. Therefore, it can be concluded that the two-dimensional simulations may be good as a first and cheaper approach, the three-dimensional simulations are necessary for an accurate description of the particle behaviors as well as the flow patterns. From our three-dimensional results by PIBM, the sedimentation efficiency of particle is found to increase with the decrease of the initial porosity.

Due to the fact that the calculation of the fluid-particle interaction force in the PIBM is simply based on the momentum conservation of the fluid particle, the LBM-PIBM-DEM scheme can be easily connected with other CFD solvers or Lagrangian particle tracking method where the conventional IBM works, e.g. with the direct numerical simulation [4]. However, during the simulations, we found that numerical instability may occur when the particle velocity is high, which seems to be a general weakness of the IBM family methods. For the sake of achieving validate results, the PIBM users are recommended to conduct a simplified case to compare with the analytical solutions/experimental observation to tune the LBM relaxation time, τ, before using it in the multi-particle simulations. This practice is competent and has been widely used in LBM-DEM [8, 11] and other simulations based on DEM [12, 13].

References

[1] J. Wu and C. Shu. An improved immersed boundary-lattice Boltzmann method for simulating three-dimensional incompressible flows . *Journal of Computational Physics*, 229(13):5022 – 5042, 2010.

[2] YH Qian, Dominique d'Humières, and Pierre Lallemand. Lattice bgk models for navier-stokes equation. *EPL (Europhysics Letters)*, 17(6):479, 1992.

[3] H. Zhang, Y. Tan, S. Shu, X. Niu, X. Trias, D. Yang, H. Li, and Y. Sheng. Numerical investigation on the role of discrete element method in combined lbm ibm dem modelling. *Computers Fluids*, 2014.

[4] Zhi-Gang Feng, Miguel Enrique Cortina Ponton, Efstathios E. Michaelides, and Shaolin Mao. Using the direct numerical simulation to compute the slip boundary condition of the solid phase in two-fluid model simulations. *Powder Technology*, (0):–, 2014.

[5] KD Kafui, C Thornton, and MJ Adams. Discrete particle-continuum fluid modelling of gas–solid fluidised beds. *Chemical Engineering Science*, 57(13):2395–2410, 2002.

[6] Roland Glowinski, T-W Pan, Todd I Hesla, and Daniel D Joseph. A distributed lagrange multiplier/fictitious domain method for particulate flows. *International Journal of Multiphase Flow*, 25(5):755–794, 1999.

[7] Zhi-Gang Feng and Efstathios E Michaelides. The immersed boundary-lattice Boltzmann method for solving fluid-particles interaction problems. *Journal of Computational Physics*, 195(2):602 – 628, 2004.

[8] Zhi-Gang Feng and Efstathios E. Michaelides. Proteus: a direct forcing method in the simulations of particulate flows. *Journal of Computational Physics*, 202(1):20 – 51, 2005.

[9] Martin Robinson, Marco Ramaioli, and Stefan Luding. Fluid-particle flow simulations using two-way-coupled mesoscale SPH-DEM and validation. *International Journal of Multiphase Flow*, 59(0):121 – 134, 2014.

[10] Schalk Cloete, Shahriar Amini, and Stein Tore Johansen. A fine resolution parametric study on the numerical simulation of gas–solid flows in a periodic riser section. *Powder Technology*, 205(1):103–111, 2011.

[11] Zhi-Gang Feng and Efstathios E Michaelides. Robust treatment of no-slip boundary condition and velocity updating for the lattice-Boltzmann simulation of particulate flows. *Computers & Fluids*, 38(2):370–381, 2009.

[12] Yuanqiang Tan, Dongmin Yang, and Y. Sheng. Study of polycrystalline Al2O3 machining cracks using discrete element method. *International Journal of Machine Tools and Manufacture*, 48(9):975 – 982, 2008.

[13] Yuanqiang Tan, Dongmin Yang, and Yong Sheng. Discrete element method (DEM) modeling of fracture and damage in the machining process of polycrystalline SiC. *Journal of the European Ceramic Society*, 29(6):1029 – 1037, 2009.

Chapter 6

Numerical investigation of the wear process on the pipe wall in particle transportation

Part of the contents of this chapter have been published as:

H Zhang, Y Tan, D Yang, FX Trias, S Jiang, Y Sheng. A Oliva Numerical investigation of the location of maximum erosive wear damage in elbow: effect of slurry velocity, bend orientation and angle of elbow. *Powder Technology. 217(2012),467-476.*

Y Tan, ***H Zhang***, D Yang, S Jiang, J Song, Y Sheng. Numerical simulation of concrete pumping process and investigation of wear mechanism of the pipe wall. *Tribology International, 46(2012), 137-144.*

Abstract.

In this chapter, a coupling model of CFD and DEM, has been developed to study the solid-fluid multiphase flow problem in concrete pumping progress. The kinematics and trajectory of the discrete particles as well as the particle-particle interaction were predicted by DEM while the motion of the continuous fluid phase was evaluated by a Navier-Stokes solver, and a pressure gradient force model was adopted to calculate the solid-fluid interaction force. A case of pneumatic conveying was utilized to demonstrate the capability of the coupling model. The concrete pumping process was then simulated, where the hydraulic pressure and velocity distribution of the fluid phase were obtained, high and low pressure domain have been identified with the highest pressure occurring at the outer wall and the lowest pressure occurring at the inner wall of the elbow. The frequency of the particles impacting on the bended pipe was monitored, a new time average collision intensity model based on impact force has been proposed to investigate the wear mechanism of the elbow, the location of maximum erosive

wear damage in elbow was predicted. Furthermore, the influences of slurry velocity, bend orientation and angle of elbow on the puncture point location were discussed. It is found that the present multi-phase coupling model can predict the wear behavior of the bended pipe accurately and consequently, provide an effective guidance for the design of concrete pumping pipe.

6.1 Equations of slurry motion

The continuity and momentum equations in the fluid are based on local mean variables as derived by Anderson and Jackson [1]

$$\frac{\partial(\epsilon\rho_f)}{\partial t} + \nabla\cdot(\epsilon\rho_f u_f) = 0 \tag{6.1}$$

$$\frac{\partial(\epsilon\rho_f u_f)}{\partial t} + \nabla\cdot(\epsilon\rho_f u_f \otimes u_f) = \nabla\xi_f + \epsilon\rho_f g - F_{fp} \tag{6.2}$$

where u and ρ_f are the fluid velocity and density, respectively; ϵ is the porosity, F_{fp} is the fluid-particle interaction force in each fluid cell, which is obtained by summing up the fluid forces f_{fpi} given in Eq. 6.5; The total local average stress tensor, ξ_f, can be written as

$$\xi_f = -p\delta + \tau_f \tag{6.3}$$

where p is the fluid pressure, δ is the identity tensor and τ_f is the viscous stress which can be written as follows:

$$\tau_f = ((\mu_b - \frac{2}{3}\mu_s)\nabla u_f)\delta + \mu_s((\nabla u_f) + (\nabla u_f)^{-1}) \tag{6.4}$$

μ_b and μ_s are the bulk and shear viscosity, respectively.

6.2 The fluid-particle interaction force

6.2.1 Two models for the coupling force

The coupling term between the particles and the fluid is the fluid-particle interaction force per unit volume F_{fp} which is obtained by summing up the fluid forces in a fluid computational cell and dividing by the volume of the fluid element ΔV_e:

$$F_{fp} = \frac{\Sigma_{i=1}^{n} f_{fpi}}{\Delta V_e} \tag{6.5}$$

where n is the number of particles in one cell, f_{fpi} is the interaction force between fluid and the ith particle in the fluid cell, f_{fpi} can be written as the sum of a component due to macroscopic variations in the fluid stress tensor, ξ_f , and a component, ϵf_{di} , due to detailed variations of the point stress tensor in the fluid flow field around the particle:

$$f_{fpi} = v_{pi}\nabla\xi_f + \epsilon f_{di} \tag{6.6}$$

where v_{pi} is the volume of particle i, ϵf_{di} can be regarded as the product of experimentally based correlations and the local porosity ϵ. Substituting Eq. 6.3 into Eq. 6.6 leads to the following expression for f_{fpi}

$$f_{fpi} = -v_{pi}\nabla p + v_{pi}\nabla\tau_f + n\epsilon f_{di} \tag{6.7}$$

By substituting for fpi f in Eq. 6.5 using Eq. 6.7, the fluid-solid interaction force F_{fp} can be written as

$$F_{fp} = -(1-\epsilon)\nabla p + (1-\epsilon)\nabla\tau_f + n\epsilon f_{di} \tag{6.8}$$

where $n = n_c/\Delta V_e$ is the number of particles per unit volume of fluid. Substituting for ξ_f and F_{fp} using Eq. 6.3 and Eq. 6.8 respectively leads to the final expression of the fluid momentum equation as

$$\frac{\partial(\epsilon\rho_f u_f)}{\partial t} + \nabla\cdot(\epsilon\rho_f u_f \otimes u_f) = -\nabla p + \nabla\cdot\tau_f + (1-\epsilon)\nabla p - n\epsilon f_{di} + \epsilon\rho_f g \tag{6.9}$$

Eq. 6.1 and Eq. 6.9 form a new set of Navier-Stokes equations. Gidaspow [2] proposed two numerical models to solve the new set the equations, namely Model A (The pressure gradient force model) and Model A (the fluid density-based buoyancy model):
Model A:

$$\frac{\partial(\epsilon\rho_f)}{\partial t} + \nabla\cdot(\epsilon\rho_f u_f) = 0 \tag{6.10}$$

$$\frac{\partial(\epsilon\rho_f u_f)}{\partial t} + \nabla\cdot(\epsilon\rho_f u_f \otimes u_f) = -\epsilon\nabla p + \nabla\cdot(\epsilon\tau_f) + \epsilon\rho_f g - F^A_{pf} \tag{6.11}$$

Model B:

$$\frac{\partial(\epsilon\rho_f)}{\partial t} + \nabla\cdot(\epsilon\rho_f u_f) = 0 \tag{6.12}$$

$$\frac{\partial(\epsilon\rho_f u_f)}{\partial t} + \nabla\cdot(\epsilon\rho_f u_f \otimes u_f) = -\nabla p + \nabla\cdot(\epsilon\tau_f) + \epsilon\rho_f g - F^B_{pf} \tag{6.13}$$

the relationship between the source terms of the two forms follows

$$F^B_{pf} = F^A_{pf}/\epsilon - \epsilon\rho_f g \tag{6.14}$$

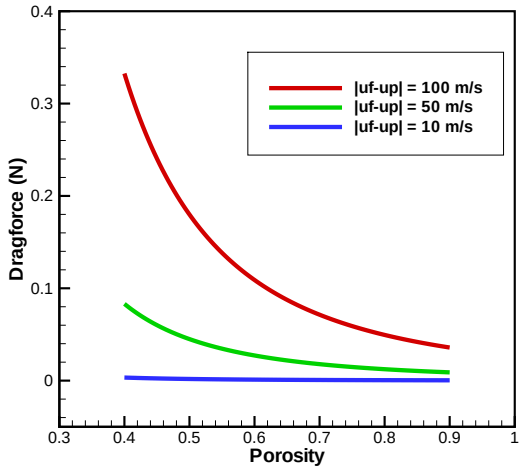

Figure 6.1: Drag forces acting on a 4 mm diameter particle as predicted using a combination of the Ergun [3] and Wen and Yu [4] correlations compared with the predictions from the Di Felice [5] correlation for a range of porosities at three superficial slip velocities

6.2.2 The drag force

Di Felice [5], using an empirical fit to a wide range of fixed and suspended-particle systems covering the full practical range of flow regimes and particle porosities, proposed a single-function correlation for the drag force on a particle of diameter d_p in a multi-particle system. In this formulation,

$$f_{di} = 0.5\rho_f A_p C_D |u_f - u_p|(u_f - u_p)\epsilon^{1-\chi} \tag{6.15}$$

where A_p is the projected area of particle $A_p = 0.25\pi d_p^2$, d_p is the particle diameter, the porosity function $\epsilon^{1-\chi}$ corrects for the presence of other particles. A dependence of this function on the flow is incorporated in the relation for χ

$$\chi = 3.7 - 0.65exp[-\frac{(1.5 - log_{10}Re_p)^2}{2}] \tag{6.16}$$

the drag coefficient in Eq. 6.21 is

$$C_D = (0.63 + 4.8/Re_p^{0.5})^2 \tag{6.17}$$

the particle Reynolds number is given by

$$Re_p = |u_f - u_p| d_p \epsilon / \mu_s \tag{6.18}$$

A combination of the Ergun [3] and Wen and Yu [4] correlations is often used in the literature for evaluating drag forces in 'dense' and 'dilute' regimes of the fluidised bed where a void fraction of 0.8 is adopted as the boundary between these two regimes.

$$f_{di} = \beta_{pf}(u_f - u_p)/\rho_f \tag{6.19}$$

when $\epsilon \leq 0.8$

$$\beta_{pf} = 150\frac{(1-\epsilon)^2}{\epsilon}\frac{\mu_s}{(\phi_p d_p)^2} + 1.75(1-\epsilon)\frac{\mu_s}{(\phi_p d_p)}|u_f - u_p| \tag{6.20}$$

when $\epsilon > 0.8$

$$\beta_{pf} = \frac{3}{4}C_D\frac{|u_f - u_p|\rho_f(1-\epsilon)}{d_p}\epsilon^{-2.7} \tag{6.21}$$

Fig.6.1 shows a comparison of the calculated drag forces on a 4 mm diameter particle as a function of the void fraction for three superficial slip velocities using the Ergun [3] and Wen and Yu [4] correlation and the Di Felic [5]. The step change inherent in the calculated drag forces from the former correlation at a void fraction of 0.8 is not acceptable from a numerical point of view and therefore the continuous single-function Di Felice [5] correlation is employed in this study.

6.3 DEM: The linear model

The motion of particles can be determined by Newton's equation of motion:

$$ma + \beta v = mg + F_{fp} + F_c \tag{6.22}$$

$$I\frac{\partial^2\theta}{\partial t^2} + \beta\omega = \tau_c \tag{6.23}$$

where m and I are respectively the mass and the moment of inertia of the particle, a is the acceleration, β is the damping coefficient, v is the velocity, θ is the angular displacement, β is the angular velocity, g is the acceleration of gravity if considered, F_c, F_{fp} and τ_c are collision force, the fluid-particle interaction force and moment of force

respectively. In this chapter, each particle, assumed to be spherical, is represented by a discrete element, a linear model is used for the normal contact between a contact pair as follow:

$$F_c = (-k_n\delta - \eta_{ni}Gn)n \tag{6.24}$$

where δ is the overlap in normal direction, G is the relative velocity between particle i and j: $G = v_i - v_j$, n is a vector from particle i to particle j, k_n and η_{ni} are the damping coefficient in normal and tangential direction, respectively.

6.4 Simulation condition

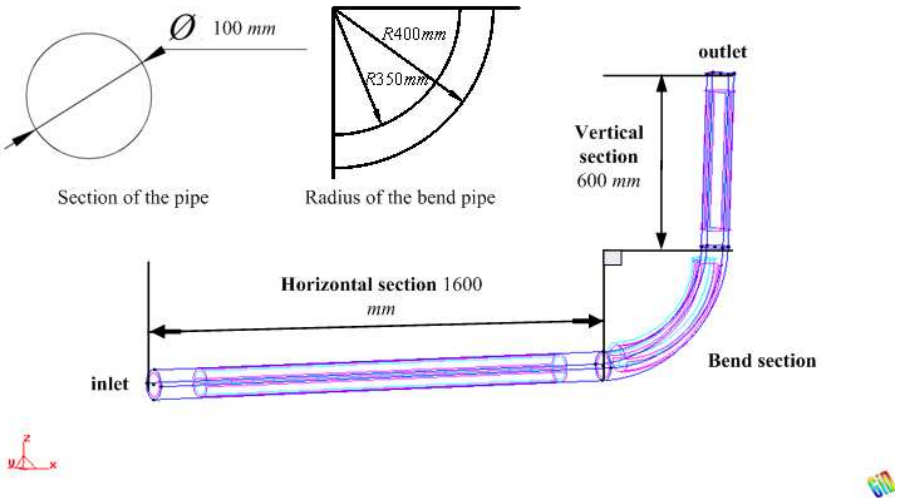

Figure 6.2: Diagram of the computational domain defined in current study

Pneumatic conveying was widely used in process industries to efficiently transport granular materials of different types, and bends are the most common set-ups for various problems, many experimental investigations were based on this configuration [6, 7, 8]. For the sake of demonstrating the capability of the current coupling scheme for investigating multi-phase flow, a pneumatic conveying simulation was conducted. Both the pneumatic conveying and later concrete pumping simulations were performed in the same bend as shown in Figure 6.2, the configuration is mainly

Phase	Density (kg/m^3)	Diameter of particle (m)
gas	1.189	–
solid	2000	0.002

Table 6.1: parameters of material content of pneumatic conveying.

Phase	Density (kg/m^3)	Diameter of particle (m)	volume fraction
gas	1.189	–	25%
solid (small)	2960	0.002	49%
solid (big)	2960	0.015	26%

Table 6.2: parameters of material content of concrete pumping.

similar with the experiments of Lee at al. [7] while the diameter of pipe is bigger in this study. The length of the horizontal pipe is 1.6 m , the length of the vertical pipe is 0.6 m , and the bend section is about 0.628 m , the diameter of the pipe is 0.1 m . The position of particles at the inlet was generated in such a way that in the bottom of the horizontal pipe, initially, the particles will have the same velocity with the fluid surrounded them, 6 m/s , the parameter of velocity is taken from Zhao [9] which is smaller than that used in the experiments [6, 7, 8]. The flow conditions in these two cases are shown in Table 6.1 and Table 6.2, respectively.

Collocated grid was used to arrange fluid variables in center of a fluid computational cell, and the whole computational domain is divided by 2000 structured hexahedron CFD cells, Patankar's SIMPLE algorithm [10] was adopted to compensate the pressure and velocity to satisfy the law of conservation of mass. It should be note that with this type of fluid-solid interaction problem, we have to accept a relatively coarse fluid grid because the particle must be small compared to the grid size, for good results, several particles should be fit inside one CFD element:

$$\frac{\Delta x_e}{d_{pi}} > 5 \tag{6.25}$$

Δx_e is the fluid element length. Trial simulations showed that finer fluid grids do not result in any noticeable change in the simulation results.

6.5 Results and discussion

6.5.1 Pneumatic conveying simulation

Roping is the most notable feature in the fluid-solid flow in bends and characterized by the phenomenon that most of the particles are close to the outer wall of the bend

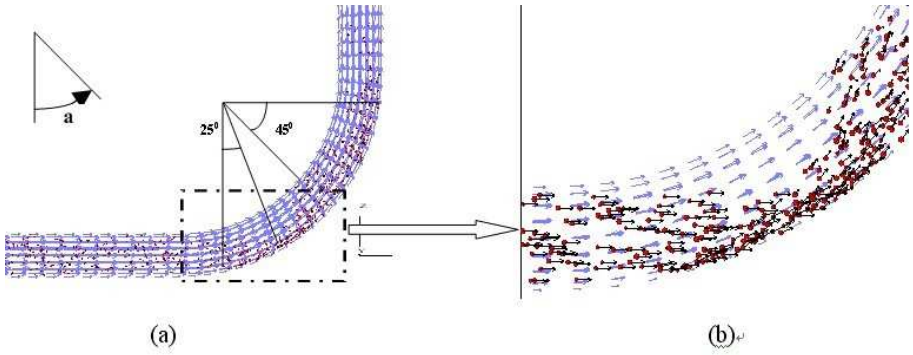

Figure 6.3: Spatial distribution of (a) particles near the elbow and (b) zoomed view of that.

and there are fewer particles close to the inner wall. It has been extensively studied in the literature since it causes segregation and uneven feeding [8, 11]. As shown in Fig. 6.3, this phenomenon has been captured in this study, particles from the horizontal inlet pipe impact on the outer wall of the bend when they enter the elbow, a rope is formed because of the collisions between particles and between particles and wall. Particles are found bounced back to the inner wall. It is indicated that the interactions between particles and between particles and wall play important roles in the particle distribution in pneumatic conveying. Fig. 6.3 also shows that the maximum particle concentration was at approximately 45^o of the inner wall and 25^o of the outer wall, this was demonstrated by the max impact force distribution of on the elbow as shown in Fig. 6.4 the trend has a good agreement with the experimental results [7, 8], qualitatively. However, the location of concentration mainly depends on the bend radius, Yilmaz [12] observed that a rope can disperse quicker in a sharp bend than in a smooth bend. Because the conditions for the present simulation and the experimental work in the literature are not exactly the same, the analysis is mainly qualitative.

6.5.2 Concrete pumping simulation: The standard case

Damage of fluid handling equipment due to erosive wear can cause significant operation problems, the reduced wall thickness can no longer withstand the operating pressure that they were original designed for and may cause premature failure of the system components, so it's critical to understand the hydro-pressure distribution in the pipeline. The wall contour plot of the hydraulic pressure is shown in Fig. 6.5, it can be seen that the pressure is generally higher along the extrados compared to the

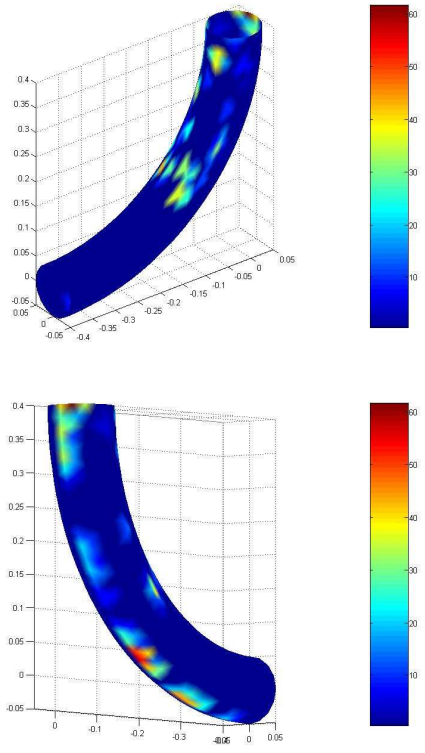

Figure 6.4: The max impact force distribution of the elbow from (a) the top and (b) the bottom.

intrados. In this point of view, the reliability problem mainly occurs at the outer wall of the elbow due to the high pressure loading.

The velocity magnitude distribution on a plane across the middle of the computational domain is shown in Fig. 6.6, it can be seen that as the flow approaches the elbow, it significantly accelerates along the intrados while decelerates along the extrados due to the favorable pressure gradient (Fig. 6.5), the effect of the presence of particles on fluid velocity is not discussed in this study. Fig. 6.7 shows the spatial distribution of the particles at the bend, from a comparison of Fig. 6.3 and Fig. 6.7 it can be seen that the rope in concrete pumping process disperses much more slower than that in the pneumatic conveying. Also particle segregation in the concrete pumping process is more obvious. This phenomena was discussed by Yilmaz and Levy [12]

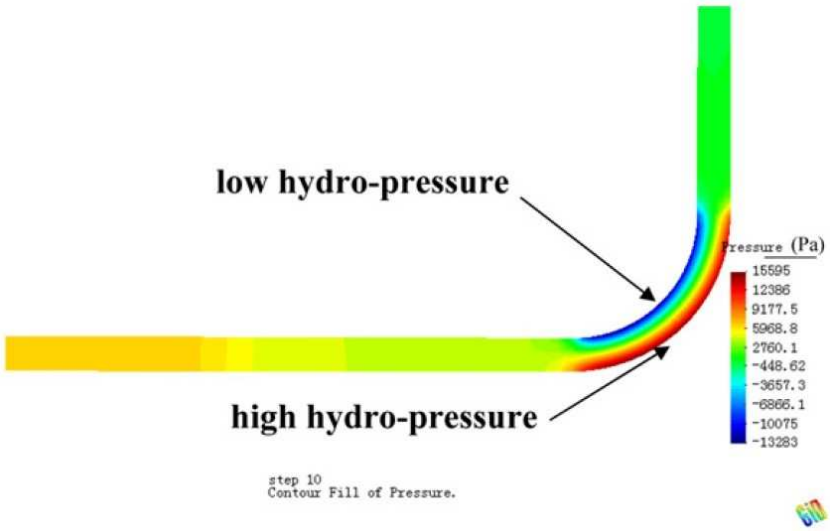

Figure 6.5: Hydraulic pressure distribution profile.

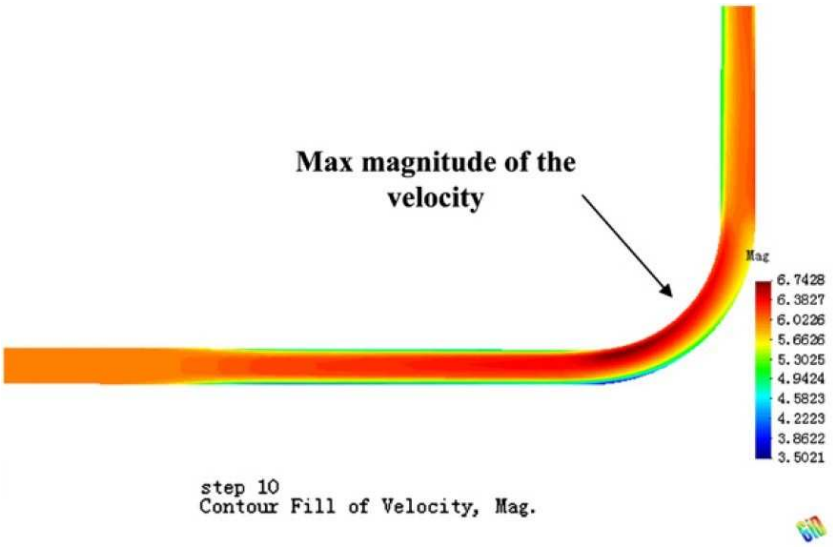

Figure 6.6: Velocity magnitude distribution profile of the particle-free slurry.

who observed that a rope can disperse quicker in a sharp bend than in a smooth bend. However, in this study, the difference can be attributed to the difference of density of the fluid phase, which dominates the fluid-solid drag force. The particles in Fig. 6.7 follow the flow motion well due to that the bounce-back force is not large enough to conquer the drag force acted on particles from the fluid slurry, so the interactions between particles or between particles and wall do not influence the particle distribution as much as in pneumatic conveying. It can be also seen from Fig. 6.7 that large particles (red) are close to the outer wall while only some small ones (black) bouncing towards the inner wall in the elbow.

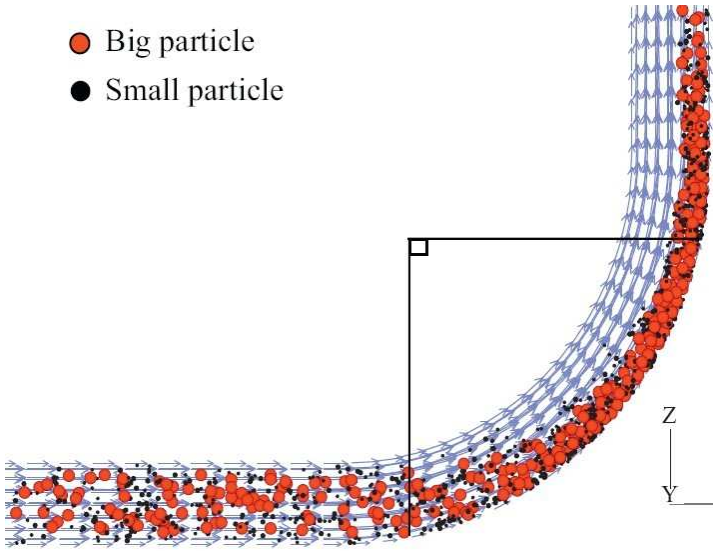

Figure 6.7: Spatial distribution of the particles in the bend.

The spatial porosity distribution in the elbow at different time is shown in Fig. 6.8, where small porosity assuredly means presence of the particles. From Fig. 6.8(a) it can be seen that the concentration of particles in the horizontal pipe are not totally uniform, the concentration of particles near the pipe wall is higher than that at the centerline because the velocity of slurry near the pipe wall is lower, it is found in the pneumatic conveying simulation that some particles were trapped beside the wall. From Fig. 6.8(b-d) it can be seen that a obvious rope is formed and the rope is unsteady since the position of maximum particle concentration change with time, the maximum concentration is always close to the outer wall, this is different from that observed in pneumatic conveying [8]. It is expected that outer wall of the elbow would suffer severer friction more continually than that in pneumatic conveying.

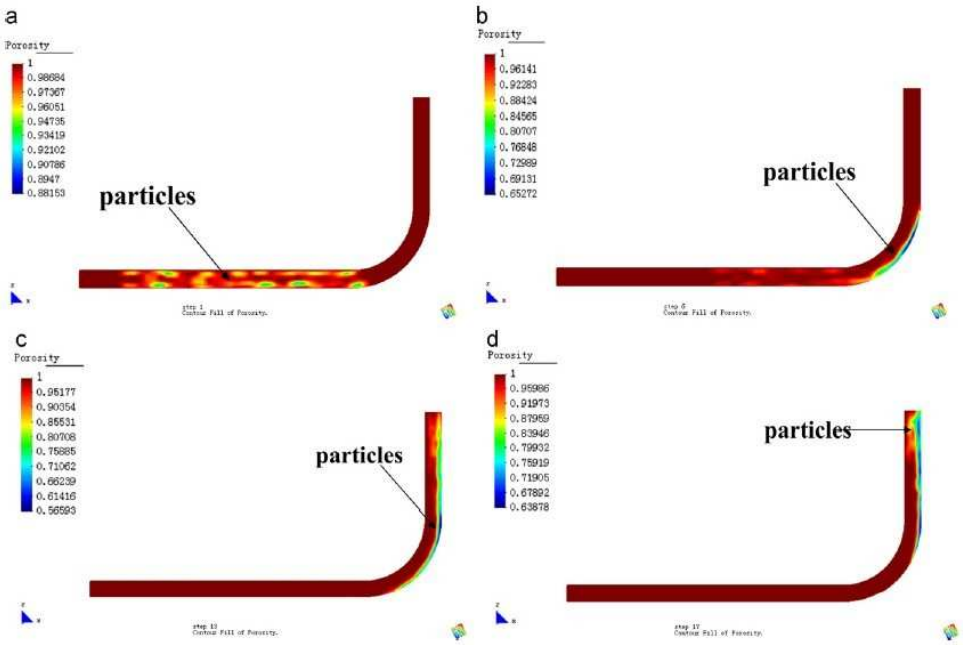

Figure 6.8: Spatial distribution of the rate of the fluid phase in the elbow at different time.

Fig. 6.9(a) and (b) shows the instantaneous spatial distribution of the porosity and fluid-particle interaction force at 0.2 s. As shown in Fig. 6.9(a), a rope is formed in the elbow and the particle segregation is very obvious. The fluid-particle interaction force (shown in Fig. 6.9 (b)) reaches its maximum in the region of highest particle concentration. This can be explained as follows according to Eq. 6.21: (i) The porosity is small in this region where the particles concentrated, the drag force on a particle is large when the porosity is low, the relationship between porosity and drag force has been summarized by Kafui et al. in [13]. (ii) The relative velocity between the two phases is large in this region, the drag force on a particle is large when the relative velocity between the phases is large. The large relative velocity is due to two aspects. On one hand, the friction between the particles and wall decelerates the velocity of the particles; on the other hand, collisions take place most frequently in this region, particles may stay or even bounced back caused by the collisions between particles.

The distribution of average force and the max impact force is shown in Fig. 6.10, from both Fig. 6.10 (a) and Fig. 6.10 (b), the maximum erosions are observed at 30^o 40^o of the outer wall. Due to maximum flow velocity at the centerline of the pipe,

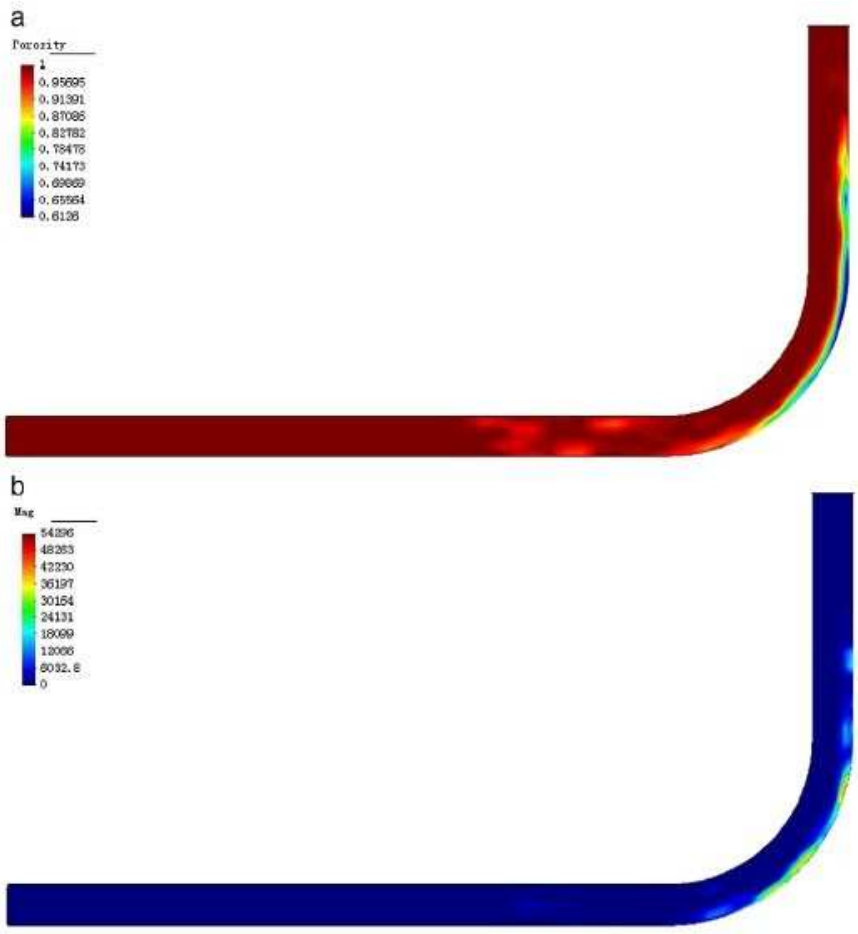

Figure 6.9: Spatial distribution of (a) porosity and (b) fluid-particle interaction force at 0.2 s.

the Fig. 6.11 The destroyed pipe corresponding impact velocity at the centerline of the pipe is also maximum. This caused the maximum erosion near the intersection of inlet flow centerline and surface of the outer radius of the elbow. In this study, the centerline of inlet flow intersects the outer wall of the elbow at approximately 25^o (Fig. 6.3). The location of maximum erosive wear damage is approximately 10^o downstream from 25^o, this is due to the fluid drag force. The computational results of the spatial distribution of elbow have also been compared with real-life destroyed

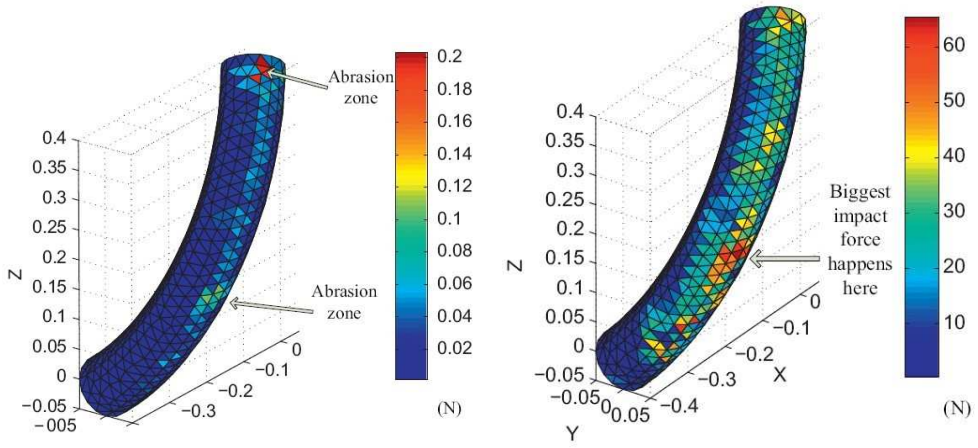

Figure 6.10: (a) average impact intensity distribution and (b) the max impact force distribution of the elbow from the bottom view.

pipe as shown in Fig. 6.11. It can be seen that they agree with each other well. The simulation results show that the frequency of collisions and the magnitude of the particle-wall interaction are important parameters for piping wall erosion prediction, synchronously our results demonstrate the capability of the coupling strategy for concrete pumping investigation.

Fig. 6.12 (a) and Fig. 6.12 (b) show the average impact intensity and max impact force distribution along the outer wall of the elbow at different azimuthal angles. The maximum average force is observed at 40^o and 89^o, the max impact force is observed at 20^o and 40^o.

6.5.3 Effect of the slurry velocity on the puncture point location

In this section, to study the effect of the slurry velocities on the puncture point location, simulations were conducted by changing the slurry velocities while leaving other parameters same as those in the standard case. Fig. 6.13 illustrates the maximum impact force distribution on the elbow at different slurry velocities when the gravity action is ignored. Fig. 6.13(a) shows the maximum impact force distribution when the slurry velocity is 6 m/s , it can be seen that the maximum erosive location is observed at approximately 42^o of the outer wall (degrees are defined in Fig. 6.16(a)). Due to the maximum flow velocity is at the centerline of the pipe, the corresponding impact velocity at the centerline of the pipe is also maximum. This causes the maximum erosion near the intersection of the inlet flow centerline and the surface

Figure 6.11: The destroyed pipe.

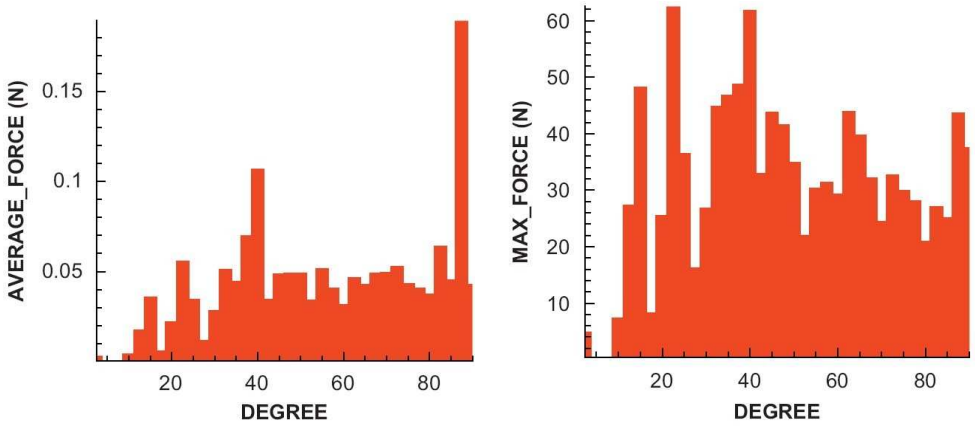

Figure 6.12: (a) average impact intensity distribution and (b) the max impact force distribution of the elbow from the bottom view.

of the outer radius of the elbow. In this study, the centerline of inlet flow intersects the outer wall of the elbow at approximately 25^o. When the slurry velocity increases

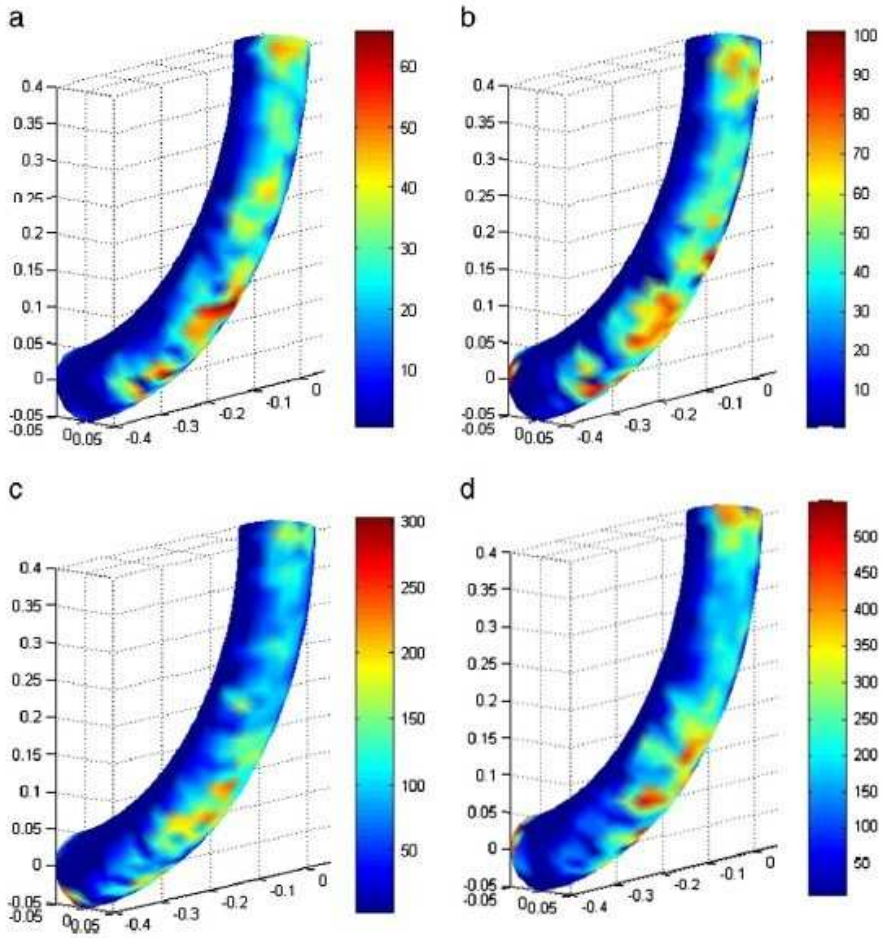

Figure 6.13: The maximum impact force (N) distribution of the elbow from the bottom view at slurry velocity: $(a)6m/s; (b)9m/s; (c)18m/s; (d)36m/s$.

from 6 m/s to 9 m/s, 18 m/s and 36 m/s, it is found in Fig. 6.13(b), (c) and (d) that the maximum erosive location does not change very much. For example, Fig. 6.13(d) shows the maximum erosion at approximately 47^o which is 42^o downstream from the puncture point of the standard case as shown in Fig. 6.13(a). But when the slurry velocity is higher, the particle-wall interaction force is higher as shown in the legends.

Fig. 6.14 shows the peak magnitude of the maximum impact force at different

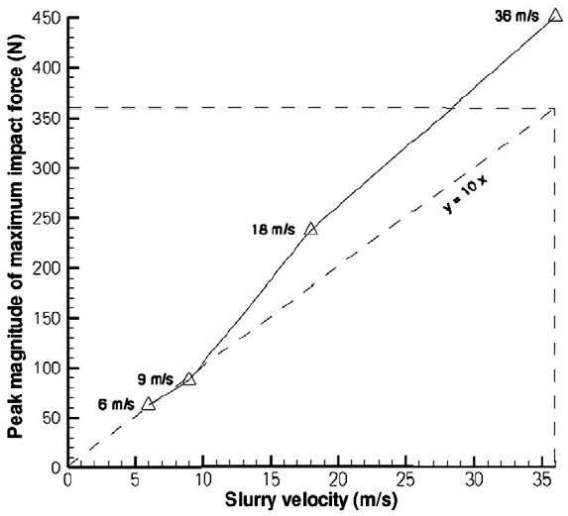

Figure 6.14: Peak magnitude of the maximum impact force at different slurry velocities.

slurry velocities. The peak magnitude of the maximum interaction force at slurry velocity 36 m/s is approximately 7.2 times higher than that in standard case, while the velocity is 6 times higher than the velocity in standard case (6 m/s). It can be seen from Fig. 6.14 that when the slurry velocity increases from 6 m/s to 9 m/s, the peak magnitude of the maximum impact force increases following a linear way; whereas the peak magnitude of the maximum impact force increases faster than the linear case when the slurry velocity increases from 9 m/s to 18 m/s and 36 m/s.

Fig. 6.15 illustrates the max impact force distribution at different slurry velocities versus the location in elbow. It can be seen from Fig. 6.15 that the interaction force is generally higher when the slurry velocity is higher, and 3 peaks were observed at approximately 15^o, 40^o and 89^o according to the trend of the lines. The first two peaks are due to the direct strike of particles from the horizontal pipe, and the fluidâsolid drag force in the elbow makes the location of the second peak move downstream from the intersection point of the centerline of the inlet flow and the outer wall of the extrados. The third peak is due to the centripetal force. In this study, we focus on the locations and the impact force on the former two peaks caused by direct strike of particles. When the slurry velocity is 6 m/s, the maximum erosive locations are observed at 15^o and 42.5^o, the interaction force is 48.2 N at first peak and 61.8 N at the second peak; when the slurry velocity is 9 m/s, the maximum erosive locations are observed at 17.5^o and 42.5^o, the interaction force is 87.5 N at the first peak and

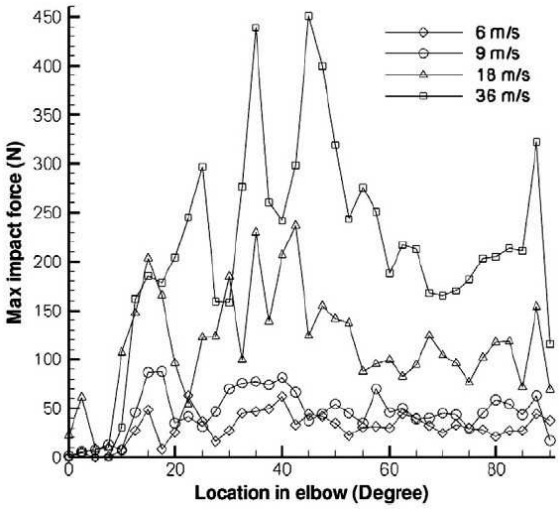

Figure 6.15: The max impact force distribution on the outer wall of the elbow at different fluid velocities.

81.0 N at the second peak; when the slurry velocity is 18 m/s, the maximum erosive locations are observed at 15^o and 45^o, the interaction force is 202.8 N at the first peak and 236.3 Nat the second peak.When the slurry velocity is 36 m/s, the maximum erosive locations are observed at 15^o and 47.5^o, the interaction force is 185.0 N at the first peak and 450.6 N at the second peak. It can be seen from Fig. 6.15 that location of the first peak does not change very much when slurry velocity increases, but the location of the second peak moves to downstream caused by fluidâsolid drag force when slurry velocity increases, which means that the lower layer of the particle flux from the inlet pipe strikes on the elbow directly then forms the first peak and the upper layer of the particle flux was dragged deeper into the elbow by the slurry flow and results in the location of the second peak moving deeper downstream, this trend is consistent with the experimental results by [6] and [14].

6.5.4 Effect of the bend orientation on the puncture point location

In this section, to study the effect of the bend orientation on the puncture point location, simulations were conducted by changing the direction of the gravity action and whereas the rest of the parameters are the same as the standard case. For the sake of comparison, in this section, results are drawn in this way that the inlet pipe was always at the left-down corner of the picture, the pipe which has the same direction

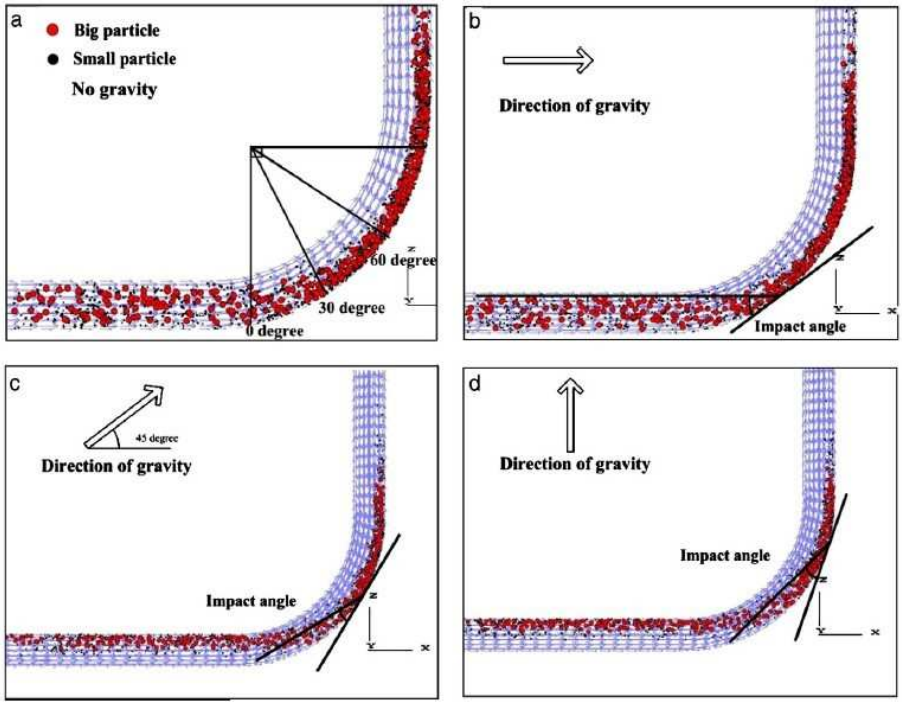

Figure 6.16: Spatial distribution of particles in: (a) no gravity considered pipe; (b) vertical to horizontally downward pipe; (c) horizontal to vertically inclined downward pipe; (d) horizontal to vertically downward pipe.

with the gravity force was regarded as a vertical pipe, while the pipe which is perpendicular to the gravity force was regarded as a horizontal pipe. Generally, the flow pattern has a great influence on the puncture point location, however it is extremely difficult to observe the flow pattern or obtain the interaction force in experiments online. Fig. 6.16(a), (b), (c), (d) indicates the particle movement in: no gravity considered (standard case), vertical to horizontally downward, horizontal to vertically inclined downward and horizontal to vertically downward pipe, respectively. In Fig. 6.16(a), the gravity action is ignored, it is shown that an obvious segregation is formed in the elbow and the particles glide cling to the outer wall due to the centripetal force. In Fig. 6.16(b), the gravity force has the same direction with the inlet pipe so has little effect on particle pattern in the inlet pipe, the gravity action results in the segregation layer of particles in the elbow thinner than that in Fig. 6.16(a), the impact angle is similar with that in the standard case. The effect of gravity action

on the particles in the inlet pipe can be observed in Fig. 6.16(c) and (d), where the gravity force leads the particles to settle down on the bottom of the inlet pipe. In the elbow, the gravity force results in most of the particles moving away from the central axis of the horizontal pipe, the particle concentration region moves deeper into the bend due to sum action of gravity and slurry drag force. This movement makes the first impact point of the particle flux move deeper into the bend and leads to a decrease of particle impact angle. This kind of biased particle distribution was also discussed in Deng's experiments [15].

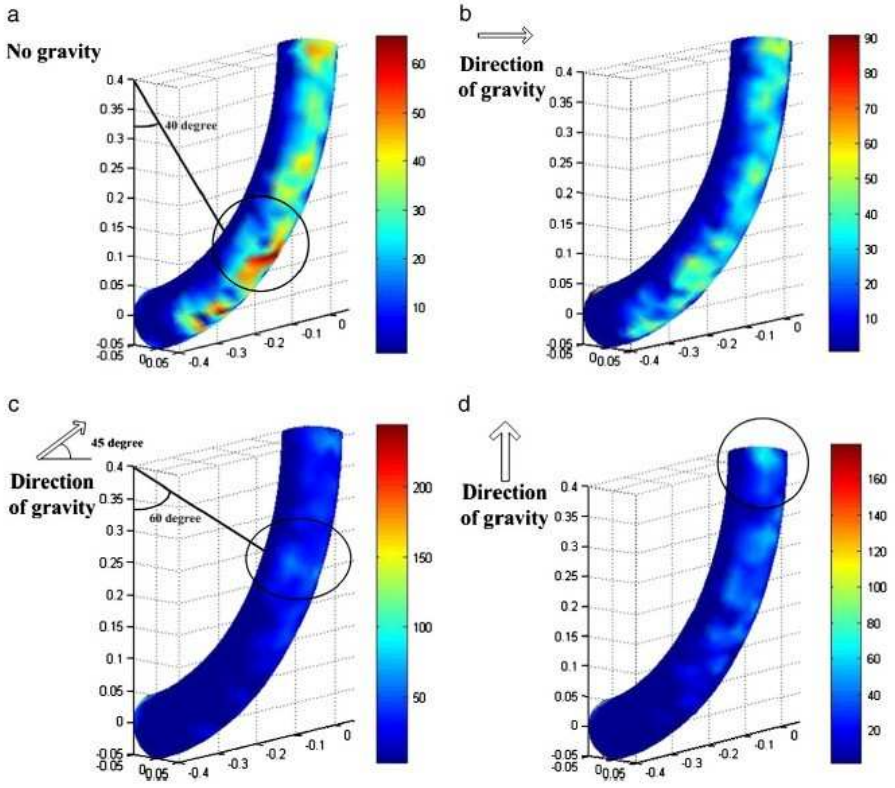

Figure 6.17: The maximum impact force (N) distribution of the elbow from the bottom view of: (a) no gravity considered pipe; (b) vertical to horizontally downward pipe; (c) horizontal to vertically inclined downward pipe; (d) horizontal to vertically downward pipe.

Fig. 6.17 shows the maximum impact force distribution corresponding to Fig. 6.16.

In Fig. 6.17(a), when the gravity action is ignored, the puncture point is observed at approximately 42^o. In Fig. 6.17(b), the puncture point location is not obvious. This is due to the gravity action, the gravity force prevents the particles from bouncing back and makes the particles still gliding cling to the outer wall closely as shown in Fig. 6.16(b), therefore a durative wear takes place at nearly the entire outer wall of the elbow. In Fig. 6.17(c), the puncture point location is observed at approximately 60^o, 20^o downstream of the puncture point location in Fig. 6.17(a). And in Fig. 6.17(d), the puncture point location is observed at approximately 90^o or further. The focus of this study is on the wear process on the elbow, so wear pattern was only investigated in this region.

Fig. 6.18 shows the maximum impact force distribution at different bend orientations versus the location in elbow and compared with the standard case. It can be seen from Fig. 6.18(b) that the average magnitude of max impact force in the vertical to horizontally downward pipe is similar with that in the standard case,whereas the amplitude is smaller due to the gravity action, the interaction force from 60^o to 90^o is higher than that in the standard case. In Fig. 6.18(c), the puncture location is observed at approximately 60^o. The puncture location in Fig. 6.18(d) is observed at approximately 72^o. From the four pictures in Fig. 6.18, it can be seen that the puncture point location is indeed significantly influenced by the bend orientation, the gravity force makes the puncture point location move deeper in a horizontal to vertically downward pipe, this phenomenon is consistent with the experimental results in [15]. Note that the interaction force at 0^o-12.5^o in Fig. 6.18(c) and 0^o-27^o in Fig. 6.18(d) is zero, which confirms that the gravity action makes the first impact point of the particle flux move deeper into the bend. However it shows in our results that the impact force at the puncture point location is lower than that in the standard case, this is different from the conclusion obtained in [15]. Deng [15] proposed that the horizontal to vertically downward pipe has the shortest service life than other bend orientations. However the impact force obviously depends on the bend radius to pipe diameter ratio and the slurry velocity employed. Suppose that in a horizontal to vertically downward pipe, given a sufficient low slurry velocity, the particles will directly drop down into vertical pipe, without any contacts forming between the particles and the outer wall of the elbow. Furthermore, the fluid velocity in [15] is much higher than that in this study, and gas was employed as the carrier phase in [15] while the carrier phase employed in this study is liquid.

6.6 Concluding remarks

Numerical simulations based on CFD and DEM have been conducted to study the solidâfluid multiphase flow problem in fluid transportation progress. Effects of the slurry velocity, bend orientation and angle of elbow on the puncture location were

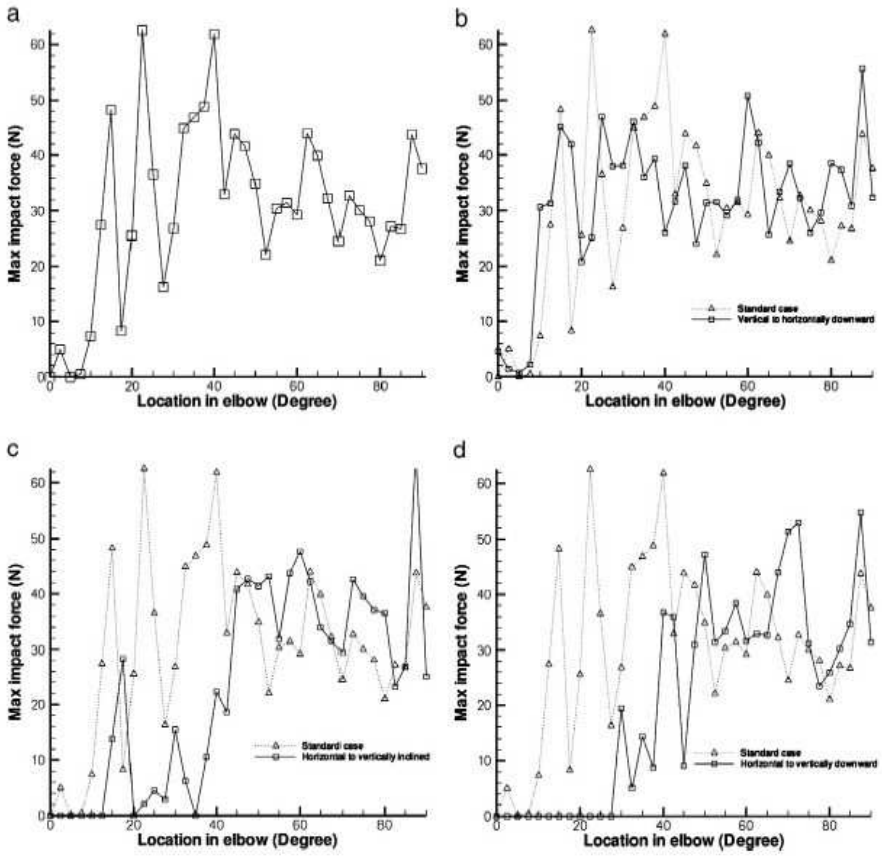

Figure 6.18: The maximum impact force distribution on the outer wall in: (a) no gravity considered pipe; (b) vertical to horizontally downward pipe; (c) horizontal to vertically inclined downward pipe; (d) horizontal to vertically downward pipe.

discussed.

According to the results of the analysis, the following conclusions can be made:

The puncture point location is influenced by the slurry velocity, the location of the maximum erosive location moves to downstream when slurry velocity increases. The impact force is higher when the slurry velocity is higher.

The puncture point location is significantly influenced by the bend orientation. In this study, the gravity force makes the segregation layer thinner in the vertical to horizontally downward pipe compared with that in no-gravity case. In the horizon-

tal to vertically downward pipe, the gravity action leads the particles to settle down on the bottom of the horizontal pipe and results in most of the particles moving away from the central axis of the horizontal pipe in the elbow. The gravity force makes the particle concentration region moves deeper into the bend due to sum action of the gravity and slurry drag force. This movement makes the first impact point of the particle flux move deeper into the bend.

References

[1] T Bo Anderson and Roy Jackson. Fluid mechanical description of fluidized beds. equations of motion. *Industrial & Engineering Chemistry Fundamentals*, 6(4):527–539, 1967.

[2] D. Gidaspow. Multiphase flow and fluidization. *San Diego, USA: Academic Press*, 1994.

[3] Sabri Ergun. Fluid flow through packed columns. *Chem. Eng. Prog.*, 48, 1952.

[4] C Yu Wen and YH Yu. Mechanics of fluidization. 2012.

[5] Di Felice R. The Voidage Function for Fluid-particle Interaction Systems. *International Journal on Multiphase Flow*, 20:153–159, 1994.

[6] Quamrul H Mazumder, Siamack A Shirazi, and Brenton S McLaury. Prediction of solid particle erosive wear of elbows in multiphase annular flow-model development and experimental validations. *Journal of Energy Resources Technology*, 130:023001, 2008.

[7] Lai Yeng Lee, Tai Yong Quek, Rensheng Deng, Madhumita B Ray, and Chi-Hwa Wang. Pneumatic transport of granular materials through a 90 bend. *Chemical Engineering Science*, 59(21):4637–4651, 2004.

[8] N Huber and M Sommerfeld. Characterization of the cross-sectional particle concentration distribution in pneumatic conveying systems. *Powder Technology*, 79(3):191–210, 1994.

[9] ZJ Zhao. *Construction technology of concrete pumping*. Beijing:China Architecture Building Press, 1988.

[10] Suhas V Patankar. *Numerical heat transfer and fluid flow*. Taylor & Francis, 1980.

[11] Avi Levy and David J Mason. The effect of a bend on the particle cross-section concentration and segregation in pneumatic conveying systems. *Powder technology*, 98(2):95–103, 1998.

[12] Ali Yilmaz and Edward K Levy. Formation and dispersion of ropes in pneumatic conveying. *Powder Technology*, 114(1):168–185, 2001.

[13] KD Kafui, C Thornton, and MJ Adams. Discrete particle-continuum fluid modelling of gas–solid fluidised beds. *Chemical Engineering Science*, 57(13):2395–2410, 2002.

[14] S Selmer-Olsen. Medium pressure flow studies of particulated and concurrent annular gas/liquid flow with relevance to material loss in unprocessed hydrocarbon systems. In *Third International Conference on Multiphase Flow, Paper*, number K4, 1987.

[15] T Deng, M Patel, I Hutchings, and MSA Bradley. Effect of bend orientation on life and puncture point location due to solid particle erosion of a high concentration flow in pneumatic conveyors. *Wear*, 258(1):426–433, 2005.

Chapter 7

Conclusions and future work

Abstract.

In the last chapter of this thesis, the main conclusions and future work were presented. The findings were listed corresponding to each chapter as where they were and followed by the work that can be done in the future.

7.1 Main conclusions

7.1.1 Chapter II

Parallelization of a serial discrete particle algorithm titled Trubal was carried out by following two steps: (1) Reconstruction of the static storage structure; (2) An essential parallelism on the relative newer code using shared memory without bank conflict and texture memory to maximize the frequency of GPU memory bandwidth based on a CPU-GPU heterogeneous architecture. The numerical cases were assessed in two platforms (i) NVIDIA Tesla C2050 card together with Intel Core-Duo 2.93 GHz CPU and (ii) NVIDIA Tesla K40c card along with Intel Xeon 3.00GHz CPU, respectively. Numerical results showed that the final version parallel code gave a substantial acceleration on the Trubal. By simulating 6000 and 60000 two-dimensional particles using a NVIDIA Tesla C2050 card together with Intel Core-Duo 2.93 GHz CPU, average speedups of 4.69 and 12.78 under platform C2050 and 6.52 and 18.60 under platform K40c in computational time were obtained, respectively. And higher speedup was achieved in three-dimensional simulation containing 20000 particles where an average speedup of 12.90 under platform C2050 and 19.66 under platform K40c in computational time were obtained. Our results reveal that the efficiency of the final version parallel code increases with the particle number as well as the contact number. Three-dimensional simulation exhibits higher acceleration than two-dimensional one. However, the list-linked contact-detection algorithm in Trubal seems to limit the effect of current study to some extent, an essential reconstruction on this part will be our work in next step.

7.1.2 Chapter III

The effect of collisions on the particle behavior in a fully developed turbulent flow in a square duct was investigated via DNS-DEM. The particle transportation by turbulent flow was studied firstly in the absence of the gravitational effect. Then, particle deposition from turbulent flow in a horizontal square duct was studied. The effect of the inter-particle collisions on the particle suspension rate and final stage of particle distribution on the duct floor were discussed. According to the results, the following conclusions can be made.

In the particle transportation process, the inter-particle collisions hardly affect the behavior of the 50 μm and 100 μm particles through the whole duct as well as the 500 μm particles near duct center. However, the particle interaction plays an important role in the distribution of the 500 μm particles especially in the near-wall regions. The inter-particle collisions enhance the particle diffusion in the direction perpendicular to streamwise flow and make the particles distribute more uniformly near the wall. This trend increases with the particle number. The 100 μm and 500 μm

particles show streaky distributions in the near-wall region and tend to concentrate to the corners. In the region very close to the wall, there are more particles in the case with collisions than without collisions.

In the particle deposition process, the gravity, collisions and secondary flow effects are all influential in determining the particle behaviors in a turbulent square duct flow. For the $50\ \mu m$ particles, the secondary flow plays the major role in determining their distribution. For the 500 μm particles, it is the gravity that dominates particle behavior and deposition. The 50 μm particles deposit more efficiently near the side walls of the duct whereas the 100 μm and 500 μm particles preferentially deposit near the center of the duct floor. The inter-particle collisions play a role like relaxation that try to return the perturbed system into equilibrium. In the inner regions, the inter-particle collisions increase the deposition rates of the $50\ \mu m$ particles but do not alter the behaviors of the 100 and 500 μm particles. In the region close to the duct floor, the particle resuspension rates are significantly enhanced by the collisions.

The final distribution of the particles on the duct floor is a combination consequence of the gravitational, secondary flow and inter-particle collision effects. For the 50 μm particles, the secondary flow plays the major role in determining their distributions and make the small particles concentrate near the duct center, the inter-particle collisions enhance this preferential concentration. For the 100 μm and 500 μm particles, the gravitational and inter-particle collision effects play the major role in determining the final distributions. It is shown a nearly uniform distribution when the inter-particle collisions are not considered. The particles move towards the bisector of the duct floor when they approach the bottom. However, the medium-sized and large particles show different behaviors during the movement. The large particles tend to jump with the bounce-back height decreasing with the collisions times while the medium-sized particles are likely to roll.

Through the work, it is clearly shown that the particle behavior can be affected by the collisions. As stated by Yu and Xu [1]: "At this stage of development the difficulty in particle-fluid flow modeling is mainly related to the solid phase rather than the fluid phase." Inter-particle collisions may play a key role in particle-fluid systems especially when the particles are densely packed. Therefore, it is essential to use a felicitous method to treat the particle collisions accurately and efficiently [2]. From this point of view, the DNS-DEM scheme is a promising solution on the particle-laden turbulent flow.

7.1.3 Chapter IV

This chapter presented a novel coupled LBM-IBM-DEM methodology for the numerical simulation of particle-fluid problems. The fluid field was solved by LBM, the hydrodynamic interactions between fluid and particles were realized through

the momentum exchange of the particles. The coupling scheme preserves the merits of LBM and IBM by using two unrelated computational meshes, an Eulerian mesh for the flow domain and a Lagrangian mesh for the moving particles. In particular the particle interactions were modeled by the DEM based on contact mechanics. The combined model has been validated by comparing the results with those from previous simulations on the settling of single sphere and the DKT problem, where good agreement was observed. It is observed that the collision scheme and parameters play a very important role in the accurate simulation of particulate flow and the LBM-IBM-DEM scheme can work well when the real physical parameters of the particles were adopted in the simulation. Finally, by conducting a numerical simulation of sedimentation we have shown that the proposed approach is a promising numerical solution for the simulation of particle-fluid interaction problems.

7.1.4 Chapter V

A PIBM for simulating the particulate flow in fluid was presented. Compared with the conventional momentum exchange-based IBM, no artificial parameters are introduced but the implementation is simpler. The PIBM is more suitable for simulating the motion of a large number of particles in fluid, particularly in the three-dimensional cases where particle collisions dominate since dozens of times speedup can be expected in two-dimensional simulation and hundreds of times in three-dimensional simulation under the same particle and mesh number.

Numerical simulations were carried out based on the LBM-PIBM-DEM scheme, our result of falling of single particle reveals that the settling velocity predicted by numerical simulation agrees well with the Stokes' law. Further multi-particle simulation results confirm that the LBM-PIBM-DEM scheme can capture the feature of the particulate flows in fluid and is a promising strategy for the solution of the particle-fluid interaction problems. By comparing two- and three-dimensional results, essential discrepancy was found due to the drawback of the two-dimensional assumption. Therefore, it can be concluded that the two-dimensional simulations may be good as a cheaper approach to capture the general features of the particle sedimentation in cavity, the three-dimensional simulations are necessary for an accurate description of the particle behaviors as well as the flow patterns.

Due to the fact that the calculation of the fluid-particle interaction force in PIBM is simply based on the momentum conservation of the fluid particle, the LBM-PIBM-DEM scheme can be easily connected with other CFD solvers or Lagrangian particle tracking method where the conventional IBM works.

7.1.5 Chapter VI

Numerical simulations based on CFD and DEM were conducted to study the solidâfluid multiphase flow problem in fluid transportation progress. Effects of the slurry velocity, bend orientation and angle of elbow on the puncture location were discussed. According to the results of the analysis, the following conclusions can be made:

The puncture point location is influenced by the slurry velocity, the location of the maximum erosive location moves to downstream when slurry velocity increases. The impact force is higher when the slurry velocity is higher.

The puncture point location is significantly influenced by the bend orientation. In this study, the gravity force makes the segregation layer thinner in the vertical to horizontally downward pipe compared with that in no-gravity case. In the horizontal to vertically downward pipe, the gravity action leads the particles to settle down on the bottom of the horizontal pipe and results in most of the particles moving away from the central axis of the horizontal pipe in the elbow. The gravity force makes the particle concentration region moves deeper into the bend due to sum action of the gravity and slurry drag force. This movement makes the first impact point of the particle flux move deeper into the bend.

7.2 Future work

7.2.1 Chapter II

A further speedup on Trubal is still needed. The list-linked contact-detection algorithm in Trubal seems to limit the effect of current study to some extent, an essential reconstruction on this part will be our work in next step.

7.2.2 Chapter III

The largest particle number considered in this chapter is 50000 which is far less than actual industrial scale. An essential parallelism of the DEM code is needed to improve the calculation efficiency. Furthermore, the collision between the particles and wall in the turbulent duct flow is quite interesting, the effect of duct geometry on the frequency of the particle-wall collision will be discussed more detailedly.

7.2.3 Chapter IV

The sedimentation of two particles was simulated and the sensitivity of the threshold to DEM was examined in this chapter showing that the numerical results were not sensitive to the lattice-units threshold. However, some suggestion on the selection of

threshold can be discussed more deeply. The LBM-IBM-DEM scheme will be further validated by simulating three-dimensional particulate flow. The tool developed in the second chapter will be adopted to achieve the target.

7.2.4 Chapter V

In the PIBM simulations, it shows that the velocity of the particle may suffer some fluctuations which increases with the ratio between the particle diameter and the lattice length. During the simulations we found that numerical instability may occur when the particle velocity is high, which seems to be a general weakness of the IBM family methods. More numerical experiments should be carried out in the future to fully assess the solution accuracy of the PIBM and find out the optimal ratio between the particle size and the lattice spacing. Since the bottle neck which limits the calculation speed of the LBM-PIBM-DEM scheme is from the PIBM part, thus, the procedure to evaluate the fluid-solid interaction force can be re-constructed based on the CPU-GPU heterogeneous architecture which is allowed due to the natural discrete features (local) of both LBM and DEM.

7.2.5 Chapter VI

A more accurate wear model is needed if the CFD-DEM is expected to be used in the actual engineering problems. Moreover, the rheological property of the fresh concrete should be considered in the model which is essential for simulating its flow behavior. More numerical and physical experiments should be carried out to calibrate the input parameters in the simulation. By using a CAD software, more complex systems can be built and other key processes in concrete engineering will be studied, such as mixing, transport and discharging.

References

[1] A B Yu and B H Xu. Particle-scale modelling of gas–solid flow in fluidisation. *Journal of Chemical Technology and Biotechnology*, 78(2-3):111–121, 2003.

[2] Hao Zhang, Yuanqiang Tan, Shi Shu, Xiaodong Niu, Francesc Xavier Trias, Dongmin Yang, Hao Li, and Yong Sheng. Numerical investigation on the role of discrete element method in combined LBM-IBM-DEM modeling. *Computers & Fluids*, 94(0):37 – 48, 2014.

Appendix A

Test case on the fluidized bed

Gas−particle flow in fluidization can be found in many industries and has been the subject of intensive research. Eulerian-Lagrangian model plays an important role in the development of a comprehensive understanding of the fundamentals of this phenomenon.

Table A.1: Parameters and bed geometry used for fluidized bed simulation

Solid phase		Gas phase	
Number of particles	1	Viscosity ($kg \cdot m^{-1} \cdot s^{-1}$)	1.0e-2
Density ($kg \cdot m^{-3}$)	7800	Density ($kg \cdot m^{-3}$)	935
Young's Module ($N \cdot m^{-2}$)	6.895e+10	Cavity height (m)	0.05
Poisson ratio ($N \cdot m^{-1}$)	0.33	Cavity width (m)	0.05
Friction coefficient	0.33	Lattice height (m)	0.0001
Diamater (m)	0.0003	Lattice width (m)	0.0001

In the Eulerian-Lagrangian models, the governing equations of surrounding fluid are solved prior to the calculation of particle motion in each computational timestep. Particle-fluid interaction force is obtained based on the empirical fit [1]. Then, the Lagrangian methodologies such as DEM [2] can be used to track the particle motion. Since the pioneering work of Tsuji [3], this kind of 'Continuum+Particle' model has been the subject of many studies [4, 5, 6, 7, 8, 9] among others on fluidized bed simulation. Firstly, two formulations of the fluid governing equation were proposed in [10], namely the so−called Model A: Pressure Gradient Force (PGF) and Model B: Fluid Density Model (FDB). Based on the research of Kafui et al. [4], Model A showed the best agreement with pressure drop-superficial gas velocity trends and minimum fluidization velocities predicted by empirical correlations. However, Feng et al. [5] made an assessment of Model A and B by comparing the physical experiments, by means of the results he argued that the model B was favored. Nowadays, both the models were adopted by researchers. Examples of Model A can be found

in: Hoomans et al. [6] and Olaofe et al. [7] investigated the bubble formation in 2D gas−fluidized bed. Xiang et al. [8] simulated the particle motion in vibrated fluidized beds. Examples of Model B can be found in: Feng at al. [5] investigated the particle segregation and mixtures in fluidized bed. Zhou et al [9] studied heat transfer in fluid bed reactors. In the current study, the continuum modeling proposed by Anderson and Jackson [11] was employed to evaluate the gas motion, Model B (FDB) [10] was adopted to approach the interaction force between the gas phase and the solid particles, while DEM [2] was used to describe the trajectory of particles and interactions between the particles or between particles and wall.

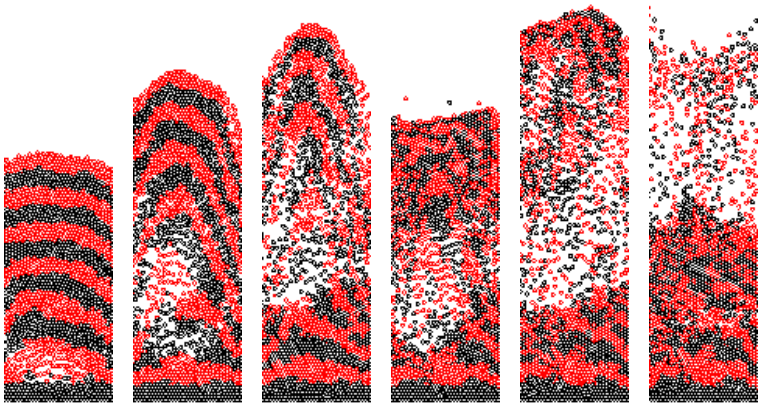

Figure A.1: The initial response of the bed to the introduction of gas injection at velocity 2.5 m/s.

Firstly, the coupling code was tested by simulating a pseudo-2D fluidized bed which was also conducted by Kafui et al [4] with TRUBAL. The most straightforward way is to use the same method as Kafui did. Therefore, we use finite-volume SIMPLER algorithm [12] with staggered grid to solve the Navier-Stokes equations, where the power-law upwinding scheme [12] was used for the convection-diffusion problem, explicit calculations of fluid velocity components was adopted when solving the temporal term. The simulations were performed under the conditions same with those used by Kafui et al [4], as listed in Table.1. The initial packing was obtained by random generation of particles without overlap in the bed, followed by a gravitational settling process for 2 s, initial porosity is 0.555. Gas is then injected into the bed from the bottom uniformly (2.5 m/s). For the boundary condition at the top,

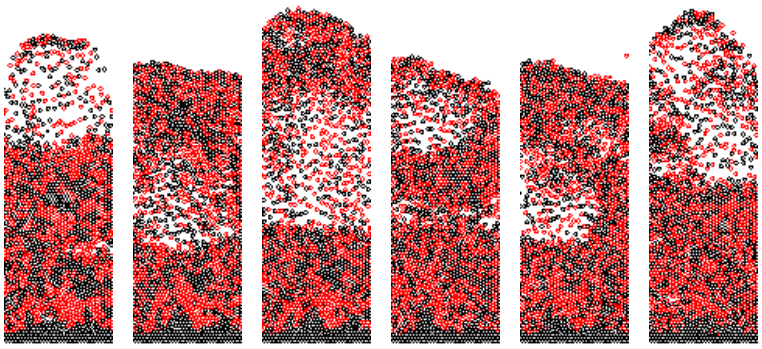

Figure A.2: Typical solid flow patterns at velocity 2.5 m/s.

the effect of the outflow on the inside domain is ignored, and the magnitude of the outflow was estimated using conservation of flow mass. The boundary conditions on the left and right sides: $\frac{\partial v}{\partial n} = 0$, where n stands for normal direction.

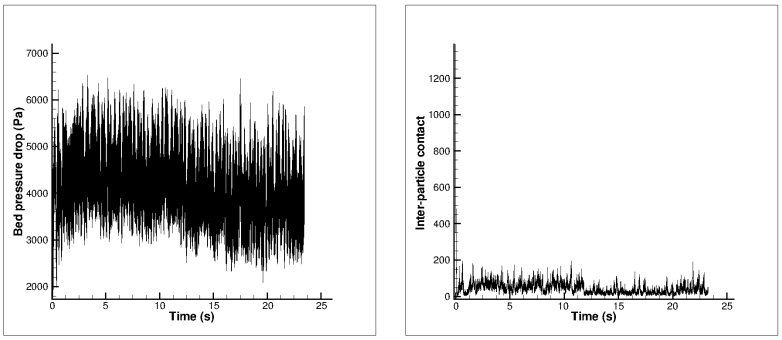

Figure A.3: Left: Variation of the bed pressure drop with time. Right: Interparticle contact fluctuations during simulation.

Figure A.1 illustrates the initial response of the bed to the introduction of the gas. The magnitude of bed expansions shown in Figure A.1 are higher than those of

Figure 4 (b) in the paper of Kafui et al [4]. That's because of that the initial velocity of the injected gas was $0.3m/s$ in the simulation of Kafui at al and then increased in steps to $3.0m/s$ whereas the velocity of the injected gas in current study is constantly $3.0m/s$ though the initial porosity is a little higher than that in [4]. Typical flow patterns during the fluidisation are shown in Figure A.2, it can be seen that a stable succession of bubble formation and disappearance is established. The bubbles travel at vertical speeds, some of them are carried all the way to the top of the bed while others are dissipated in the bed especially when they encounter falling particles. The degree of mixing attained after 23 s in this monodispersed particle system is considerable. In both Figure A.1 and A.2, a defluidized layer can be found. In this layer, the particles are entrapped by surrounding jetsam particles and cannot move upward. The succession can be also observed from the pressure drop across the bed and the number of interparticle contacts profile as shown in Figure 3. In our simulation, the mean pressure drops is 3.48 kPa, which is a little lower than the bed weigh pressure of 3.56 kPa, the pressure fluctuates around mean pressure drop with succession of the expansions. And because a higher injection velocity is adopted in this study, the contact number is obviously lower than that in [4]. Lower interparticle contact number stands for more drastical fluidisation.

References

[1] R Di Felice. The voidage function for fluid-particle interaction systems. *International Journal of Multiphase Flow*, 20(1):153–159, 1994.

[2] P. Cundall. A computer model for simulating progressive large scale movements in blocky system. *In: Muller led, ed. Proc Symp Int Soc Rock Mechanics, Rotterdam: Balkama A A*, 1:8–12, 1971.

[3] Y. Tsuji, T. Kawaguchi, and T. Tanaka. Discrete particle simulation of two-dimensional fluidized bed. *Powder Technology*, 77(1):79 – 87, 1993.

[4] K.D. Kafui, C. Thornton, and M.J. Adams. Discrete particle-continuum fluid modelling of gas-solid fluidised beds. *Chemical Engineering Science*, 57:2395–2410, 2002.

[5] YQ Feng and AB Yu. Assessment of model formulations in the discrete particle simulation of gas-solid flow. *Industrial & Engineering Chemistry Research*, 43(26):8378–8390, 2004.

[6] BPB Hoomans, JAM Kuipers, WJ Briels, and WPM Van Swaaij. Discrete particle simulation of bubble and slug formation in a two-dimensional gas-fluidised bed: a hard-sphere approach. *Chemical Engineering Science*, 51(1):99–118, 1996.

[7] OO Olaofe, MA Van der Hoef, and JAM Kuipers. Bubble formation at a single orifice in a 2D gas-fluidized bed. *Chemical Engineering Science*, 66(12):2764–2773, 2011.

[8] Li Xiang, Wang Shuyan, Lu Huilin, Liu Goudong, Chen Juhui, and Liu Yikun. Numerical simulation of particle motion in vibrated fluidized beds. *Powder Technology*, 197(1):25–35, 2010.

[9] ZY Zhou, AB Yu, and P Zulli. A new computational method for studying heat transfer in fluid bed reactors. *Powder Technology*, 197(1):102–110, 2010.

[10] D. Gidaspow. Multiphase flow and fluidization. *San Diego, USA: Academic Press*, 1994.

[11] T.B. Anderson and R. Jackson. A fluid mechanical description of fluidised beds. *Industrial and Engineering Chemistry Fundamental*, 6:527–539, 1967.

[12] S.V. Patankar. Numerical Hear Transfer and Fluid Flow. *Hemisphere, New York*, 1980.

Appendix B

From the physical units to the LB units

B.1 The dimensional NS equations

Here, we take the configuration of the DKT problem in Section 4.3.4 as an example. A 0.02 m (width) $\times$ 0.08 m (height) channel is defined.

Table B.1: Properties of particles and fluid.

Solid phase		Gas phase	
Number of particles	2	Viscosity ($kg \cdot m^{-1} \cdot s^{-1}$)	1.0e-3
Density ($kg \cdot m^{-3}$)	1010	Density ($kg \cdot m^{-3}$)	1000
Young's Module (GPa)	68.95	Channel height (m)	0.08
Poisson ratio ($N \cdot m^{-1}$)	0.33	Channel width (m)	0.02
Friction coefficient	0.33	Lattice height (m)	0.0001
Diameter (m)	0.002	Lattice width (m)	0.0001

And the physical properties of particles and fluid are shown in Table.B.1. The NS Equations with dimension read

$$\frac{\partial(\rho u)}{\partial t} + \nabla \cdot (u \otimes u) = -\nabla p + \nu \nabla^2 u + \rho g \tag{B.1}$$

where ρ is the density, u is the velocity, p is the pressure, ν is the viscosity and g is the gravitational acceleration.

B.2 From the physical units to the Non-dimensional units

Firstly, we pick the characteristic variables in physical scales as given in Table.B.2. Other variables can be derived using the basics ones, e.g., $t^c_{NS} = L^c_{NS}/u^c_{NS}$ and $p^c_{NS} = \rho^c_{NS} u^{c2}_{NS}$.

Physical scales		Non-dimensional scales	
Characteristic length	$L^c_{NS} = 1cm$	Non-dimensional length	$L^{'}$
Characteristic velocity	$u^c_{NS} = 10cm/s$	Non-dimensional velocity	$u^{'}$
Characteristic density	$\rho^c_{NS} = 1g/cm^3$	Non-dimensional density	$\rho^{'}$
Characteristic time	$t^c_{NS} = 0.1s$	Non-dimensional time	$t^{'}$

Table B.2: Characteristic and Non-dimensional variables in the physical systems.

Using the characteristic variables in NS scales to nondimensionalize Eq.B.5. We have the Non-dimensional form NS Equations

$$\frac{\rho^c_{NS} u^{c2}_{NS}}{L^c_{NS}} \frac{\partial(\rho^{'} u^{'})}{\partial t^{'}} + \frac{\rho^c_{NS} u^{c2}_{NS}}{L^c_{NS}} \nabla \cdot \left(u^{'} \otimes u^{'} \right) = -\frac{\rho^c_{NS} u^{c2}_{NS}}{L^c_{NS}} \nabla p^{'} + \nu \frac{u^c_{NS}}{L^{c2}_{NS}} \nabla^2 u^{'} + \frac{\rho^c_{NS} u^{c2}_{NS}}{L^c_{NS}} \rho^{'} g^{'} \tag{B.2}$$

Both sides of the equation are divied by $(\rho^c_{NS} u^{c2}_{NS})/L^c_{NS}$, we have

$$\frac{\partial(\rho^{'} u^{'})}{\partial t^{'}} + \nabla \cdot \left(u^{'} \otimes u^{'} \right) = -\nabla p^{'} + \frac{1}{Re} \nabla^2 u^{'} + \rho^{'} g^{'} \tag{B.3}$$

where $Re = \frac{u^c_{NS} L^c_{NS}}{\frac{\eta}{\rho^c_{NS}}} = \frac{u^c_{NS} L^c_{NS}}{\upsilon}$

B.3 From the LB units to the Non-dimensional units

The characteristic variables in LBM scales are given in Table.B.3. It should be stressed that the Characteristic velocity in the LBM scales is always 1, and the Non-dimensional variables in the NS and the LBM systems are the same.
Using the characteristic variables in LBM scales to nondimensionalize Eq.B.5. We have another Non-dimensional form NS Equations

$$\frac{\rho^c_{LB} C^2}{L^c_{LB}} \frac{\partial(\rho^{'} u^{'})}{\partial t^{'}} + \frac{\rho^c_{LB} C^2}{L^c_{LB}} \nabla \cdot \left(u^{'} \otimes u^{'} \right) = -\frac{\rho^c_{LB} C^2}{L^c_{LB}} \nabla p^{'} + \nu \frac{u^c_{LB}}{L^{c2}_{LB}} \nabla^2 u^{'} + \frac{\rho^c_{LB} C^2}{L^c_{LB}} \rho^{'} g^{'} \tag{B.4}$$

Both sides of the equation are divided by $(\rho^c_{LB} C^2)/L^c_{LB}$, we have

LBM scales		Non-dimensional scales	
Characteristic length	$L^c_{LB} = 1cm$	Non-dimensional length	$L^{'}$
Characteristic velocity	$C^c = 1cm/s$	Non-dimensional velocity	$u^{'}$
Characteristic density	$\rho^c_{LB} = 1g/cm^3$	Non-dimensional density	$\rho^{'}$
Characteristic time	$t^c_{LB} = 1s$	Non-dimensional time	$t^{'}$

Table B.3: Characteristic and Non-dimensional variables in LBM systems.

$$\frac{\partial(\rho^{'}u^{'})}{\partial t^{'}} + \nabla \cdot \left(u^{'} \otimes u^{'}\right) = -\nabla p^{'} + \frac{1}{Re}\nabla^2 u^{'} + \rho^{'} g^{'} \tag{B.5}$$

where $Re = \frac{CL^c_{LB}}{\frac{\eta}{\rho^c_{LB}}} = \frac{CL^c_{LB}}{\upsilon}$. Since $Re_{LB} = \frac{u^c_{NS}L^c_{LB}}{\upsilon}$, $Re = \dfrac{C}{u^c_{NS}}Re_{LB}$.

B.4 From the physical units to the LB units

Because the Non-dimensional variables can be achieved from two different scales, by which a bridge can be established between X_{NS} in the NS scales and X_{LB} in the LB scales. Let's say

$$\begin{array}{lllll}
\text{Re} & & & \Longrightarrow & Re_{LB} = \dfrac{u^c_{NS}}{C}Re \\
\text{Velocity} & u^{'} = \dfrac{u_{NS}}{u^c_{NS}} = \dfrac{u_{LB}}{C} & & \Longrightarrow & u_{LB} = \dfrac{C}{u^c_{NS}}u_{NS} \\
\text{Time} & t^{'} = \dfrac{L_{NS}/u_{NS}}{L^c_{NS}/u^c_{NS}} = \dfrac{L_{LB}/u_{LB}}{L^c_{LB}/C} & & \Longrightarrow & t_{LB} = \dfrac{u^c_{NS}}{C}t_{NS}
\end{array}$$

B.5 From the relaxation parameter to the physical time step

Since the relaxation time, τ, is related to the kinematic viscosity of the fluid by the following expression:

$$\nu = (2\tau - 1)/6 \tag{B.6}$$

The values for the relaxation time chosen in the simulations render the viscosity of the fluid equal to the viscosity of pure water. The choice of the viscosity also affects the time step of the computations through the following relationship:

$$\Delta t = (\Delta x)^2 \frac{\nu}{\nu_r} \tag{B.7}$$

where Δx is the physical grid size and ν_r is the physical fluid kinematic viscosity. In the DKT simulation, the relaxation time is $\tau = 0.65$, $\nu = 0.05$, $\Delta x = 0.0001m$ and $\nu_r = 10^{-6} m^2/s$. Therefore, $\Delta t = 0.0005s$.

List of Publications

This is an exhaustive list of publications carried out within the framework of the present thesis.

On International Journals

H Zhang, FX Trias, A Gorobets, A Oliva, D Yang, Y Tan, Y Sheng. Effect of Collisions on the Particle Behavior in a Turbulent Square Duct Flow. *Powder Technology. 269(2015),320-336.*

H Zhang, FX Trias, A Oliva, D Yang, Y Tan, Y Sheng. PIBM: Particulate Immersed Boundary Method for Fluid-Particle Interaction Problems. *Powder Technology. x(2015), y-z.*

H Zhang Y Tan, S Shu, X Niu, FX Trias, D Yang, H Li, Y Sheng. Numerical Investigation on the Role of Discrete Element Method in Combined LBM-IBM-DEM Modeling. *Computers & Fluids. 94(2014), 37-48.*

H Zhang, Y Tan, D Yang, FX Trias, S Jiang, Y Sheng. Numerical Investigation of the Location of Maximum Erosive Wear Damage in Elbow: Effect of Slurry Velocity, Bend Orientation and Angle of Elbow. *Powder Technology. 217(2012),467-476.*

X. Yue, ***H Zhang***, C Ke, C Luo, S Shu, Y Tan, C Feng. A GPU-based Discrete Element Modelling Code and Its Application in Die Filling. *Computers & Fluids. n(2015), x-y.*

Y Tan, ***H Zhang***, D Yang, S Jiang, J Song, Y Sheng. Numerical Simulation of Concrete Pumping Process and Investigation of Wear Mechanism of the Pipe Wall. *Tribology International, 46(2012), 137-144.*

Y Tan, R Deng, Y Feng, ***H Zhang***, S Jiang, X Xiao. Numerical Study of Concrete Mixing Transport Process and Mixing Mechanism of Truck Mixer. *Engineering Computations. n(2014), x-y.*

X Yue, ***H Zhang***, C Luo, S Shu, C Feng. Parallelization of a DEM Code based on CPU-GPU Heterogeneous Architecture. *Parallel Computational Fluid Dynamics, 405(2014), 146-159.*

G Cao, ***H Zhang***, Y Tan, J Wang, R Deng, X Xiao, B Wu. Study on the Effect of

Coarse Aggregate Volume Fraction on the Flow Behavior of Fresh Concrete via DEM. *Procedia Engineering. n(2014), x-y.*

C Ke, ***H Zhang***, X Yue, S Shu, Y Tan, C Feng. Numerical Simulation of the Emergency Brake Process in Granular Material Transportation using DEM. *Procedia Engineering. n(2014), x-y.*

X Xiao, Y Tan, ***H. Zhang***, S Jiang, J Wang, R Deng, G Cao, B Wu. Numerical Investigation on the Effect of the Particle Feeding Order on the Degree of Mixing using DEM. *Procedia Engineering. n(2014), x-y.*

Y Tan, G Cao, ***H. Zhang***, J Wang, R Deng, X Xiao, B Wu. Study on the Thixotropy of the Fresh Concrete using DEM. *Procedia Engineering. n(2014), x-y.*

FX Trias, A Gorobets, ***H Zhang***, A Oliva. New Differential Operators and Discretization Methods for Eddy-viscosity Models for LES. *Procedia Engineering 61(2013), 179-184.*

Y Tan, ***H Zhang***, M Li. Modeling and Simulation of Abrasive Flow in Chemical Mechanical Polishing using Discrete Element Method. *China Mechanical Engineering. 22(2011),597-603.*

Y Tan, J Song, ***H Zhang***, J Wang, R Deng, D Yang. Numerical Investigation of Wear Process on the Pipe Wall using Discrete Element Method. *China Mechanical Engineering. 25(2014), 2091-97.*

H.B. Wei, Y.Q. Tan, ***H. Zhang***, M Li. Numerical Simulation of Pressure Distribution of Flow Field in the Technology of Double-sided Polishing. *Chinese Journal of Applied Mechanics. 27(2010), 500-504.*

Papers submitted to International Journals

H Zhang, FX Trias, A Gorobets, A Oliva, Y Tan. Direct Numerical Simulation on Fully Developed Turbulent Flow in a Square Duct up to Re_τ=1200. *International Journal of Heat and Fluid Flow. n(2015),x-y.*

R Deng, Y Tan, ***H Zhang***, S Jiang, J Wang, X Xiao, W Gao. Numerical Study on the Discharging Homogeneity of Fresh Concrete in Truck Mixer: Effect of Motion Parameters. *Advanced Powder Technology. n(2015), x-y.*

C Ke, ***H Zhang***, X Yue, S Shu, Y Tan, C Feng. Numerical simulation of the emer-

gency brake process in granular material transportation. *Chinese Journal of Applied Mechanics. n(2014), x-y.*

On Conferences Proceedings

H Zhang, FX Trias, A Gorobets, A Oliva, D Yang, Y Tan. Numerical Investigation on Particle Resuspension in Turbulent Duct Flow via DNS-DEM: Effect of Collisions. 11th. World Congress on Computational Mechanics (WCCM XI). 2014. Barcelona, Spain.

G Cao, ***H Zhang***, Y Tan, J Wang, R Deng, X Xiao, B Wu. Study on the Effect of Coarse Aggregate Volume Fraction on the Flow Behavior of Fresh Concrete via DEM. The 7th World Congress of Particle Technology (WCPT7). 2014. Beijing, China.

C Ke, ***H Zhang***, X Yue, S Shu, Y Tan, C Feng. Numerical simulation of the emergency brake process in granular material transportation using DEM. The 7th World Congress of Particle Technology (WCPT7). 2014. Beijing, China.

Y Tan, G Cao, ***H. Zhang***, J Wang, R Deng, X Xiao, B Wu. Study on the thixotropy of the fresh concrete using DEM. The 7th World Congress of Particle Technology (WCPT7). 2014. Beijing, China.

X Xiao, Y Tan, ***H. Zhang***, S Jiang, J Wang, R Deng, G Cao, B Wu. Numerical investigation on the effect of the particle feeding order on the degree of mixing using DEM. The 7th World Congress of Particle Technology (WCPT7). 2014. Beijing, China.

Y.Q. Tan, J.H. Song, J.Q. Wang, ***H. Zhang***. Numerical Investigation of Concrete Pumping Process using Discrete Element Method. III International Conference on Particle-based Methods Fundamentals and Applications. 2013. Stuttgart, Germany.

FX Trias, A Gorobets, ***H Zhang***, A Oliva. New Differential Operators and Discretization Methods for Eddy-viscosity Models for LES. Proceedings of 25th International Conference on Parallel Computational Fluid Dynamics 2013. Changsha, China.

X Yue, ***H Zhang***, C Luo, S Shu, C Feng. Parallelization of a DEM Code based on CPU-GPU Heterogeneous Architecture. Proceedings of 25th International Conference on Parallel Computational Fluid Dynamics 2013. Changsha, China.

H Zhang, Y Tan, D Yang, R Deng. Numerical Modelling of Wear Investigation of the Pipe Wall in Pneumatic Conveying. Conference of bulk material handling conveyor. 2012. Hangzhou, China.

H Zhang, Y Tan, D Yang, Y Sheng. Eulerian-Lagrangian Modeling for Fluidized Bed. Conference of Computational Mechanics of Granular Materials. 2012. Zhangjiajie, China.

Y Tan, C Liu, ***H. Zhang***, X Xiao, M Xu. Discrete Element Method Simulation and Experimental Investigation on the Cutting Process of Soft Rock. Conference of Computational Mechanics of Granular Materials. 2012. Zhangjiajie, China.

S Jiang, Y Tan, ***H Zhang***, D Yang. Some Applications of the Discrete Element Method in Mechanical Engineering Process. Conference of Computational Mechanics of Granular Materials. 2012. Zhangjiajie, China.

Y Tan, R Deng, S Jiang, ***H Zhang***, X Xiao. The Numerical Simulation Research for Concrete Mixing and Conveying Process based on the Discrete Element Method. Conference of Computational Mechanics of Granular Materials. 2012. Zhangjiajie, China.

FX Trias, ***H Zhang***, A Gorobets, A Oliva. DNS and Regularization Modeling of a Turbulent Flow Through a Square Duct up to Re_tao = 1200. Proceedings of 24th International Conference on Parallel Computational Fluid Dynamics 2012. Atlanta, USA.

S Jiang, Y Tan, ***H Zhang***, D Yang. DEM Simulation of the Mechanical Properties of SiC Ceramic under Pre-stressing. II International Conference on Particle-based Methods Fundamentals and Applications. 2011. Barcelona, Spain.

H Zhang, FX Trias, Y Tan, D Yang, Y Sheng, A Oliva. Numerical Simulation of Particle-laden Turbulent Flow using Discrete Element Method. II International Conference on Particle-based Methods Fundamentals and Applications. 2011. Barcelona, Spain.

Y Tan, ***H Zhang***, D Yang, Y Sheng. Some Applications of Discrete Element Method in Tribology. Proceedings of 6th China International Symposium on Tribology. 2011. Lanzhou, China.

H Zhang, FX Trias, Y Tan, Y Sheng, A Oliva. Parallelization of a DEM/CFD Code for the Numerical Simulation of Particle-laden Turbulent Flows. Proceedings of 23th International Conference on Parallel Computational Fluid Dynamics 2011. Barcelona, Spain.